Durham E-Theses

Numerical Investigations of the Thermal State of Overhead Lines and Underground Cables in Distribution Networks

MAKHKAMOVA, IRINA

How to cite:

MAKHKAMOVA, IRINA (2011) *Numerical Investigations of the Thermal State of Overhead Lines and Underground Cables in Distribution Networks*, Durham theses, Durham University. Available at Durham E-Theses Online: http://etheses.dur.ac.uk/866/

Use policy

Numerical Investigations
of the Thermal State of Overhead Lines
and Underground Cables
in Distribution Networks

Irina Makhkamova

A Thesis presented for the Degree of

Doctor of Philosophy

Energy Group
School of Engineering and Computing Sciences
Durham University
UK
April 2011

Numerical Investigations of the Thermal State of Overhead Lines and Underground Cables in Distribution Networks

Irina Makhkamova

Submitted for the Degree of Doctor of Philosophy

April 2011

Abstract

As part of extensive activities on the reduction of CO_2 emissions, a rapid expansion of power generation using new more fuel efficient technologies (large, medium and embedded scale with combined heat and power (CHP) projects) and renewable energy (wind, biomass, solar PV) is currently taking place in numerous European countries, including the UK. The research presented in this thesis is a part of a UK government funded project, which aims to find answers to how to accommodate increased renewable energy into the distribution network. Current ratings, which are limited by the temperature of the conductors used in the distribution network, are based on worst case scenario conditions and are conservative. The temperature limits can be lifted if one takes into consideration the dynamic changes in the surrounding environmental conditions of the conductors. Implementation of real-time thermal rating of existing power systems could result in greater installed capacities of distributed generation (DG). This research aims to provide new insights into the thermal state of overhead line conductors (OHL) and underground cables (UGC) by using Computational Fluent Dynamic methods. An algorithm consists of building the geometry of the calculation domain, meshing, choosing a model, inputting initial conditions, initiation of the calculation, and analysing results.

A part of the UK power system was chosen by Scottish Power Energy Networks for monitoring essential data of OHL conductors in order to validate results of the temperatures of the conductors.

DECLARATION

The thesis summarises the results of a study carried out at Durham University. This thesis has not been submitted for any other degree or qualification before and represents all my own work.

Acknowledgements

NOMENCLATURE

Symbols

A	Cross-sectional area of conductor, mm^2
A'	Projected area of conductor (square feet per linear foot)
A_1	Constant
A_2	Constant
$\boldsymbol{a}$	Conductor cross-sectional area, m^2
B	Constant
B_1	Constant
B_2	Constant
C	Specific heat of soil, J/kg K
C	Capacitance per unit length, F/m
C_p	Heat capacity, J/kg K
c_p	Specific heat at constant pressure
c_v	Specific heat at constant volume
c	Volumetric thermal capacity of the material, J/m^3K
C_{w1}	Constants
C_{w2}	Constants
C_{w3}	Constants
d	Diameter of conductor, m
d	Diameter of a wire, m
$\dfrac{d\theta}{dx}$	Temperature gradient, K/m
D	External diameter of an OHL conductor, in
D	Sag, m
D	Diameter of circumscribing circle, m
D	Density of soil, kg/m^3
E	Energy, J
e	Internal energy, J

$\vec{F}$	External body forces
f	Frequency, H
f_{v1}	Viscous damping function
G_v	Production of turbulent viscosity in the near-wall region
g	Gravity constant, m/s^2
g	Thermal resistivity of soil, °C·m/W
Gr	Grashof number
H	Height of the roughness elements, m
(H/D)	Surface roughness
h_c	Convective heat transfer coefficient, W/m^{2}K
H_c	Altitude of sun, degrees
I	Current, A
I	Unit tensor
I	Current in the conductor, A
$\boldsymbol{I_{ac}}$	Conductor AC current, A
$\boldsymbol{I_{dc}}$	Conductor DC current, A
I_f	Final current, A
I_f	Final current, A
I_i	Initial current, A
I_i	Initial current, A
k	Conductivity, J/(kg K)
k	Kinetic energy of turbulence, J
k	Von Karman constant
k_j	Coefficient, which takes into account skin effects
$\boldsymbol{K_1 , K_2}$	Coefficients
K_{angle}	Cooling term factor
k_f	Thermal conductivity of air, W/(m·K)
k_f	Thermal conductivity of air at temperature T_{film}, W/(ft·°C)
L	Physical length of the conductor, m
L	Latent heat of evaporation of water, J/mol
M	Mass, kg
$\boldsymbol{M}$	Mass of conductor per unit length, kg/m
m_1	Constant
m_2	Constant

Symbol	Description
M_w	Gas/fluid molecular weight
n	Number of load-carrying conductors in the cable (conductors of equal size and carrying the same load)
n	Number of loops in the network
n	Constant
Nu	Nusselt number
Nu_{cor}	Corrected Nusselt number
p	Factor for apportioning the thermal capacitance of a dielectric
p	Pressure, Pa
$P(s), Q(s)$	Polynomials
P_c	Convection heat loss, per unit length per unit time, W/m
P_i	Ionization heat gain, per unit length per unit time, W/m
P_j	Time constant, s^{-1}
P_j	Joule heat gain, per unit length per unit time, W/m
P_k	Production of turbulence, J/m^3
P_M	Ferromagnetic heat gain, per unit length per unit time, W/m
P_r	Radiation heat loss, per unit length per unit time, W/m
Pr	Prandtl number
P_s	Solar heat gain, per unit length per unit time, W/m
P_t	Total heat input, W/m
$-\rho \overline{u'^2}$	Reynolds stresses, Pa
$-\rho \overline{v'^2}$	Reynolds stresses, Pa
$-\rho \overline{\omega'^2}$	Reynolds stresses, Pa
$-\rho \overline{u'v'}$	Reynolds stresses, Pa
$-\rho \overline{u'\omega'}$	Reynolds stresses, Pa
$-\rho \overline{v'\omega'}$	Reynolds stresses, Pa
$Q_i(t)$	Temperature rise at node i at time t, °C
Q_c	Thermal capacitance of conductor
Q_i	Total thermal capacitance of dielectric per conductor
Q_j	Thermal capacitance of outer covering
Qs	Ratio of losses in conductor and sheath to losses in conductor
Q_{sol}	Solar energy incident, W/m^2
Q_s	Total solar and sky radiated heat flux, W/ft^2
q	Heat flux, W/m^2

q_c	Convective heat loss, W/ft
q_r	Radiated heat loss, W/m
q_s	Heat gain from the sun, W/m
R	Resistance, Ω/m
R	Specific gas constant
R	AC resistance of the copper conductor, Ω/m
$R(T_c)$	AC resistance per linear foot of conductor at T_c, Ω/ft .
R_{ac}	AC resistance per unit length
R_{dc}	DC resistance per unit length
Re	Reynolds number
R_f	Roughness of conductor
R_u	Universal gas constant
S	Scalar measure of the deformation tensor
S	Global solar radiation
S	Span length, m
$S_{heat\ source}$	Source terms, W/m^3
Sh	Heat of chemical reaction or volumetric heat sources
Δs	Displacement vector from the upstream cell centroid to the face centroid
T	Temperature, K
t	Time, s
t_1	Time from the beginning of the step, s
T_1	Total thermal resistance of dielectric per conductor
T_1	Thermal resistance per unit length between one conductor and the sheath, K·m/W
T_2	Thermal resistance per unit length of the bedding between sheath and armour (K·m/W);
T_3	Thermal resistance per unit length of the external serving of the cable (K·m/W);
T_4	Thermal resistance per unit length between the cable surface and the surrounding medium;

T_3	Thermal resistance of outer covering
T_a	Ambient temperature, K
T_a	Ambient temperature, °C
T_{av}	Conductor mean temperature, °C
T_c	Conductor temperature, °C
T_A, T_B, T_C	Elements of equivalent thermal circuit
T_f	Film temperature, K
T_i	Initial temperature of the conductor, K
T_{ij}	**C**oefficient, °Cm/W
T_s	Temperature on the surface of the OHL conductor, K
$\boldsymbol{U_0}$	Voltage to earth, V
u, v, ω	Gas velocity components along x, y and z-axis, respectively, m/s
V_w	Velocity of air stream, ft/h
v	Wind velocity, m/s
$\widetilde{v}$	Transported variable
W_{ent}	Rate of energy entering the cable, W/m
W_{out}	Rate at which energy is dissipated by conduction, convection, and radiation, W/m
W_{int}	Rate of heat generated internally in the cable, W/m
ΔW_{st}	Rate of change of energy stored within the cable, W/m
W_c	Conductor losses including skin and proximity effects, W/m
W_d	Dielectric loss per unit length, W/m
W_I	Total loss per unit length of each cable in the group, W/m
x_{wa}	Mole fraction of water in air in the atmosphere
x_{ws}	Mole fraction of water in air in the atmosphere at the free surface of the water film
Y	Heights above sea level, m
Y_s	Correction factors for the skin effect
Y_p	Correction factors for the proximity effect
$Y_{\boldsymbol{v}}$	Destruction of turbulent viscosity in the near-wall region
$\boldsymbol{Z}$	factor, which allows for cable stranding and for the lay, $Z = 0.03$ for single core cables with cross-sectional area equal to or less than 500mm^2, and 0.04 for larger cables

Z_c	Azimuth of sun, degrees
Z_i	Azimuth of line, degrees

Greek symbols

α	Thermal diffusivity of soil, m^2/s
α	Temperature coefficient of resistance per degree K
α_s	Absorptivity of conductor surface
α_s	Velocity of sound, m/s
β	Thermal expansion coefficient
δ	Angle of attack
δ	The dielectric loss angle
δ	Thermal diffusivity of soil, m^2/s
δ_{ij}	Kronecker delta
ε	Emission coefficient
ε	Relative permittivity of the insulation
ε_0	Permittivity of free space
$\bar{\phi}$	Mean component
ϕ'	Fluctuating component
λ	Thermal conductivity, W/(m·K)
λ_f	Thermal conductivity of air, W/(m·K)
λ_1	Ratio of losses in the metal sheath to total losses in all conductors in the cable
λ_2	Ratio of losses in the armouring to total losses in all conductors in the cable
μ	Molecular viscosity, Pa·s
μ_t	Turbulent viscosity, Pa·s
μ_f	Absolute viscosity of air, lb/ft·h
v	Kinematic viscosity, m^2/s
θ	Effective angle of incidence of the sun's rays (degrees)
$\theta_{c\,max}$	Maximum operating temperature, ºC
θ_S	Absolute temperature on the surface of the cable, K
θ_{amb}	Ambient temperature, K
ρ_f	Density of air, lb/m^3

ρ	Density, kg/m^3
ρ	Thermal resistivity, K·m/W
ρ	Resistance, Ω/m
ρ	Resistivity, Ω·m
ρ	Thermal resistivity of soil, Km·/W
ρ_0	Air density at sea level, kg/m^3
ρ_0	Resistivity of conductor metal at 20 ºC, Ω· m
ρ_f	Density of air, lb/m^3
σ_B	Stefan Boltzmann constant, $\sigma_B = 5.67 \cdot 10^{-8}$ W/m^2·K^4
σ_k	Constant
τ	Thermal time constant of the conductor, s
$\vec{\tau}$	Stress tensor
$\left(\tau_{ij}\right)_{eff}$	Deviatoric tensor
$\tau_{xx}, \tau_{xy}, \tau_{xz}$	Shear stress, Pa
$\tau_{yx}, \tau_{yy}, \tau_{yz}$	Shear stress, Pa
$\tau_{zx}, \tau_{zy}, \tau_{zz}$	Shear stress, Pa

Acronyms

AAAC	All Aluminium Alloy Conductors
AAC	All – Aluminium Conductors
AACSR	Aluminium Alloy Conductors Steel Reinforced
AASC	Aluminium Alloy Stranded Conductor
AC	Alternating Current
ACAR	Aluminium Conductor Alloy Reinforced
ACSR	Aluminium Conductor Steel Reinforced
AWS	Automatic Weather Station
BCC	Bare Copper Conductors
CFD	Computational Fluid Dynamics
CHP	Combined Heat and Power
CIGRE	International Council on Large Electric Systems (Conseil International des Grands Reseaux Électriques)
CPU	Central Processing Unit
DC	Direct Current
DES	Detached Eddy Simulation
DG	Distributed Generation
DIUS	Department for Innovation, Universities and Skills
DNOs	Distribution Network Operators
DNS	Direct Numerical Simulation
ENA	Energy Networks Association
EPR	Ethylene Propylene Rubber Insulation
FANS	Favre-Averaged Navier-Stokes
FD	Finite Difference
FDM	Finite Differences Method
FEA	Finite Element Analysis
FEM	Finite Element Method
FVM	Finite Volume Method
HSM	Hybrid Sag Method
IEC	International Electrotechnical Commission
IEEE	The Institute of Electrical and Electronics Engineers
LES	Large Eddy Simulation

MDPE	Medium Density Polyethylene
MIND	Mass Impregnated Non Draining
N-S	Navier-Stokes (equations)
NSM	Numerical Sag Method
OHL	Overhead Lines
PILC	Paper Insulation Lead Covered
PV	Photo-Voltaic
PVC	Polyvinyl Chloride
RANS	Reynolds Averaged Navier-Stokes
RMSE	Root Mean Square Error
RNG	Renormalization-group
RSM	Stress Transport Model
SAW	Surface Acoustic Wave
SOU	Second Order Upwinding
SPEN	Scottish Power Energy Networks
T&D	Transmission and Distribution
TRXLPE	Tree Retardent XLPE
UDFs	User-Defined Functions
UGC	Underground Cables
WAsP	Wind Atlas Analysis and Application Program
XLPE	Crosslinked Polyethylene
2-D	2 dimensional
3-D	3 dimensional

CONTENTS

LIST OF FIGURES

LIST OF TABLES

CHAPTER 1

INTRODUCTION

As part of extensive activities to reduce CO_2 emissions, a rapid expansion of power generation using new more fuel efficient technologies (large, medium and embedded scale, combined heat and power (CHP) projects) and renewable energy (wind, biomass, solar PV) is currently taking place in numerous European countries including the UK.

The growth of renewable power generation can result in some cases in significant increases in the power flow requirements placed on transmission and distribution (T&D) networks. An attribute of current distribution networks are their predominantly passive nature, which can be explained by historical reasons in [1, 2]. Ilic suggested in [1] that "instead of over-designing capacity, much could be gained by using the right resources at the right time and in the right place within the network", and "one needs a careful balance between operating the system very close to its limits and maintaining the right amount of reserve capacity". Therefore, operating closer to the system's reliability limits allows reducing "cost of meeting customers' needs". For that reason improved knowledge of the temperature

distribution within conductors and of the speed at which the temperature changes will allow effective management of electrical networks. Historically the most important motivation for utilities has been to use proven technologies to meet an estimated demand, assuming the worst case environmental conditions for maximum load, so resulting in conservative ratings. Therefore the validity of the standards which were based on such assumptions is a subject of study for many researchers [3-7].

Strbac in [7] shows that the future development of power systems requires major changes to the overall design philosophy. The structure of the present electricity transmission and distribution networks was designed and particularly adapted for transmission and distribution of large amounts of power and assures electrical system reliability. The impact of the growth of distributed generation (DG) into distribution networks requires significant changes in the development of electricity systems in order to fully integrate DG and to share the responsibility for delivery of system support services (e.g. load, frequency and voltage regulation).

1.1 Background

Distribution network operators (DNOs) - the companies licensed to distribute electricity in the UK - face a number of challenges, not least those due to load growth, distributed generation growth and the problem of environmental opposition to building new infrastructure. Therefore, it has become very important to try to increase the utilisation of existing power system infrastructure in a safe and cost effective manner. This research supports this aim by investigating the heat transfer mechanisms associated with overhead lines (OHL) and underground cables (UGC).

This research forms part of a Department for Innovation, Universities and Skills (DIUS) project which seeks to evaluate a prototype Distributed Generation (DG) output controller, which will make use of dynamic thermal ratings derived from component power system models and relevant meteorological data.

Large power transfer benefits can be achieved by a small increase in ampacity. As a result, many utilities are considering operating their overhead conductors at utilisation levels that would have been thought unrealistic a few years ago.

In the majority of cases the components of the DN operate in very complex steady or unsteady conditions, which make it difficult to use simplified heat transfer correlations obtained for simple cases to predict the thermal state of the components.

1.2 Research objectives

The research described in this thesis aims to provide new insights into the thermal state, not only of single OHL conductors but also of complex systems, such as a group of UGC, for which it is difficult to obtain experimental data. This information could be employed by electrical network companies in their activities regarding the evaluation of existing operating methods and quantification of the scope in ampacity that could be exploited.

Modern OHL conductors can successfully operate at temperatures that exceed 100 ^{0}C. The higher levels of current create increased electrical losses due to resistance to the flow of current, which results in decreasing ground clearances. Additionally, overhead lines are quite often exposed to solar radiation, which also

increases the temperature of the line. Heat from the conductors is dissipated by the circulation of air surrounding the lines (free convection and wind) and also by the re-radiation mechanism. At these high load conditions monitoring and the prediction of the thermal state of components in the electrical distribution network becomes of paramount importance for the safe operation of the network and the reliable supply of electricity to consumers.

The serious consequence of the excessive temperature levels in overhead lines is the resulting increasing sag due to the ability of the conductor material to expand during heating; as a result the power lines elongate and sag. For underground cables high temperatures may cause the destruction or degradations of the insulation layers.

Numerical simulations of heat transfer processes could be an attractive alternative to experimental investigations, which are usually costly and time consuming. Numerical derivation of the series of refined heat transfer correlations for accurate estimation of the thermal state of the main components of the electrical distribution network will be the main and novel contribution to academic and industrial knowledge in the field arising from this research.

The main research objectives of this Doctoral Thesis are:

- To investigate heat transfer processes using 2 and 3 dimensional (2-D and 3-D) CFD models of an overhead line conductor and 2–D model of an underground cable for steady-state and transient conductor temperature;

- To identify the potential for increasing the ampacity of existing overhead lines and underground cables.

In order to achieve this goal the following problems must be solved:

- To analyse steady-state heat transfer processes analytically;

- To calculate steady-state / transient heating of electrical conductors characteristics using 2-D and 3-D CFD models.

- To validate the obtained results by using available experimental data and existing standards based on lumped parameter models.

1.3 Thesis structure

The thesis is structured in the following way:

Chapter 2: Literature review

This chapter summarises the key points of existing practice used by DNOs for estimation of the thermal state of major components of the distribution network, and also presents results of the critical analysis of published theoretical and experimental investigations in the field. The critical analysis of the existing methods and published results was performed to recognise limitations in the existing practice and identify ways to improve accuracy in the determination of the thermal state of electrical components which operate under both steady and transient conditions.

Chapter 3: Lumped parameter modelling

This chapter describes the theoretical background of mathematical modelling using IEEE and CIGRE methods for the determination of the thermal state of OHL conductors in steady-state and transient modes of operation. The above methods are based on application of the energy balance equation, assuming that the temperature in conductors is uniformly distributed in its volume. The section also presents an

example of the calculation of the thermal state of an OHL conductor using the CIGRE method.

Chapter 4: Basic theoretical background of numerical methods

This chapter describes a set of governing equations including continuity, momentum and energy equations, and major numerical methods used for heat transfer investigations of the components of electrical networks. These equations, along with appropriate boundary conditions, provide a solution at any point in the flow field. In the absence of analytical methods, the governing equations are usually solved using advanced numerical methods, such as Finite Differences Method (FDM), Finite Element Method (FEM) and Finite Volume Method (FVM). Turbulence modelling and the choice of the turbulence models in Fluent and associated Solution Procedure using the Finite Volume Method are described in detail.

Chapter 5: Steady-state thermal behaviour of overhead lines

Most wind farms in the UK are connected to the 33 kV system and there is a tendency to connect larger wind farms to 132 kV system [1]. The Lynx type conductor was chosen as a subject of the study because it is commonly used in distribution networks at these voltage levels. This chapter shows the geometry and calculation scheme of the Lynx conductor and also presents the conductor temperature results obtained for cross and parallel wind conditions, including the impact of meteorological factors and temperature dependent material properties.

Chapter 6: CFD modelling of the transient thermal behaviour of overhead lines

A discussion of the results obtained using CFD models for overhead lines are

presented in this chapter. CFD modelling results were obtained for transient responses when the current instantaneously increases from 433 A, which is a typical current rating for Lynx conductors, to 866 A. Additionally, three intermediate cases, when the final current increased was 25%, 50% and 75% greater than the initial current, were investigated. Four more cases were modelled when the current instantaneously decreased by 25%, 50%, 75% and 100%. A 3-D model was used to simulate the transient response for parallel wind conditions when the current changes from 433 A to 866 A. Results for the transient response at cross wind and parallel wind conditions are compared.

Chapter 7: Validation - comparison with industrial standards and experimental data
 from Scottish Power

This chapter describes investigations into the possibility of increasing the thermal rating of OHL conductors in distribution networks. Three published papers also support a statement that the ratings, which are used in industrial standards, are static and conservative and can be safely increased if the cooling effect of the wind could be adequately taken into consideration. The dynamic nature of the temperature of the conductor can be modelled using the CFD technique taking into consideration a number of changes in weather conditions and also in properties of the conductor. The input data files with wind velocity and current profiles are created with a 30-second time step and incorporated into a subroutine which in turn was integrated with the CFD solver.

Chapter 8: Modelling of the steady thermal state of underground cables

The objectives of investigations carried out in this chapter were to obtain numerical

results regarding the thermal state of the single 33 kV copper conductor cable buried in the soil in different configurations, taking into account the physical properties of the soil for a range of values of moisture content for summer and winter conditions. In this chapter a CFD model of the cable, consisting of a calculation scheme of the cable and the surrounding soil, and taking into account heat losses, is described. The results on the temperature obtained using the CFD technique are compared with the maximum temperatures recommended in corresponding industrial standards. Additionally, the effect of the wind just above the ground level on the temperature of the cables buried in soil is investigated in order to explore the possibility of increasing the load on underground cables.

Chapter 9: Modelling of the transient thermal state of an underground cable

In this chapter 2-D unsteady CFD simulations of the thermal state of a copper underground power cable are carried out for several cases when the magnitude of the electrical current passing through the conductor instantaneously changes from 470 to 940 A.

Chapter 10: Conclusions and Suggestions for further work

The objective of this thesis was to explore the thermal limits of OHLs and UGCs, which are the main cause of restriction of transferred electrical power. This chapter draws conclusions regarding the scope for transmitting additional power which could be exploited if the meteorological factors, such as the wind velocity, are taken into consideration in analysing the process of heat transfer around OHL and UGC conductors. Finally, a number of suggestions are proposed for further investigations in this field.

CHAPTER 2

LITERATURE REVIEW

Most of new generation technologies are embedded into electrical distribution network and this leads to a significant rise of transferred energy. Upgrading and erecting new lines is often costly for network operators and, consequently, there is pressing a necessity to operate transmission and distribution lines at higher currents and, as a result, at higher temperatures.

Accuracy of methods for the estimation of the thermal state of conductors is crucial, particularly in situations when the network is exploited under high load conditions. The existing monitoring methods require human presence in the vicinity of the line, together with transportation facilities during undertaking readings.

The main detection techniques based on physical measurements are: the ultrasonic detection method, the measurement of the corona pulse current inconsistency, using the partial discharge detector, the infrared inspection of overhead transmission lines, the radio noise detection, the solar-blind power line inspection, the corona current

9

monitoring in high voltage power lines, the fibre optic application for transmission line inspections, audible noise metering, etc [8]. Bernauer reported in [9] that the Surface Acoustic Wave (SAW) sensor technology could be used successfully for continuous monitoring of the temperature of transmission line conductors. The key element of this technology is implementing a radio link between sensors and the measuring unit. In spite of the fact that all these monitoring techniques have developed rapidly, as Douglass mentioned in [10] "optical, ultrasonic, radar and laser-based sag measurement methods have not yet progressed to operational use". Real-time rating methods, based on either tension or sag measurements, provide a basis for estimation of the thermal state of the conductors.

This chapter consists of three parts. The first part concerning OHL is structured in the following way: Section 1 provides a description of OHL conductors; Section 2 describes and compares existing theoretical methods for the estimation of the thermal state of OHL conductors and their comparisons; Section 3 describes the various models available to evaluate sag and the loss of strength of the conductor; Section 4 discusses the impact on temperature of the conductor of forced convection taking into consideration the quality of the conductor surface; Section 5 focuses on implementation of numerical methods to study OHL conductors and Section 6 describes air flow around a cylinder. The second part concerning UGC opens with a description of major world wide practices of installation of UGC systems, followed in Section 2 by the introduction of a variety of lumped parameter models of UGC. Then Section 3 shows some examples of the implementation of numerical methods for the prediction of the thermal state of

underground cables. The third part of this chapter summarises the key points of the literature review.

2.1 Theoretical modelling of the thermal state of OHL conductors

Power transmission and distribution networks comprise a number of key elements, such as towers, insulators and conductors, which must satisfy the requirements in terms of the electrical, thermal and mechanical strengths.

2.1.1. Description of OHL conductors

Copper can be considered as a reasonable conducting material and therefore initially transmission lines used stranded copper conductors, but due to economic reasons they have been replaced by aluminium conductors, although the electrical resistivity of aluminium is approximately 1.66 times greater than of copper. Bare copper conductors (BCC), according to British standard (BS) [11], and All − Aluminium conductors (AAC), according to [12], are available in several specific sizes and can incorporate 7, 19, or 37 wires, see Fig. 2.1.
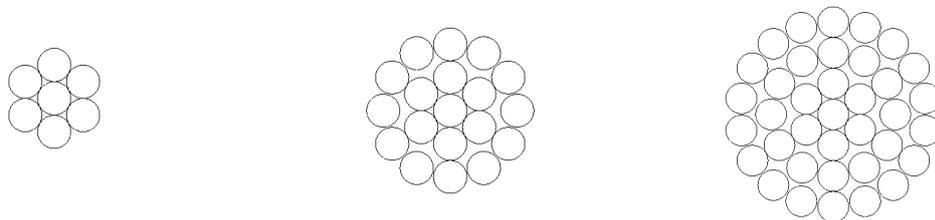
Fig. 2.1 Cross sections of BCC and AAC conductors

In order to increase the breaking strength of the aluminium conductor, it is common practice to use an aluminium conductor with a steel core made of a galvanized steel wire, and such an arrangement is referred to as the aluminium conductor steel reinforced (ACSR). The overhead line conductors in the UK have names based on animals and insects, and in the North America names based on birds and flowers. The nominal aluminium area, the number of aluminium and steel wires, are indicated in the description of the conductor. For example, an ACSR cable with 30 aluminum conductors that requires a core of 7 steel conductors will be identified as 30/7 ACSR Lynx conductor.

Some of frequently used ACSR conductors are illustrated below in Fig. 2.2.

a   b   c   d
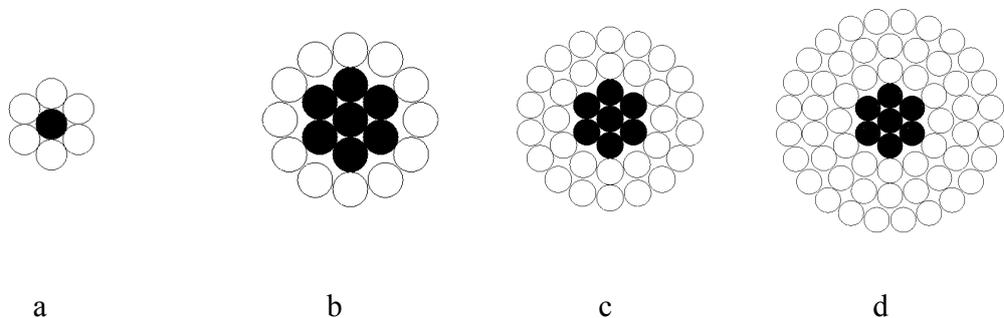
Fig. 2.2 ACSR conductors used in the UK (aluminium is shown unshaded): a) 6/1 Mink; b) Skunk; c) 30/7 Lynx; d) 54/7 Zebra

ACSR conductors may suffer galvanic corrosion due to the presence of dissimilar metals (aluminium and steel) under sea or industrial atmospheres. The aluminium strands under these circumstances may act as the anode of the galvanic cell, being corroded very

rapidly and promoting the premature failure of the conductor [13]. Penetration of aqueous corrosives can be avoided by the use of grease within the strands of the conductor [14].

The manufacturing and testing requirements for all aluminium alloy conductors (AAAC), aluminium conductor alloy reinforced (ACAR), aluminium alloy stranded conductor (AASC) and aluminium alloy conductors steel reinforced (AACSR) are specified in [12].

2.1.2 Existing theoretical methods for estimation of the thermal state of OHL conductors

There is a realisation that some of the existing theoretical methods used in the industry for the estimation of the thermal state of conductors are not sufficiently accurate and restrictive, hence providing conservative predictions. Rating recommendations may also vary from utility to utility. However, in general, the thermal ratings of overhead line conductors are normally calculated using IEEE and CIGRE methods [15, 16]. These methods are based on solving the energy balance equation written for the conductors. Such mathematical models used to estimate the thermal state of the conductors are also called lumped-parameter models. The calculation procedures employed in IEEE and CIGRE methods have some differences, however, the general methodologies are very similar and ratings calculations are based on the coincident high ambient temperature, full solar radiation and an effective wind velocity. The value of the latter varies in different standards - for example, UK Engineering Recommendations P27 [17] uses the

value of 0.5 m/s as a wind velocity value for the calculation of ratings. The IEEE/CIGRE surveys show that a number of utilities have gradually increased their line ratings by relaxing some of the rating assumptions. At present a number of utilities assume an effective wind velocity of 0.91 m/s or even higher [10].

Douglass also stressed in [10] that it is very important to take into consideration the fact that in highly loaded lines the core temperature of a large conductor may be 10-15°C higher than its surface temperature and therefore sag calculations should use an effective average temperature of the cross section instead of the surface temperature.

In [18] Schmidt shows that both standards, namely the IEEE and the CIGRE method, based on the same heat transfer equation use different approaches to calculate the thermal rating. Whereas the IEEE standard neglects magnetic core losses, the CIGRE method includes magnetic core losses and skin effect in the equation.

As a case study the 400 mm^2 Drake ACSR is used, and the difference between the two rating calculations is less than 2%. The CIGRE method assumes that a radial temperature distribution exists, but does not provide a solution which takes this fact into consideration, and in the IEEE method it is assumed that the temperature across the conductor is constant.

The main difference between IEEE and CIGRE methods is that IEEE relies on the use of tabular data to determine various energy balance terms in the equation, whilst CIGRE

uses closed form equations to calculate the same terms. The IEEE method is restricted in application due to the limited environmental situations considered. For most practical line designs and operational conditions both methods produce similar results. However, for some less typical applications, such as high wind velocity and/or parallel wind velocity calculations, there are significant variations in the estimates of the ratings and the engineers make a decision on which of the above two methods should be used.

2.1.3 The effect of the sag on the thermal limits of the conductor

The sag of the conductor depends on the tension and it is formed due to thermal expansion of the components due to increase of the temperature (see Fig.2.3).
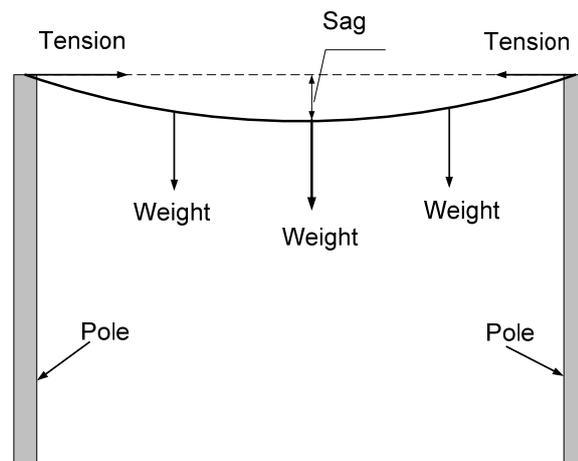
Fig. 2.3 Formation of sag between two poles

A method to calculate the sag for overhead conductors was developed and tested in [19]. The method, called the hybrid sag method (HSM), is based on modifications to the numerical sag method (NSM) [20] and combines the graphical load distribution

extracted from stress–strain curves of overhead conductors. HSM provides bilinear sag–temperature curves which closely follow the experimental sag performance data.

According to [19] the sag can be evaluated by using the simplified correlation (2-1), which connects the sag (D), the span length (S) and the physical length of the conductor (L):

$$D = \sqrt{\frac{3 \cdot S \cdot (L - S)}{8}} \tag{2-1}$$

Fig. 2.4 shows how the sag increases with the temperature for 152.4 m and 274.3 m span lengths.
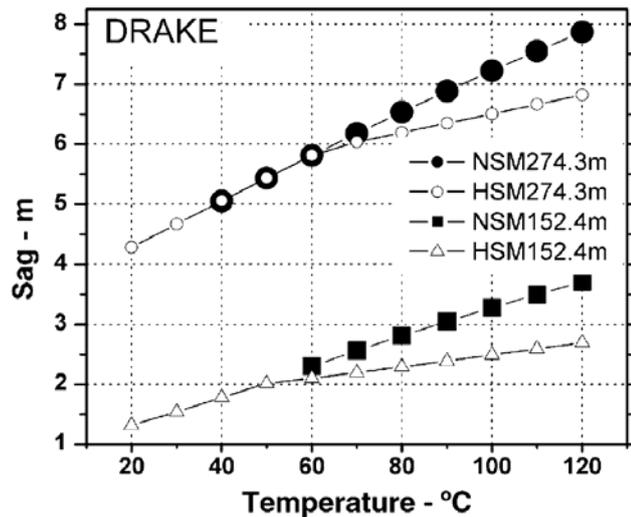
Fig. 2.4 Comparison between NSM and HSM for the Drake conductor with the outer diameter of 28.14 mm [19]

When ACSR conductors operate at temperatures in excess of approximately 93 ºC, the aluminium starts to anneal. (Annealing is used mostly in metallurgy as a heat treatment in order to change material properties such as strength and hardness).

The annealing deteriorates the conductor and it can result in the breaking of the conductor under high wind or ice conditions. To prevent this from happening, utilities generally limit the temperatures to 75º C for ACSR conductors [21].

A computer program consisting of a combined real-time ampacity and sag tension calculations was described in [22]. The program uses information on the conductor current and weather conditions. It was designed to provide accurate results for all commonly used overhead conductors for conductor temperatures up to 250 ^{0}C. The accuracy of the program was determined by comparing the predicted real-time sag for two different ACSR conductors that operated over a five-year period in the outdoor test span.

2.1.4 Impact of various meteorological parameters on the temperature of the conductor

In [23] Smolleck et al. analysed the influence of various meteorological parameters on the thermal rating of the ACSR, based on the heat equations from the standard IEEE 738-1993, and discussed how this information could be used by utility industry personnel to estimate the impact of various factors.

The current carrying capacity of the overhead line is greatly influenced by cooling of the conductor due to the forced convection. The losses due to radiation and evaporation are considerably lower at the ambient temperature. An extended version of the energy balance equation to determine the correlation between the current of the conductor and

its temperature for the steady-state was presented by Morgan [24]. In this work the heat gains (per unit length per unit time) due to Joule, ferromagnetic, solar and ionization (corona) heating are balanced by the heat losses by convection, radiation and evaporation. Joule heating was calculated as a function of the current, the ambient temperature and the resistance of the conductor, depending on the temperature of the conductor. Solar heating depends on the diameter of the conductor and its position relative to the horizon, the absorptivity of the surface of the conductor, the intensity of sunbeam, the solar altitude and on the reflectance of the conductor. Unlike the IEEE approach when the temperature in the conductor is assumed to be uniform, the radial temperature distribution proposed in [24] is given by equation 2-2:

$$T_c - T_s = \frac{P_t}{2\pi\lambda}(\frac{1}{2} - \frac{D_2^2}{D_1^2 - D_2^2}\ln\frac{D_1}{D_2}), \qquad (2\text{-}2)$$

where T_c is the temperature of the steel core (^{o}C); T_s is the surface temperature of the conductor (^{o}C); P_t is the total heat input (W/m), and D_1 and D_2 are the external and internal diameters (m), respectively. In [25] Black et al. also investigated how the ampacity of the conductor depends on the temperature gradient inside of the conductor by means of isothermal and non isothermal models. The comparison shows that the isothermal model predicted the ampacity rating sufficiently accurately. The maximum temperature difference obtained from the above models for the stranded conductor was less than 10°C at a maximum conductor temperature less than 100°C.

Morgan in [26] discussed in details how different factors influence the thermal rating for a 596 mm^2 ACSR conductor. Some of these factors, namely the velocity, direction and intensity of turbulence of the wind, and the air temperature, are more important than

others, such as the altitude of the Sun and the inclination of the conductor. It was also pointed out that in cases when the absorptivity of the conductor is equal to its emissivity then the impact of solar radiation on the thermal rating is very small.

2.1.5 Experimental investigations and implementation of numerical methods for evaluation of the thermal state of the conductor.

Heat losses by convection are calculated using tabular data based on the Nusselt, Prandtl and Grashof numbers. The Nusselt number *(Nu)* is used in heat transfer analysis very frequently. The Nusselt number is referred to as a group of parameters, which contain the heat transfer coefficient, a characteristic linear dimension and thermal conductivity of the fluid. It can be expressed as the product of two other groups of parameters, namely the Prandtl *(Pr)* number and Reynolds *(Re)* number, which describe flow, in another words: *Nu = f(Pr, Re)*. The Prandtl number is usually constant and can be found in property tables alongside other properties. Typical values for *Pr* for air and a number of other gases are 0.7-0.8. The Reynolds number is used to define a character of the flow, such as laminar or turbulent. The flows with natural convection are described by the Grashof number.

In [27] results of experimental investigations in a wind tunnel on the effect of the forced convective cooling on the thermal state of the ACSR410 for wind velocities in the range from 0.2 m/s to 4 m/s at a current equal to 1340 A were described.

The heat dissipation around the conductor is:

$$P_c = \pi \lambda_f (T_s - T_a) Nu .$$

(2-3)

The relationship between Nu and Re numbers in general form can be presented as

$$Nu = B \times Re^n.$$ (2-4)

Using experimental results, the authors refined equations employed for calculations of the thermal state of the conductor. The surface roughness (*H/D*) for a stranded conductor is defined as the roughness ratio and equals

$$H/D = (d/2) \cdot (D-d),$$ (2-5)

where H is height (m); d is diameter of a wire (m), and D is diameter of circumscribing circle (m). Thus, in the case of the forced convection with the wind velocity less than 1 m/s the authors found that

$$Nu = 1.566 \times Re^{0.343} \quad \text{for surface roughness} <0.1;$$ (2-6)

$$Nu = 1.325 \times Re^{0.362} \quad \text{for surface roughness} >0.1.$$ (2-7)

A study of the thermal state of a number of roughened cylinders exposed to natural and forced air convection was conducted in [28] by Morgan using stranded overhead electrical conductors for the transmission network placed in still air condition in a wind tunnel. The results show that the heat transfer rate in the still air is the same for both smooth and roughened cylinders for $2 \cdot 10^2 \leq (Gr, Pr) \leq 4 \cdot 10^5$. In cases of forced convection the convective heat transfer is not significantly changed by the roughening of the surface for $0.042 \leq (H/D) \leq 0.366$ provided that the Reynolds number does not exceed a critical value.

In [29] and [30] Lin investigated heat transfer from a Drake ACSR conductor using mathematical models, equations of which were solved using the finite difference

method. In the solution an assumption was made that the radial temperature gradient in the conductor was constant. The obtained numerical results were verified against experimental data from a number of indoor and outdoor tests.

In [31] Weedy used the finite difference method to solve equations of the mathematical model of the thermal state of three conductors widely utilised in the USA. The heat balance equation used was

$$I^2 \times R(T_c) = q_c + q_r - q_s, \qquad (2\text{-}8)$$

where q_c is convective heat loss (W/m); q_r is radiated heat loss (W/m); q_s is heat gain from the sun (W/m); I is conductor current (A); $R(T_c)$ is 60 Hz AC resistance at the temperature T_c (Ω/m).

$$q_r = \pi \cdot D \cdot \varepsilon \cdot \sigma_B \cdot \left(T_s^{\,4} - T_a^{\,4}\right), \qquad (2\text{-}9)$$

where D is the external diameter of the conductor ; ε is the emission coefficient; σ_B Stefan Boltzmann constant, $\sigma_B = 5.67 \cdot 10^{-8}$ W/m$^2 \cdot$K^4; T_s is the temperature on the surface of the conductor (K) and T_a is the ambient temperature (K).

$$q_s = \alpha_s \cdot Q_{sol} \cdot D, \qquad (2\text{-}10)$$

where α_s is absorptivity of conductor surface and Q_{sol} is solar energy incident per unit area (W /m^2), D is the external diameter of the conductor.

For the cases with natural convection

$$Nu = 0.53 \cdot (Gr \cdot Pr)^{0.25}, \qquad (2\text{-}11)$$

where $Pr = 0.71$ and

$$Gr = 0.896 \cdot 10^8 \cdot (T_s - T_a). \qquad (2\text{-}12)$$

21

Since

$$Nu = h \cdot d / k , \tag{2-13}$$

then

$$h = 1.29 \cdot \left(\frac{T_s - T_a}{d} \right). \tag{2-14}$$

Thus the convective heat transfer can be found as

$$q_c = 1.29\pi \cdot d^{0.75} \cdot (T_s - T_a)^{1.25} . \tag{2-15}$$

If a wind is present, then

$$Nu = 10^{-0.7 + 0.315 \cdot \ln Re + 0.0355 \cdot (\ln Re)^2} . \tag{2-16}$$

To solve the heat balance equation an iteration procedure was applied in which the initial value of the conductor temperature was assumed and therefore the current value was determined and consequently T_s was evaluated. The calculations proceeded until the changes in temperature were less then 0.1 degrees. The time step of 7 s was used to solve the transient equations. At every time step a new value of the resistance and also new values of the convective and radiative losses were used.

In [32] Ilgevicius et al. used the finite volume method to investigate the heat transfer inside the insulated electrical wire, modelling the wire as a solid body with volume distributed heat sources. The results of the temperature were presented in the form of diagrams, which then were approximated using analytical equations with a set of coefficients applicable only to the specific wire.

2.1.6 Flow around a circular cylinder

The heat transfer investigations of the thermal state of conductors can be considerably simplified using results obtained from studying fluid flow around a circular cylinder. Zdravkovich in [33] states that flow around a cylinder is governed by three transitions: in-the-near-wake, along the free shear layers and along the boundary layers; each transition is characterized by several flow regimes, which can be classified according to the Reynolds number. The accumulated experimental observations have revealed an enormous variety of regular and irregular flow patterns around circular cylinders.

Wu et al. in [34] used the numerical approach, identified as the spectral element method, in order to study the unsteady fluid problems around a single cylinder for laminar flows (at Reynolds number between 7 and 200). Experimentally, the soap-film flow visualization method has been used to derive the separation angle for the first time to validate the results. Fig. 2.5 shows the flow around the cylinder when the Reynolds number is 100.

Time = 1/6*T*

2/6*T*

3/6*T*

4/6*T*

5/6*T*

6/6*T*
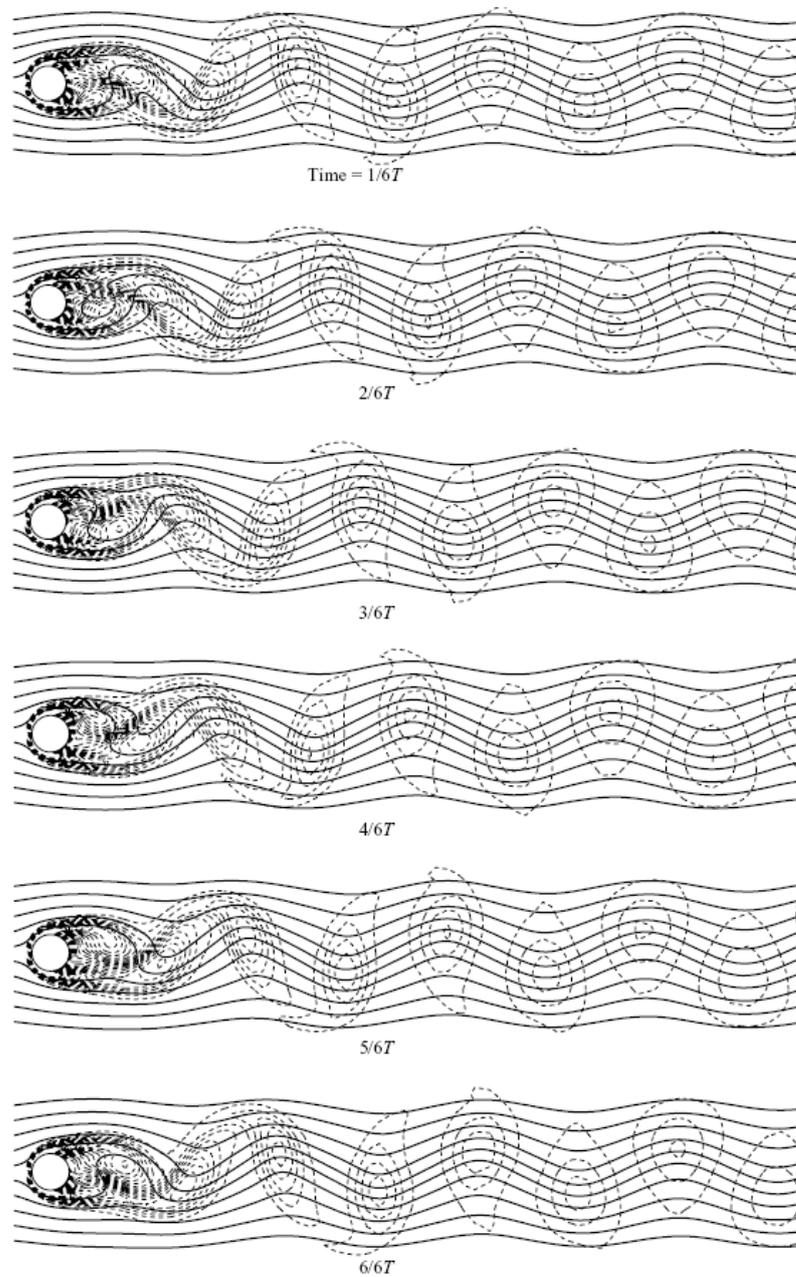
Fig. 2.5 The streamlines (the solid lines) and vorticity lines (the dashed lines)

for *Re* = 100 [34]

24

The streamlines are plotted as the solid lines and the constant-vorticity lines are shown as the dashed lines, revealing an overall view of how the streamlines and vorticity field are transformed within an entire period of vortex shedding.

2.2 State-of-the-art in the determination of the thermal state of underground cables

2.2.1 Basic cable systems for medium voltage and installation practices.

Cable installation practices in Holland, Canada, Germany, Switzerland, Australia, Japan and UK are discussed in [35]. The two basic cable systems for medium voltage are widely used in various countries across the world, which are PILC (paper insulation, fluid filled, lead covered) and extruded dielectric cable.

The extruded dielectric cables can be divided into

- XLPE (crosslinked polyethylene),

- TRXLPE (tree retardent XLPE),

- EPR (ethylene propylene rubber insulation).

The extruded dielectric cable consists of stranded conductor, conventional conductor shield, strippable insulation shield, bare copper concentric neutral wires without a jacket.

In the UK medium voltage PILC, XLPE, TRXLPE and EPR are installed by direct burial, except in London and for other urban networks where duct banks and some tunnels are used. Currently the extensive PILC system is being converted to extruded

dielectric. Mass impregnated non draining cables (MIND) are extensively used in 33 kV distribution systems and they must sustain a temperature of 90º C. The outer coverings are made of medium density polyethylene (MDPE) to minimise moisture migration.

In parallel with the increase in installation of three cores designs of XLPE cables, there also has been a rise in installation of some TRXLPE and EPR single core cables.

2.2.2 The lumped parameter models

Sellers et al. in [36] provide the brief overview of investigations of ampacity of underground cables starting with the first very simplified models for calculating the current carrying capacity of underground cables that were created more than 100 years ago, see Kemelly et al. [37] and Rosh [38]. Since publication of the Neher-McGrath paper [39], its method has been used as the standard for determining the current-carrying capacity of underground cable. The mathematical model described in the Neher-McGrath paper used knowledge about heat transfer available at that time and included several assumptions. However, more recent developments were incorporated into an improved version of an underground ampacity (current-carrying capacity in amperes) model. The goals in the work by Sellers et al. [36] were to "objectively examine several improvements to the Neher-McGrath model, to incorporate recent heat transfer correlations, and to remove several assumptions considered in [39]". The suggested changes resulted in a more complex ampacity model, which lead to an increase in ampacity in some cases and a decrease in others.

When cables are placed in ducts the thermal resistance of the fluid layer that surrounds the cables must be determined in order to calculate the ampacity. Neher-McGrath's paper [39] presents two expressions for the resistance of this layer which are simplified forms of an earlier expression developed by Buller and Neher in [40]. These expressions consider all three modes of heat transfer: conduction, convection and radiation between the surface of the cable and the inside surface of the duct. The total resistance of the medium can then be determined by adding the resistances in parallel.

The thermal resistance between the cable surface and the inner wall of the duct is only a function of the outer diameter of the cable, the number of conductors within the duct, and the thermal properties of the duct which are incorporated into the values for the two constants. The assumptions used in the derivation of the above equation greatly simplify its form. However, they also reduce its accuracy and even "can produce erroneous results".

Cable thermal ratings are also defined by the backfilling soil properties. According to [41] and [42], the high temperature increases considerably the risk of backfill drying out, which subsequently causes damage to the cable. Hartley and Black predicted a two-stage drying process which occurred in the soil, and described it in their study in [43]. The first stage is "characterized by a decrease in moisture content until a critical value is reached. In the second stage, the drying occurs more rapidly, eventually leading to a high thermal resistivity layer surrounding the cable". The second stage produces a thermal runaway condition which has been classified as a thermally unstable soil. It was

highlighted in [43] that the thermal stability of soil was as an important factor governing the rating of underground power cables.

The authors of [43] described the results obtained using a computer program which solves the transient form of the conservation equations in radial coordinates. The program was applied to the soil surrounding the cable in order to predict the local instantaneous temperature and moisture content. The results of the simulations were used to predict those soil properties and cable operating conditions which would produce stable and unstable behaviour. Two separate experimental tests took place in order to validate the results. The comparison showed, that "the prediction of thermal instability could be accurately achieved with small diameter heat sources". Therefore, it was not necessary to perform simulations on full size cable systems.

In [44] Moya et al. performed an experimental analysis of heat and moisture transfer around a heated cylinder surrounded by an unsaturated soil, see Fig. 2.6. A goal of this study was to apply the results of this work to high-voltage electrical power distribution in urban areas. Experiments were performed for both constant and cyclic heating ranging from 7 to 79 W/m. The location of thermocouples in the experimental set is shown in Fig. 2.7. Spatial, as well as temporal, temperature heat flux and moisture content results were also reported. Fig. 2.8 - 2.10 present some data from experiments. Computations using a 2-D model were also performed and it was reported that a good agreement prevailed between numerical and experimental results, although Fig. 2.9 indicates the presence of a significant deviation between numerical and experimental

data. It was found by the authors of [44], that well-graded soils, such as the one used in their work, had a great capacity for retaining moisture, which is an important feature if high thermal conductivities around the heat source are desired.
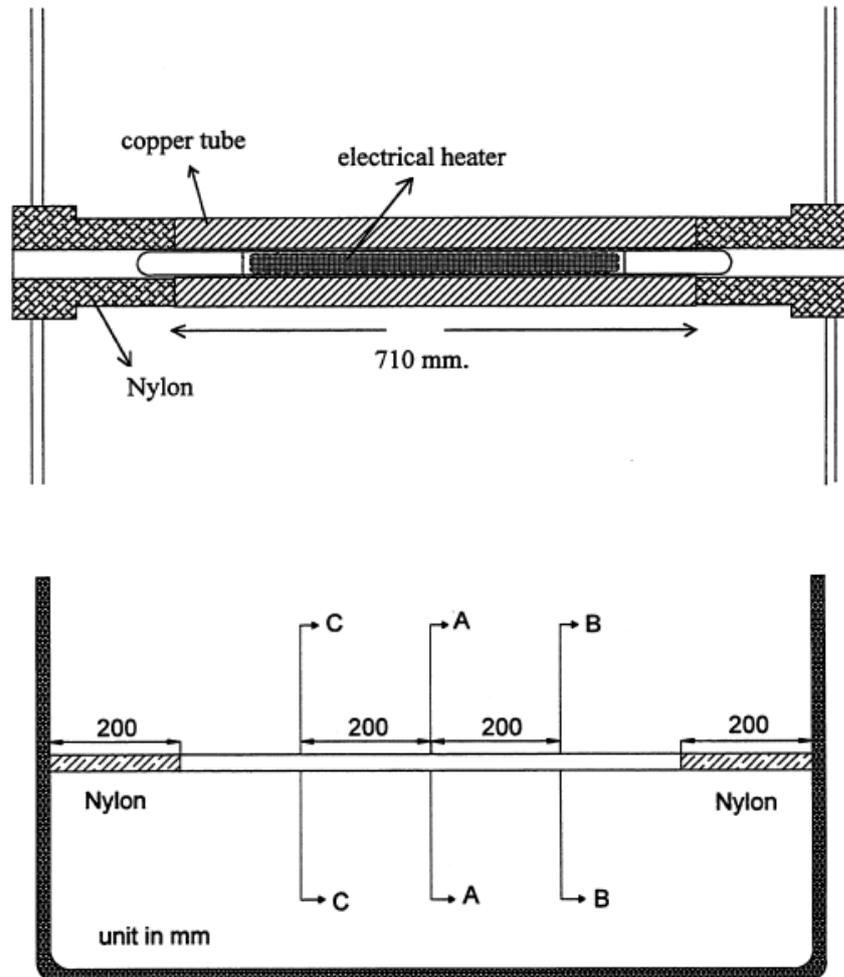
Fig. 2.6 Schematic view of the heat source installed in the container and a detailed view of the heating cylinder [44]
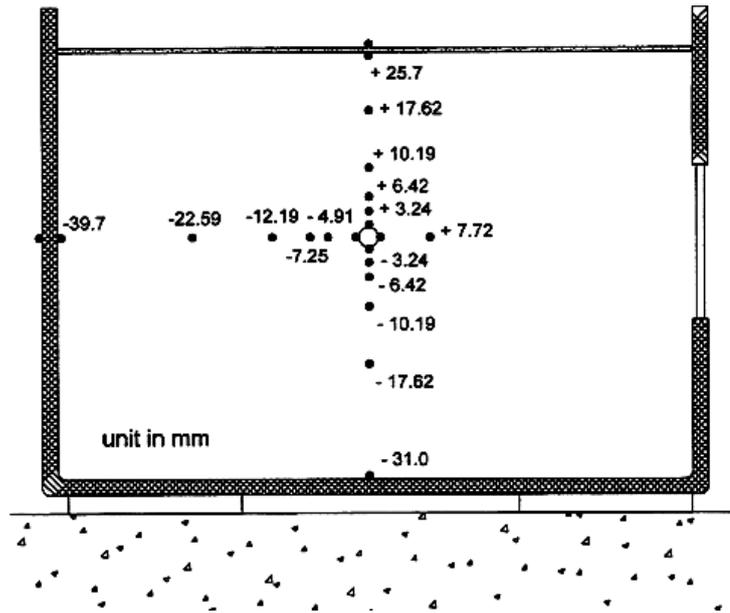
Fig. 2.7 Thermocouples location on plane A according to Fig. 2.6 [44]
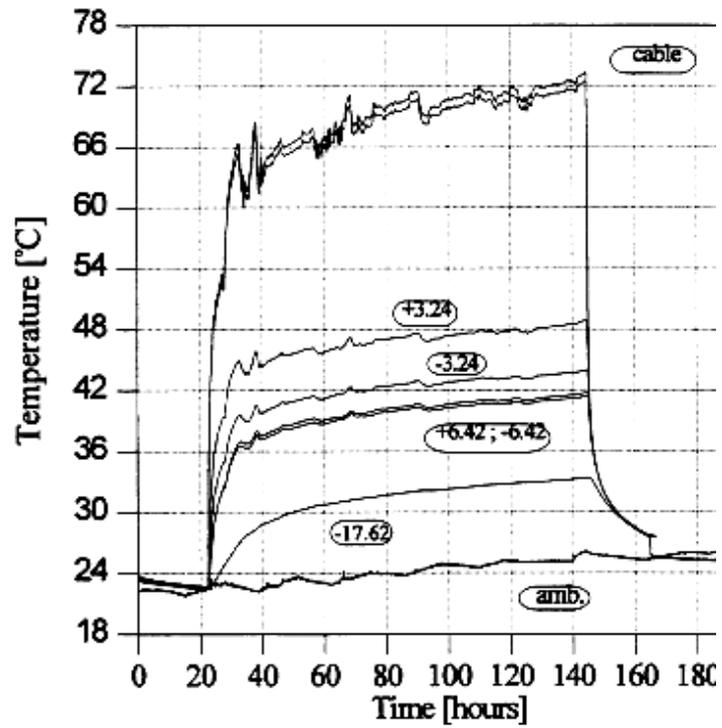
Fig. 2.8 Variation with time of the soil temperature at different vertical locations for 79 W/m in plane A in Fig. 2.6 [44]
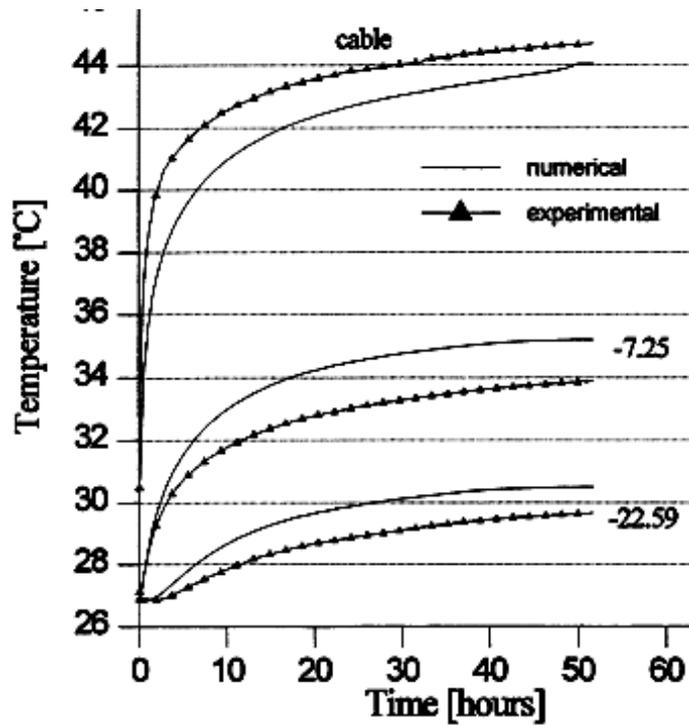
Fig. 2.9 Comparisons between numerical and experimental results for the temperature at different horizontal locations in plane A of Fig. 2.6: the heat flux is 17 W/m [44]
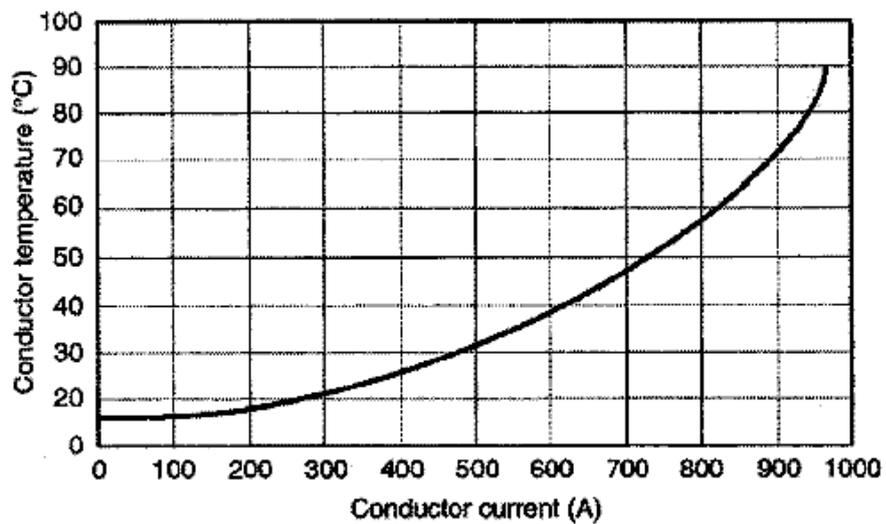
Fig. 2.10 Conductor temperature as a function of conductor current for a three-conductor armoured cable [44]

31

Anders and Brakelmann reported in [45] a method which obtains accurately the conductor operating temperature. In some cases when the fitting of the temperature sensing devices on cables is costly or impossible, "an approximate method of real-time rating analysis based on the current measurements alone might prove to be very beneficial". The calculation of the loss factor as a function of conductor temperature was also introduced.

In [46] Lu et al. reported an improved model for predicting soil thermal conductivity from its water content. The thermal conductivity and water content relationship is required for the quantitative study of heat and water transfer processes in saturated and unsaturated soils. In [46] the soil thermal conductivity was estimated using soil bulk density, sand (or quartz) fraction and water content. The suggested model was first calibrated using measured thermal conductivity from eight different soils. As a first step in the validation, the predicted thermal conductivity from the calibrated model was compared with the measured thermal conductivity for four additional soils. Except for the sand, the root mean square error (RMSE) of the new model ranged from 0.040 to 0.079 W m^{-1} K^{-1}, considerably less than that reported in other models (0.073–0.203 W m^{-1} K^{-1} or (0.100–0.174 W m^{-1} K^{-1}). The authors of [46] stated that their model provided accurate approximations of the soil thermal conductivity for a wide range of soils. The models tested demonstrated sensitivity to the quartz fraction of coarse-textured soils.

2.2.3 Implementation of numerical methods for evaluation of the thermal state of UGC

A computer program described by Black et al. in [47] can be used to calculate the ampacity of cables in trays surrounded by fire barrier material. Numerical results were validated using an extensive thermal test program. A fire barrier ampacity correction factor was defined by comparing the predicted ampacity of cables in fire protected trays and the ampacity stated in the ICEA/NEMA code for an open, unprotected tray. The results show "that a current derating in the range of 25 to 60 percent can be expected for typical fire barrier materials and typical barrier designs". The results show that when fire barrier material was used to protect the cables in a tray the thickness of the fire barrier material had the greatest influence on the ampacity, followed by the thermal resistivity of the material. The heat generated by the cables was transferred from the cable mass "predominately by the radiative mode because the convective mode was reduced by the thin, nearly-stagnant air layers that were trapped by the presence of the fire barrier material". This conclusion suggests that one way to minimize the derating effect caused by the protection system is to select a fire barrier material with a high emissivity and to eliminate multiple air layers next to the cables in the tray. The ampacity correction factor is not a function of the conductor size or cable diameter and it is only a weak function of the cable depth in the tray.

In [48] Chaves et al. presented numerical solutions for the transient natural convection heat transfer by double diffusion from a heated cylinder buried in a saturated porous medium. Both the cylinder and the medium surfaces were kept at the constant uniform

temperature and concentration. Such approach can be applied for buried underground cables. The governing equations were handled numerically by the control volume method.

2.2.3.1 Finite Element Method

Quite extensive investigations of underground cables were carried out using the finite element method. M.S. Al-Saud et al. in [49] presented a new approach to underground power cable thermal field sensitivities and ampacity computations using a proposed algorithm of the perturbed finite-element analysis. The modelling allows application of the range of parameters without repeating the finite element analysis process; therefore, the results can be obtained very fast. Fig 2.11 shows a system of 132 kV XLPE which was used as one of the case studies.
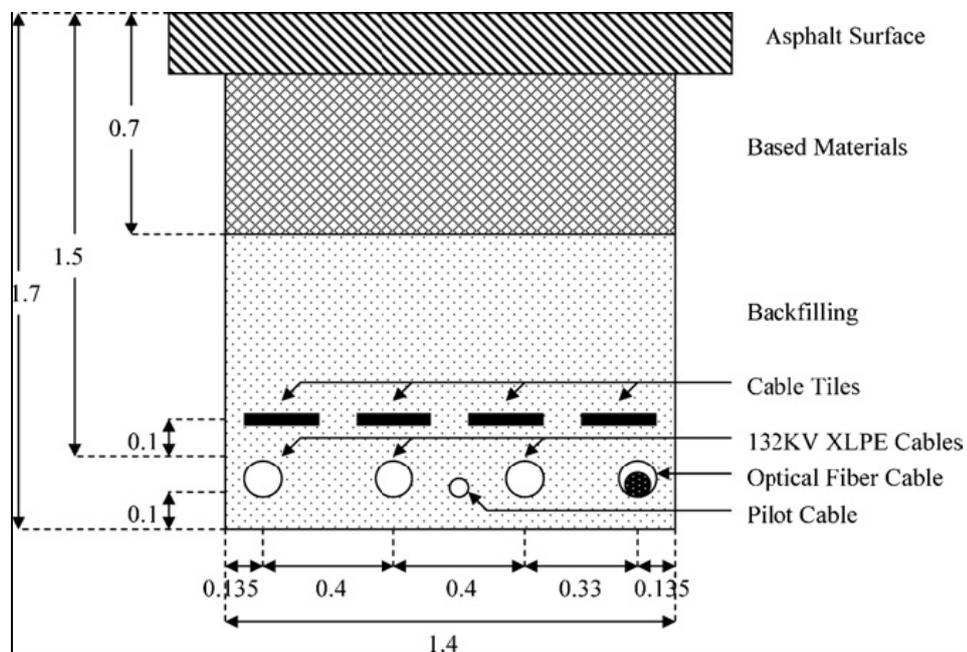
Fig. 2.11 A system of 132 kV XLPE cables [49]

Fig. 2.12 shows a part of a mesh, which was generated in a soil domain and included two middle power cables and a pilot cable.
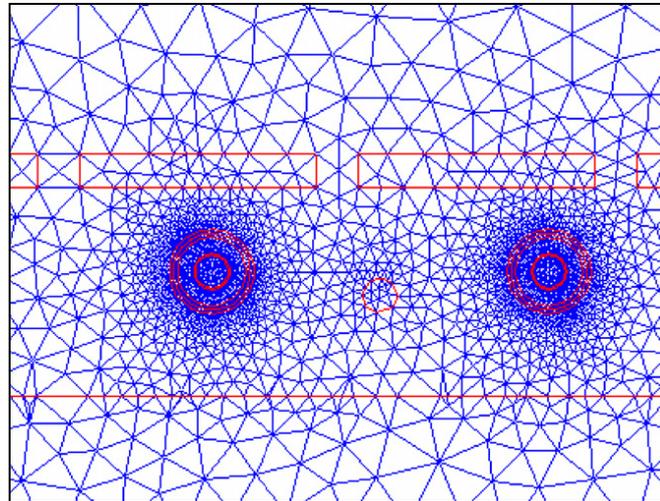
Fig. 2.12 Portion of the discretized region shows middle and right cables of the 132 kV cable system [49]

Fig. 2.13 below presents the relationship between maximum temperatures in the cables for different values of the soil thermal conductivity.
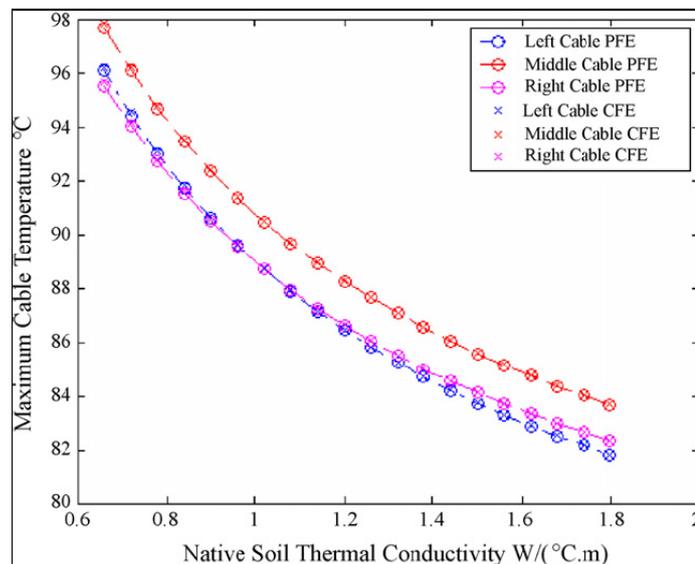
Fig. 2.13 The effect of variation of the native soil thermal conductivity (132 kV cable system) [49]

The technique is applicable to "both the design phase and the operational aspects of power cables buried in complex media of soil, heat sources and skins and variable boundary conditions". The new technique "was tested and verified by the laboratory experiments and was applied to several practical cable systems yielding important practical findings".

Miller in [50] proposed a model which takes into account migration of moisture in the soil. He conducted experimental tests on the cable in the trefoil formation and compared numerical results with experimental data. The conclusion made was that more accurate experimental measurements were needed.

The main conclusion drawn in this work is as follows: "It has been shown through experimentation with this model that the dominant effect on the estimate of the temperature of a burial cable is the air temperature, and that wind speed and solar radiation do not affect the cable temperature greatly."

Swaffield in [51] also described several models employed for the calculation of comparative continuous ratings of a directly buried 400 kV cable group. Ratings were obtained using three methods, namely the standard analytical approach (IEC 60287), a 1-D finite difference (FD) and a 2-D finite element analysis (FEA). An equation for the calculation of a resultant heat-flux has been derived to more precisely model the dielectric loss in 2-D and 3-D FEA models. All models show good agreement for the modelling of the isothermal ground surface condition. Also, the validation was carried

out on the 2-D FEA model against established approaches. The FEA model was used to investigate ground surface boundary conditions and the effect on the rating of the wind with the velocity of 1 m/s and 10 m/s. The comparison shows that at a typical buried depth of 800 mm the cable rating was slightly lower for the wind velocity of 1 m/s, and it would be equal to the rating for the wind velocity of 10 m/s if the buried depth of the cable group increases to 900 mm.

2.2.3.2 Finite Volume Method

Existing commercial CFD software can be employed for the analysis of heat transfer and flow in the conductors and surrounding domains. There are no publications on the application of CFD packages for OHL conductors or UGC; although a number of cases with similar geometries were investigated using the CFD software. For example, an implementation of Fluent CFD [52], software based on the finite volume method, was presented by Hatipoglu in [53] in order to visualise flow around a cylinder and the separation regions in particularly. A number of cases at Reynolds numbers of 1.3×10^4 and 2.6×10^4 were investigated, see Fig.2.14.
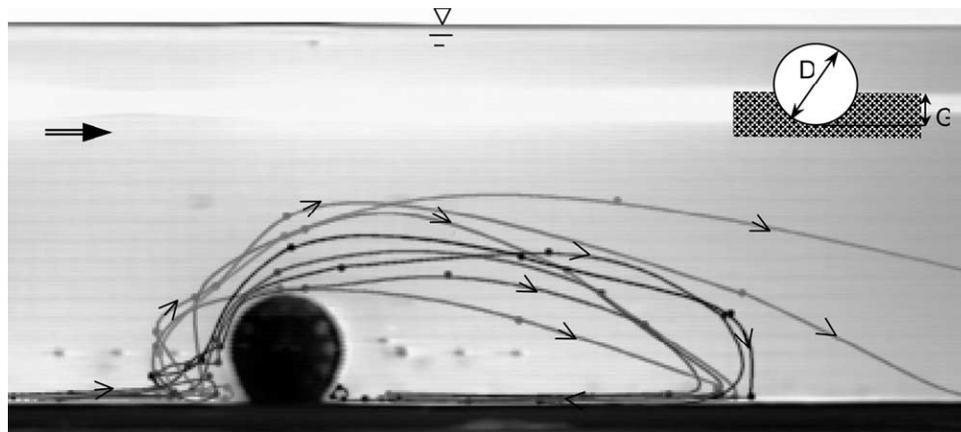
a)
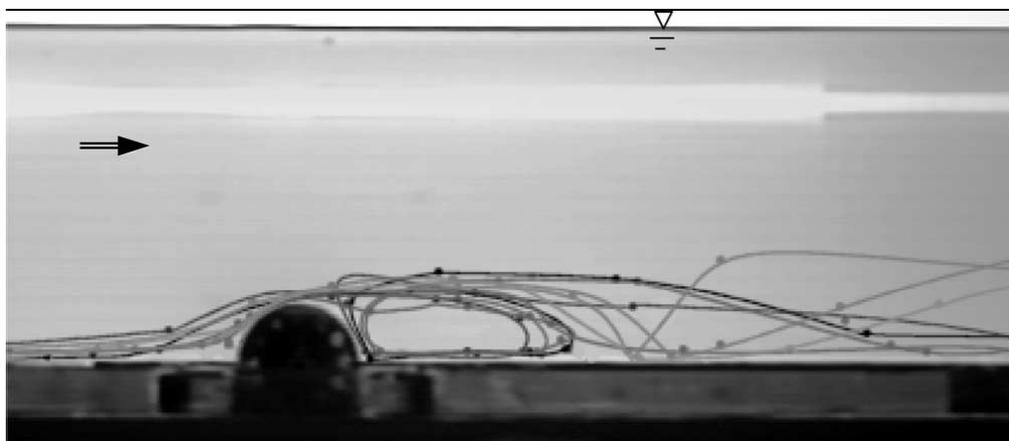
b)

Fig.2.14 Separation regions: a) for surface mounted cylinder, *G/D*=0; b) for semi buried cylinder, *G/D*=0.50 [53]

The numerical results obtained from the application of Fluent are presented for illustration in Figures 2.15 and 2.16.
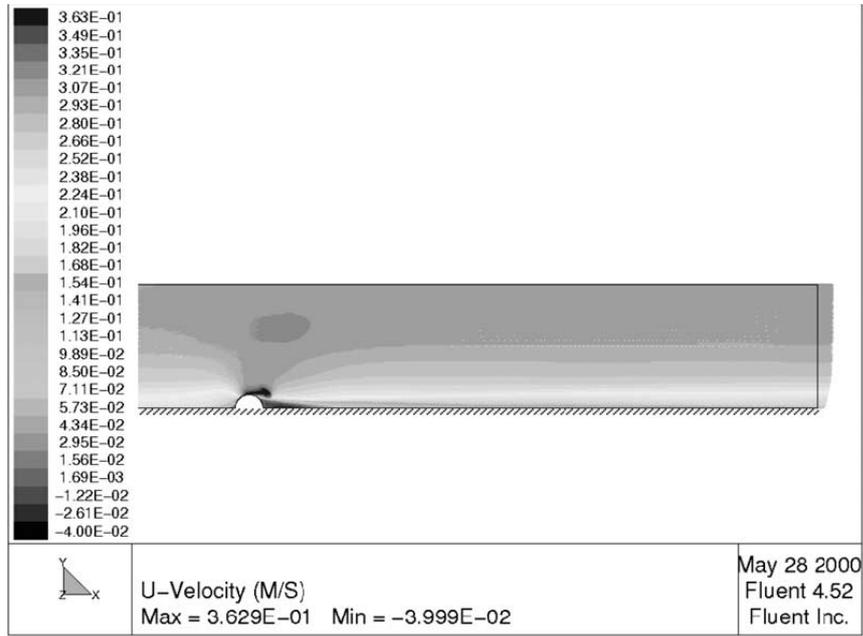
Fig. 2.15 Simulated separation regions for semi-buried cylinder, *G/D*=0.5 [53]
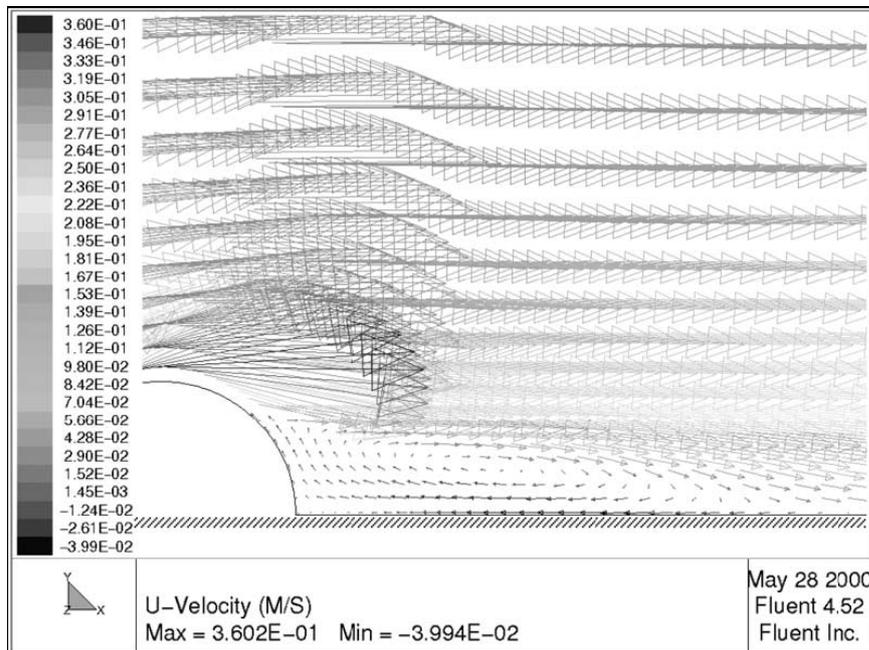
Fig. 2.16. Simulated primary downstream separation region for the semi-buried cylinder, *G/D*=0.50 [53]

It was found both numerically and experimentally that the length of the separation regions decreased with an increase of the burial ratio. Deviations between simulated and measured lengths of the separation regions were less than 30%. The authors stressed that "the results have significant implications, both for the illustration of the potential for using CFD software, and the meeting of the need for data of two dimensional flows around the buried cylinder".

Numerical methods allow engineers to take into account numerous factors more accurately in the real process compared to analytical or lumped parameter models. The idealizations concerning various structural details and the inhomogeneity of materials used in cable trenches, inevitable in analytical approaches, negatively effect the results and make it impossible to assess in more detail the effects of the trench geometry and of the backfill material type and formation.

2.3 Conclusions on Literature Review

The growth of renewable power generation can result in some cases in a significant increase in the power flow requirements placed on transmission and distribution networks. The existing industrial standards are usually conservative in predicting ampacity of overhead conductors and by using more accurate analysis and predicting tools it is possible to provide network operators with information to fully exploit the scope in the overhead line power capacity in a safe manner.

2.3.1 Overhead lines

The literature review performed on overhead conductors indicates that numerous lumped parameter models have been developed, but these existing models quite often provide contradicting results.

Analysis of the published works also shows that a very limited number of studies have been dedicated to the use of numerical heat transfer methods for predicting the thermal state of overhead cables, although it is possible to use the same approach which was employed for the analysis of heat transfer processes in complex heat exchanger geometries.

The methods of calculation of the thermal state of mainly single conductors described in the published works are usually based on lumped parameter models. This type of model employs various semi-empirical correlations for the determination of heat losses due to free and forced convection.

Until now only a single research paper has been published in which the application of the control volume method technique was used for the thermal analysis of an insulated electrical wire placed in air [32]. The case considered was very simple and the energy conservation equation only was solved, with the flow of air around the wire not taken into account. Application of the CFD technique to the analysis of the heat transfer and flow in domains containing overhead lines and underground cables would be a highly novel research in this area.

Application of CFD methods could considerably expand the capabilities of the analysis. CFD methods can be used effectively for studying both steady state and dynamic load conditions and can refine information on the magnitude of heat losses as a function of numerous factors, such as variable resistivity of the conductor, ambient temperature, insolation, wind velocity and its direction.

2.3.2 Underground cables

In addition to a wide range of lumped parameter models for the modelling of the thermal state of different configurations of underground cables, a wider application of FE methods is taking place for solving related heat transfer problems [54]. However, most of FE models developed to date for the simulation of underground cables deal with solving the heat conduction equation only, and only a few take into account the cooling effect due to underground flows or wind on shallow buried cables. This task can be effectively analysed using CFD methods. More extensive application of CFD models for the analysis of such complex systems as a group of underground cables will provide deeper insight into heat transfer processes in such systems and provide more accurate results for engineers. Finally, results of CFD simulations for steady state and transient conditions can be used to refine existing recommendations or produce completely new correlations on the calculation of the thermal state of underground cable systems.

CHAPTER 3

LUMPED PARAMETER MODELLING

When using lumped parameter modelling approaches, single values of discretized scalars are used instead of spatially distributed parameters.

3.1 Lumped parameter models of OHL

In engineering practice, the thermal ratings of overhead line conductors are normally calculated using IEEE (The Institute of Electrical and Electronics Engineers) and CIGRE (Conseil International des Grands Reseaux Électriques - The International Council on Large Electric Systems) methods [15, 16]. These methods are based on what are commonly referred to as lumped parameter models which essentially solve the energy balance equation formed for the OHL assuming that determined scalars (e.g. the temperature) are uniformly distributed in the conductors. There is some difference in the calculation procedures employed in IEEE and CIGRE methods; however, the general methodologies and approaches are very similar and rating calculations are performed for extreme conditions when the high ambient temperature, full solar radiation and an effective wind velocity coincide in time.

The lumped parameter model solutions for overhead lines operating at steady-state conditions are found as the outcome of an iterative procedure involving the use of physical intuition on the value of the temperature of the conductor following the completion of each iteration.

3.1.1 The IEEE mathematical model for evaluation of the conductor temperature in the steady (or quasi-steady) state (normal operation)

The conductor can be deemed to be in the steady state thermally when the heat generated in the conductor due to Joule losses and the heat gained by the conductor from solar radiation is equal to the heat which is dissipated from the conductor due to convective losses and re-radiation, see Fig. 3.1.
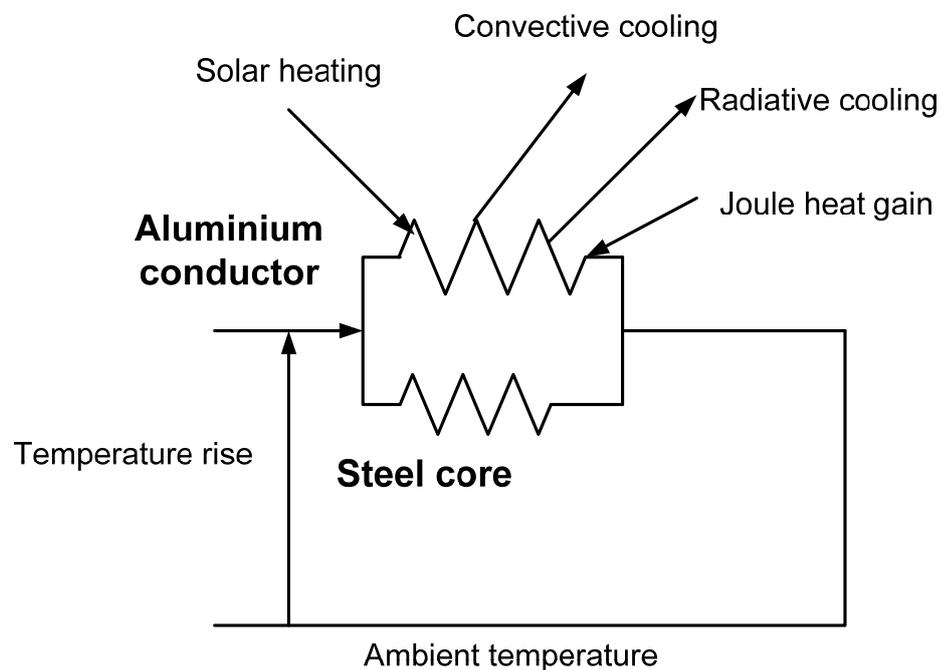
Fig. 3.1 A lumped parameter model of ACSR

The meteorological parameters which have the strongest influence on the thermal state of the conductor are the wind velocity and its direction, the ambient temperature and solar radiation. The heat balance equation in the steady state is given by equation 3-1.

$$I^2 \times R(T_c) + q_s = q_c + q_r, \qquad (3\text{-}1)$$

where I is current, A; $R(T_c)$ is 60 Hz ac resistance per linear foot of conductor at $T_c\left(\Omega/ft\right)$ (it is an American standard); q_s is heat gain from the sun (watt per linear foot of conductor); q_c

is convective heat loss (watt per linear foot of conductor; q_r is radiated heat loss (watt per linear foot of conductor) [15].

Joule losses

The product of the current squared and of the resistance ($I^2 \times R(T_c)$) accounts for Joule losses, which occur due to the electrical resistivity of the material of the conductor. The resistivity indicates how strongly material opposes the flow of electrical current. Resistivity for metals increases with an increase in the temperature.

The resistance of the conductor at an arbitrary temperature T_c can be calculated using the following interpolation:

$$R(T_c) = \left[\frac{R(T_{High}) - R(T_{Low})}{T_{High} - T_{Low}} \right] \cdot (T_c - T_{Low}) + R(T_{Low}).$$ (3-2)

In the equation (3.2) the high (T_{High}) and low (T_{Low}) temperatures are 75 and 25 ℃, respectively.

Solar heat gain

The magnitude of the solar heat gain depends on the geographical location, the time of day and the time of the year. The maximum value of the solar heat gain is at the angle of inclination of 90 degrees, which corresponds to the lowest value of ampacity.

In the general case, the solar heat gain can be determined as shown in equation 3-3.

$$q_c = \alpha \cdot Q_s \cdot (\sin \theta) \cdot A',$$ (3-3)

where α is solar absorptivity (0.23 to 0.91); Q_s is total solar and sky radiated heat flux(W/ft^2);

A' is projected area of conductor (square feet per linear foot); θ is effective angle of incidence of the sun's rays (degrees):

$$\theta = \cos^{-1} \cdot \left[(\cos H_c) \cdot \cos(Z_c - Z_l)\right]. \tag{3-4}$$

Here H_c is altitude of sun, degrees; Z_c is azimuth of sun, degrees; Z_l is azimuth of line, degrees.

The values of H_c, Z_c, are tabulated for various latitudes (in the range between 20 to 70 degrees) in the Northern hemisphere for the local times at 10 am, noon and 2 pm with sun declination of 23° [15]. The values of the total radiated heat flux Q_s are also tabulated for conditions of clear and industrial atmosphere.

Convection heat losses

The temperature of the conductor is usually higher than that of the surrounding air and the calculation of convection heat losses is different with respect to the intensity of cooling due to the forced convection at low and high wind velocities and also for natural convection conditions. In the IEEE standard it is assumed that the transition from laminar to turbulent regime of the air flow occurs at the Reynolds number of 1000.

Depending on wind velocity conditions determination of the forced convective heat losses can be calculated using equations (3-5) and (3-6):

a) for low wind velocity conditions

$$q_{c1} = \left[1.01 + 0.371 \times \left(\frac{D \times \rho_f \times V_w}{\mu_f}\right)\right]^{0.52} \times k_f \times (T_c - T_a), \tag{3-5}$$

b) for high wind velocity conditions

$$q_{c2} = 0.1695 \times \left(\frac{D \times \rho_f \times V_w}{\mu_f} \right)^{0.6} \times k_f \times (T_c - T_a) \bullet \qquad (3\text{-}6)$$

Here D is conductor diameter (*in*); ρ_f is density of air (lb/m^3); V_w is velocity of air stream (*ft/h*); k_f is thermal conductivity of air at temperature T_{film} (W/ft·°C); T_c is the conductor temperature (°C); T_a is the ambient temperature (°C); μ_f is absolute viscosity of air ($lb/ft \times h$).

The greater value of the forced convective losses calculated by (3-5) and (3-6) is used in the heat balance equation.

In order to take into account the influence of the wind direction the convective cooling term should be multiplied by the cooling term factor K_{angle}:

$$K_{angle} = 1.194 - \cos\varphi + 0.194 \cdot \cos 2\varphi + 0.368 \cdot \sin 2\varphi, \qquad (3\text{-}7)$$

where φ is the angle between the wind direction and the conductor axis.

Heat losses due to natural convection are calculated as follows:

$$q_c = 0.283 \times \rho_f^{0.5} \times D^{0.75} \times (T_c - T_a)^{1.25}. \qquad (3\text{-}8)$$

Properties of air, namely the density, its absolute viscosity and thermal conductivity are temperature dependent. The IEEE standard provides this data at the so called film temperature:

$$T_{film} = \frac{T_c + T_a}{2}. \qquad (3\text{-}9)$$

These data are presented in Fig. 3.2.

Viscosity, density and thermal conductivity of air
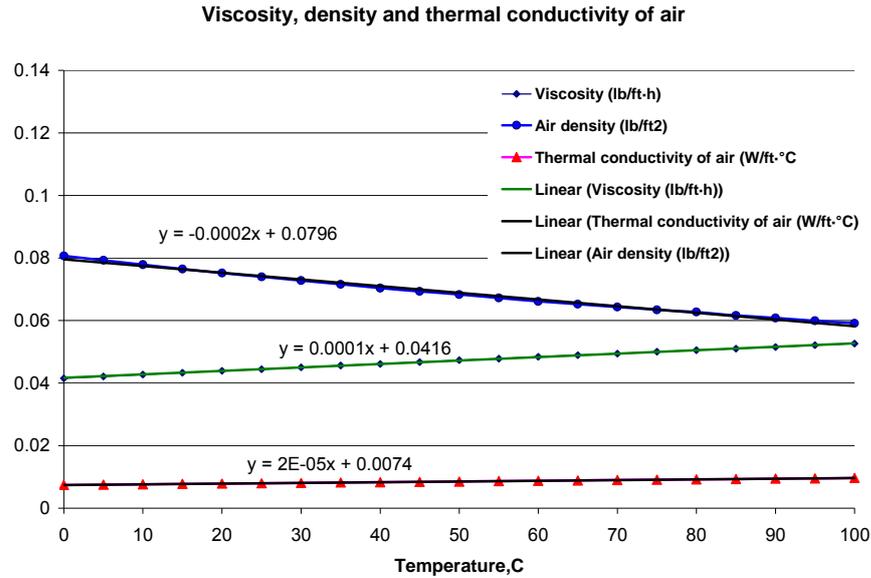
Fig. 3.2 Viscosity, density and thermal conductivity of air as function of the temperature

Calculation of re-radiation heat losses

At typical conductor operating temperatures the magnitude of the re-radiation heat losses is usually very small compared to that of the convective heat losses.

In the general case these losses are calculated as shown in equation 3-10.

$$q_r = 0.138 \cdot D \cdot \varepsilon \left[\left(\frac{T_c + 273}{100} \right)^4 - \left(\frac{T_a + 273}{100} \right)^4 \right], \tag{3-10}$$

where ε is the emissivity coefficient, which increases with the age of the conductor and the pollution of its surface.

3.1.2 CIGRE evaluation of the conductor temperature in the steady (or quasi-steady) state

In this method for steady-state operating conditions the energy balance equation is used to correlate between the current of the conductor and its temperature as shown in equation 3-11:

$$P_j + P_M + P_S + P_i = P_c + P_r + P_w, \tag{3-11}$$

where P_j, P_M, P_s and P_i are the heat gains (per unit length per unit time) due to Joule, ferromagnetic, solar and ionization (corona) heating, respectively, and P_c, P_r and P_w are the heat losses by convection, radiation and evaporation, respectively [16].

The Joule heat gain for non-ferrous conductors is calculated as

$$P_j = k_j I^2 R_{dc} \cdot [1 + \alpha \cdot (T_{av} - 20)], \tag{3-12}$$

where I is the effective current (A); R_{dc} is the dc resistance per unit length (Ω/m); α is the temperature coefficient of resistance per degree K; T_{av} is the mean temperature (°C); k_j is the coefficient, which takes into account skin effects, and its typical value is 1.0123.

The Joule heat gain (P_J) for steel cored conductors is defined as

$$P_j = I_{dc}^2 R_{dc} \cdot [1 + \alpha \cdot (T_{av} - 20)]. \tag{3-13}$$

For the same temperature of the conductor the power input is identical for both AC and DC and can be written as

$$I_{ac}^2 R_{ac} = I_{dc}^2 R_{dc}. \tag{3-14}$$

For the ACSR conductor with 2 layers of aluminium wires and a nominal cross section of greater than 175 mm^2

$$I_{ac} = \frac{I_{dc}}{\sqrt{1.0045 + 0.09 \cdot 10^{-6} \cdot I_{dc}}}. \tag{3-15}$$

The resistance value and the temperature coefficient of the resistance are tabulated in IEC publications.

Magnetic heating (P_M) occurs in ACSR conductors because a longitudinal magnetic flux is produced in the steel wires by the current in the aluminium wires spiralling around the steel core. The skin effect results in an increase in the conductor resistance which is a function of the frequency of the alternating current. Ferromagnetic losses constitute three components: eddy losses, hysteresis and magnetic viscosity. Accounting for ferromagnetic heating in multilayer conductors results in a 5–10 % increased resistance in the 3rd and 5th layers for the maximum load. The summarised magnetic heating and skin effect have a relatively small influence (0-3%) on the ampacity rating depending on the number of wire layers and voltage [18].

Corona heating (P_i) should be considered in high voltage transmission lines when convective and evaporating cooling are intensive (under wet and strong wind conditions).

Solar heating

The calculation of solar heating is carried out as follows:

$$P_s = \alpha_s \cdot S \cdot D \ , \tag{3-16}$$

where α_s is the absorptivity of the conductor surface; S is global solar radiation; D is external diameter of conductor (m).

A more complex method for the calculation of the solar heating term is given in [16], where the correlation includes direct radiation together with diffused and reflected components and takes into account the latitude, the position of the sun and the day of the year. This method can be used if this data is available. The absorptivity coefficient in (3-16) ranges from 0.27 to 0.95 for a new and old conductor, respectively. It is recommended to use the value of 0.5 for most purposes.

Calculation of convective heat losses

The convective heat losses are calculated with the use of dimensionless coefficients such as the Nusselt (*Nu*), Reynolds (*Re*), Prandtl (*Pr*) and Grashof (*Gr*) numbers.

For a film temperature, defined in accordance with (3-9), the Nusselt number at forced convection conditions is

$$Nu = h_c \cdot D / \lambda_f, \tag{3-17}$$

where h_c is the convective heat transfer coefficient (W/m^{2}K); λ_f is the thermal conductivity of air (W/m·K).

The Reynolds number is given in equation 3-18

$$Re = \rho_f \cdot \upsilon \cdot D / \nu, \tag{3-18}$$

where υ is the wind velocity (m/s); ν is the kinematic viscosity (m^2/s); ρ_f is the relative air density:

$$\rho_f = \rho / \rho_0. \tag{3-19}$$

Here ρ is the air density at altitude in question and ρ_0 is the air density at sea level (kg/m^3).

The Grashof number

$$Gr = \frac{D^3 \cdot (T_s - T_a) \cdot g}{(T_f + 273) \cdot \nu^2}, \tag{3-20}$$

where *g* is gravitational constant, $g = 9.807$ m/s^2.

The variables in 3-20 are determined as follows

$$\nu = 1.32 \cdot 10^{-5} + 9.5 \cdot 10^{-8} T_f; \tag{3-21}$$

$$\lambda_f = 2.42 \cdot 10^{-2} + 7.2 \cdot 10^{-5} T_f; \tag{3-22}$$

$$Pr = 0.715 - 2.5 \cdot 10^{-4} T_f; \tag{3-23}$$

$$T_f = 0.5 \cdot (T_s + T_a) ; \tag{3-24}$$

$$\rho = e^{-1.16 \cdot 10^{-4} \cdot y} , \tag{3-25}$$

where y is the height above sea level (m).

The convective heat loss is calculated as

$$P_c = \pi \cdot \lambda_f \cdot (T_s - T_a) Nu , \tag{3-26}$$

where the value of the Nusselt number is calculated using different equations depending on the type of the convection (free or forced). In the case of forced convection different expressions are used for high and low wind velocities.

Forced convection

The roughness of the surface increases the heat transfer, especially for high wind velocities, and can be calculated as

$$Nu = B_1 (Re)^n , \tag{3-27}$$

where B_1 and n are constants, which depend on Re number and R_f, which is the roughness of the conductor,

$$R_f = d / [2(D - 2d)], \tag{3-28}$$

where d is the wire diameter (m) and D is overall diameter of the conductor (m).

For the Lynx conductor R_f is equal to 0.1.

Table 3.1 presents values of B_1 and n for various surfaces and Reynolds numbers.

Table 3.1 Constants for calculation of forced convective heat transfer from conductors with steady crossflow of air [16]

Surface	Re		B_1	n
	from	To		
Stranded all surfaces	10^2	$2.65 \cdot 10^3$	0.641	0.471
Stranded $R_f \le 0.05$	$>2.65 \cdot 10^3$	$5 \cdot 10^4$	0.178	0.633
Stranded $R_f > 0.05$	$>2.65 \cdot 10^3$	$5 \cdot 10^4$	0.048	0.800

The effect of the wind direction is taken into account as follows:

$$Nu_\delta = Nu_{\delta=90} \cdot \left[A_1 + B_2 \cdot (\sin \delta)^{m_1} \right].$$

(3-29)

Here δ is angle of attack (degrees), A_1, B_2 and m_1 are constants depending on δ. Table 3.2 shows the values of these constants.

Table 3.2 Constants for calculation of forced convective heat transfer from conductors with steady flow of air taking into consideration the angle of attack

The angle of attack	A_1	B_2	m_1
$0<\delta<24°$	0.42	0.68	1.08
$24<\delta<90°$	0.42	0.58	0.9

For the wind velocity less than 0.5 m/s the Nusselt number can be calculated as follows:

$$Nu_{cor} = 0.55 Nu_{\delta=90},$$

(3-30)

where Nu_{cor} is the corrected Nusselt number

Natural convection conditions

Under natural convection conditions the Nusselt number can be defined as a product of Grashof and Prandtl numbers:

$$Nu = A_2 (Gr \cdot Pr)^{m_2} \qquad\qquad (3\text{-}31)$$

where A_2 and m_2 are constants, depending on the value of $Gr \cdot Pr$, see Table 3.3.

Table 3.3 Constants for calculating of natural convective heat transfer from conductors

Gr·Pr		A_2	m_2
From	to		
10^2	10^4	0.850	0.188
10^4	10^6	0.480	0.250

The re-radiation losses are calculated as

$$P_r = \pi \cdot D \cdot \varepsilon \cdot \sigma_B \cdot \left((T_c + 273)^4 - (T_a + 273)^4 \right), \qquad\qquad (3\text{-}32)$$

where σ_B is Stefan Boltzmann constant, T_a and T_c is ambient and the conductor temperature, respectively (ºC); ε is the emissivity and it varies from 0.27 to 0.95, depending on the state of the surface of the conductor. It is recommended to use 0.5 as the value of the emissivity.

The heat losses due to evaporation in CIGRE method are not presented due to the small effect on cooling of the conductor, although it can be determined using correlation which is given in [24]:

$$P_W = \pi \cdot D \cdot L \cdot (x_{ws} - x_{wa}), \qquad\qquad (3\text{-}33)$$

where D is the diameter of the conductor (m); L is the latent heat of evaporation of water (J/mol); x_{wa} is the mole fraction of water in air in the atmosphere; x_{ws} is the mole fraction of water in air in the atmosphere at the free surface of the water film.

3.1.3 Non-steady-state heat balance calculations according to IEEE standard 738-1993

An exact analytical solution of the non-steady state heat balance equation does not exist due to the fact that some terms which are part of this equation are nonlinear. The equation itself is given as

$$q_c + q_r + mC_p \frac{dT}{dt} = q_s + I^2 \times R(T_c), \tag{3-34}$$

where m is the mass of the conductor (kg/m); C_p is the total heat capacity of the conductor (J/kg·K).

For ACSR it is possible to present the term mC_p as

$$mC_p = m_{al} \cdot C_{pal} + m_{st} \cdot C_{pst}. \tag{3-35}$$

For the Lynx conductor

$$m_{al} \cdot C_{pal} = 0.4957 \cdot 900 = 446.18 \text{ J/m·K}; \tag{3-36}$$

$$m_{st} \cdot C_{pst} = 0.3368 \cdot 502.48 = 169.23 \text{ J/m·K}. \tag{3-37}$$

Therefore,

$$mC_p = 615.41 \text{ J/m·K}. \tag{3-38}$$

The approximation method for the solution of (3-34) is described in [15] and is based on the following equation:

$$\frac{d(T_c - T_a)}{dt} = K_1 \cdot (T_c - T_a) + K_1 \cdot I^2. \tag{3-39}$$

The solution for a time step change is presented as

$$T_c(t) = T_i + (T_f - T_i) \cdot (1 - e^{-t/\tau}), \tag{3-40}$$

where I_i is the initial current (A), I_f is final current (A).

The thermal time constant, τ, in the transient regime is calculated as

$$\tau = \frac{(T_f - T_i) \cdot mC_p}{R(T_c) \cdot (I_f^2 - I_i^2)}. \tag{3-41}$$

3.1.4 Example of CIGRE calculations of the thermal state of a conductor

The following is an example of the determination of the thermal state of the conductor in accordance with the CIGRE method.

The conductor to be considered is 183-AL1/43-ST1A-30/7 Lynx. Calculations are performed for the following conditions:

-Wind velocity: 1 m/s;

-Ambient temperature: 20ºC;

-Height above sea level, y: 100 m;

-I_{ac}: 433A (UK Engineering Recommendations P27 [17]).

The calculation starts with an initial guess that the temperature of the conductor is equal to 40ºC.

The energy balance equation states that heat generated in the conductor due to Joule losses (the heat gained because of solar radiation is neglected), is equal to the heat which is dissipated from the conductor as convective losses and due to re-radiation:

$$P_j = P_c + P_r,$$
(3-42)

here P_j is the heat gain (per unit length per unit time) due to Joule heating; P_c is heat due to convection and P_r is heat due to re-radiation.

The Joule heat gain is calculated as

$$P_j = I^2 R_{dc} \cdot [1 + \alpha \cdot (T_{av} - 20)],$$
(3-43)

where I is the effective current (A); R_{dc} is the DC resistance per unit length (Ω/m), α is the temperature coefficient of resistance per degree K. T_{av} is the mean temperature of the conductor, °C.

Taking into account equation 3-15:

$$I = I_{dc} = I_{ac} \cdot \sqrt{1.0045 + 0.09 \cdot 10^{-6} \cdot I_{ac}} = 433 \cdot \sqrt{1.0045 + 0.09 \cdot 10^{-6} \cdot 433} = 434 \text{ A};$$ (3-44)

$$P_j = I^2 R_{dc} \cdot [1 + \alpha \cdot (T_{av} - 20)] = 434^2 \cdot 0.000157 \cdot [1 + 0.00403 \cdot (20 - 20)] = 31.955 \text{ W/m}$$ (3-45)

The film temperature is calculated as

$$T_{film} = \frac{T_c + T_a}{2} = \frac{20 + 20}{2} = 20 \text{ °C},$$ (3-46)

The air density at the altitude in question, ρ is

$$\rho = e^{(-1.16 \cdot 10^{-4} \cdot y)} = 0.98846702 \text{ kg/m}^3.$$ (3-47)

ρ_0 is the air density at sea level, which is equal to 1.2 kg/m^3.

ρ_f is the relative air density:

$$\rho_f = \rho / \rho_0 = 0.823722517.$$ (3-48)

The kinematic viscosity, v, using (3-21) for the film temperature of 20 °C is 0.00001605 m^2/s.
The Reynolds number for the wind velocity of 1m/s is

$$Re = \rho_f \cdot v \cdot D/v = 0.823722517 \cdot 1 \cdot 0.0195 / 0.00001605 = 1000.784.$$ (3-49)

The thermal conductivity of air for the film temperature of 20 °C is

$$\lambda_f = 2.42 \cdot 10^{-2} + 7.2 \cdot 10^{-5} \cdot 20 = 0.02636 \text{ W/m·K}.$$ (3-50)

The convective heat loss can be calculated as

$$P_c = \pi \cdot \lambda_f \cdot (T_s - T_a) Nu. \tag{3-51}$$

The conductor surface roughness can be calculated using equation (3-28), and it is equal to 0.1. Values of the corresponding constants depending on the roughness and used for the calculations of the Nusselt number are found in Table 3.1.

Nusselt number then is calculated as

$$Nu = 0.641 \cdot (Re)^{0.471} = 16.59657,$$

and

$$P_c = \pi \cdot \lambda_f \cdot (T_c - T_a) Nu = \pi \cdot 0.02636 \cdot (40 - 20) \cdot 16.59657 = 27.488 \text{ W/m}.$$

The re-radiation heat losses are calculated as given in equation 3-32:

$$P_r = \pi \cdot 0.00195 \cdot 0.5 \cdot 5.67 \cdot 10^{-8} \cdot \left((40 + 273)^4 - (20 + 273)^4 \right) = 3.869263 \text{ W/m}.$$

Substituting the above values in (3-42) gives

$$31.95539 = 27.48803 + 3.869263 \text{ W/m}.$$

To satisfy equation 3-42 it is necessary to repeat the process of calculations with a new value of the conductor temperature (iterative process). The energy balance equation is satisfied if

$$T_c = 40.0704 °C.$$

Steady-state conductor temperature calculations for wind velocities in the range from 2 to 15 m/s

Similar calculations were performed for wind velocities in the range from 2 to 15 m/s. For a wind velocity less than 0.5 m/s the Nusselt number was calculated using Equation (3-31). Results of the calculations are presented in Fig. 3.3. It can be seen that the temperature of the

conductor was 313 K at the wind velocity of 0.5 m/s and it reduces with the increase of the wind velocity and was 296 K when the wind velocity was 15 m/s.
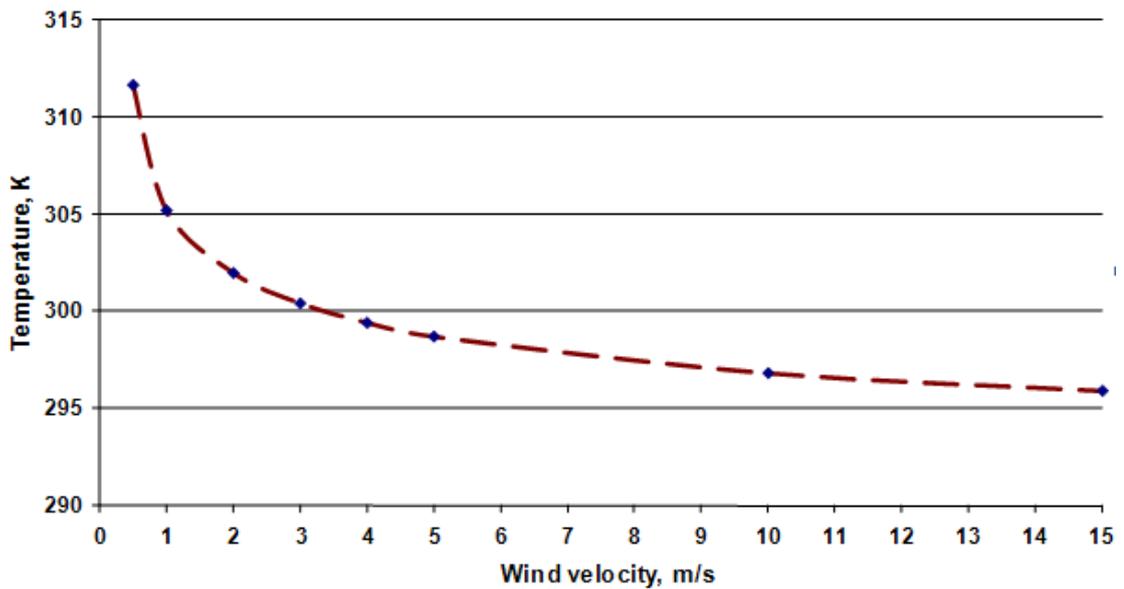
Fig. 3.3 The temperature of the conductor calculated in accordance with CIGRE method as a function of the wind velocity

Calculation of natural convective cooling

The calculation starts with assumption that the temperature of the conductor in this case is 66 ºC. Joule losses are calculated as

$$P_j = I^2 R_{dc} \cdot [1 + \alpha \cdot (T_{av} - 20)] = 434^2 \cdot 0.000157 \cdot [1 + 0.00403 \cdot (66 - 20)] = 35.05393 \text{ W/m}$$

The Grashof, Prandtl and Nusselt numbers are calculated as follows:

$$Gr = \frac{0.0195^3 \cdot (66 - 20) \cdot 9.803}{(43 + 273) \cdot (1.7285\text{E} - 05)^2} = 35440.91;$$

$$Pr = 0.715 - 2.5 \cdot 10^{-4} \cdot 43 = 0.70425;$$

$$Nu = 0.48 \cdot (35440.91 \cdot 0.70425)^{0.25} = 6.03322;$$

$$P_c = \pi \cdot 0.027296 \cdot (66 - 20) \cdot 6.03322 = 23.79885 \text{ W/m}$$

$$P_r = \pi \cdot 0.00195 \cdot 0.5 \cdot 5.67 \cdot 10^{-8} \cdot \left((66 + 273)^4 - (66 + 273)^4 \right) = 10.13704 \quad \text{W/m}$$

Substituting the above values in (3-42)

$$35.05393 = 33.93589 \text{ W/m}$$

Using an iterative process it was possible to find that T_c = 340.59 K (67.59 $^\circ$C) satisfies the energy balance equation.

3.2 Lumped parameter model of UGC

The objectives of the calculations are to determine the temperature of the conductor for a given current loading or to determine the maximum current loading for a given temperature of the conductor. The calculation methods for buried cables include two parts – steady-state rating and transient rating. Both calculations are presented in IEC 60287 [55] and based on the basic heat transfer equations. The popularity of an analytical approach, based on lumped parameter models can be explained by the following advantages:

- This method has been used since 1957 when Neher and McGrath's article was published.

- Expensive high powered computing equipment is not required for the calculations.

But it also has a disadvantage: it is suitable only for simple geometries.

The energy balance equation for underground cables is shown in equation 3-52.

$$W_{ent} + W_{int} = W_{out} + \Delta W_{st} . \qquad (3\text{-}52)$$

Here W_{ent} is the rate of energy entering the cable;

W_{int} is the rate of heat generated internally in the cable by joule or dielectric losses;

W_{out} is the rate at which energy is dissipated by conduction, convection and radiation. The cable system includes the surrounding soil for underground buried cables;

60

ΔW_{st} is the rate of change of energy stored within the cable.

The two dimensional heat flow scheme is shown in Fig. 3.4.
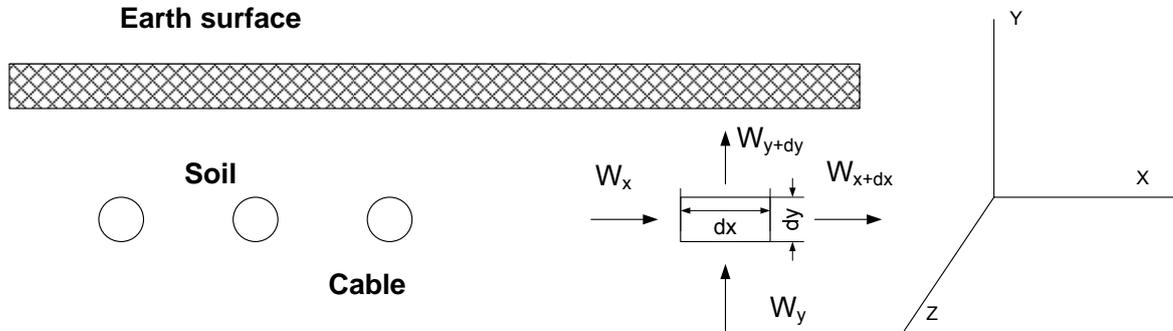
Fig. 3.4 The heat transfer (conduction) scheme in UGC

Current generates heat in a conductor, which dissipates into soil, therefore the parameters of the surrounding medium, such as soil type, moisture content, the soil temperature and the ambient temperature, are the most important factors affecting the heat dissipation process.

Conduction

The Fourier's law is usually used to define the heat flux emitted by conduction.

$$q = -\frac{1}{\rho} \cdot \frac{d\theta}{dx},$$
(3-53)

where q is the heat flux (W/m^2); ρ is thermal resistivity (K·m/W); $\frac{d\theta}{dx}$ is the temperature gradient (K/m).

Radiation

Heat flux due to radiation obeys the Stefan-Boltzmann law:

$$q = \varepsilon \sigma_B \theta_s^4,$$
(3-54)

where ε is emissivity of a conductor; σ_B is the Stefan-Boltzmann constant; and

$\sigma_B = 5.67 \cdot 10^{-8}$ W/m$^2 \cdot$K^4; θ_s is the absolute temperature on the surface of the cable, K.

Heat flux between the cable and the surroundings are calculated by the formulae

$$q = \varepsilon \sigma_B (\theta_s{}^4 - \theta_{amb}{}^4) \text{,}$$ (3-55)

where θ_{amb} is the ambient temperature, K.

3.2.1 IEC evaluation of the underground power cable in the steady state

The temperature of the underground power cable can be derived from the expression for the temperature rise above the ambient temperature for the current flowing in the conductor. In order to solve the heat conduction problem electrical engineers use the similarity between the flow of electric current and the heat flow.

The lumped parameter model for a single buried cable is presented in Fig.3.5
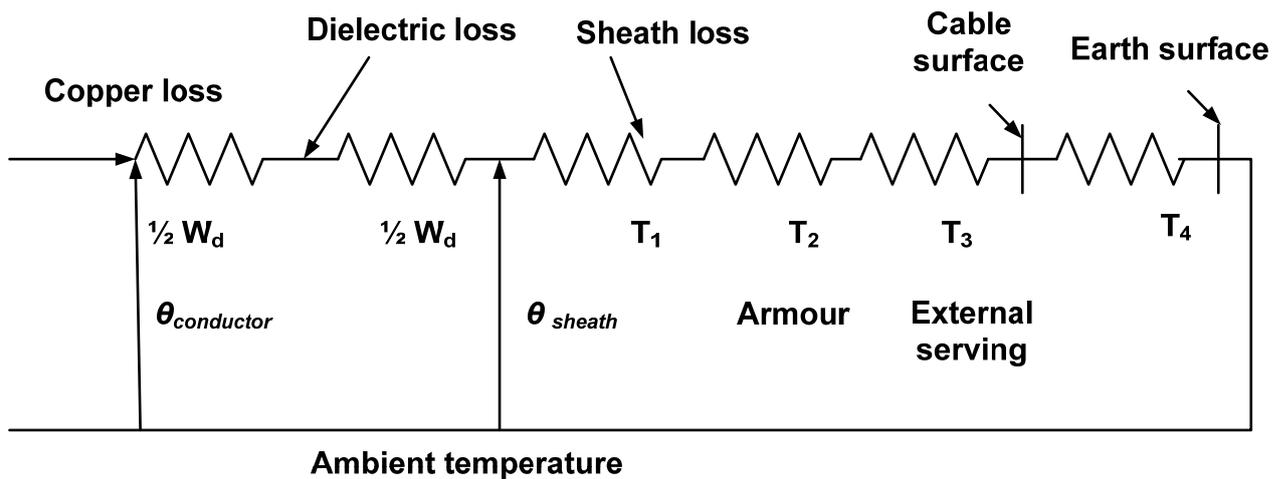
Fig. 3.5 Lumped parameter thermal circuit for a directly buried cable

The permissible current rating of an a.c. cable can be derived from the expression for the temperature rise above ambient temperature: [56]

$$\theta_c - \theta_a = \left(I^2 \cdot R_{ac} + \frac{1}{2} W_d \right) \cdot T_1 + \left(I^2 \cdot R_{ac} \cdot (1 + \lambda_1) + W_d \right) \cdot n \cdot T_2$$

$$+ \left(I^2 \cdot R_{ac} \cdot (1 + \lambda_1 + \lambda_2) + W_d \right) \cdot n \cdot (T_3 + T_4), \qquad (3\text{-}56)$$

where I is the current flowing in one conductor (A);

$\theta_c - \theta_a$ is the conductor temperature rise above the ambient temperature (K);

R is the alternating current resistance per unit length of the conductor at the maximum operating temperature (Ω/m);

W_d is the dielectric loss per unit length for the insulation surrounding the conductor (W/m);

T_1 is the thermal resistance per unit length between one conductor and the sheath (K·m/W);

T_2 is the thermal resistance per unit length of the bedding between sheath and armour (K·m/W);

T_3 is the thermal resistance per unit length of the external serving of the cable (K·m/W);

T_4 is the thermal resistance per unit length between the cable surface and the surrounding medium;

n is the number of load-carrying conductors in the cable (conductors of equal size and carrying the same load);

λ_1 is the ratio of losses in the metal sheath to total losses in all conductors in that cable;

λ_2 is the ratio of losses in the armouring to total losses in all conductors in that cable.

3.2.1.1 Calculation of losses

Conductor losses are the biggest source of losses within the cable and they are proportional to the resistance and to the square of the current transferred through the cable:

$$W_c = I^2 \cdot R_{ac}. \qquad (3\text{-}57)$$

Resistance is a function of material and dimensions of the conductor and depends on the temperature.

R_{dc} is d.c. resistance and can be calculated from

$$R_{dc} = \frac{\rho_0}{a} \cdot \left[1 + \alpha_{20} \cdot \left(\theta_{cmax} - 20° \right) \right] \cdot \left(1 + Z \right) \quad \Omega/\text{m},$$
(3-58)

where ρ_0 is resistivity of conductor metal at 20 ºC ($\Omega \cdot$ m);

a is conductor cross-sectional area (m^2);

α is the temperature coefficient of resistance per ºC at the reference temperature, (α = 0.00393 ºC^{-1} for copper);

$\theta_{c\max}$ is the maximum operating temperature (ºC)

Z is a factor, which allows for cable stranding and for the lay, $Z = 0.03$ for single core cables with cross-sectional area equal to or less than 500mm^2, and 0.04 for larger cables.

A.C. resistance is higher than D.C. resistance by ΔR, which shows the increase of resistance due to "skin" and "proximity" effects:

$$\Delta R = R_{dc} \cdot \left(Y_s + Y_p \right).$$
(3-59)

Here Y_s and Y_p are correction factors for the skin and proximity effects, respectively.

$$R_{ac} = R_{dc} + \Delta R = R_{dc} \cdot \left[1 + Y_s + Y_p \right].$$
(3-60)

Skin and proximity effects arise due to an alternating magnetic field which occurs within conductors. These effects increase when the frequency, cross-section, permeability, or electrical conductivity of the material increases.

The cause of the skin effect is self-inductance, which results in the current density being higher at the outer surface of the conductor.

Proximity effect arises due to mutual induction between the conductors of adjacent phases making the current to flow along one side of the conductor's cross-section. Proximity effects can be disregarded for cables with cross-sections smaller than 185 mm^2.

The dielectric loss is voltage dependent. According to IEC 60287 [55] the dielectric loss per unit length is given by:

$$W_d = \omega \cdot C U_0^2 \cdot tan\delta,$$
(3-61)

where C is the capacitance per unit length (F/m); U_o is the voltage to earth (V), $tan\delta$ is the loss factor and

$$\omega = 2 \cdot \pi \cdot f.$$
(3-62)

Here f is frequency (H).

3.2.1.2 Calculation of thermal resistances for single-core cables

Thermal resistance between one conductor and sheath (T$_1$)

The thermal resistance between one conductor and the sheath T$_1$ is given by:

$$T_1 = \frac{\rho_T}{2\pi} \cdot \ln\left[1 + \frac{2t_1}{d_c}\right],$$
(3-63)

where ρ_T is the thermal resistivity of insulation (K·m/W); t_1 is the thickness of insulation between conductor and sheath (mm); d_c is the diameter of the conductor (mm).

Thermal resistance between sheath and armour (T$_2$)

Single-core, two-core and three-core cables have a common metallic sheath.

The thermal resistance between sheath and armour, T_2, is given by:

$$T_2 = \frac{\rho_T}{2\pi} \cdot \ln\left[1 + \frac{2t_2}{D_s}\right],$$
(3-64)

where t_2 is the thickness of the bedding (mm); D_s is the external diameter of the sheath (mm).

Thermal resistance of outer covering (T₃)

The external servings are generally in the form of concentric layers and the thermal resistance T_3 is given by:

$$T_3 = \frac{\rho_T}{2\pi} \cdot \ln\left[1 + \frac{2t_3}{D_a}\right],$$
(3-65)

where t_3 is the thickness of serving (mm); D_a is the external diameter of the armour (mm).

Thermal resistance between outer covering and soil (T₄)

For a single isolated buried cable

$$T_4 = \frac{\rho_T}{2\pi} \cdot \ln\left[u + \sqrt{u^2 - 1}\right],$$
(3-66)

where ρ_T is the thermal resistivity of the soil (K·m/W) and

$$u = \frac{2L}{D_e},$$
(3-67)

where L is the distance from the surface of the ground to the cable axis (mm); D_e is the external diameter of the cable (mm).

T_4 for three cables, which have approximately equal losses, laid in a horizontal plane and equally spaced apart is given by equation:

$$T_4 = \frac{\rho_T}{2\pi} \cdot \ln\left[u + \sqrt{u^2 - 1}\right] + \ln\left[1 + \left(\frac{2 \cdot L}{s_1}\right)^2\right],$$
(3-68)

where s_1 is the axial separation between two adjacent cables (mm).

3.2.2 A steady-state sample calculation of the 630 mm^2 copper cable temperature, using the IEC method

In this section the temperature of the middle cable in the group of three cables for summer conditions with average soil moisture and a rating of 950 A is calculated. The cables are laid in a horizontal plane and equally spaced apart. The copper cable has an overall radius of 30.2 mm and is buried at a depth of 800 mm.

Initial data is as follows:

Area of concentric stranded conductor	630 mm ^{2}
AC Resistance of conductor	28.3 µ·Ω/m
Diameter over conductor	28.32 mm
Diameter over insulation	48.7 mm
Diameter over outside covering, D_e	60.4 mm
Ambient temperature	15 Cº
The soil thermal resistivity, g	1.2 Cº·m/W
Axial spacing between centre lines of conductors, s_1	120.8 mm
Depth to centre line of conductors	800 mm

The fundamental equation for a buried cable is equation 3-56, which is repeated below

$$\theta_c - \theta_a = \left(I^2 \cdot R_{ac} + \frac{1}{2} W_d \right) \cdot T_1 + \left(I^2 \cdot R_{ac} \cdot (1 + \lambda_1) + W_d \right) \cdot n \cdot T_2$$
$$+ \left(I^2 \cdot R_{ac} \cdot (1 + \lambda_1 + \lambda_2) + W_d \right) \cdot n \cdot (T_3 + T_4);$$

with $R_{ac} = R_{dc} \cdot \left(1 + y_s + y_p \right).$

According to [42]

$$R_{dc} = R' \cdot \left(1 + \alpha_{20} \cdot \left(\theta - 20^\circ C \right) \right) \ \Omega \cdot m^{-1},$$

67

where R' is d.c. resistance at 20 °C, which is 0.0000283 Ω/m for the copper cable with a cross sectional area of 630 mm², θ is operating temperature (°C); α is the temperature coefficient of resistance per °C at the reference temperature (α = 0.00393 °C⁻¹ for copper).

At the conductor temperature of 20°C the AC resistance can be calculated as

$$R_{ac} = R_{dc} \cdot (1 + y_s + y_p) = 0.0000283 \cdot (1 + 2.02485 \cdot 10^{-8} + 0.057762) = 2.99347 \cdot 10^{-5} \text{ Ω/m},$$

$$I^2 R_{ac} = 950^2 \cdot 2.99347 \cdot 10^{-5} = 27.01605 \text{ W/m}.$$

The thermal resistance T_1 between one conductor and the sheath is

$$T_1 = \frac{3.5}{2\pi} \cdot \ln\left(1 + \frac{2 \cdot 10.19}{28.32}\right) = 0.302 \text{ °C/W}.$$

Thermal resistance T_2 between sheath and armour is assumed to be negligible:

$$T_2 = 0.$$

The external servings are generally in the form of concentric layers and the thermal resistances T_3 and T_4 are given by:

$$T_3 = \frac{5}{2\pi} \cdot \ln\left(1 + \frac{60.4}{48.7}\right) = 0.171338 \text{ W/m},$$

and

$$T_4 = \frac{\rho_T}{2\pi} \cdot \ln\left[u + \sqrt{u^2 - 1}\right] + \ln\left[1 + \left(\frac{2 \cdot L}{s_1}\right)^2\right] = \frac{1.2}{2\pi} \cdot \ln\left[\frac{2 \cdot 800}{60.4} + \sqrt{\left(\frac{2 \cdot 800}{60.4}\right)^2 - 1}\right]$$

$$= 1.746087 \text{ W/m}$$

The dielectric loss per unit length in each phase is given by

$$W_d = \omega \cdot CU_0^2 \cdot \tan\delta = 2 \cdot \pi \cdot f \cdot CU_0^2 \cdot \tan\delta,$$

where

$$C = \frac{2 \cdot \pi \cdot \varepsilon_0 \cdot \varepsilon}{\ln\left(\frac{d_c}{D_s}\right)} = \frac{2 \cdot \pi \cdot 8.85 \cdot 10^{-12} \cdot 2.3}{\ln\left(\frac{48.7}{28.32}\right)} = 2.359 \cdot 10^{-10} \text{ F/m}.$$

The values of relative permittivity and loss factor were stated in IEC 60287 [55] (Part1, Table 3).

$$W_d = 2 \cdot \pi \cdot 50 \cdot C \cdot \left(\frac{127000}{\sqrt{3}}\right)^2 \cdot 0.004 = 1.59389 \text{ W/m}.$$

$$\theta_c - \theta_a = (27.01605 + 0.5 \cdot 1.59389) \cdot 0.302$$

$$+ (27.01605 + 1.59389) \cdot 1 \cdot (0.171338 + 1.746087) = 63.2 \text{ °C}.$$

Therefore, the temperature on the conductor surface was 78.2 °C or 351.2 K.

3.3 Transient heating of cables

In order to solve the heat conduction problem electrical engineers commonly use the similarity between the flow of electric current and the heat flow. So the thermal circuit is modelled in a similar way to an electrical circuit in which voltages and currents correspond to temperatures and to heat flows, respectively.

The conductor is divided into small parts with their own thermal resistances and capacitances. The thermal resistance specifies the ability of a material to obstruct the heat flow and the thermal capacitance defines the ability of the material to store heat. A thermal circuit can be built for different formations, using thermal resistance and thermal capacitance as components of the circuit to construct a thermal ladder network to obtain the time dependent temperature distribution within the cable and its surroundings.

Due to the fact that length of the conductor is considerable larger than its diameter the energy balance equation for 2-D (see Fig.3.4) can be written as [52]:

$$\frac{d\theta}{dx}\left(\frac{1}{\rho}\frac{d\theta}{dx}\right) + \frac{d\theta}{dy}\left(\frac{1}{\rho}\frac{d\theta}{dy}\right) + W_{int} = c\frac{d\theta}{dt}, \tag{3-69}$$

where ρ is thermal resistivity (K·m/W); $\dfrac{d\theta}{dx}$ is the temperature gradient (K/m);

c is the volumetric thermal capacity of the material (J/m³K).

This equation is usually solved with an equation which describes the boundary conditions

The boundary condition is

$$\theta = \theta_B , \tag{3-70}$$

where θ_B is the boundary temperature (K).

The conductor heat loss, W_{int}, can be calculated as

$$W_{int} = I^2 R . \tag{3-71}$$

Since information regarding the soil temperature distribution is not always available, simplifying assumptions are made such as the surrounding soil being homogeneous and the surface of the soil being isothermic. This assumption can be considered to be reasonably accurate due to the fact that the depth of burial of the conductor should be a minimum of 10 times more than the diameter of the conductor. For shallow buried conductors and for cables with large diameters correction factors or numerical methods are often used.

The thermal resistance of the insulation of a cable is the largest obstruction to the heat flow (the heat resistance of the metal parts are considerably lower and can be neglected). The thermal resistance of insulation can be calculated as

$$T = \frac{\rho_{th}}{2\pi} \ln \frac{r_2}{r_1} , \tag{3-72}$$

where r_1, r_2 internal and external radii of insulation.

The thermal equivalent of Ohm's law using an analogy between electrical and thermal networks is

70

$$W = \frac{\Delta \theta}{T}.$$

<div align="right">(3-73)</div>

Thermal capacitance is defined as

$$Q = V \cdot c,$$

<div align="right">(3-74)</div>

where V is volume (m^3); c is volumetric specific heat of the material (J/m^3·K).

$$Q = \frac{\pi}{4}\left(D_2^2 - D_1^2\right) \cdot c,$$

<div align="right">(3-75)</div>

where D_1 and D_2 are internal and external diameter of insulation, respectively (m).

3.3.1 A ladder network for calculation of transient temperature response

Lumped parameter models are widely used in thermal analysis of cable systems since they allow the analysis of complex cable systems without the deployment of expensive resources.

The thermal circuit is divided into two parts, such as the thermal circuit of the conductor and the thermal circuit of the environment of the cable. The dielectric is represented by lumped thermal constants. The complete transient behaviour is based on two partial transient responses. These two parts are combined by the implementation of the attainment factor, which can be computed as a ratio of the temperature rise across the first part at time t during the transient regime to the temperature rise across the same part in the steady state. Then, the temperature transient response of the second part of the thermal circuit is created from its response to a step function of heat input multiplied by a reduction coefficient, which is time dependent and equal to the attainment factor of the first part [57].

A ladder network represents an electrical circuit with a number of units of resistance and capacitance. The ladder networks for short and long duration transients are different. To calculate long and short duration transients in electrical standards Van Wormer's method [58] is used. This is based on an assumption that the temperature distribution in the insulation

follows a steady-state logarithmic distribution for the period of the transient. The thermal capacity of the insulation is divided between the conductor and the sheath and total heat in the dielectric is assumed to be unchanged.

The criteria for selecting the thermal circuits to be used for the calculation of the individual transients depends on the duration of the transient response; and for single cables long duration transients are define when the transient response exceeds more than one third of the product of the internal cable thermal resistances, $\sum T$, and capacitances, $\sum Q$, that is $> \frac{1}{3}\Sigma T \cdot \Sigma Q$. Fig.3.6 illustrates a ladder network for a long duration transient, when the total thermal capacity of the dielectric is divided between the conductor and the sheath.

Conductor   Outside diameter of insulation
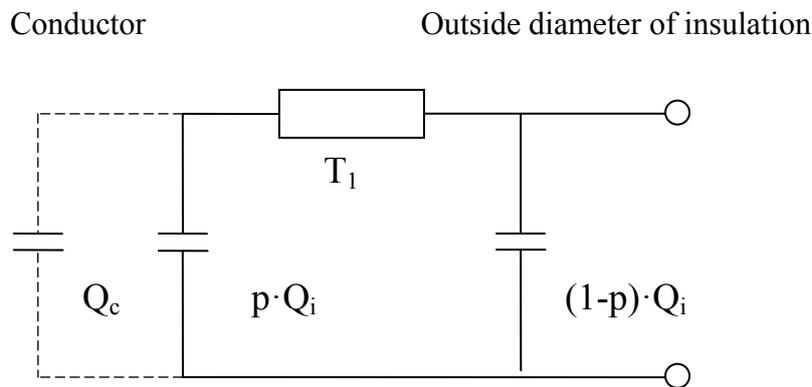
Fig. 3.6 Representation of the dielectric for times greater than $> \frac{1}{3}\Sigma T \cdot \Sigma Q$ [57]

To distribute the thermal capacitance of dielectric for long-duration transient (longer than 1 hour), the Van Wormer coefficient p is calculated as

$$p = \frac{1}{2\ln\left(\dfrac{D_i}{d_c}\right)} - \frac{1}{\left(\dfrac{D_i}{d_c}\right)^2 - 1}, \tag{3-76}$$

where D_i is outer diameter of insulation (m) and d_c is external diameter of the conductor (m).

Short-duration transients last usually between 10 min and about 1 h. The method is the same as for long-duration transients, except that the cable insulation is divided at diameter $d_x = \sqrt{D_i \cdot d_c}$, giving two portions having equal thermal resistances, as shown in Fig. 3.7.
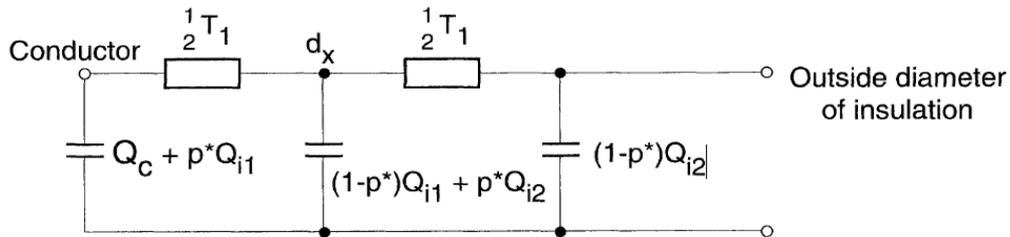
Fig. 3.7 Representation of the dielectric for times less than or equal $\leq \frac{1}{3}\Sigma T \cdot \Sigma Q$ [57]

The Van Wormer coefficient for this case is given by

$$p^* = \frac{1}{2\ln\left(\dfrac{D_i}{d_c}\right)} - \frac{1}{\left(\dfrac{D_i}{d_c}\right)^2 - 1} . \qquad (3\text{-}77)$$

A variety of cable designs were reduced to one simplified scheme with a two loop circuit and was adopted by the electrical standards, which have a reasonable accuracy in practical installations. A network with v number of resistances and $v+1$ capacitors, see Fig. 3.8, can be altered by a two looped circuit, see Fig. 3.9
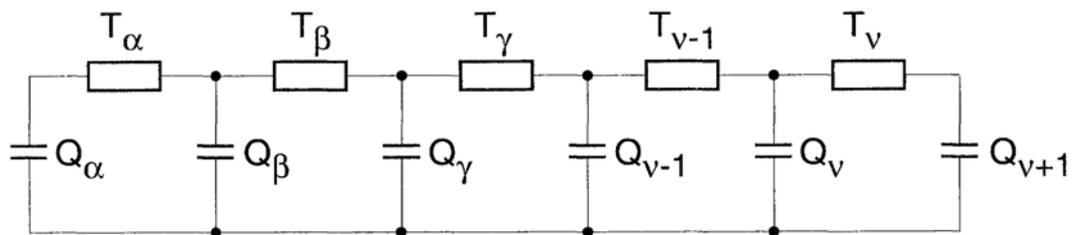
Fig. 3.8 General ladder network representing a cable [57]
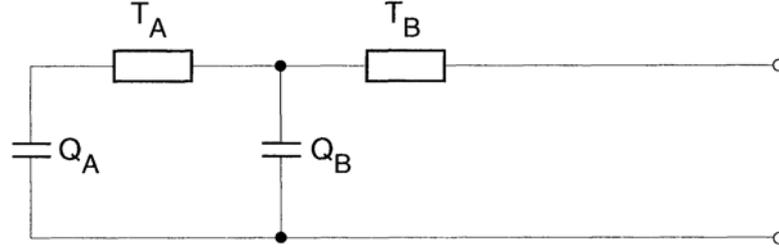
Fig. 3.9 Two loop equivalent cable network for calculation of transient response [57].

The first section of network represents the thermal capacitance of the conductor and the inner portion of the dielectric, along with the thermal resistance of the dielectric. The second section of network represents of the thermal capacitance and the thermal resistance of the remainder of the cable.

T_B and Q_B are given by Anders [59] as

$$T_B = T_\beta + T_\gamma + ... + T_\nu \tag{3-78}$$

and

$$Q_B = Q_\beta + \left(\frac{T_\gamma + T_\delta + ... + T_\nu}{T_\beta + T_\gamma + ... + T_\nu} \right)^2 Q_\gamma + \left(\frac{T_\delta + T_\varepsilon + ... + T_\nu}{T_\beta + T_\gamma + ... + T_\nu} \right)^2 Q_\delta . \tag{3-79}$$

$$T_A = T_1; \tag{3-80}$$

$$T_B = q_s T_3; \tag{3-81}$$

$$Q_A = Q_c + pQ_i; \tag{3-82}$$

and

$$Q_B = (1-p) \cdot Q_i + \frac{Q_s + p'Q_j}{q_s}, \tag{3-83}$$

where T_1 is total thermal resistance of dielectric per conductor (K·m/W);

Q_i is total thermal capacitance of dielectric per conductor (J/m·K);

p is factor for apportioning the thermal capacitance of a dielectric,

Q_c is thermal capacitance of conductor (J/m·K);

Q_j is thermal capacitance of outer covering (J/m·K);

Q_s is ratio of losses in conductor and sheath to losses in conductor(J/m·K); and

T_3 is thermal resistance of outer covering (K·m/W).

3.3.2 Calculation of transient temperature response

The transient response of the cable is based on an exponential integral formula for the steady state which is used in IEC Standard 287 [42] for groups of separate cables.

3.3.2.1 Temperature rise in the internal parts of the cable

The internal parts of the cable include the complete serving with its outermost serving. The Laplace transform of the network's transfer function is given by a ratio [59].

$$H(s) = \frac{P(s)}{Q(s)}. \tag{3-84}$$

Here $P(s)$ and $Q(s)$ are polynomials, their forms depending on the number of loops in the network. Node i can be the conductor or any other layer of the cable. In terms of time, the response of this network is expressed by Van Valkenburg in [60].

The temperature rise in a node i in the cable is given by

$$Q_i(t) = W_c \sum_{j=1}^{n} T_{ij} (1 - e^{P_j t}) \tag{3-85}$$

where $Q_i(t)$ is temperature rise at node i at time t (°C);

W_c is conductor losses including skin and proximity effects (W/m);

T_{ij} is coefficient (°Cm/W);

P_j is coefficient used for calculating cable partial transient temperature rise (s^{-1});

t is time from the beginning of the step(s); and

n is number of loops in the network.

The transfer function for the network shown in Fig.3.9 is given by

$$H(s) = \frac{(T_A + T_B)s T_A T_B Q_B}{1 + s(T_A Q_A + T_B Q_B + T_B Q_A) + s^2 T_A Q_A T_B Q_B}.$$

(3-86)

If the following parameters are introduced:

$$M_0 = \frac{1}{2}(Q_A\{T_A + T_B\} + Q_B \cdot T_B)$$

(3-87)

$$N_0 = Q_A \cdot T_A \cdot Q_B \cdot T_B)$$

(3-88)

$$a = \frac{M_0 + \sqrt{M_0^2 - N_0}}{N_0}$$

(3-89)

$$b = \frac{M_0 - \sqrt{M_0^2 - N_0}}{N_0}$$

(3-90)

$$T_a = \frac{1}{a - b} \cdot \left[\frac{1}{Q_A} - b \cdot (T_A + T_B) \right]$$

(3-91)

$$T_b = T_A + T_B - T_a$$

(3-92)

then the transient temperature rise is

$$\theta_c(t) = W_c \cdot \left[T_a \cdot (1 - e^{-at}) + T_b \cdot (1 - e^{-bt}) \right]$$

(3-93)

where W_c is the power loss per unit in a conductor (W/m).

The conductor to cable surface attainment factor is given in equation 3-94

$$a(t) = \theta_c(t)/[W_c \cdot (T_A + T_B)].$$

(3-94)

3.3.2.2 The transient temperature rise of the outer surface of the cable

The calculation of transient temperature rise $Q_e(t)$ of the outer surface of the cable can be evaluated exactly in the case when the cable is represented by a line source located in a homogeneous, infinite medium with an uniform initial temperature. For practical applications, the hypothesis of Kennelly (see Fig 3.10), which assumes that the Earth's surface must be an isotherm is used. Under this hypothesis, the temperature rise at any point M in the soil is, at any time, the sum of the temperature rises caused by the heat source *Wt* and by its fictitious image placed symmetrically with the earth surface as the axis of symmetry and emitting heat.
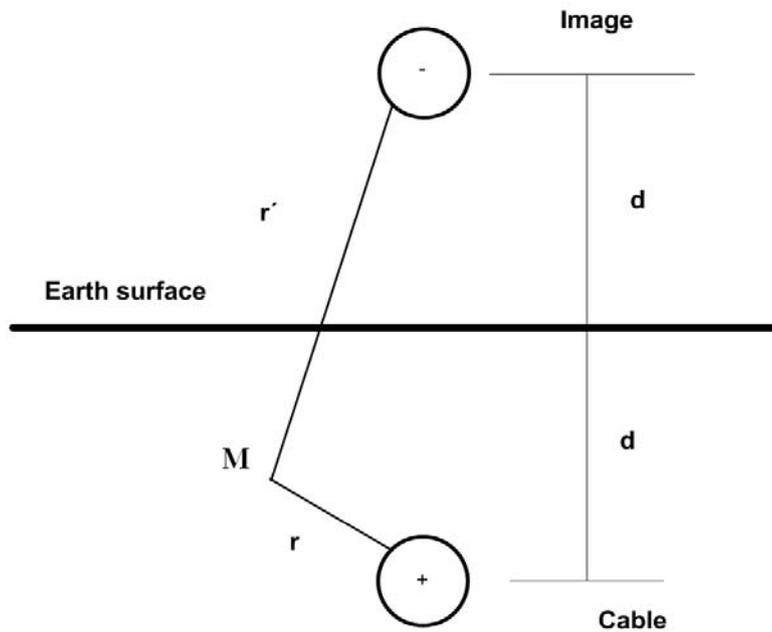
Fig. 3.10 The illustration of the Kennely hypothesis

The transient temperature rise above ambient of the outer surface of the hottest cable in the group of cables under the same load is calculated as

$$Q_e(t) = \frac{\rho_T W_I}{4 \cdot \pi} \cdot \left\{ \left[-Ei \cdot \left(\frac{-D_e^2}{16 \cdot t \cdot \delta} \right) - \left[-Ei \cdot \left(\frac{-L^2}{t \cdot \delta} \right) \right] \right] + \sum_{k=1}^{k=N-1} \left[-Ei \cdot \left(\frac{-(d_{pk})^2}{4 \cdot t \cdot \delta} \right) - \left[-Ei \cdot \left(\frac{-(d_{pk})^2}{4 \cdot t \cdot \delta} \right) \right] \right] \right\}, \quad (3\text{-}95)$$

where W_I is the total power loss per unit length of each cable in group (W/m);

$-Ei(-x)$ is the exponential integral function as provided in [57] ;

ρ is soil thermal resistivity (Km·/W);

D_e is external surface diameter of the cable (m);

δ is soil thermal diffusivity (m^2/s);

t is time from the moment of application of heating (s);

L is axial depth of burial of hottest cable (m);

d_{pk} is distance from centre of cable k to the centre of hottest cable p (m);

d'_{pk} is distance from image of centre of cable k to the centre of hottest cable p (m);

N is number of cables.

The complete transient temperature response can be calculated as

$$Q(t) = Q_c(t) + \alpha(t) \cdot Q_e(t), \tag{3-96}$$

where $Q(t)$ is transient temperature rise of conductor above ambient (K);

$Q_c(t)$ is transient temperature rise of cable surface above ambient from $t = 0$, assuming total losses from cable surface (K);

$Q_e(t)$ is transient temperature rise of conductor above ambient (K);

α is the attainment factor

3.3.2.3 Example of calculating temperature of the conductor one hour after switching of load

The following calculations are made for a cable with 950 A of loaded current, buried at a depth of 800 mm with average soil moisture. The cable has an overall radius of 30.2 mm. It is required to find the temperature rise on the surface of this cable one hour after switching of the load. Load generated a total heat of 36 Wm^{-1} in the cable for current of 950 A, and resistance of copper 630 mm^2 cable at 90º C is equal to 0.0405 Ohm per km, or

$$W = I^2 R = 950^2 \cdot 0.0405 / 1000 = 36 \ \text{Wm}^{-1}.$$

The soil density is 1900 kg m^{-3} and its specific heat is 830 Jkg^{-1} °C^{-1}. The soil thermal resistivity is 1.2 °CmW^{-1} and the ambient temperature is 15°C.

The temperature rise in the cable is determined as

$$\theta = \frac{W_c \cdot g}{2 \cdot \pi} \cdot G(t),$$

(3-97)

where

$$G(t) = \ln \frac{r'}{r} + \frac{1}{2} \int_0^{y_1} \frac{1 - e^{-y_1}}{y_1} dy_1 - \frac{1}{2} \int_0^{y_2} \frac{1 - e^{-y_2}}{y_2} dy_2$$

(3-98)

$$y_1 = \frac{r^2}{4\alpha t} \quad \text{and} \quad y_2 = \frac{r'^2}{4\alpha t}$$

(3-99)

Here r is the overall radius (mm) of the cable; r' is a depths of burial (mm); α is the thermal soil thermal diffusivity (m·K/W); t is time (3600s).

The thermal diffusivity of soil is defined as

$$\alpha = \left(\frac{1}{D \cdot C \cdot g} \right) = \frac{1}{1900 \cdot 830 \cdot 1.2} = 0.528 \cdot 10^{-6} \text{ m·s}^{-1}.$$

$$\frac{r'}{r} = \frac{2 \cdot 800}{30.2} = 52.98;$$

$$\ln \frac{r'}{r} = 3.97;$$

$$y_1 = \frac{r^2}{4\alpha t} = \frac{0.0302^2}{4 \cdot 0.528 \cdot 10^{-6} \cdot 3600} = 0.1199;$$

$$y_2 = \frac{r'^2}{4\alpha t} = 52.98 \cdot 0.1199 = 337.$$

Applying approximate formulae

$$\int_0^{y_1} \frac{1 - e^{-y_1}}{y_1} dy_1 = y_1 - \frac{y_1^2}{4} = 0.1163;$$

and

$$\int_0^{y_2} \frac{1 - e^{-y_2}}{y_2} dy_2 = \gamma + y_2 = 0.577216 + 5.82 = 6.397 \quad (\ln y_2 = \ln 337 = 5.82).$$

Therefore after one hour the temperature rise on the surface of the cable is

$$\theta'_{cab} = \frac{36 \cdot 1.2}{2\pi} \left[3.97 + \frac{0.1163}{2} - \frac{6.397}{2} \right] = 5.7 \text{ °C}$$

The actual temperature of the cable is

$$\theta_{cab} = 15 + 5.7 = 20.7 \text{°C}$$

So after one hour the temperature rise on the surface of the cable will be 5.7 ° C when generated heat is 36 Wm⁻¹, which corresponds to a transferred current of 950 A.

CHAPTER 4

THE THEORETICAL BACKGROUND OF COMPUTATIONAL FLUID DYNAMICS TECHNIQUES

Computational fluid dynamics (CFD) with associated numerical techniques is one of the branches of fluid mechanics that uses numerical methods to solve problems involving fluid flows, heat transfer and chemical reactions. Computers are used to perform calculations required to simulate the interaction of liquids and gases with surfaces defined as boundaries of the domain. CFD numerical investigations are used extensively in the research described in this thesis and this chapter describes the theoretical background of Computational Fluid Dynamics techniques.

The physical phenomena considered in this work involves the air flow around high voltage overhead power conductors which are heated due to Joule losses in the conductor and solar irradiance. This air flow is associated with combined heat transfer due to conduction inside the conductor, air convection on its external surface and re-radiation from the conductor to the surroundings.

The thermal state of underground power cables is defined by the heat transfer in

solid bodies, such as the conductor itself and surrounding soil or protection structures. Additionally, situations exist when underground power cables are also exposed to the flow of water, usually with low velocities. Finally, in some cases it is necessary to take into account the cooling effect of airflow over the ground where the cable is buried.

This Chapter first presents the system of governing equations describing generic flow and heat transfer phenomena, then moves on to a discussion of the most commonly used numerical methods for the solution of these equations.

Unlike laminar flow, the velocities of fluid particles in turbulent flows change unpredictably in space and in time, making the solution of the governing equation a complicated task and require substantial computational recourses. Turbulent models incorporate different techniques in order to simplify and solve heat transfer problems. General principles of turbulence modelling are described in the third section of the Chapter, followed by a detailed description of the two most frequently used models for the solution of equations of turbulent flow, namely Spalart-Allmaras (one-equation) and k-ε (two-equation) models. Section 5 also describes the basics of other turbulence models available in the CFD software package Fluent [52]. Finally, the solution procedure using finite volumes method is described in detail in Sections 6, 7 and 8.

4.1 Governing equations

The general equations governing fluid flow and heat transfer are the conservation of continuity, momentum and energy equations. These conservation equations are

generally called Navier-Stokes (N-S) equations, although to be accurate N-S equations consist of momentum equations only. The equations governing the physical phenomena of air flow and heat transfer in the domain with the conductor are the Navier-Stokes equations for 2-D or 3-D steady and transient flow of compressible (air) or incompressible (fluid, oil) non-reacting fluid. The flow of liquids depend on velocity can be categorized as laminar or turbulent.

The continuity, momentum and energy equations (in the form of partial differential equations) are directly obtained by applying the relevant conservation principles to an infinitesimally small element (model) fixed in space; see Fig. 4.1 [56].

4.1.1 Continuity equation

The general equation for conservation of mass, i.e. continuity equation for an unsteady compressible flow can be written as:

$$\frac{\partial \rho}{\partial t} + \frac{\partial}{\partial x_j}.\left(\rho \cdot u_j\right) = 0 , \tag{4-1}$$

where ρ is the density of the fluid; u_j stands for u_1, u_2 and u_3, which are the velocity components in 3-D flows.

4.1.2 Momentum conservation equation

The momentum conservation equation for unsteady, compressible, viscous flow with body forces in an inertia reference frame may be written as:

$$\frac{\partial}{\partial t}(\rho u_i) + \frac{\partial}{\partial x_j}\left(\rho \cdot u_i u_j\right) = -\frac{\partial p}{\partial x_i} + \frac{\partial \tau_{ij}}{\partial x_j} + \rho g_i + F_i , \tag{4-2}$$

where ρ is the density of the fluid (kg/m^3); p is the static pressure (Pa); τ_{ij} is the

stress tensor (Pa); ρg_i is the gravitational body force (N); and F_i are the external

body forces (N).

$$v + \frac{\partial v}{\partial y} \cdot \delta y$$
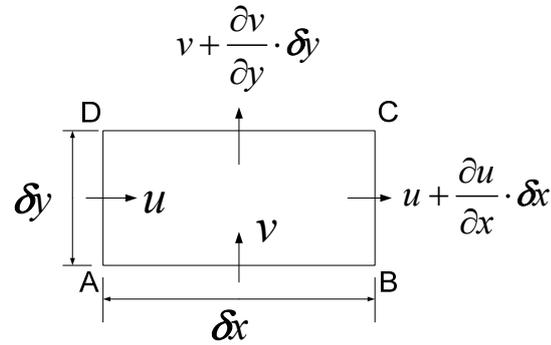
(a) Geometry and Velocities

$$\left(\tau + \frac{\partial \tau}{\partial y} \delta y \right) \cdot \delta x$$
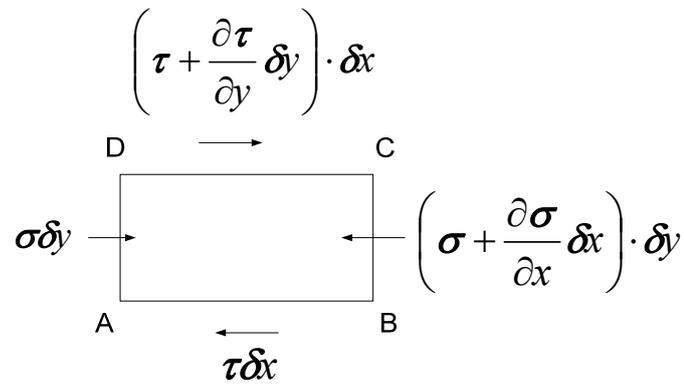
(b) Forces in X – direction

Fig. 4.1 Flow into a patch of fluid [56]

For Newtonian fluid the viscous stress term is

$$\tau_{ij} = \mu \left[\left(\frac{\partial u_i}{\partial x_j} + \frac{\partial u_j}{\partial x_i} \right) - \frac{2}{3} \frac{\partial u_l}{\partial x_l} \delta_{ij} \right], \tag{4-3}$$

where j=1, 2, 3. If index appears twice then the sum of three terms is used; δ_{ij} is the

Kronecker delta (δ_{ij}= 1 if $i=j$, else δ_{ij}=0). Coefficient μ in equation 4-3 is the

dynamic viscosity of fluid (Pa·s).

84

4.1.3 Energy equation

The energy conservation equation for unsteady, compressible, viscous flow with heat transfer (assuming heat flux is given by Fourier's law) and chemical reaction/volumetric heat sources may be written as:

$$\frac{\partial}{\partial t}(\rho E) + \frac{\partial}{\partial x_j}(\rho \cdot u_j \cdot E) = -\frac{\partial}{\partial x_j}(u_j \cdot p) + \frac{\partial}{\partial x_j}\left(k\frac{\partial T}{\partial x_j}\right) + \frac{\partial}{\partial x_j}(u_i \tau_{ij}) + Sh, \qquad (4\text{-}4)$$

where $E = e + \dfrac{u^2}{2}$.

Here e is the internal energy, k is the conductivity, Sh is the heat of chemical reaction or volumetric heat sources and T is the static temperature.

The Navier - Stokes equations which include the continuity equation (4-1), momentum equations (4-2) and energy equation (4-4) are a coupled system of non-linear differential equation which is not closed, since the number of unknowns (ρ, p, u_x, u_y, u_z and e) is greater than the number of equations by 1. The additional equation required to close the system of equations is the equation of state, for perfect gas it is

$$p = \rho \cdot R \cdot T, \qquad (4\text{-}5)$$

where $R = \dfrac{R_u}{M_w}$ with R, R_u being the specific and the universal gas constant, respectively, and M_w is the gas/fluid molecular weight. Equation (4-5) introduces an additional unknown - the temperature T. The last equation to close the entire system must be a thermodynamic relation between state variables. For example, $e = e(T, p)$ and for thermally perfect gas (where specific heat is a function of temperature), this relation would be:

$$e = c_v \cdot T ,\qquad\qquad\qquad\qquad (4\text{-}6)$$

where c_v is the specific heat at constant volume and it is a function of temperature.

4.2 Numerical solution methods

The Navier-Stokes equations (4-1), (4-2), (4-4) and caloric equation of state (4-6), along with appropriate boundary conditions (no slip, velocities/mass flow rates and heat flux/temperatures) are expected to provide a solution at any point in the flow field. However, since the governing equations are a coupled system of non-linear partial differential equations, there are very difficult to solve analytically. In the absence of any analytical solution scheme, the governing equations are usually solved using advanced numerical scheme/procedure.

There are three major numerical methods for solution of a system of partial differential equations:

- Finite Differences Method (FDM);
- Finite Element Method (FEM);
- Finite Volume Method (FVM).

The above methods differ from each other in the approximation of the variables and in the discretisation techniques.

4.2.1 Finite Difference Method (FDM)

Finite-difference methods (FDM) approximate solutions by substituting derivatives with approximately equivalent difference quotients [56, 61]. Extensive application of the FD method can be explained by the mathematical simplicity of the discretisation procedure.

The error in a solution is defined as the difference between its approximation and the exact analytical solution. The two sources of error in finite difference methods are round-off, the loss of precision due to computer rounding of decimal quantities, and truncation error or discretization error, the difference between the exact solution of the finite difference equation and the exact quantity assuming no round-off. To use a finite difference method to attempt to solve a problem, the physical problem domain must be first discretized. This is usually done by dividing the domain into a uniform grid. This means that finite-difference methods produce sets of discrete numerical approximations (algebraic equations) to the derivative.

The first-order derivative can be defined as:

a forward difference:

$$\frac{dU}{dx} = \frac{U(x+h) - U(x)}{h} + O(h), \qquad (4\text{-}7)$$

or a backward difference:

$$\frac{\partial U}{\partial x} = \frac{U(x) - U(x-h)}{h} + O(h), \qquad (4\text{-}8)$$

where h is the small displacement in the x direction, also called a numerical mesh size and $O(h)$ denotes that terms of higher order exist, but if the distance h is very small then these terms might be neglected.

In general case, when a time-dependant problem is considered, the Crank-Nicolson method is based on an application of the central difference at time $t_{n+1/2}$ and a second-order central difference for the space derivative at position x_j, is used, see Fig. 4.2. The scheme is always numerically stable and convergent and requires solving a system of differential equations on each time step.

87
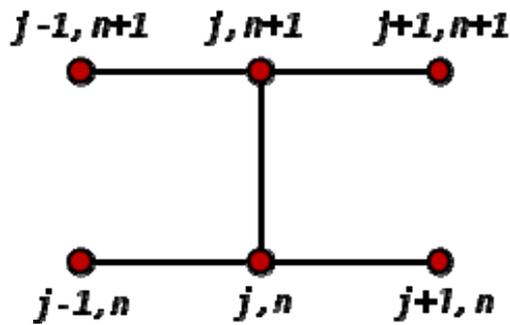
Fig. 4.2 The Crank–Nicolson stencil

The disadvantage of the method is that only domains with relatively simple geometries can be considered.

4.2.2 Finite Element Method (FEM)

The finite element method has been in use since the 1950s and initially was designed for solving structural mechanics problems. Currently, several types of finite element method exist (Generalized Finite Element Method, hp-FEM, Extended FEM or XFEM etc.). In this method the geometry of a physical domain needs to be divided into a large number of small elements, and then the differential equations are approximated by the variational principle, usually the weighted residual approach (the variation of parameters inside the elements is described using special functions). The solution approach is based either on eliminating the differential equation completely (steady state problems), or converting PDEs into an approximating system of ordinary differential equations, which are then numerically integrated using standard techniques such as Euler's method or Runge – Kutta. More information about FEM can be found in [62].

4.2.3 Finite Volume Method (FVM)

The finite volume method deals with a small volume which surrounds each node on a mesh and calculates the values of the conserved variables averaged across the volume. The finite volume method is a method for representing and evaluating partial differential equations in the form of algebraic equations.

In the finite volume method, volume integrals in partial differential equations that contain a divergence term are converted to surface integrals using the divergence theorem. These terms are then evaluated as fluxes at the surfaces of each finite volume. Because the flux entering a given volume is identical to that leaving the adjacent volume, these methods are conservative. Another advantage of the finite volume method is that it can be used in unstructured meshes.

Based on the control volume formulation of analytical fluid dynamics the finite volume method is used in many computational fluid dynamics packages, such as CFX, Star CD and Fluent. Fluent CFD software is employed in this study and the finite volume method will be described in more details in the following sections.

4.2.4 The comparison between Finite Element and Finite Difference Methods

The differences between FEM and FDM are:

- The most attractive feature of the FEM is its ability to handle complicated geometries (and boundaries) with relative ease. While FDM in its basic form is restricted to handle rectangular shapes and simple alterations, the handling of geometries in FEM is theoretically straightforward.

- The most attractive feature of finite differences is that it can be very easy to

implement.

- In general FDM can be considered as a special case of the FEM approach. Basis functions can be chosen as either piecewise constant functions or Dirac delta functions. In both approaches, the approximations are defined on the entire domain, but need not be continuous.

- There are reasons to consider the mathematical foundation of the finite element approximation more sound, for instance, because the quality of the approximation between grid points is poor in FDM.

- The quality of a FEM approximation is often higher than in the corresponding FDM approach, but this is extremely problem dependent and several examples to the contrary can be provided.

Generally, FEM is the method of choice in all types of analysis in structural mechanics (i.e. solving for deformation and stresses in solid bodies or dynamics of structures).

4.3 Turbulence modelling

The FVM is the most accepted method for solution of CFD problems, which usually require discretization of the domain into a large number of cells/gridpoints (millions and more).

Directly solving the governing system of equations for turbulent flow is very expensive computationally. Implementation of simple, lower order approximation within each cell can decrease the cost of the solution.

Therefore, the N-S equations are time averaged to produce a modified set of

governing equations, which contains additional unknown variables. This section describes details of the turbulence modelling methodology for developing additional equations for dealing with extra unknowns in the time averaged equations. This is followed by the description of numerical discretization scheme employed for solving the time averaged N-S equations. Finally, some convergence/stability definitions are presented.

As mentioned above, a direct numerical simulation (DNS) of the governing system of equations for turbulent flows, which are characterised by fluctuating velocity fields and transport properties, is not currently realistic due to the level of computational requirements for resolving large and small scale flow structures. Instead, the governing equations are usually time/ensemble - averaged to remove the fluctuating small scales, resulting in a modified system of equations that is computationally less expensive to solve. The averaging process introduces additional unknown variables in the time averaged set of governing equations and therefore, turbulence models are required to have additional transport equations for unknown scalar quantities to close the system of time averaged equations.

In Reynolds averaging procedure, the flow variables in the instantaneous N-S equations are split into the mean and fluctuating components. Let ϕ represent scalar quantities such as pressure, energy, etc., then:

$$\phi = \overline{\phi} + \phi', \tag{4-9}$$

where $\overline{\phi}$ and ϕ' are the mean and fluctuating components. Similarly, for vector quantities like velocity

$$u_i = \overline{u}_i + u_i', \tag{4-10}$$

where, $\bar{u}_i$ and u'_i are mean and fluctuating velocity components (i =1, 2, 3).

Substituting the form given by equation (4-9) and (4-10) for flow variables into the continuity and momentum equations in tensor notion and taking time average and dropping the overbar on the mean yields ensemble-averaged equations. For steady flow, they can be written:

$$\frac{\partial}{\partial x_i}(\rho u_i) = 0 \,; \qquad\qquad (4\text{-}11)$$

$$\frac{\partial}{\partial x_j}(\rho u_i u_j) = -\frac{\partial p}{\partial x_i} + \frac{\partial}{\partial x_j}\left[\mu \cdot \left(\frac{\partial u_i}{\partial x_j} + \frac{\partial u_j}{\partial x_i}\right) - \frac{2}{3}\frac{\partial u_i}{\partial x_i}\delta_{ij}\right] + \frac{\partial}{\partial x_j}\left(-\rho\overline{u'_i u'_j}\right). \ (4\text{-}12)$$

The ensemble-averaged equation for continuity (4-11) and momentum (4-12) are referred Reynolds-averaged Navier-Stokes (RANS) equations. They are the same general form as the instantaneous Navier-Stokes equations, with velocities and flow variables representing time/ensemble-averaged values. Additional terms appear in the ensemble-averaged equation, which represent the effects of turbulence. When equations (4-11) and (4-12) are applied to variable density flows with the velocities representing mass-averaged (density weighted time average) values, they are referred as Favre-averaged Navier-Stokes (FANS).

The additional unknown term which appears in equation (4-12), namely, $-\rho\overline{u'}_i\overline{u'}_j$ is known as Reynolds stresses and renders the set of partial differential equations unclosed. In order to obtain a closed form of equations that can be solved, it is necessary to model the Reynolds stresses. A common method is to employ the Boussinesq hypothesis (Linear Eddy Viscosity Model, EVM) to relate the Reynolds stress to the mean velocity gradients. Boussinesq suggested that

turbulence could be described by the same type of stress-strain relationship as

$$- \rho \overline{u'_i u'_j} = \mu_t \cdot \left(\frac{\partial u_i}{\partial x_j} + \frac{\partial u_j}{\partial x_i} \right) - \frac{2}{3} \cdot \left(\rho k + \mu_t \frac{\partial u_k}{\partial x_k} \right) \delta_{ij} \,, \qquad (4\text{-}13)$$

where μ_t is the turbulent viscosity and $k = \dfrac{\overline{u'_i u'_j}}{2}$ is the kinetic energy of

turbulence. The term $\dfrac{2}{3} \rho k \delta_{ij}$ in equation (4-13) is included in order to ensure that

the trace of Reynolds stress tensor is equal to $(- 2\rho k)$, as it should be. In contrast to

molecular viscosity (μ), turbulent viscosity (μ_t) is not a fluid property but depends

strongly on the state of turbulence. It may vary significantly from one point in the

fluid flow to another and also from flow to flow.

The introduction of equation (4-13) alone does not constitute a turbulence model but

only provides the framework for constructing such model; the main problem is now

shifted to determining the distribution of μ_t. If a separate turbulence model is used to

calculate μ_t and k, the governing ensemble-averaging equation along with turbulence

model equation form a closed system of partial differential equations, which can be

solved numerically. Turbulence models and corresponding governing equations are

discussed in latter paragraphs.

Similar to time/ensemble-averaging of the continuity and momentum equations, the

energy equation can also be ensemble-averaged to give a modified instantaneous

energy equation with resultant unknown terms representing turbulence. In Fluent,

turbulent energy/heat transport is modelled using the concept of Reynolds analogy to

turbulent momentum transfer. The 'modelled' energy equation is given by:

$$\frac{\partial}{\partial x_i}\left[u_i \cdot (\rho \cdot E + p)\right] = \frac{\partial}{\partial x_j}\left[\left(k + \frac{c_p \mu_t}{Pr_t}\right)\frac{\partial T}{\partial x_j} + u_i \left(\tau_{ij}\right)_{eff}\right], \quad (4\text{-}14)$$

where k is the thermal conductivity, c_p is the specific heat at constant pressure and $\left(\tau_{ij}\right)_{eff}$ is the deviatoric tensor defined as

$$\left(\tau_{ij}\right)_{eff} = \mu_{eff} \cdot \left(\frac{\partial u_i}{\partial x_j} + \frac{\partial u_j}{\partial x_i}\right) - \frac{2}{3}\mu_{eff}\frac{\partial u_k}{\partial x_k}\delta_{ij}, \quad (4\text{-}15)$$

where $\mu_{eff} = \mu + \mu_t$.

The ensemble-averaging of steady energy equation without chemical reaction/heating source, yields a modified equation which contains many unknown terms, of which two turbulence terms are more significant (while the rest of the unknowns are neglected). Of the two significant terms associated with turbulence, one is modelled analogous to the Fourier heat conduction equation and the other is modelled in the same fashion as Reynolds stresses. Therefore equation (4-15) contains an additional modelled term added to the thermal conductivity and a modified stress tensor term to take care of the Reynolds stresses.

4.4 The most frequently used type of turbulent models

There is no single turbulence model that is universally accepted as being superior to all classes of problems. The choice of the turbulence model depends on characteristics of the flow, the level of accuracy required, the available computational resources and the amount of time available for the simulation [52]. Therefore it is necessary to understand the capabilities and limitations of the turbulence models in order to make an appropriate choice. Due to enormous computational requirement, direct numerical simulation (DNS) and large eddy

simulation (LES) were not used in this work. The $k - \varepsilon$ model was employed for most of computational simulations performed and two models, namely Spalart-Allmaras and $k - \varepsilon$ are considered in detail in this section to demonstrate approaches used to simulate turbulent flows.

Turbulence models like Spalart-Allmaras, k -ε and $k - \omega$ employ the Boussinesq approach for modelling Reynolds stresses. The central issue is, how the eddy/turbulent viscosity, μ_t, is calculated in each of the above models. An alternate to the Boussinesq approach is the Reynolds stress transport model (RSM), which solve transport equations for each of the terms in Reynolds stress tensor directly.

The advantage of Boussinesq approach model over RSM is the relatively low computational cost associated with the computation of the turbulent viscosity, μ_t. The disadvantage of the Boussinesq hypothesis is that it assumes turbulent viscosity as an isotropic scalar quantity, which may not be correct. RSM is superior for situations in which the anisotropy of turbulence has a dominant effect on the mean flow, such as highly swirling flows and stress-driven secondary flows. However, for many cases, models based on the Boussinesq hypothesis perform very well and the additional computational expense of the Reynolds stress model is not justified.

It terms of computation, Spalart-Allmaras is the least expensive turbulence model, since only one turbulence transport equation needs to be solved. The two-equation models, like k-ε and k–ω, require more computational effort than the Spalart-Allmaras model.

4.4.1 Spalart-Allmaras model theory

The model proposed by Spalart and Allmaras is a relatively simple one-equation model that solves a modelled transport equation for a quantity that is a modified form of the kinematic eddy (turbulent) viscosity. The Spalart-Allmaras model was designed specifically for aerospace application involving wall-bounded flows and has been shown to give good results for boundary layers subject to adverse pressure gradient [52]. However, no claim is made regarding the suitability of the Spalart-Allmaras to all types of complex engineering flows. Further, one-equation models are often criticized for their inability to rapidly accommodate changes in the length scale.

The transported variable in the Spalart-Allmaras model, $\widetilde{v}$, is identical to the turbulent kinematic viscosity except in the near-wall (viscous-affected) region. The scalar transport equation for $\widetilde{v}$ is given by:

$$\frac{\partial}{\partial t}(\rho\widetilde{v}) + \frac{\partial}{\partial x_i}(\rho \cdot \widetilde{v} u_i) = G_v + \frac{1}{\sigma_{\widetilde{v}}}\left[\frac{\partial}{\partial x_j}\left(\mu + \rho \cdot \widetilde{v}\right)\frac{\partial\widetilde{v}}{\partial x_j} + C_{b2}\rho\left(\frac{\partial\widetilde{v}}{\partial x_j}\right)\right] -$$

$$Y_v + S_{\widetilde{v}} \qquad\qquad (4\text{-}16)$$

where G_v is the production of turbulent viscosity and Y_v is the destruction of turbulent viscosity in the near-wall region; $S_{\widetilde{v}}$ is a user defined source term; $\sigma_{\widetilde{v}}$ and C_{b2} are constants and v is the molecular kinematic viscosity.

Modelling the turbulent viscosity (μ_t)

The turbulent viscosity is computed from

$$\mu_t = \rho\widetilde{v}f_{v1}, \qquad\qquad (4\text{-}17)$$

96

where the viscous damping function, f_{v1}, is given by

$$f_{v1} = \frac{\chi^3}{\chi^3 + C_{v1}^3} \; ; \quad \chi \equiv \frac{\widetilde{v}}{v}. \tag{4-18}$$

Modelling the turbulent production

The production term, G_v, is modelled as

$$G_v = C_{b1} \cdot \rho \cdot \widetilde{S} \cdot \widetilde{v}, \tag{4-19}$$

where

$$\widetilde{S} \equiv S + \frac{\widetilde{v}}{k^2 \cdot d^2} \cdot f_{v2} \quad \text{and} \quad f_{v2} = 1 - \frac{\chi}{1 + \chi f_{v1}}. \tag{4-20}$$

In equations 4-19 and 4-20 C_{b1} and k are constants, d is the distance from the wall and S is a scalar measure of the deformation tensor and can be calculated as

$$S \equiv \sqrt{2 \cdot \Omega_{ij} \cdot \Omega_{ij}}, \tag{4-21}$$

where Ω_{ij} is the mean rate of the rotation tensor:

$$\Omega_{ij} = \frac{1}{2} \cdot \left(\frac{\partial u_i}{\partial x_j} - \frac{\partial u_j}{\partial x_i} \right). \tag{4-22}$$

For wall bounded flows the expression for S is justified by the fact that turbulence is found only where vorticity is generated (near the walls).

Modelling the turbulent destruction:

The destruction term, Y_v, *in* (4-16) is modelled as

$$Y_v = C_{w1} \cdot \rho \cdot f_w \cdot \frac{\tilde{v}}{d}, \qquad (4\text{-}23)$$

where

$$f_w = g\left[\frac{1 + C_{w3}^6}{g^6 + C_{w3}^6}\right]^{\frac{1}{6}}; \ g = r + C_{w2} \cdot \left(r^6 - r\right); \ r \equiv \frac{\tilde{v}}{\tilde{S}k^2 d^2}. \qquad (4\text{-}24)$$

Here C_{w1}, C_{w2} and C_{w2} are constants and $\tilde{S}$ is given by equation (4-20)

Model constants

The following are the default values for the model constants:

$$C_{b1} = 0.1355; \ C_{b2} = 0.622; \ \sigma_{\tilde{v}} = \frac{2}{3}; \ C_{v1} = 7.1;$$

$$C_{w1} = \frac{C_{b1}}{k^2} + \frac{1 + C_{b2}}{\sigma_{\tilde{v}}}; \ C_{w2} = 0.3; \ C_{w3} = 2.0; \ k = 0.4187.$$

Near-wall treatments for wall-bounded turbulent flows

Turbulent flows are significantly affected by the presence of walls. First, the mean velocity is affected through the no-slip condition existing at the wall. Secondly, very close to the wall, viscous damping reduces the tangential velocity fluctuations, while kinematic blocking reduces the normal fluctuations. Towards the outer part of the near-wall region, however, the turbulence is rapidly increased by the production of turbulence kinetic energy due to the large gradients in the mean velocity.

Modelling of the flow in the near-wall region determines successful prediction of wall-bounded turbulent flows, because in the near wall region the solution variables have large gradients. The near-wall region can be subdivided into three layers. In the innermost layer, called the "viscous sublayer", the flow is almost laminar and the

molecular viscosity plays a dominant role in momentum and heat/mass transfer. In the outer layer, called the fully turbulent layer (log-law region), turbulence plays a major role. In the interim region between the viscous sublayer and the fully turbulent layer, the effects of molecular viscosity and turbulence are equally important.

Unlike the k-ε model, the RSM and the LES model, which are primarily valid for turbulent core flows; the Spalart-Allmaras and k–ω models were designed to be applied throughout the boundary layer, provided that the near -wall mesh resolution is sufficient.

Wall boundary conditions for Spalart-Allmaras model

The modified turbulent kinematic viscosity $\tilde{v}$ is set to zero at walls. When the mesh is fine enough to resolve the laminar sublayer, the wall shear stress is obtained from the laminar stress-strain relationship:

$$\frac{u}{u_\tau} = \frac{\rho u_\tau y}{\mu}. \tag{4-25}$$

If the mesh is too coarse to resolve the laminar sublayer, it is assumed that the centriod of the wall-adjacent cell falls within the logarithmic region of the boundary layer and log law of the wall is employed:

$$\frac{u}{u_\tau} = \frac{1}{k} \ln E\left(\frac{\rho u_\tau y}{\mu}\right), \tag{4-26}$$

where u is the velocity parallel to the wall; u_τ is the shear velocity; y is the distance from the wall; $k = 0.4187$ is the von Karman constant and $E = 9.793$.

4.4.2 The standard k-ε turbulence model

The standard k-ε model is a two-equation model, one for the turbulent kinetic energy, k, and another for the rate of dissipation of turbulent kinetic energy ε. The instantaneous kinetic energy of a turbulent flow is the sum of the mean and the turbulent kinetic energy.

The standard k-ε model [52] provides two additional equations, one for k and another for ε. Velocity scale φ and length scale l are given as follows:

$$\varphi = k^{1/2}; \quad l = \frac{k^{3/2}}{\varepsilon}. \tag{4-27}$$

Hence turbulent eddy viscosity is specified as follows:

$$\mu_t = C\rho\varphi l = \rho C_\mu \frac{k^2}{\varepsilon}, \tag{4-28}$$

where C_μ is a dimensionless constant.

The standard model uses the following transport equations for k and ε:

$$\frac{\partial}{\partial t}(\rho k) + \frac{\partial}{\partial x_i}(\rho u_i k) = \frac{\partial}{\partial x_i}\left(\mu + \frac{\mu_t}{\sigma_k}\right)\frac{\partial k}{\partial x_i} + G_k + G_b - p\varepsilon - Y_{Mk} \tag{4-29}$$

$$\frac{\partial}{\partial t}(\rho \varepsilon) + \frac{\partial}{\partial x_i}(\rho u_i \varepsilon) = \frac{\partial}{\partial x_i}\left(\mu + \frac{\mu_t}{\sigma_\eta}\right)\frac{\partial \varepsilon}{\partial x_i} + C_{1\varepsilon}\frac{\varepsilon}{k}P_k + C_{2\varepsilon}\rho\frac{\varepsilon^2}{k} \tag{4-30}$$

where P_k is the rate of production of k and is given by

$$P_k = \tau_{ij}\left(\frac{\partial u_i}{\partial x_j}\right) = \mu_t\left(\frac{\partial u_i}{\partial x_j} + \frac{\partial u_j}{\partial x_i}\right)\left(\frac{\partial u_i}{\partial x_j}\right). \tag{4-31}$$

The standard k-ε model employs values for the constants that are obtained by

comprehensive data fitting for various turbulent flows:

$$C_\mu = 0.09; \qquad \sigma_k = 1.00; \qquad \sigma_\varepsilon = 1.30; \qquad C_{1\varepsilon} = 1.44; \qquad C_{2\varepsilon} = 1.92$$

At high Reynolds number, the standard k-ε model avoids the need to integrate equations through to the wall by making use of the behaviour of near-wall flows. The following wall functions can be used for high Reynolds numbers:

$$u^+ = \frac{U}{u_\tau} = \frac{1}{\kappa} \ln\left(Ey_P^+\right); \qquad k = \frac{u_\tau^2}{\sqrt{C_\mu}}; \qquad \varepsilon = \frac{u_\tau^3}{\kappa y}. \qquad (4\text{-}32)$$

For heat transfer the universal near-wall temperature distribution valid at high Reynolds numbers is used:

$$T^+ \equiv -\frac{(T - T_w)C_p \rho u_\tau}{q_w} = \sigma_{T,t}\left[u^+ + P\left(\frac{\sigma_{T,l}}{\sigma_{T,t}}\right)\right], \qquad (4\text{-}33)$$

where T is the temperature at near wall point y_p; T_w is the wall temperature; q_w is wall heat flux; C_p is the fluid specific heat at constant pressure; $\sigma_{T,t}$ is the turbulent Prandtl number; $\sigma_{T,l} = \mu C_p/\Gamma_T$ is the Prandtl number; Γ_T is the thermal conductivity; P is a correction function

At low Reynolds numbers, the k-ε model requires some modifications by adding a few wall damping functions f_μ, f_1 and f_2, and additional terms L_k and L_ε to account for non-isotropic dissipation process:

$$\mu_t = C\rho\varphi l = \rho f_\mu C_\mu \frac{k^2}{\varepsilon}; \qquad (4\text{-}34)$$

$$\frac{\partial(\rho k)}{\partial t} + \mathrm{div}(\rho k U) = \mathrm{div}\left(\left(\mu + \frac{\mu_t}{\sigma_k}\right)\mathrm{grad}\,k\right) + P_k - \rho\varepsilon + L_k \qquad (4\text{-}35)$$

$$\frac{\partial(\rho\varepsilon)}{\partial t} + \text{div}(\rho k U) = \text{div}\left(\left(\mu + \frac{\mu_t}{\sigma_\varepsilon}\right)\text{grad}\,\varepsilon\right) + C_{1\varepsilon}f_1\frac{\varepsilon}{k}P_k - C_{2\varepsilon}f_2\rho\frac{\varepsilon^2}{k} + L_\varepsilon \quad (4\text{-}36)$$

The advantages and disadvantages of the *k-ε* model are as follows [52]:

Advantages:

- Simplest turbulence model for which only initial and/or boundary conditions need to be supplied;

- Excellent performance for many industrially relevant flows;

- Well established; the most widely validated turbulence model;

Disadvantages:

- More expensive to implement than mixing length model

- Poor performance in a variety of important cases, such as some unconfined flows, flows with large extra strains, rotating flows and fully-developed flows in non-circular ducts.

4.5 The choice of the turbulent models in Fluent

Fluent CFD [52] software provides the following choices of turbulence models, which depends on the level of accuracy, time available, computer capabilities

- Spalart-Allmaras model;

- *k-ε* models:

  o Standard *k-ε* model;

  o Renormalization-group (RNG) *k-ε* model;

  o Realizable *k-ε* model;

- *k-ω* models:

  o Standard *k-ω* model;

  o Shear-stress transport (SST) *k-ω* model;

- v^2-f model;

- Reynolds stress model (RSM);

- Large eddy simulation (LES) model;

- Detached eddy simulation (DES) model.

The basics of the Spalart-Allmaras model and the standard k-ε model were described above.

In Fluent two additional k-ε models are available:

- the RNG k-ε model;

- the realizable k-ε model.

4.5.1 The turbulent models available in Fluent

The RNG k-ε model includes the following improvements in comparison with standard k-ε model:

1. The RNG model has an additional term in its ε equation that significantly improves the accuracy for rapidly strained flows.

2. The effect of swirl on turbulence is included in the RNG model, enhancing accuracy for swirling flows.

3. The RNG theory provides an analytical formula for turbulent Prandtl numbers, while the standard k-ε model uses user-specified, constant values.

4. While the standard k-ε model is a high-Reynolds-number model, the RNG theory provides an analytically-derived differential formula for effective viscosity that accounts for low-Reynolds-number effects.

These features make the RNG k-ε model more accurate and reliable for a wider class of flows than the standard k-ε model.

The realizable k-ε model differs from the standard k-ε model in two important ways:

1. The realizable k-ε model contains a new formulation for the turbulent viscosity.

2. A new transport equation for the dissipation rate, ε, has been derived from an exact equation for the transport of the mean-square vorticity fluctuation.

It provides accurate predictions for flows involving rotation, boundary layers under strong adverse pressure gradients, separation and recirculation.

The k-ω model is also one of common turbulence models. It is a two equation model, which means it includes two extra transport equations to represent the turbulent properties of the flow. The first transported variable is turbulent kinetic energy, k. The second transported variable in this case is the specific dissipation, ω. It is the variable that determines the scale of the turbulence, whereas the first variable, k, determines the energy in the turbulence.

$$\frac{\partial}{\partial t}(\rho k) + \frac{\partial}{\partial x_i}(\rho k u_i) = \frac{\partial}{\partial x_j}\left(\Gamma_k \frac{\partial k}{\partial x_j}\right) + G_k - Y_k + S_k\,; \qquad (4\text{-}37)$$

$$\frac{\partial}{\partial t}(\rho \omega) + \frac{\partial}{\partial x_i}(\rho \omega u_i) = \frac{\partial}{\partial x_j}\left(\Gamma_k \frac{\partial \omega}{\partial x_j}\right) + G_\omega - Y_\omega + S_\omega\,. \qquad (4\text{-}38)$$

Here G_k represents the generation of turbulence kinetic energy due to the mean

velocity gradients and G_ω is the generation of ω; Γ_k and Γ_ω represent the effective diffusivity for k and ω due to turbulence; S_k and S_ω are user defined source terms.

The v^2-f model is a low Reynolds number turbulence model, similar to k-ε model. In this model the velocity scale, $\bar{v}^2$, is used instead of the turbulent kinetic energy. The anisotropic wall effects are modelled through the elliptic relaxation function, f, by solving a separate elliptic equation.

The Reynolds stress model is the most complex and time consuming model due to the fact that it requires five additional transport equations and encompasses the effects of swirl and rotation more accurately than two equation models.

The exact transport equation for the transport of the Reynolds stresses is written as

$$
\underbrace{\frac{\partial}{\partial t}\left(\rho \overline{u_i' u_j'}\right)}_{Local\ Time\ Derivative} + \underbrace{\frac{\partial}{\partial x_k}\left(\rho u_k \overline{u_i' u_i'}\right)}_{C_{ij} \equiv Convection} =
$$

$$
= -\underbrace{\frac{\partial}{\partial x_k}\left(\rho \cdot \overline{u_i' u_j' u_k'} + p \cdot \left(\delta_{kj} \cdot u_i' + \delta_{ik} \cdot u_j'\right)\right)}_{D_{T,ij} \equiv Turbulent\ Local\ Time} +
$$

$$
+ \underbrace{\frac{\partial}{\partial x_k}\left(\mu \frac{\partial}{\partial x_k}\left(\overline{u_i' u_j'}\right)\right)}_{D_{L,ij} \equiv Molecular\ Diffusion} - \underbrace{\rho\left(\overline{u_i' u_k'}\frac{\partial u_j}{\partial x_k} + \overline{u_j' u_k'}\frac{\partial u_i}{\partial x_k}\right)}_{P_{ij} \equiv Stress\ Production} - \underbrace{\rho\beta(g_i \overline{u_j' \theta} + g_j \overline{u_i' \theta})}_{G_{ij} \equiv Buoyancy\ Production} +
$$

$$
+ \underbrace{p\left(\frac{\partial u_i'}{\partial x_j} + \frac{\partial u_j'}{\partial x_i}\right)}_{\phi_{ij} \equiv Pressure\ Strain} - \underbrace{2\mu\frac{\partial u_i'}{\partial x_k}\frac{\partial u_j'}{\partial x_k}}_{\varepsilon \equiv Dissipation} - \underbrace{2\rho\Omega k\left(\overline{u_j' u_m'}\varepsilon_{ikm} + \overline{u_j' u_m'}\varepsilon_{ikm}\right)}_{F_{ij} \equiv Production\ by\ System\ Rotation} + \underbrace{S_{user}}_{User\text{-}Defined\ Source\ Term} \qquad (4\text{-}39)
$$

Here C_{ij}, $D_{L,ij}$, P_{ij} and F_{ij} do not require any modelling, but $D_{T,ij}$, G_{ij}, φ_{ij} and ε need to be modelled.

Large-eddy simulation models are implemented in simulating complex flows which contain a huge number of large and small eddies. LES models are based on the belief that momentum, mass, energy and other passive scalars are transported mostly by large eddies and are strongly dependent on the geometries and boundary conditions and small eddies are less dependent on the geometry and more universal.

LES models have advantages over direct numerical simulation (DNS) and Reynolds-averaged Navier-Stokes (RANS) methods. Modelling using DNS is very costly, therefore it is not implemented in industry. RANS models are very computationally efficient, but cannot model real flow. They are dealing with the mean characteristic of the flow and are used to predict major parameters, such as lift and drag. In LES flows large scales are computed directly, as in DNS, and the small scales are modelled. LES models are not as expensive as DNS models and provide a more realistic picture of the flow than RANS models.

Detached eddy simulation approach is based on the Spalart-Allmaras model. The core of DES modelling is implementation of the combination of LES modelling with RANS modelling for high Reynolds number flow – in cases when LES model cannot be used.

4.5.2 Comparison between frequently used turbulence models from the point of computational time and memory storage

The Spalart-Allmaras model is the least expensive turbulence model of the options provided in Fluent, since only one turbulence transport equation is solved.

The standard k-ε model clearly requires more computational effort than the Spalart-Allmaras model since an additional transport equation is solved. The realizable k-ε model requires only slightly more computational effort than the standard k-ε model.

However, due to the extra terms and functions in the governing equations and a greater degree of non-linearity, computations with the RNG k-ε model tend to take 10-15% more CPU time than with the standard k-ε model. Like the k-ε models, ***the k-ω models*** are also two-equation models, and thus require about the same computational effort.

Compared with the k-ε and k-ω models, the RSM requires additional memory and CPU time due to the increased number of the transport equations for Reynolds stresses. On average, the RSM in Fluent requires 50-60% more CPU time per iteration compared to the k-ε and k-ω models. Furthermore, 15-20% more memory is needed [52].

4.6 Solution procedure using Finite Volume Method

The time/ensemble-averaged N-S equations consisting of continuity (4-1), momentum (4-2) and energy (4-4), along with equation of state (4-6) and the scalar transport equation, constitute a set of closed partial differential equations describing the problem flow physics. These equations when solved along with appropriate boundary conditions yield the solution to the flow field under investigation. As with the exact governing N-S equations, the time averaged N-S equations, along with the scalar equation representing turbulence, form a set of coupled nonlinear partial differential equations which has no known general analytical solution procedure.

The implicit density-based solver of Fluent, which is intended for compressible flows, is used in the present exercise. A control-volume based technique is used for the discretization of the governing equations and consists of:

- Division of the domain into discrete control volumes using computational grid.

- Integration of the governing differential equations on the individual control volumes to construct algebraic equations for the discrete dependent unknown variables, such a velocities, pressure, temperature and conserved scalars (modified kinematic viscosity pertaining to the Spalart- Allmaras- model)

- Linearization of the discretized equations and solution of the resultant linear equation system to yield updated values of the dependent variables.

The density-based solver solves the governing equations of continuity, momentum and energy simultaneously. The governing equation for turbulence scalar (modified kinematic viscosity) is solved afterwards and sequentially. For the reason that the governing equations are nonlinear and coupled, several iterations of solution must be performed before a converged solution will be obtained.

Each of iterations includes the following steps:

- Update the fluid properties based on the current solution (if the calculation has just begun, the fluid properties will be updated based on the initialized solution).

- Solve continuity, momentum and energy equations simultaneously.

- Solve equation for scalar (modified kinematic viscosity) using previously

updated values of the other variables.

- Check for convergence of the equation set.

The above steps are continued until the convergence criteria are met.

In the density-based solution methods, the discrete, non-linear governing equations are linearized to produce a system of equations for the dependent variables in every computational cell. The resultant linear system is then solved to yield an updated flow-field solution. The manner in which the governing equations are linearized may take an 'implicit' or 'explicit' form with respect to the dependent variables of interest. In this study the implicit density solver is used.

The implicit density solver solves for all variables (pressure, velocities and temperature) in all cells at the same time and for a given variable. The unknown value in each cell is computed using a relation that includes both existing and unknown values of the neighbouring cells. Therefore each unknown will appear in more than one equation in the system and these equations must be solved simultaneously to give the unknown quantities.

4.7 Illustration of discretization and solution procedure for general scalar transport equation

A general scalar transport equation in vector form (independent of coordinate system) for an arbitrary scalar variable, ϕ, is given below:

$$\frac{\partial}{\partial t}(\rho\phi) \quad + \quad \nabla.(\rho \cdot \vec{v} \cdot \phi) \quad = \quad \nabla.(\Gamma_\phi \nabla\phi)+ \quad S\phi. \tag{4-40}$$

$$\textit{Unsteady} \qquad \textit{Convection} \qquad \textit{Diffusion} \qquad \textit{Source}$$

The volume integration of scalar equation (4-40) is given by

$$\iiint_V \frac{\partial}{\partial t}(\rho\phi)dV + \iiint_V \nabla.(\rho \cdot \vec{v} \cdot \phi)dV = \iiint_V \nabla.(\Gamma_\phi \nabla\phi)dV + \iiint_V S\phi dV. \qquad (4\text{-}41)$$

The integration over the volume V may be transformed to integration over the surface of the volume by the use of Gauss theorem. Thus integral equation (4-41) can be rewritten as:

$$\iiint_V \frac{\partial}{\partial t}(\rho\phi)dV + \iint_S \rho \cdot \vec{v} \cdot \phi.d\vec{A} = \iint_S \Gamma_\phi \nabla\phi.d\vec{A} + \iiint_V S_\phi dV. \qquad (4\text{-}42)$$

where ρ is the density; $\vec{v}$ is the velocity vector; $\vec{A}$ is surface area vector; Γ_ϕ is diffusion coefficient for ϕ; S_ϕ is source of ϕ per unit volume and $\nabla\phi$ is gradient of ϕ.

Equation (4-42) is applied to each control volume/cell, in the computational domain.

An example, a 2-D triangular cell shown in Fig. 4.3.
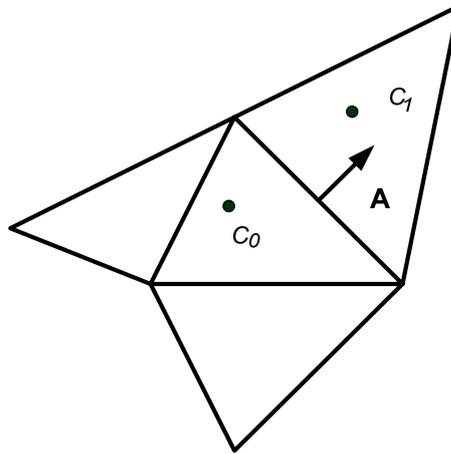
C_0 and C_1 are the cell centroids of the respective cell.

Fig. 4.3 Control volume – to illustrate discretisation of scalar transport equation [52]

Discretization of equation (4-42) on a given cell yields:

$$\frac{\partial}{\partial t}(\rho\phi)V + \sum_f^{N_{faces}} \rho_f \cdot \vec{v}_f \cdot \phi_f d\vec{A}_f = \sum_f^{N_{faces}} \Gamma_f \nabla\phi_f d\vec{A}_f + S_\phi \cdot V \qquad (4\text{-}43)$$

110

where N_{faces} - is the number of faces enclosing the cell; ϕ_f is the value of ϕ, convected through face f; $\rho_f \cdot \vec{v}_f . \vec{A}_f$ is the mass flux through the face f; $\vec{A}_f$ is area of surface f; $\nabla\phi_f$ is gradient of ϕ at face f; V is the cell volume.

All the scalar equations solved for the flow problem take the same general form as the one given by equation (4-43).

4.7.1 Temporal discretization

For transient simulations the governing equations must be discretized in both space and time. The spatial discretization for the time-dependent equations is identical to the steady-state case. Temporal discretization involves the integration of every term in the differential equations over a time step Δt. A generic expression for the time evolution of a variable ϕ is given by:

$$\frac{\partial \phi}{\partial t} = F(\phi), \tag{4-44}$$

where F incorporates any spatial discretization. If the time derivative is discretized using backward differences, the first-order accurate temporal discretization is given by:

$$\frac{\phi^{n+1} - \phi^n}{\Delta t} = F(\phi), \tag{4-45}$$

where ϕ is a scalar; n is value at current time t; $n+1$ is value at time $t + \Delta t$.

Once the time derivative has been discretized, $F(\phi)$ can be evaluated at future time level (implicit time integration) or at current time level (explicit time integration). To evaluate $F(\phi)$ at the future time level:

$$\frac{\phi^{n+1} - \phi^n}{\Delta t} = F\left(\phi^{n+1}\right) \qquad\qquad (4\text{-}46)$$

This is referred to as 'implicit' integration since ϕ^{n+1} in a given cell is related to ϕ^{n+1} in the neighbouring cells through $F(\phi^{n+1})$. The above implicit equation can be solved iteratively at each time level before moving to the next time step. The advantage of the fully implicit scheme is that it is unconditionally stable with respect to the time step size.

In the density based solver, the coupled set of governing equations (continuity, momentum and energy) is discretized in time for both steady and unsteady calculations. In the steady case it is assumed that the time marching proceeds until a steady-state is reached.

4.7.2 Spatial discretization

The scalars (and also other flow variables) are stored at the cell centers $(c_0$ and c_1 in Fig. 4.2). However, face values ϕ_f are required for the convection terms in equation (4-43) and must be interpolated from the cell centre values. This is accomplished using an upwind scheme. Upwinding implies that the value ϕ_f is derived from quantities in the cell upstream, or upwind, relative to the direction of the normal velocity. In first order discretization the face value ϕ_f is set equal to the cell-center value of ϕ in the upstream cell; also first order discretization generally gives better convergence. When second-order accuracy is desired (as in the present problem), quantities at the cell faces are computed using a Taylor series expansion of the cell-centered solution about the cell centroid. So, when second order upwinding (SOU) is selected, the face value ϕ_f is described as

$$\phi_{f,SOU} = \phi + \nabla\phi \cdot \Delta s, \tag{4-47}$$

where ϕ and $\nabla\phi$ are the cell-centered value and its gradient in the upstream cell and Δs is the displacement vector from the upstream cell centroid to the face centroid. The gradient $\nabla\phi$ needs to be calculated in each cell. In addition, gradients are required for computing diffusion terms and velocity derivatives. When the Green-Gauss theorem is used to compute the gradient of the scalar ϕ at the cell centre c_0, the following discrete form can be written:

$$(\nabla\phi)_{c_0} = \frac{1}{V} \bar{\phi}_f \cdot A_f, \tag{4-48}$$

where ϕ_f is the value of ϕ at the cell face centroid. In Green-Gauss cell-based gradient evaluation, $\bar{\phi}_f$ is computed from the arithmetic average of the values at the neighbouring cell centers, i.e.

$$\bar{\phi}_f = \frac{\phi_{c_0} + \phi_{c_1}}{2}. \tag{4-49}$$

The discretized scalar transport equation (4-47) contains the unknown scalar variable at the cell centre, as well as the unknown values in surrounding neighbouring cells. This equation will in general be a non-linear with respect to these variables. However, a linearized form of equation (4-47) can be written as:

$$a_P \cdot \phi = \sum_{nb} a_{nb} \cdot \phi_{nb} + b, \tag{4-50}$$

where the subscript nb refers to neighbour cells; a_P and a_{nb} are the linearized coefficients for ϕ and ϕ_{nb}.

The number of neighbours for each cell is typically equal to the number of faces enclosing the cell (boundary cells being the exception). Similar equations can be

written for each cell in the grid. This results in a set of algebraic equations with a sparse coefficient matrix. The linear system of equation for scalar ϕ is solved using the implicit Gauss-Seidel method.

4.8 Convergence criteria for numerical simulation

There is no universal metric for judging convergence. Therefore it is required to judge convergence not only by examining residual (defined below) levels but also monitoring relevant integrated quantities, such as mass flow, heat transfer coefficient, etc. For the present problem, the scaled residual (defined below) of 10^{-3} is selected as the convergence criterion for all the equations, except the energy equation, for which the criterion is 10^{-6}.

In addition, wall bounded compressible flow requires the monitoring of the mass imbalance between the inlet and the outlet. Mass imbalance of less than 0.2 % usually implies a converged solution. Thus convergence of wall bounded flow requires monitoring scaled residuals as well as percentage mass imbalance between the inlet and the outlet. Solution marching is truncated as soon as both of the above convergence criteria are met.

Definition of Residuals for scalars

The discretized transport equation for scalar ϕ at a cell P is given by equation (4-50) and it rewritten below for discussion.

$$a_P \cdot \phi_P = \sum_{nb} a_{nb} \cdot \phi_{nb} + b, \qquad (4\text{-}51)$$

where a_P is the cell centre coefficient; a_{nb} are the influence coefficients for the

114

neighbouring cells and b is the contribution of the constant part of the source term S_c in $S = Sc + S_{P\phi}$ and of the boundary conditions. The cell centre coefficient is shown in equation 4-51.

$$a_P = \sum_{nb} a_{nb} - S_P .$$ (4-52)

The residual R^ϕ is the imbalance in equation (4-51) summed over all the computational cells. This is referred as the "unscaled" residual. It may be written as:

$$R^\phi = \sum_{cellsN} \left| \sum_{nb} a_{nb} \cdot \phi_{nb} + b - a_P \phi_P \right| .$$ (4-53)

It is generally difficult to judge convergence by examining the residuals defined by equation (4-53), since no scaling is employed. The residual given by equation (4-53) is scaled using a scaling factor representative of the flow rate (flux) of ϕ through the domain. This "scaled" residual is defined as

$$R^\phi = \frac{\sum_{cellsN} \left| \sum_{nb} a_{nb} \cdot \phi_{nb} + b - a_P \phi_P \right|}{\sum_{cellsN} \left| a_P \phi_P \right|}$$ (4-54)

Fig. 4.4 shows an example of the residuals of all variables plotted in a consol window. Histories of residuals can be saved automatically in the data files.

4.9 Conclusions

General principles of numerical methods, turbulence modelling, and the two most frequently used models for the solution of equations of turbulent flow, namely

Spalart-Allmaras (one-equation) and k-ε (two-equation) models and other turbulence models available in the CFD software package Fluent and also the solution procedure using finite volumes method were described in detail.
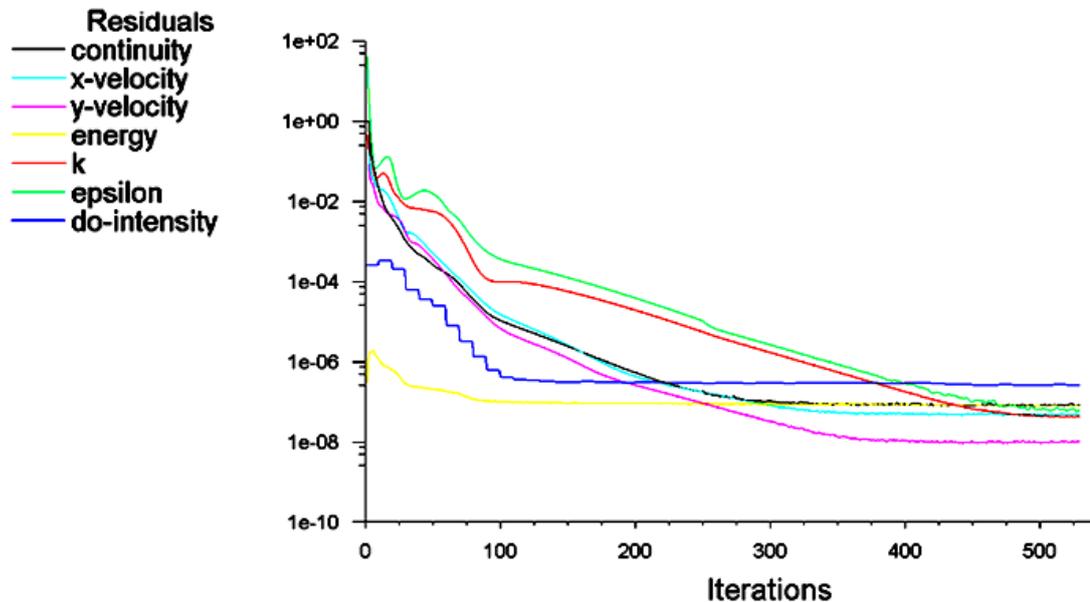
Fig. 4.4 An example of graphic representation of residuals in Fluent

Numerical methods are used when it is impossible to get analytical solution for the time averaged governing equations for flow and the heat transfer phenomena. The most applicable methods are FEM, FDM and FVM.

FEM is implemented in all types of analysis in structural mechanics (i.e. solving for deformation and stresses in solid bodies or dynamics of structures). CFD tends to use FDM or FVM. Commercial package Fluent utilizes the finite (control) volume method, the domain is divided into a number of control volumes, such that there is a control volume surrounding each grid point. The differential equation is integrated over each control volume to form the algebraic equations containing the grid point values; therefore the numerical procedure yields solutions only at discrete points and

116

not throughout (continuously) the flow domain.

Unlike laminar flow, the velocities of fluid particles in turbulent flows change unpredictably in space in time, making the solution of the governing equation a complicated task and requiring substantial computational resources. Turbulence models incorporate different techniques in order to simplify and solve flow and heat transfer problems.

CHAPTER 5

STEADY - STATE THERMAL BEHAVIOUR OF OVERHEAD LINES

5.1 CFD model

The main objectives of this chapter are to analyse the heat transfer between the Lynx conductor and the ambient air under cross wind conditions (when the wind is perpendicular to the axis of the conductor) and parallel wind conditions (when the wind is parallel to the axis of the conductor) and the conductor is in a steady state. The thermal state is described by a certain number of properties, such as temperature, pressure and density. These properties have constant values for a given state.

As mentioned in Chapter 2, ENA P27 [17] uses a wind velocity of 0.5 m/s as initial data for calculating the line ratings for cross wind conditions, which can be applied for 3 sets of ambient temperatures, such as summer (20°C), winter (2°C) and spring/autumn (9°C) and for 3 design core temperatures 50°C, 65°C and 75°C.

The calculations of the thermal state of the conductor for various cross and parallel wind velocities were carried out for the case in which the transmitted load corresponded to 433 A with

a design core temperature of 50°C, which is the static summer rating for a Lynx conductor with an ambient temperature of 293 K and a cross wind velocity of 0.5 m/s [17].

The commercial CFD package, Fluent was used for solving the governing equations of flow around the conductor. Fluent provides modelling capabilities to solve the steady state and transient problem and allows the dependencies of thermo-physical properties of the conductor, such as heat capacity, conductivity and resistivity on temperature, to be taking into account.

The ACSR conductor Lynx consists of 30 strands of aluminium wire and 7 strands of steel wire, see Fig. 5.1.
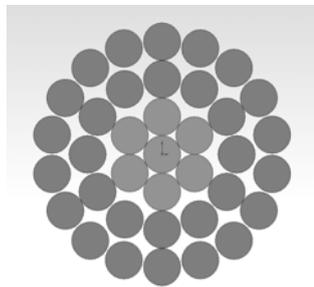
Fig. 5.1 The real geometry of the Lynx conductor [63]

The maximum diameter of the aluminium cylinder and of the steel core is 19.5 and 8.37 mm, respectively, with the cross sectional area of the aluminium part being 183.4 mm^2, see Appendix A. For modelling purposes the conductor was assumed to be a combination of two coaxial cylinders in order to simplify calculations, as demonstrated in Fig. 5.2. More complex models will result in increasing computational time and would require a significant amount of memory to store the associated data. For this calculation scheme the diameter of the steel core was increased to 12.1 mm to keep the outer diameter and the aluminium cross-section of the conductor equal to their real values. The conductor is placed in the relatively large square-shaped air-domain which is 1,000 mm ×1,000 mm in order to eliminate the wall effects on the flow around the conductor.   The computational results on velocity and temperature values

demonstrate that these dimensions of the air domain are large enough to produce a size-independent solution.

The scheme of the computational domain and the section of the computational mesh are presented in Fig. 5.3 and Fig. 5.4.
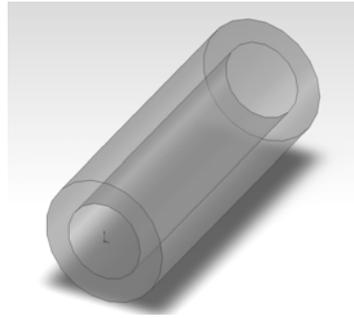
Fig. 5.2 The model with increased steel core in comparison to the real conductor
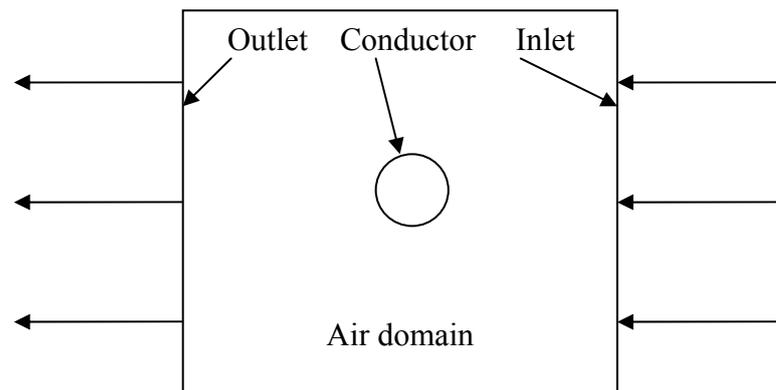
Fig. 5.3 The computational domain scheme

The whole domain incorporates the air domain, the aluminium section and the steel part of the conductor. The equations describing heat and mass transfer in the computational domain are discretised using the finite volume method in which the whole domain is split into an array of much smaller control volumes/elements in the computational mesh.
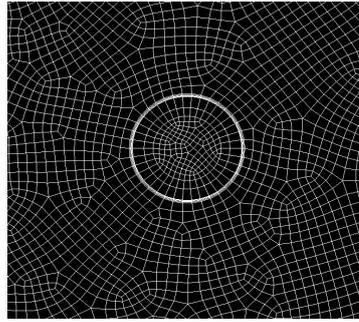
Fig. 5.4 The section of the computational mesh used in the modelling process

In this case a mesh with 90,539 cells was created. Mesh refinement tests were conducted in order to ensure that the solutions are not mesh dependent and the computational mesh with 90,539 cells was selected to conduct numerical investigations. In order to obtain accurate results of the heat transfer, a very fine mesh was created in the vicinity of the surface of the conductor to reflect the specifics of the flow and heat transfer in the boundary layer zone around the conductor. Simplified thermal models of the conductor with illustration of building geometry, specification of boundary type, checking of quality of the meshes are presented in detail in Appendix B. Furthermore, the effect on the temperature of a conductor with different meshes was also studied.

The solution of the system of governing heat and mass transfer equations is subject to the set of boundary conditions. The velocity inlet and the outflow boundary conditions were prescribed on the right and left external boundaries of the computational domain, respectively. Air enters the computational domain with a uniform constant velocity and ambient temperature. The outflow boundary condition applied assumes that air leaves from the outlet of the computational domain with the same mass flow rate as it entered the domain. The upper and bottom boundaries of the computational domain are considered in calculations to be walls and a zero heat flux boundary conditions were specified on these walls. The ambient temperature was assumed to be 293 K. The laminar flow model was used in calculations for the wind velocity equal to 0.1 m/s. For

greater values of the wind velocity the standard k–ε model, which is a semi-empirical model which includes the turbulence kinetic energy (k) and its dissipation rate (ε) for the calculation the turbulent viscosity, with the enhanced wall treatment, was employed to model the turbulence within the air domain. The k–ε models, the RSM and the LES model were designed to use mostly for turbulent flows in the regions far from walls. They can also be suitable for wall-bounded flows by choosing one of the options of wall treatment approach. The enhanced wall treatment was chosen because it can be used for the majority of flows and allows more accurate predictions than standard wall treatment, which is used mostly for flows with high Reynolds numbers.

 The internal heat generation rate ($S_{heat\,source}$) is included as the energy source term in the energy conservation equation and this represents the amount of heat uniformly generated within the aluminium part of the conductor, but not within the conductor core. It is defined as a ratio of the power generated within the object to its volume. The energy source term is calculated as

$$S_{heat.source} = \frac{I^2 \cdot R}{A \cdot L} = \frac{433 \cdot 0.157}{183.4 \cdot 10^{-6} \cdot 10^3} = 160,500 W/m^3 , \qquad (5\text{-}1)$$

where I is the current through the conductor, A is the cross section area of the aluminium part of the conductor and R/L is the DC resistance of the conductor. The per-unit resistance of the Lynx conductor is 0.157 Ω/Km [12].

As in this case the conductor has a higher temperature than its surroundings, the resulting heat losses due to radiation from the surface of the conductor have been included in these simulations.

A 3-D CFD model is used for parallel wind conditions, when wind velocity coincides with the axis of the conductor. The calculation scheme of the conductor in 3-D simulations is identical to that used in 2-D CFD modelling. Due to the computer RAM limitations it was decided that it

would not be feasible to employ a computational domain larger than a parallelepiped with dimensions 3 m × 1 m × 1 m (L × H × W). These dimensions of the air domain are also large enough to produce a size-independent solutions. The same mathematical models have been used for solving the system of governing equations describing heat and mass transfer processes in the computational domain as in 2-D simulations, except that the system of equations was modified to reflect the 3-D geometry.

Fig. 5.5 presents the geometry of the computational domain used for 3-D CFD modelling (which is the parallelepipedal air domain surrounding the conductor). A 3-D computational mesh, consisting of 627,400 hexahedron elements (10,900 hexahedron elements for steel cylinder; 7,500 hexahedron elements for aluminium part of the conductor and 609,000 mixed elements for air domain) is shown in Fig. 5.6. When creating the computational mesh special care was taken in order to reflect the presence of boundary layers around the surface of the conductor. Hence the resolution of the mesh provides mesh independent numerical results.
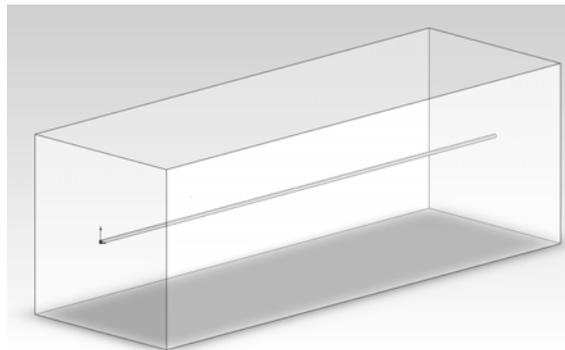
Fig. 5.5 The computational domain scheme
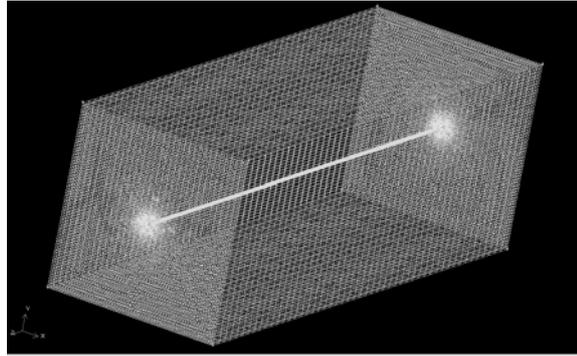
Fig. 5.6 The 3-D computational mesh used in the modelling process

Two vertical planes of the parallelepiped which are perpendicular to the axis of the conductor are the air inlet and outlet, respectively. Other planes limiting the volume of the computational domain are assumed to be walls.

The temperature distribution within the conductor and its surroundings can be determined by solving the system of the governing energy, continuity and momentum equations using the segregated solver with an implicit linearization scheme, a single variable such as pressure is solved in all cells at the same time. Then similar calculations take place for velocities, temperatures and also k–ε for the turbulence model.

Boundary conditions applied are identical to those applied to the 2-D case with the cross wind conditions. At the inlet air enters the computational domain with a uniform constant velocity and the ambient temperature equal to 293 K. The outflow boundary condition is applied at the air outlet and it is assumed that air leaves from the outlet the computational domain at the same mass flow rate as it entered the domain. Zero heat flux boundary conditions were set on the walls surrounding the conductor.

5.2 Thermal state of the conductor exposed to the cross wind

Fig. 5.7 illustrates a comparison between 2-D and 3-D simulations of the thermal state of the conductor exposed to the cross wind. The numerical simulations were performed for a number of cases in which the wind velocity was varied from 0.1 to 15 m/s. Such a range was chosen because it includes the working range of wind turbines which start to operate when the wind velocity is approximately 4 m/s, reaching the maximum efficiency at 15 m/s, see Appendix C.
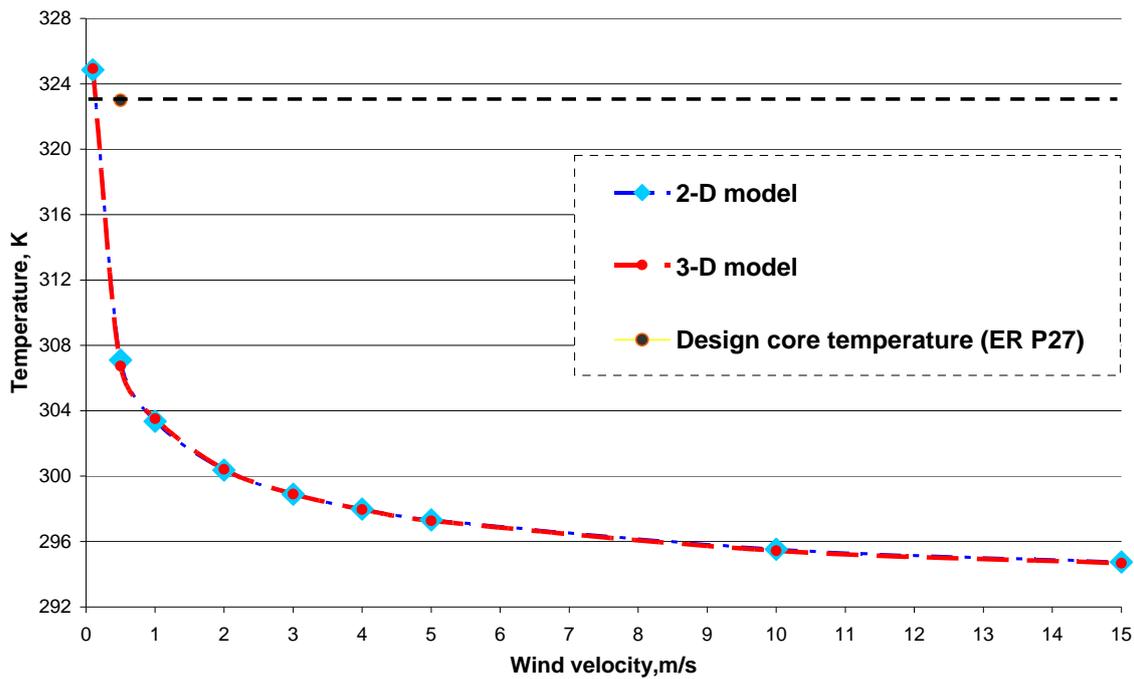
Fig. 5.7 Temperature of the conductor vs. wind velocity

The calculations performed demonstrated that the results obtained using 2-D and 3-D CFD models are almost identical: the difference between data does not exceed 0.27 K. The temperature of the conductor strongly depends on the wind velocity at low wind conditions (particularly in the range of 0-1 m/s) and the rate of the change in the thermal state of the conductor is relatively small when the wind velocity exceeds 10 m/s.

Fig. 5.8 and Fig. 5.9 illustrate some general views of velocity vectors and temperature fields around the conductor for wind velocities of 1 and 15 m/s, respectively.
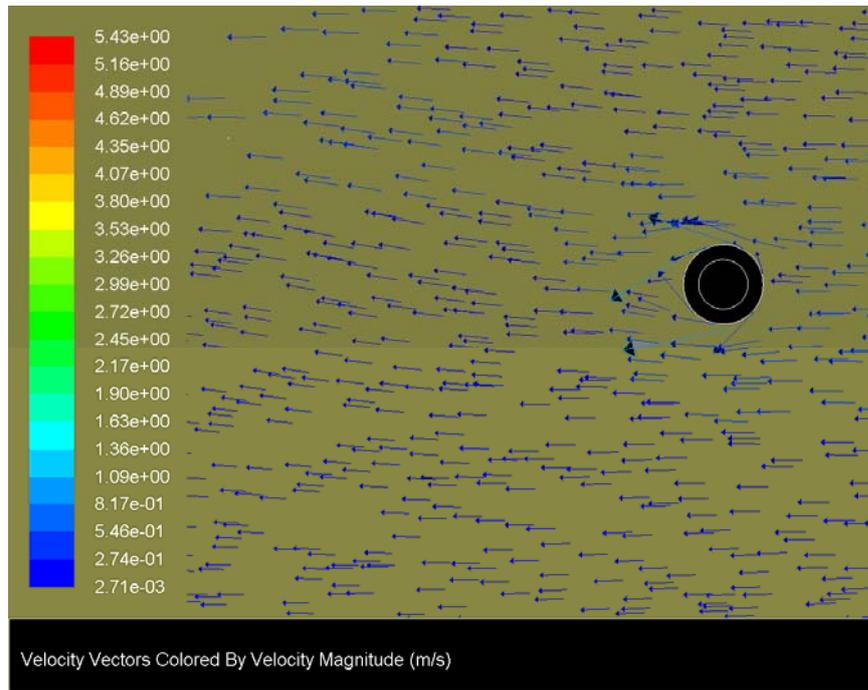
a)
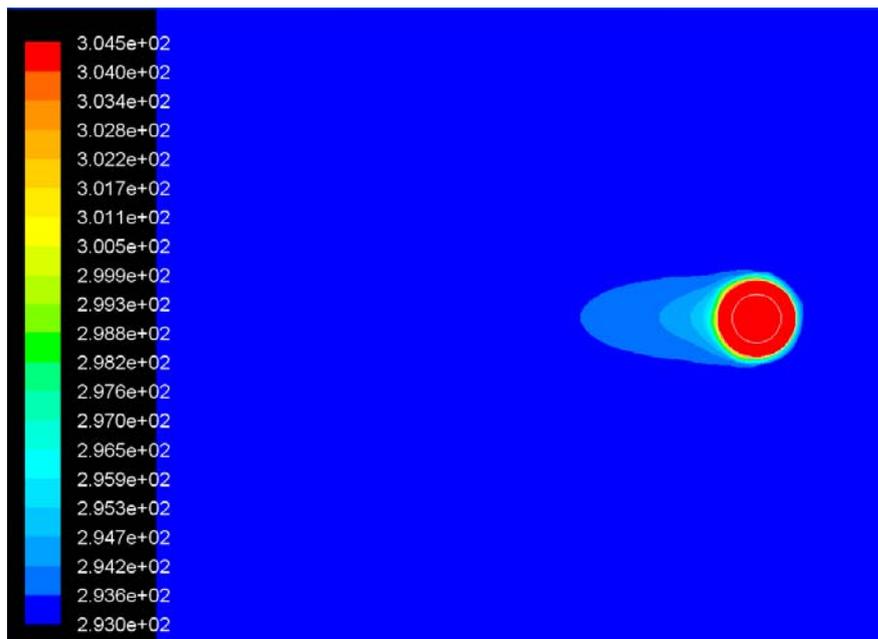
b)

Fig. 5.8 Velocity vectors (a) and temperature fields (b) around the conductor for wind velocities of 1 m/s. (Reynolds number is $1.28 \cdot 10^3$)

126
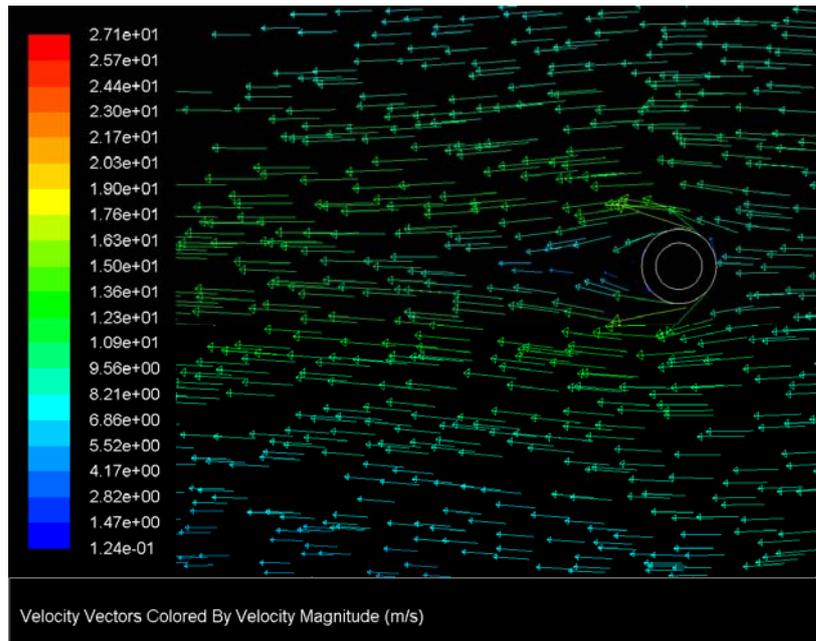
a)
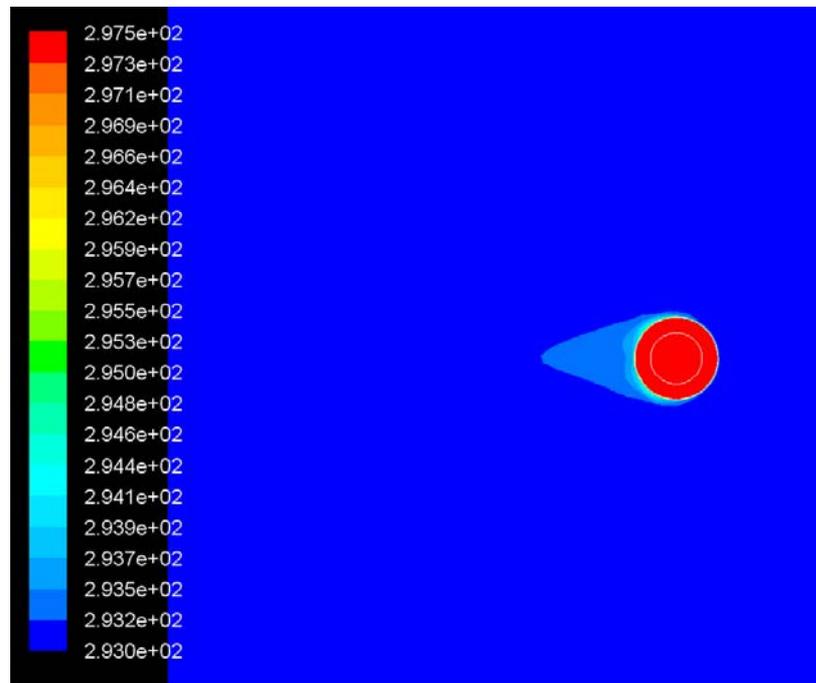
b)

Fig. 5.9 Velocity vectors (a) and temperature fields (b) around the conductor for wind velocities of 15 m/s (Reynolds number is $19.2 \cdot 10^3$)

From the velocity distribution picture it can be seen that separation of the flow takes place at approximately the same locations, but the wake region is much longer in the second case. The boundary layers are thinner as the free stream velocity of the fluid increases; therefore heat dissipation becomes more intensive with an increase of velocity of the fluid.

Engineering Recommendations P27 indicate that the design core temperature is 323 K (for the cross wind velocity of 0.5 m/s and 433 A loading) and according to the CFD modelling the temperature of the conductor for the same conditions is 307 K (34 ^{0}C, which is 16 degrees lower than the limit).

In order to evaluate the power which could be transmitted additionally, a number of simulations were performed to find out at what current the temperature in the conductor will reach 323 K. A wind velocity of 15 m/s was chosen for modelling, since it is in the range of 12-16 m/s when a wind turbine reaches rated capacity and would be of interest for power system engineers considering the integration of wind power into power systems. According to the modelling results, 1600A transmitted current results in the 322 K conductor temperature.

The power is the product of current and voltage. In a three - phase electrical system the power can be calculated as [64]:

$$Power = \sqrt{3} \times Current \times Voltage . \qquad (5\text{-}2)$$

For 132 kV network the electrical power which could be transferred is

$$\text{for } I = 433A : Power = \sqrt{3} \times 433 \times 132000 = 98997095.96 \text{ W or 99 MW;} \qquad (5\text{-}3)$$

$$\text{for } I = 1600A : Power = \sqrt{3} \times 1600 \times 132000 = 365809130.6 \text{ W or 366 MW.} \qquad (5\text{-}4)$$

Therefore, the model suggests, that when the conductor experiences a cross wind velocity of 15 m/s, the theoretical maximum power transfer capability of the conductor is increased by a factor of 3.7.

5.3 Thermal state of the conductor exposed to the parallel wind

Fig. 5.10 presents results obtained for the conductor exposed to parallel wind conditions and it can also be seen that the temperature of the conductor is approximately 19 K higher for low wind

conditions when it is exposed to parallel wind. With the increase of the air velocity this temperature difference gradually reduces and is about 5 K for a 15 m/s wind velocity. It is most likely that the results for different wind angles will be placed within a "cross and parallel wind" results envelope.
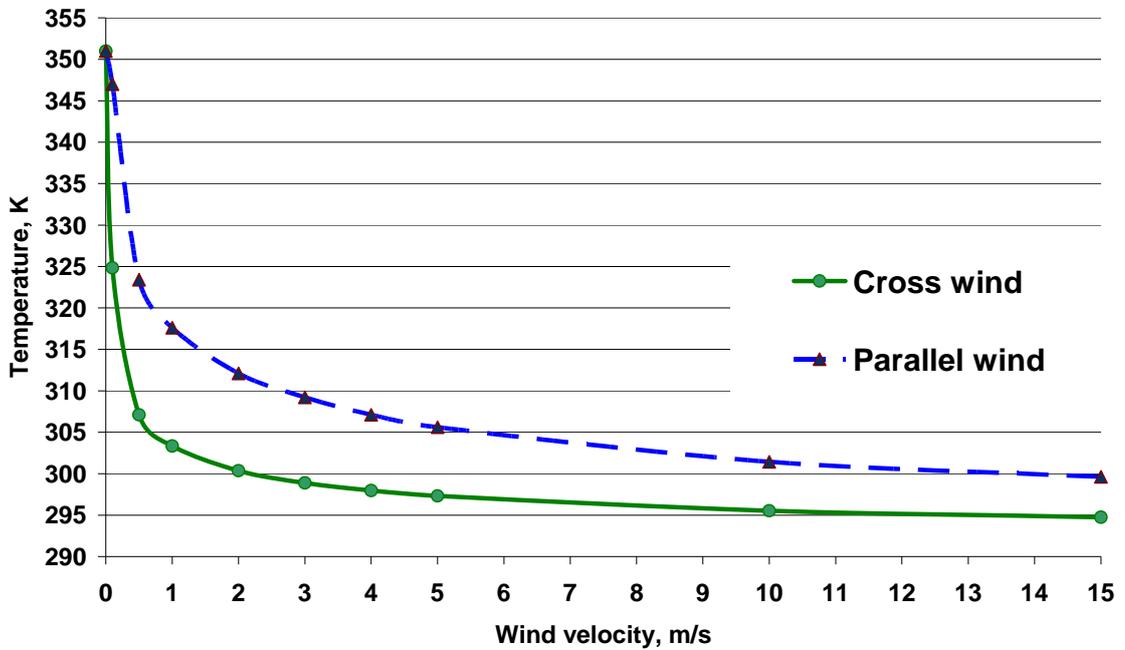
Fig. 5.10 The average temperature on the surface of the Lynx conductor vs. wind velocity for cross and parallel wind conditions

If the obtained CFD results are accurate, there is scope for increasing transmitted power even during fairly modest wind conditions. According to the CFD modelling results, increased transmitted current by factor of 2.3 leads to the 323 K conductor temperature, which is a design core temperature; therefore for 132 kV network the electrical power which could be transferred is

$$Power = \sqrt{3} \times 2.3 \times 433 \times 132000 = 227693321\,\text{W} = 22.769\,\text{MW} \qquad (5\text{-}5)$$

Therefore, the model suggests that when the conductor experiences a parallel wind velocity of 15 m/s, the theoretical maximum power transfer capability of the conductor is increased by a factor of 2.3.

129

Compared to Engineering Recommendations P27, CFD modelling shows that there is appreciable scope for increasing the rating. The preliminary results from this research suggest that with careful management it may be possible to temporarily increase the rating and utilisation of existing overhead lines. This increase could lead to benefits, such as the avoidance of costly network reinforcement and improved network access for distributed generation.

At low Re numbers viscous forces dominate over inertial forces. Re number can be calculated as

$$Re = (\rho v l / \mu), \tag{5-5}$$

where ρ is density (kg/m^3), v is velocity in the flow (m/s), l is linear dimension(m), μ is dynamic viscosity (Pa·s). The Nusselt number is the ratio of convective to conductive heat transfer across the boundary. Nusselt numbers for corresponding surface elements can be calculated as

$$Nu = hl / k, \tag{5-6}$$

where h is heat transfer coefficient (W/m^2·K), k is thermal conductivity (W/K·m).

Finally, Fig. 5.11 presents results of heat transfer coefficients from the surface of the Lynx conductor in the form of $Nu=f\ (Re)$ form.
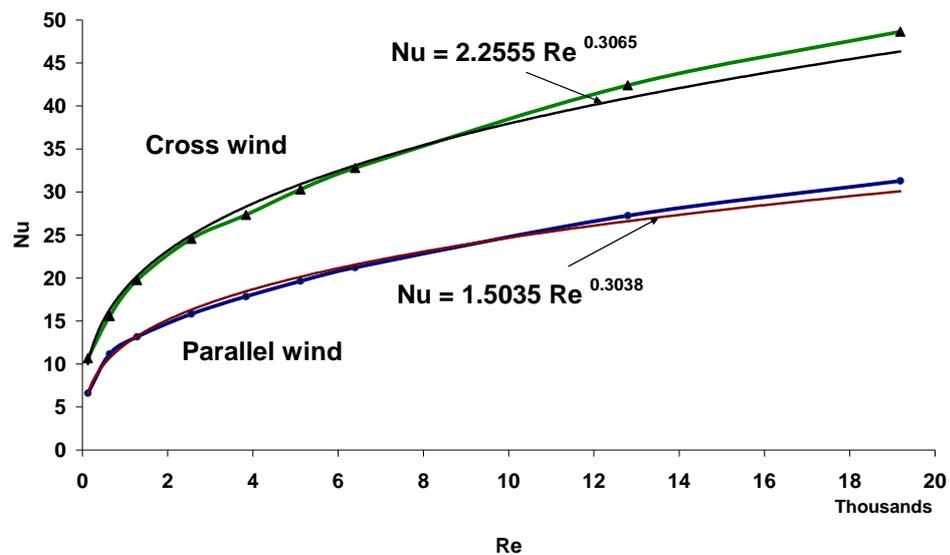
Fig. 5.11 Nusselt number as a function of Reynolds number for the cross- and parallel wind

130

Convective heat transfer from the surface of the conductor can be calculated using the following equations:

$$Nu=2.2555\times Re^{0.3065} \text{ (for cross wind)};$$ (5-7)

$$Nu=1.5035\times Re^{0.3038} \text{ (for parallel wind)}.$$ (5-8)

It can be seen that the heat transfer coefficient is proportional to the wind velocity and is higher for the case when the wind is perpendicular to the axis of the conductor.

5.4 The effect of the temperature dependence on the material properties of the temperature of the Lynx conductor

During numerical modelling of the thermal state of the Lynx conductor, the effect of temperature dependence on the physical properties of the material of the conductor and the influence of solar radiation were investigated.

Fig. 5.12 presents results of CFD investigations of the thermal state of the Lynx conductor for different magnitudes of cross wind. Two situations were investigated, namely when the resistivity of aluminium was assumed to be constant and when it is dependent on the temperature of the conductor. It can be seen that when the variation of resistivity is taken into account temperatures are higher by approximately 0.5-2 degrees for wind velocities less than 3 m/s. Numerical results show that the effect of the dependency of the heat capacity coefficient on the temperature is very small (fraction of a degree) and therefore can be neglected in the analysis.
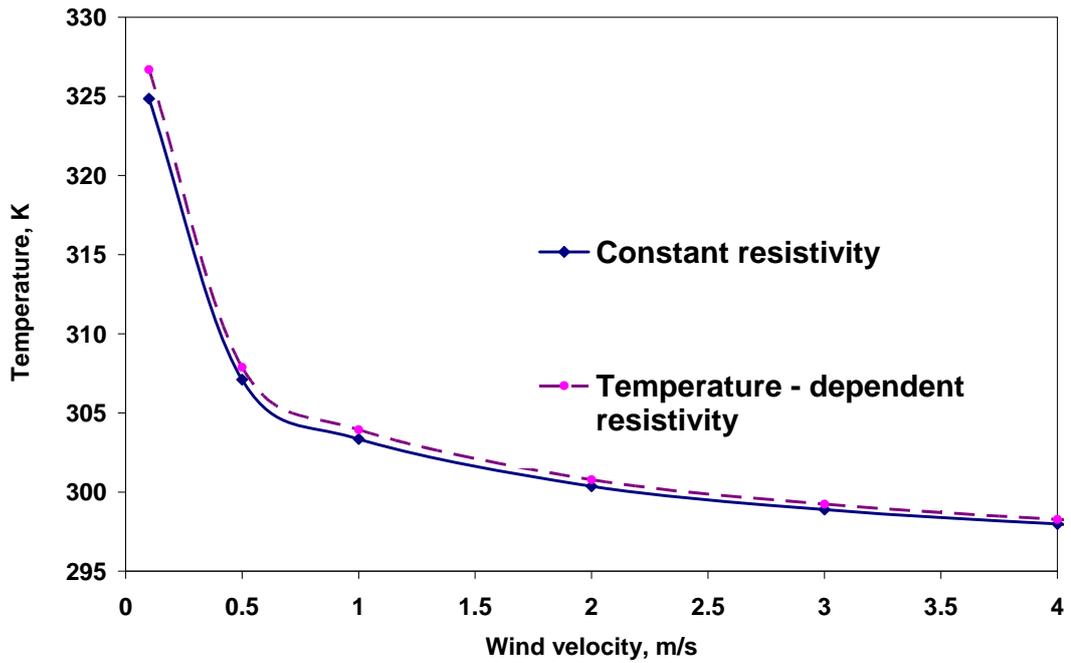
Fig. 5.12 The average temperature on the surface of the Lynx conductor as a function of the wind velocity

5.5 The influence of solar radiation

During the operational life of a conductor there is a considerable period of time when they are exposed to solar radiation, which is an additional source of heat. The temperature of conductors increase depending on the level of solar radiation and the condition of the conductor surface, which can be specified by the value of the absorption coefficient. The additional source of heat which emanates from solar radiation can be calculated as

$$q_s = \alpha \cdot d \cdot s \qquad \qquad (5\text{-}9)$$

where q_s is solar heat gain in the conductor (W/m); d is diameter of conductor (m); α is the solar absorption coefficient, which usually varies from 0.3 to 0.9; s is the intensity of solar radiation (W/m^2) with a typical value being 800 (W/m^2).

A conductor which has been in service for a considerable period of time usually has a darkened surface due to oxidation and pollutants and a typical value of the absorption coefficient for such conductor is about 0.9. The absorption coefficient of a new shiny conductor is about 0.3.

Table 5.1 presents computational results on the thermal state of the Lynx conductor when the ambient temperature is set to be 293 K, wind velocity is assumed to be 2m/s and the current is equal to 433 A taking into account solar radiation.

Table 5.1 The effect of solar radiation on the thermal state of the Lynx conductor; when resistivity of aluminium was assumed to be constant and when it was assumed to be dependent on the temperature of the conductor material

	CFD model: constant resistance, convective losses, re-radiation	CFD model: temperature dependent resistance; convective losses, re-radiation	CFD model: temperature dependent resistance, convective losses, re-radiation and solar radiation		
			$\alpha = 0.3$	$\alpha = 0.5$	$\alpha = 0.9$
Conductor temperature, K	300.37	300.78	302.2	303.45	305.9

It can be seen in Table 5.1 that the temperature of the darkened conductor rises by about 6 degrees for the given set of boundary conditions when insolation is taken into account.

It can also be observed that the influence of re-radiation from the conductor is not significant when the difference between the temperature of the conductor and that of the ambient is about 7 degrees, but re-radiation losses increase sharply with the rise of the conductor temperature.

5.6 The influence of the temperature on thermal properties of aluminium and steel

Thermal conductivity, K_T, (W/m·K) is the property of the material which shows the ability to conduct heat. It is defined as the quantity of heat transmitted during time Δt through a thickness x, in a direction normal to a surface of area A, per unit area of A, due to a temperature difference ΔT. It is a constant in the Fourier law of heat conduction. In solids the conduction of heat occurs due to vibrations of molecules and internal radiation. There are a vast number of mobile electrons in metals which provide the heat transfer. For the most metals the thermal conductivity decreases when temperature increases.

Heat capacity, Cp, (J/kg· K) shows how much energy is needed to increase the temperature of a unit of a material by one degree.

Fig. 5.13 presents the thermal conductivity and the heat capacity of the material as temperature dependent functions plotted using tabular data from [65], see Appendix D.
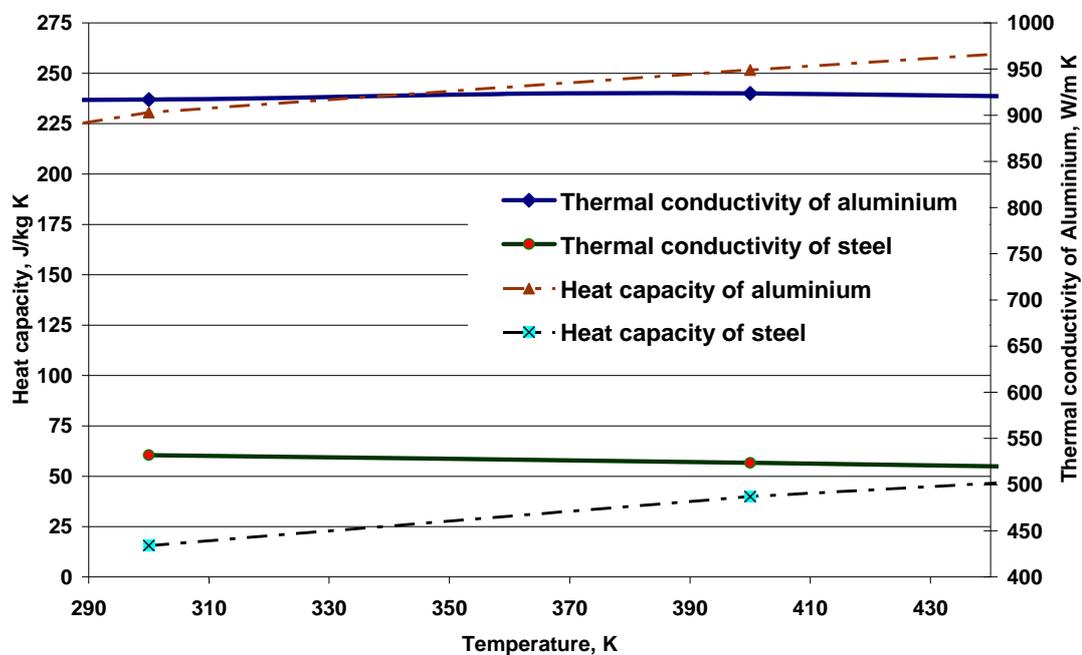
Fig. 5.13 The thermal conductivity and heat capacity of conductor material as a function of temperature

The comparison of results obtained for parallel and cross wind conditions is shown in Table 5.2. The simulations were performed for a case when the wind velocity was equal to 2 m/s and the ambient temperature of 293 K.

Table 5.2. The effect of temperature on the material properties of Lynx conductor; the temperature in the conductor shown in the table is the maximum temperature obtained from the CFD model without consideration of radiative heat losses

Temperature of the conductor, K		
The wind direction	Parallel wind	Cross wind
Cp (J/kg K) and K_T (W/m K) assumed to be constant	303.38	326.45
Cp (J/kg K) and K_T (W/m K) assumed to be temperature dependent	303.56	326.43

It can be seen that the impact on the temperature magnitude in the conductor due to the temperature dependent thermal conductivity and heat capacity is negligible in the considered range of the wind velocity.

5.7 Conclusions

Comparison of numerical results obtained by CFD modelling and lumped parameter models, used in industrial standards, for the case when the cross-wind velocity is 0.5 m/s, the ambient temperature is 293 K and the current is 433 A, show that the latter over estimates the temperature of the conductor by about 18 degrees. This indicates that there is scope for increasing the ampacity of the Lynx overhead conductor. The model suggests that the theoretical maximum power transfer capability of the conductor can be increased by a factor of 3.7 and 2.3, when the conductor experiences a cross and a parallel wind velocity of 15 m/s, respectively.

Numerical results obtained indicate that the effect on the conductor temperature due to the temperature dependent resistivity is small, since the difference in temperature of the conductor is less than 2 K at low wind conditions, when the temperature of the conductor is approximately 325 K.

Comparison of numerical results between cross and parallel wind shows that convective heat transfer from the surface of the conductor can be calculated using the following equations:

$$Nu=2.2555 \times Re^{0.3065} \text{ (for cross wind);}$$

$$Nu=1.5035 \times Re^{0.3038} \text{ (for parallel wind).}$$

The increase of the temperature of the Lynx conductor with a darkened surface due to typical average insolation of 800 W/m^2 is about 6 degrees.

It could be seen that the impact on the conductor temperature due to the temperature dependent thermal conductivity and heat capacity is negligible in the range of conductor operational temperatures and wind velocities.

CHAPTER 6

CFD MODELLING OF THE TRANSIENT THERMAL BEHAVIOUR OF OVERHEAD LINES

Very often distributed generation (DG) systems operate under variable output and climatic conditions which affect the thermal state of overhead conductors. Rapid increases in the current passing through the line or sudden drops in the wind velocity are extreme examples of such dynamic conditions. In these cases it is essential for network operators to have information on the time available to react to protect valuable network assets. This time is determined by the period of time which elapses from the moment the current increases or the wind drops to the point in time at which the conductor reaches its maximum allowable temperature level. These rapid increases in current passing through a conductor could also be caused by network faults, resulting in circuits being disconnected from the network. This results in sudden increased loading in the remaining circuits. Changes in the wind direction are also important due to terrain or vegetation shielding and also the wind direction dependent cooling properties, with respect to the overhead line. In addition, dynamic modelling results are useful for network operators to develop short term rating strategies for exploitation of networks with significant levels of DG.

6.1 Concept of the transient thermal state of the conductor

The following are basic definitions when modelling the transient thermal state of the conductor:

- "Transient thermal rating is that final current that yields the maximum allowable conductor temperature in a specified time after a step change in electrical current from some initial current".

- "Thermal time constant: The time required for the conductor temperature to accomplish 63.2% of a change in initial temperature to the final temperature when the electrical current going through a conductor undergoes a step change" [15].

Fig.6.1. illustrates how the temperature in the overhead conductor changes in response to the current change. The parameters of the surroundings are assumed to be constant.
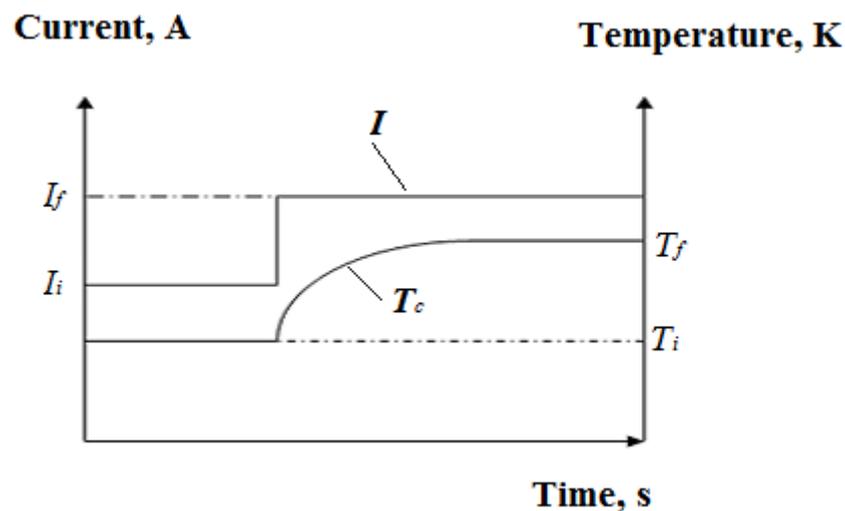
Fig. 6.1 A step change from initial (I_i) current to final current (I_f) [15]

T_i and T_f are initial and final temperature, respectively;

T_c is the temperature of the conductor

After the current step change takes place, the temperature of the conductor starts to rise due to the increased heat generation rate. The transient thermal state of the conductor in the lumped-parameter mathematical model (IEEE 738-1993) can be determined by the solution of the following time-dependent energy balance equation (3.34):

$$q_c + q_r + mC_p \frac{dT}{dt} = q_s + I^2 \times R(T_c),$$

where q_c is convective heat loss (Watts per linear foot of conductor), q_r is radiated heat loss (Watts per linear foot of conductor), q_s is heat gain from the sun (Watts per linear foot of conductor), I is conductor current (A), $R(T_c)$ is 60 Hz (in USA) or 50 Hz (in UK) resistance per linear foot of conductor at $T_c(\Omega/ft)$; T_c is the temperature of the conductor, mC_p is the total heat capacity of conductor (Ws/ft° C). The physical domains and computational meshes used previously in Chapter 5 for the cross and parallel winds conditions were deployed for numerical simulations of the transient behaviour of the conductor.

The following are the results of CFD simulations of the response in thermal state of the conductor to an instantaneous change in the value of the electrical current for the cross and parallel wind conditions and to an instantaneous change in the magnitude of the cross wind for a fixed value of the electrical current, respectively The computational meshes and boundary conditions used are identical to those deployed for the analysis of the steady thermal state of the conductor.

6.2 Response to an instantaneous change in current under cross wind conditions

Fig. 6.2 shows the variation in the current which was simulated in numerical investigations for the case when the cross wind velocity is constant and equal to 0.5 m/s. In this case the Lynx conductor remains at the steady thermal condition until the moment when the current is instantaneously changed (increased in the magnitude) in the form of a step function.
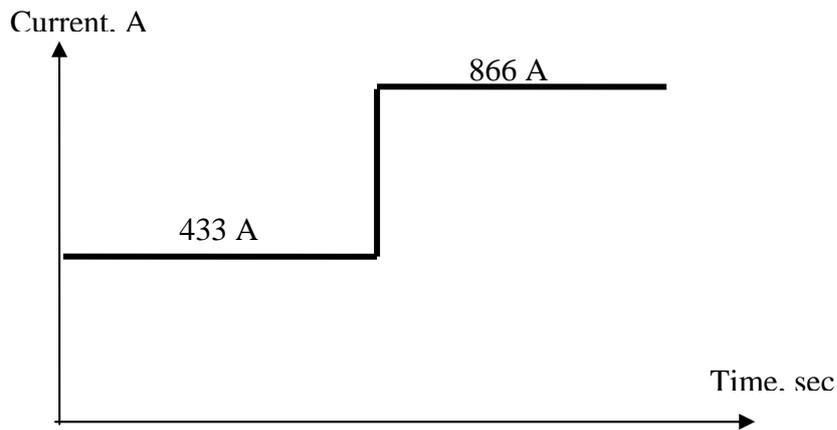
Fig. 6.2 An instantaneous increase in the electrical current passing through the Lynx conductor

Fig. 6.3 presents results of numerical simulations obtained by means of an UDF subroutine, see Appendix E. It can be seen that for the current of 433 A, the steady-state temperature of the conductor is 308 K and this temperature increases to 364 K when the amount of the electrical current is instantaneously doubled. The increase in the temperature is 56 degrees K.
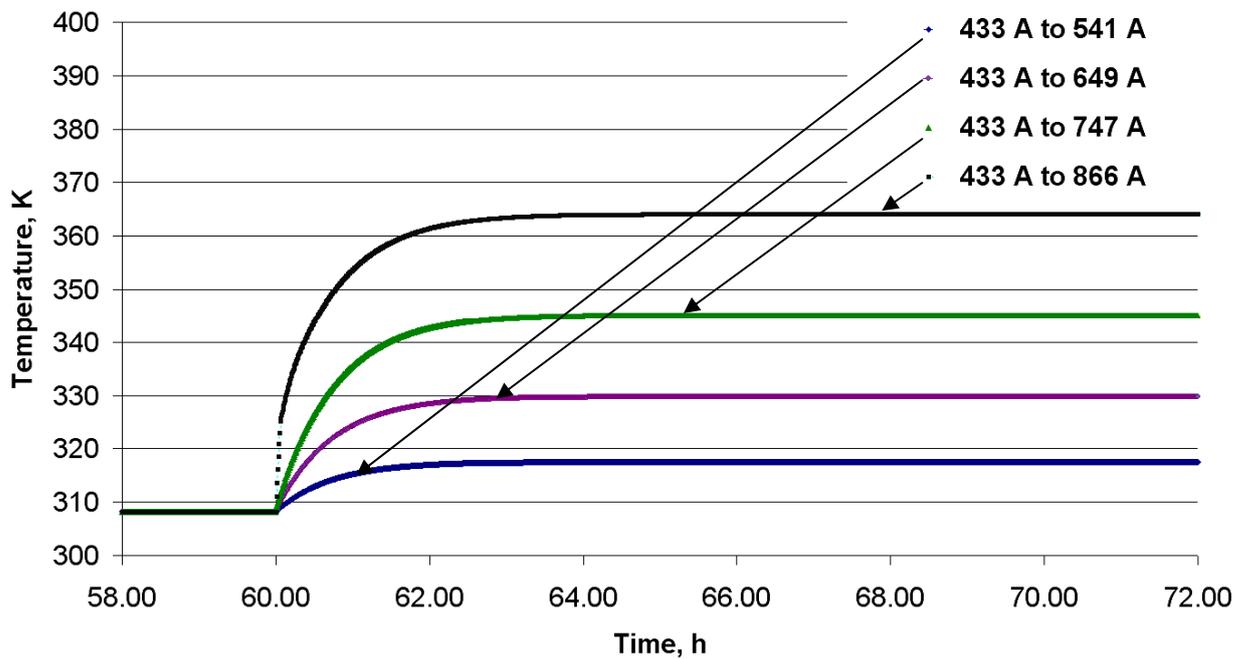
Fig. 6.3. Variation of the temperature of the conductor with increase in the magnitude of the current

Fig. 6.4 presents variation of the time constant for a transient process when the temperature of the conductor changes due to an instantaneous rise in the current.

It can be seen that the time constant parameter increases gradually from 42 to 44 min when the current increases from 433 A to 541 A and from 433 A to 750 A, respectively, and then diminishes to 29 minutes for the current rise from 433 to 866 A. The calculations were repeated using several values of the final electrical current in the range between 757 and 866 A. The tendency in the reduction of the time constant value for the rise of the final electrical current value from 757 to 866 A for the fixed value of the initial electrical current of 433 A was confirmed. Such variation of the time constant parameter is due to the different levels of contribution of the effect of Joule heat generation inside the conductor and heat losses due to re-radiation and convection to the final thermal state of the conductor. At the 866 A current level the heat generation due to Joule losses dominates over the convection and re-radiation heat losses and determines the rapid temperature rise in the conductor.
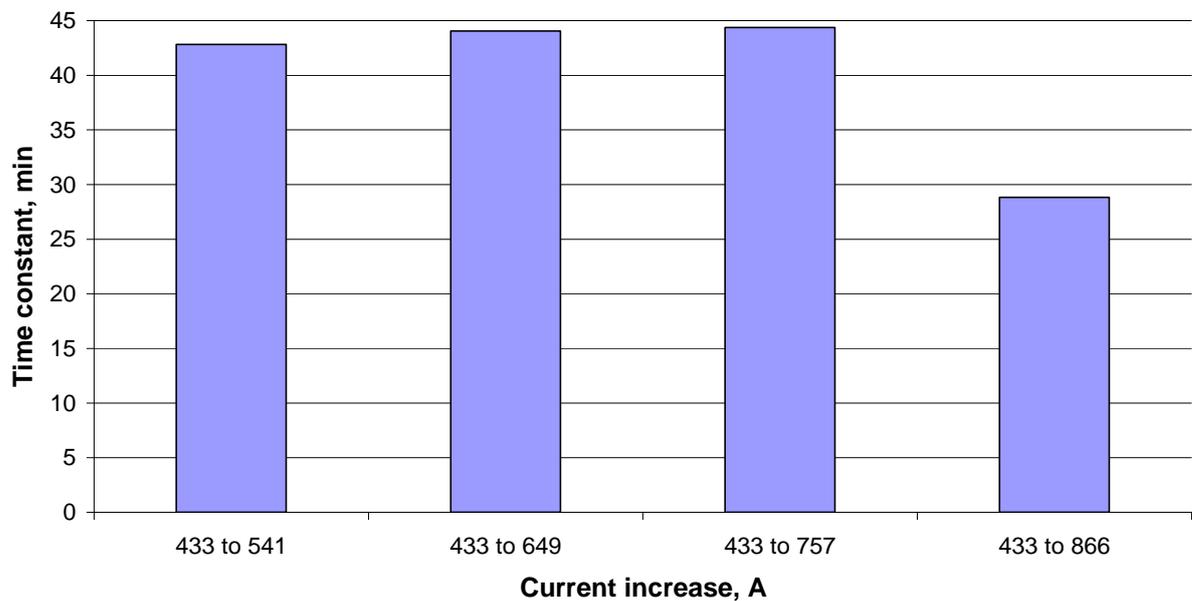
Fig. 6.4 Variation of the time-constant parameter for a transient process when the current instantaneously increases

In a similar way, the situation when the current instantaneously falls is shown in Fig.6.5.
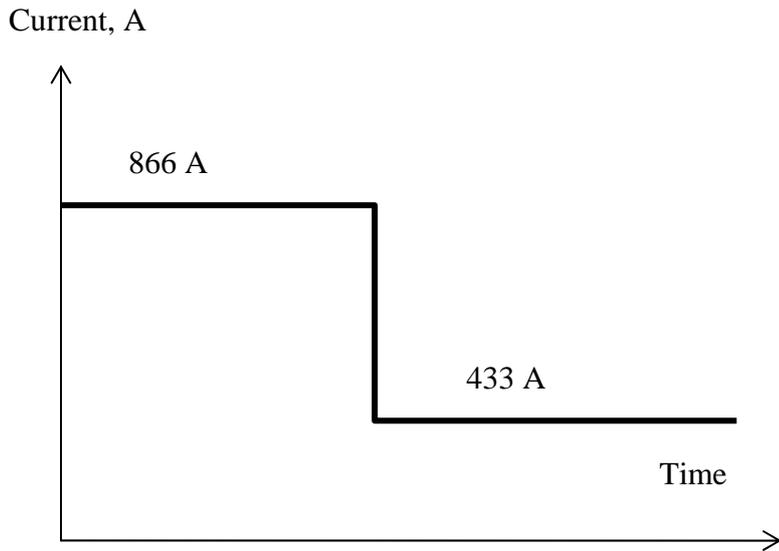
Fig. 6.5 An instantaneous decrease in the electrical current passing through the Lynx conductor
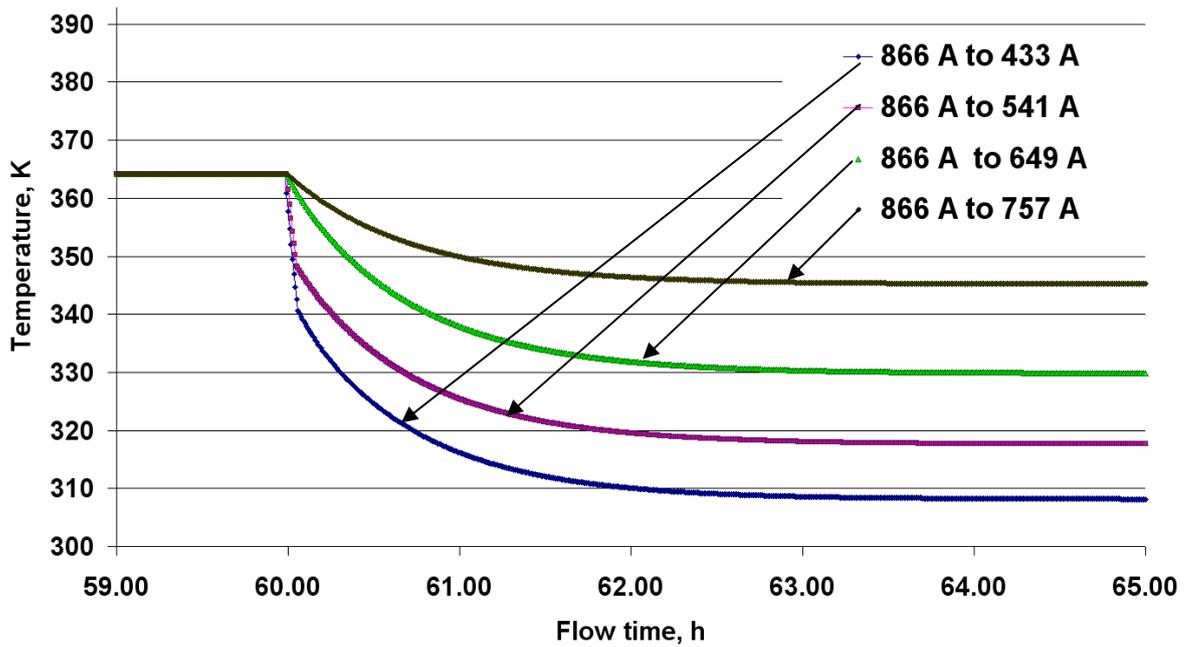
Fig. 6.6 Variation of the temperature of the conductor with the decrease in the magnitude of the current

The CFD results demonstrate, see Fig. 6.6, that the time constant in the cooling process is 7.5 min less than that in the heating-up case. Thus, this parameter is equal to 21.5 minutes when the current decreases from 866 to 433 A, see Fig. 6.7.
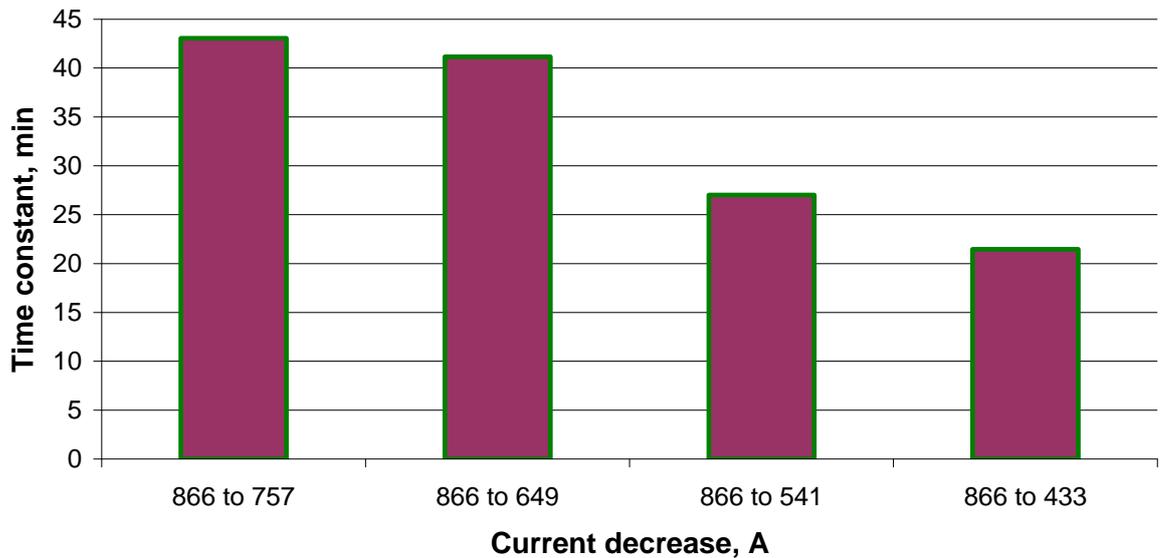
Fig. 6.7 Variation of the time-constant parameter for a transient process when the current instantaneously decreases

6.3 Response to an instantaneous change in current under parallel wind/cross wind conditions

Fig. 6.8 presents results of numerical simulations when the current undertakes the step change from 433 A to 866 A for parallel wind conditions. It can be seen that for current of 433 A the steady-state temperature of the conductor is approximately 327 K, and this temperature increases to 440 K when the amount of the electrical current is instantaneously doubled. The temperature rise in the conductor under cross wind conditions is also presented for comparative purposes. The comparison shows that the temperature difference for two cases before the step change was 19 K and at final steady state it has increased to 76 K.

It can also be seen that the result agrees with that which was calculated using a constant heat source for the calculation of the steady state of the conductor.
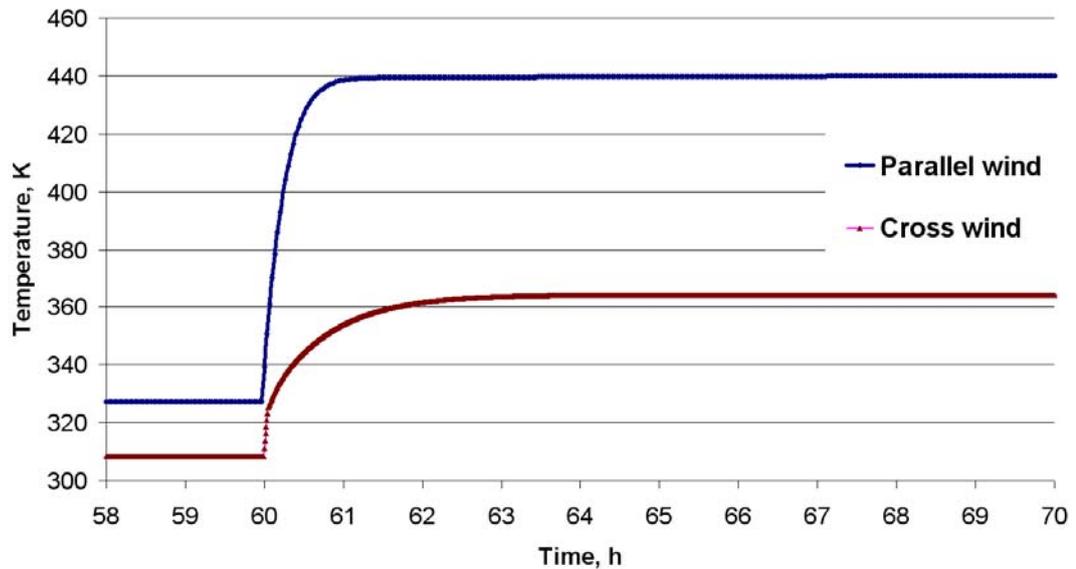
Fig. 6.8 Comparison of temperature in Lynx conductor under cross and parallel wind condition, when the current undertakes a step change from 433 A to 866 A

The calculated value of the time constant in the parallel wind case was 16 min, which was 13 minutes less than in the cross wind case, so the heat from the conductor dissipates slower in the parallel wind case.

6.4 Response to an instantaneous change in the cross-wind velocity

In this section 2-D unsteady CFD simulations of the thermal state of the Lynx conductor have been carried out for several cases when the amount of the electrical current passing through the conductor remains constant and equal to 433 A at the constant ambient temperature of 293 K (the initial conditions set up in Engineering Recommendations P27). For the above cases the effect of the rapid decrease in the magnitude of the cross wind, as shown in Fig. 6.9, on the thermal state of the conductor have been investigated.

144
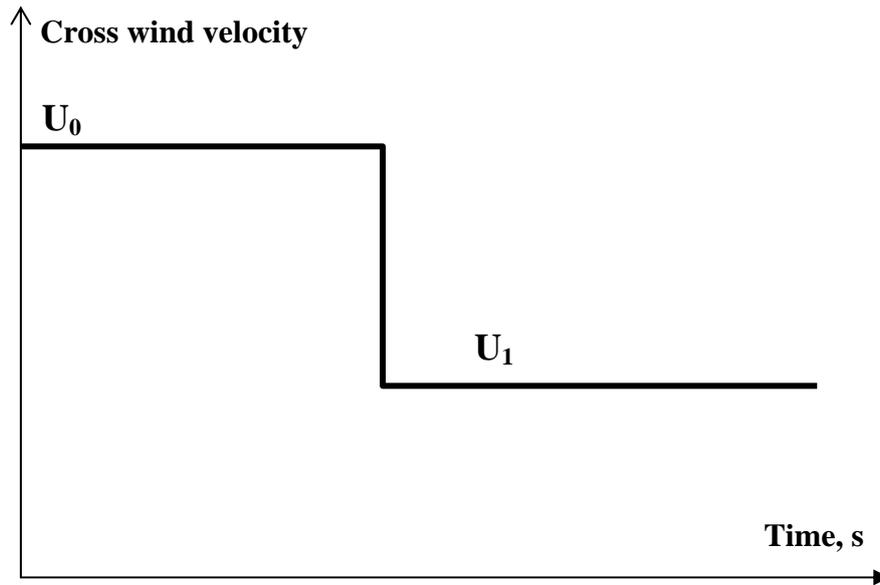
Fig. 6.9 A step-function form of the decrease in the cross wind velocity magnitude

Four cases were investigated, namely when the cross wind velocity decreased from 15 m/s to 10, 5, 2.5 and 0.5 m/s, respectively. A thirty seconds time step was used during transient CFD simulations. The number of time-steps was chosen in such a way that initially the steady thermal state of the conductor is obtained for conditions when the velocity of the cross wind was 15 m/s. Modelling then is continued after the instance of time corresponding to the decrease in the magnitude of the wind velocity and the time increment was stopped when a new steady thermal state was achieved.

Fig. 6.10 presents the results obtained on the temperature of the conductor for the above four situations. The numerical results demonstrate that in the steady state the temperature of the conductor was approximately 295 K when the current passing through the conductor was 433 A, the ambient temperature was 293 K, and the cross wind velocity was 15 m/s.
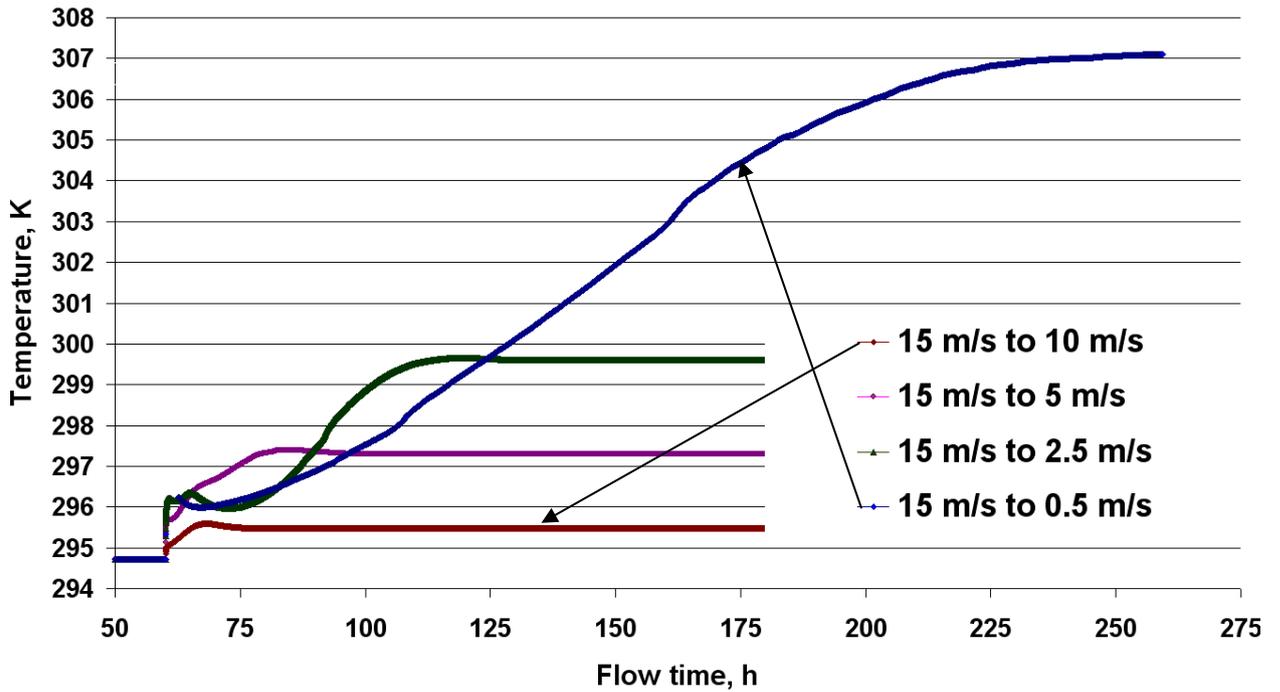
Fig. 6.10 Variation of the temperature of the conductor with decrease in the magnitude of the cross wind velocity

It can be seen that with a decrease in the wind velocity to 10, 5, 2.5 and 0.5 m/s the temperature of the conductor gradually rises up to 295.5, 297.3, 299.6 and 307 K, respectively. The results of the steady thermal states of the conductor during transient simulations are identical to those obtained in steady-case simulations for the above wind velocities. Furthermore, it can be seen in Fig. 6.11 that a transition from the steady thermal state of the Lynx conductor corresponding to the wind velocity of 15 m/s to a new thermal state corresponding to the wind velocity of 10, 5, 2.5 and 0.5 m/s takes approximately 2.3, 5.4, 32 and 85 hours, respectively.
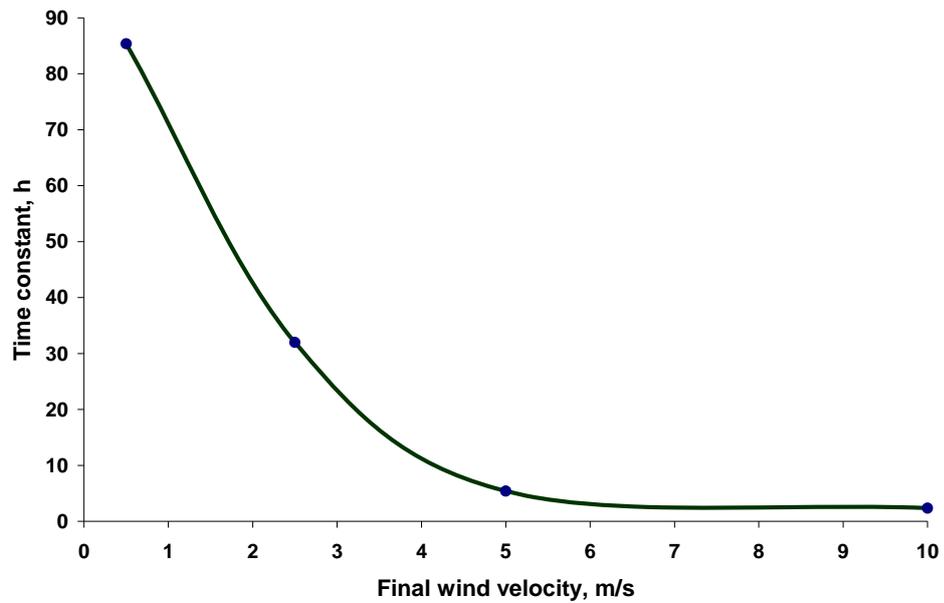
Fig. 6.11 Variation of the time constant when the wind rapidly decreases from 15 m/s

The results obtained from transient CFD simulations of the thermal state of the Lynx conductor demonstrate that for the effect of a rapid decrease in the magnitude of the cross wind velocity on the temperature of the conductor to take place it requires a considerably longer period of time, compared to the situation when there is an instant change in the current. Therefore the network operator has much longer in these cases to take the necessary action to protect the network and also that in many cases the wind speed is likely to have recovered before the overhead line reaches a dangerous temperature.

6.5 Conclusions

This chapter has considered the transient thermal state of the Lynx conductor in order to investigate its thermal limits. CFD modelling results were obtained for transient responses when the current instantaneously increased from 433 A, which is a typical current rating for Lynx conductors, to 866 A. The results show that the temperature of the conductor increased by 56 degrees (from 308 K to 364 K) and the time constant was 29 minutes. Additionally, three intermediate cases, when the final current was 25%, 50% and 75% greater than the initial

current, were simulated. The time constant was found to be least when the current was increased by 100%.

Four cases were modelled when the current instantaneously decreased by 25%, 50%, 75% and 100% from the 866 A level. Again the fastest response, or the least time constant, was in the case in which the current decreased by 100%. The time constant for such case was 21.5 minutes. The temperature of the conductor reduced by 56 degrees from 308 K to 364 K, when the current decreased from 866 A to 433 A.

Numerical results demonstrate that with a decrease in the wind velocity from 15 to 10, 5, 2.5 and 0.5 m/s the temperature of the conductor gradually rises up by 0.8, 2.6, 4.9 and 10.7K. Furthermore, it was calculated that the time constant in the transition from the steady thermal state of the Lynx conductor corresponding to the wind velocity of 15 m/s, to a new thermal state corresponding to the wind velocity of 10, 5, 2.5, and 0.5 m/s is approximately 2.3, 5.4, 32 and 85 hours, respectively. It was found that the time constants are considerably longer for the cases when the wind velocity rapidly increases or decreases than in cases when the current instantaneously changes. These are significant periods of time which could be exploited by network operating companies to assist them during unplanned network outages or unexpected demand surges.

A 3-D model was used to simulate the transient response for parallel wind conditions when the current changed from 433 A to 866 A. Through comparisons between both cases (the transient response for the cross wind conditions and the parallel wind conditions), it was found that in the case of the parallel wind, the temperature in the conductor was 76 K higher and the time constant was 12 minutes less than in the case for the cross wind. Such difference in temperature shows that the wind direction is a significant factor in determining the rating of an overhead line.

CHAPTER 7

VALIDATION – COMPARISON WITH

INDUSTRIAL STANDARDS AND

EXPERIMENTAL DATA FROM SCOTTISH

POWER

This chapter begins with a brief overview of published experimental investigations regarding ratings of some of the most commonly used OHL conductors when taking into account the wind cooling effect. Three published papers also support a statement that the ratings which are used in Industrial Standards, are static and conservative and they can be safely increased if the cooling effect of wind could be adequately taken into consideration. Also two projects were mentioned which aim to develop a calculation method of the enhanced rating and the possibility of the monitoring of the conductor temperature and weather data at a number of sites along an OHL, hence enabling the obtained results to be validate.

The dynamic nature of the temperature of the conductor can be modelled using CFD techniques which take into consideration a number of changes in the weather conditions. Chapter 7 is divided into two parts; Section 7.1 deals with comparison between the models - the CFD model and a lumped parameter model, according to the CIGRE method - and experimental FMCT data

when the Lynx conductor was in a steady state; Section 7.2 presents a comparison between the CFD model and FMCT data when the Lynx conductor was in transient state.

Most wind farms in the UK are connected to 33 kV systems and there is a tendency to connect larger wind farms to 132 kV systems [1]. The Lynx type conductor is commonly used for 132 kV lines, as well as Upas and Zebra conductors. The ratings of the most common ACSR OHL conductors are plotted in Fig. 7.1 for 75 °C and for wind velocities from 0.5 to 10 m/s for sheltered and unsheltered conditions.
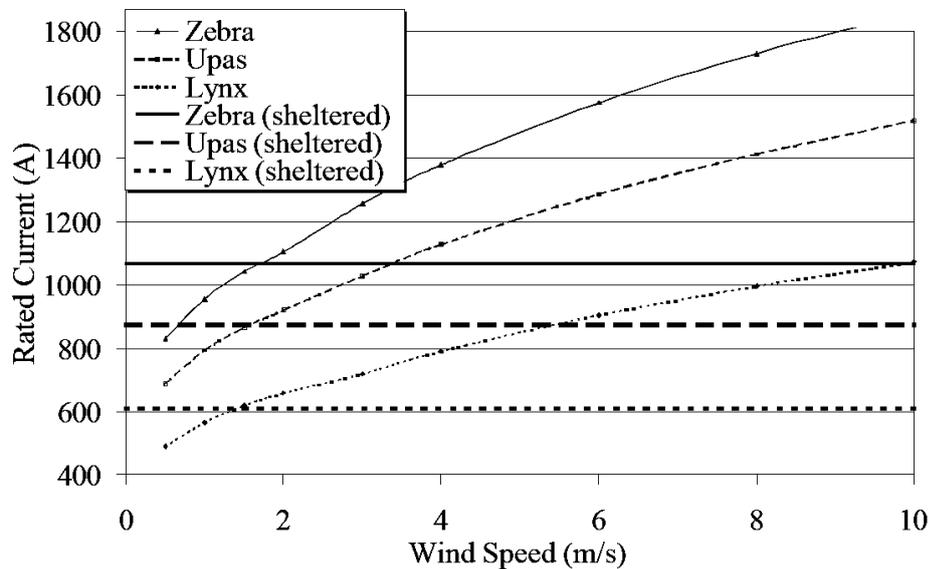
Fig. 7.1 The ratings of common 132 kV conductors at 75 °C [1]

The horizontal lines show the standard rating of conductors without solar gain.

A number of studies have been carried out on dynamic ratings [3, 5 and 6]. These articles discuss the static ratings according to ENA Industrial Recommendations P27 for a Lynx conductor and suggest methods of increasing the ratings, taking into consideration the wind cooling effect on a conductor.

150

Significant research carried out in 2002 [3] shows that there is a strong connection between wind power output and power line rating. The wind velocities incident on an OHL were calculated using data collected at the wind farm, applying the industry standard software WASP (the Danish National Laboratory) and a code WAKE. The results were published in [4].

Two cases in [3] were set up and analysed – for a medium-sized 50-100 MW offshore wind farm, see Fig. 7.2, and several wind farms in Scotland with potential export of nearly 140 MW, see Fig. 7.3. The assigned rating for a Lynx conductor was 523 A at 75 °C; and the wind velocities were measured at four points along the line such as: a built up area near the coast; in a wood; on exposed marshland and at a river crossing some way inland. Whereas the lowest wind velocities were recorded in the woodland, the highest wind velocities occurred in close proximity to a river crossing with a maximum velocity difference being 1.1 m/s.
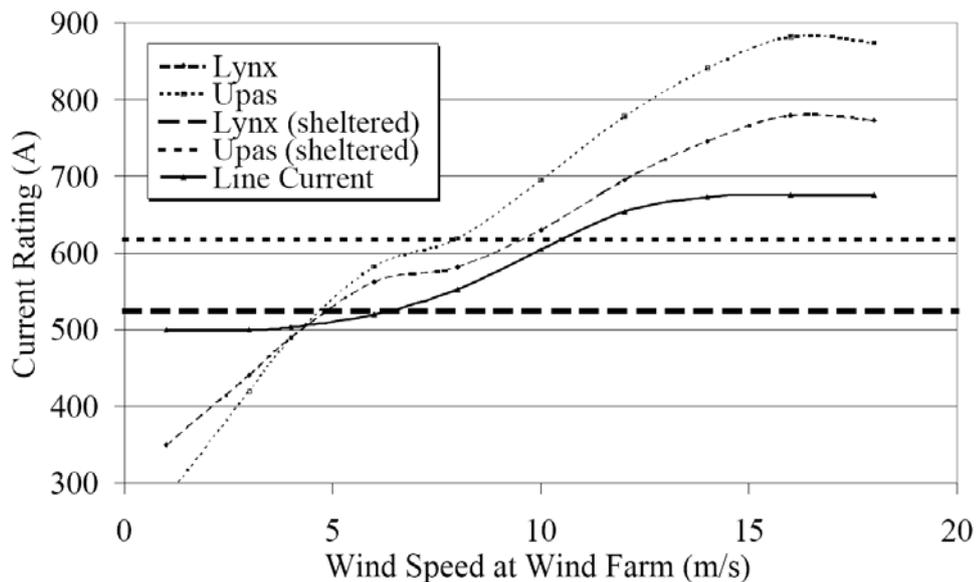
Fig. 7.2 Offshore results [3]

The results of the case study which was carried out in Scotland are presented in Fig. 7.3. The circuit included ten hydroelectric schemes and one wind farm (with total output of 111 MW), with a plan to install another three farms adding 45 MW.
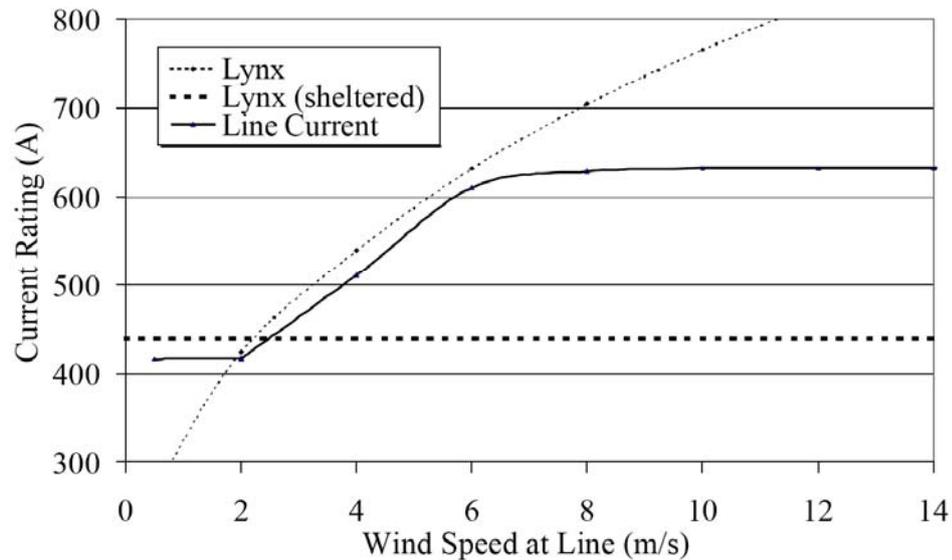
Fig. 7.3 Scottish Power results [3]

The 132 kV circuit includes an OHL Lynx conductor which was rated at 50 °C and which in the case of an outage could export the whole load. The graph shows that at wind velocity of 6 m/s the wind farm reached its maximum output.

A graph plotting the ampacity of the conductor against the wind velocity in Fig. 7.4 for 3 sets of the ambient temperature is presented in [5] relating the dynamic rating and ENA Industrial Recommendations P27 for a Lynx conductor. The grey area shows the practical limitations in the rating due to other circuit components, such as joints and switchgear.

Belben et al. [1] state that even a gentle breeze of force 3 (from 3.4 m/s to 5.4 m/s) can add 20% to the rating of a power line; a gale of force 7-8 (from 14 m/s to 20 m/s) will double the rating, therefore there is scope for increasing transmitted power even during fairly modest wind conditions. In order to investigate such a possibility, the consortium of Scottish Power Energy Networks (SPEN), AREVA T&D, Imass and PB Power and Durham University formed a collaboration research team designed to tackle the UK government-funded project to investigate the thermal properties of power system components in order to implement the enhanced thermal

rating using the developed algorithms. In order to validate the results a section of the SPEN distribution network has been selected, see Fig. 7.5, for field trials where electrical and thermal monitoring equipment has been installed.
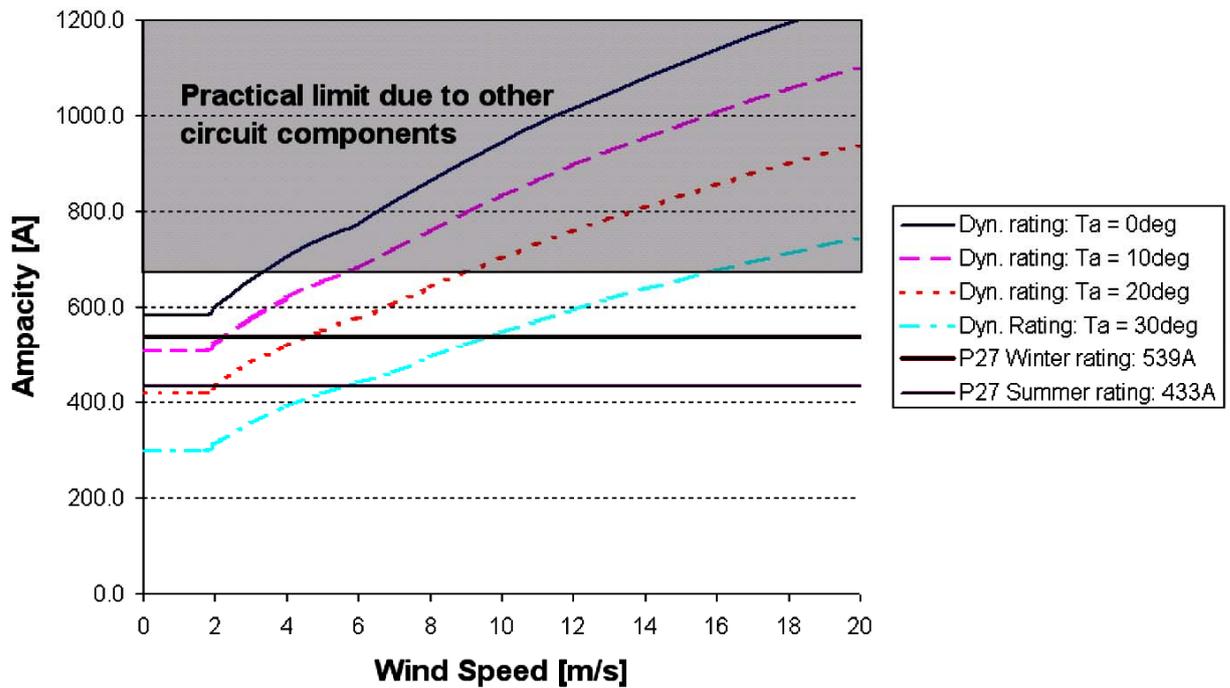
Fig. 7.4. Dynamic ampacity as a function of wind speed for different ambient temperatures T_a [5]

A similar project was carried out in Northern Ireland by a consortium of wind developers (RES and Airtricity), equipment developers (FMCT Ltd) and academics (Queen's University Belfast) [6]. This study was supported by Northern Ireland Electricity plc (NIE) which is the electricity transmission company.

Unlike other companies which use measurements of the ambient temperature, sag, conductor tension or sag at some points along the line, NIE implemented a hybrid method which included the monitoring of the conductor temperature and weather data at a number of sites along an OHL.

The instantaneous wind velocity was measured and correlated with either the wind statistics or the wind farm output. NIE intended to collect data over 12 months in order to evaluate probabilistic overall rating of the existing circuit.

Fig. 7.5 A part of SPEN network (7 km) OHL 132 kV from Rhyl to St.Asaph on north east coast of Wales

7.1 Steady-state thermal behaviour of overhead lines

7.1.1 Comparison between CFD model and lumped parameter model according to the CIGRE method

The CIGRE method was discussed in detail in Chapter 3. In addition a number of case scenarios were presented when the wind velocities were increased from 1 m/s to 15 m/s, and also a free convection case, when the wind velocity was assumed to be zero.

The numerical simulations were performed for similar cases in which the wind velocity was varied from 0.01 to 15 m/s, see Chapter 5, for the situation when the electrical current passing through the conductor remains constant and equal to 433 A at a constant ambient temperature of 293 K.

Fig. 7.6 presents a comparison between the results obtained using CIGRE and CFD methods on the temperature of the conductor as a function of the wind velocity.
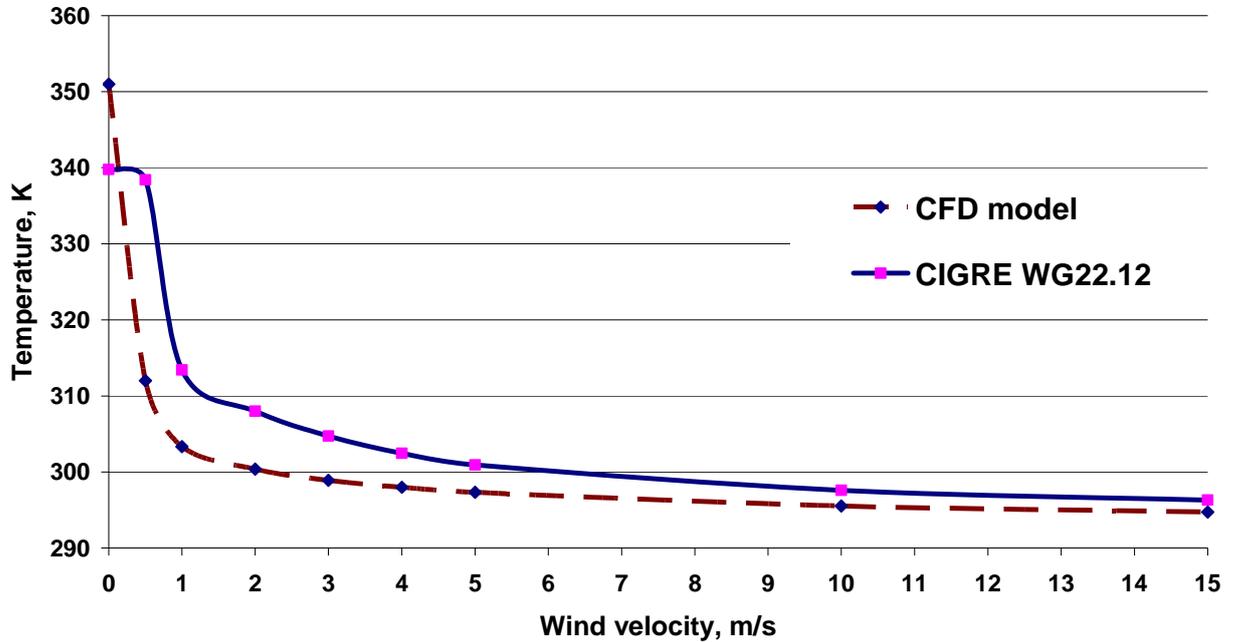
Fig. 7.6 Temperature of conductor for wind velocities in the range of 0 to 15 m/s calculated using lump parameters method and CFD modelling

The graph in Fig. 7.6 demonstrates that the results obtained using the above two methods are almost identical over the wind velocity range 5 to 15 m/s. For the free convection case the CFD model produces a higher prediction of the temperature of the conductor by 10 K, but for the wind velocities above 0.5 m/s the temperature calculated by the CFD model was lower than the temperature calculated by the CIGRE method. Such a difference can be explained by the fact that the calculation of convective losses at low wind velocity in the CIGRE method uses three approaches and the highest value is submitted in the heat balance equation. However, in general the results are very close and the difference between the predictions decreases approximately from 4 K to 1 K for the wind velocities from 4 m/s to 15 m/s, respectively.

7.1.2 Comparison between CFD model results and experimental FMCT data

The major monitoring techniques of the OHLs focussed on sag, tension, the conductor temperature and weather data monitoring. They can be divided into two types of measurements, such as direct (when the conductor temperature, sag and tension are measured with monitoring equipment from the line) and indirect (when the temperature of the conductor is calculated using data from a nearby weather station and the transferred current is known).

Table 7.1 presents a segment of data regarding records of the temperature of the Lynx conductor as a function of the transferred current and variable conditions, such as the ambient temperature, wind velocity, its direction and insolation which were sampled every five minutes and experimentally recorded by Scottish Power in the North Wales region between St. Asaph and Holywell.

Table 7. 1 A sample of experimental data on the thermal state of the Lynx conductor operating in conditions with the variable current, ambient temperature, wind velocity and wind direction

Analysis of data shows that the variation of the conductor temperature follows a random pattern reflecting the stochastic change in the velocity of the wind, load and insolation. Since experimental data for steady conditions was not available, an attempt was made to produce the appropriate data for pseudo-steady conditions.   This was achieved with the use of data from

Table 7.1 by averaging parameters for periods of time when their variation could be assumed to be over an acceptably small range.

Using the recorded data three separate cases were produced with conditions corresponding to pseudo-steady regimes of operation. These cases are presented in Table 7. 2:

Table 7. 2 The cases with pseudo-steady regimes of operation

Case	Ambient Temperature (° C)	Wind Velocity Avg (m/s)	Current, A	Source, W/m
1	-1	0	138.11	14946.77
2	3.8	0	62.35	3110.656
3	6.6	5.3	139.09	15740.29

The thermal state of the Lynx conductor was then numerically simulated for the above three cases using   a 2-D CFD modelling technique. Since the wind velocity is equal to zero in Cases 1 and 2 a free convection model was employed during the simulation process. Fig.7.7 shows the typical temperature distribution in the Lynx conductor and air-domain for Case 1. The maximum temperature in the conductor is 279 K, which is 44 K less then the maximum design temperature (323 K). In the "no wind" conditions air is heated up from the surface of the conductor and flows upwards with a relatively low velocity of only few millimetres per second.
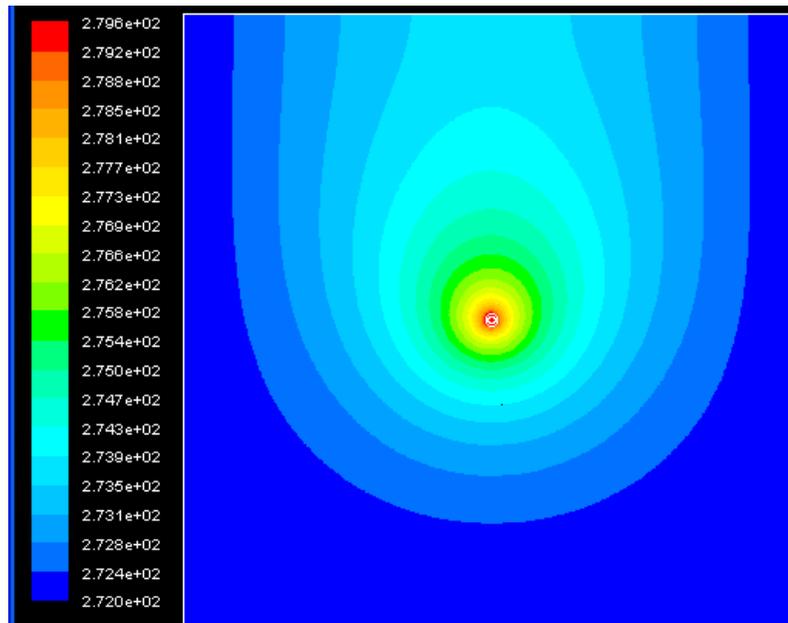
Fig. 7.7 The temperature (K) distribution around the conductor (the free convection case)

The standard $k\text{-}\varepsilon$ turbulence model was employed in simulations for Case 3 because the wind velocity is 5.3 m/s which corresponds to Re=6780 (a turbulent flow). Fig. 7.8 shows the temperature distribution in the Lynx conductor and air-domain for the Case 3 with a maximum temperature of 280 K being in the core of the conductor. Table 7.3 shows comparison of experimental and CFD data for the above three cases.
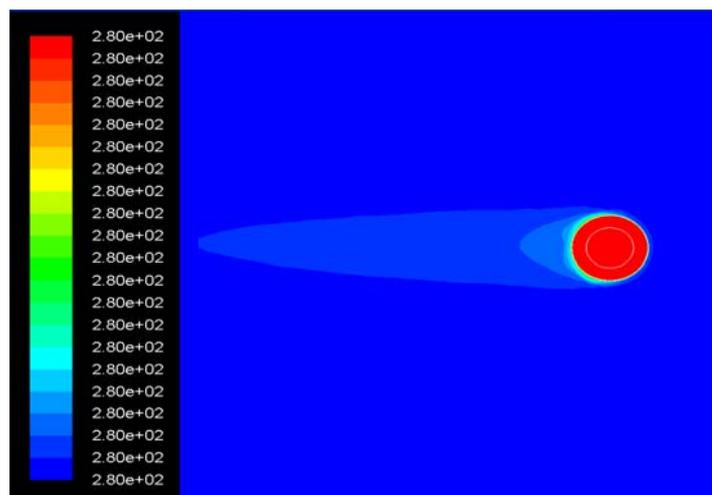
Fig. 7.8 The temperature (K) distribution around the conductor (the turbulent model)

Table 7. 3 Comparison of FMC experimental data for pseudo-steady conditions and CFD results

Case	T ambient	Current, A	Experimental data	CFD results, K	Difference, K
1	-1 deg C (272 K)	138.11	2.1 deg C (275.1 K)	278.6	3.5
2	3.8 deg C (276.8 K)	62.35	5.2 deg C (278.2 K)	276.9	1.3
3	6.6 deg C (279.6 K)	139.09	7.7 deg C (280.7 K)	279.9	0.8

It can be seen that CFD modelling of the thermal state of the conductor generally provides accurate results, with a maximum difference of 3.5 K for Case 1. The difference between experimental and numerical data for Case 3 (the turbulent flow) is only 0.8 K.

7.1.3. Comparison between CFD and lumped parameter model results and experimental data

CFD modelling of the steady thermal state of the Lynx conductor was performed for conditions close to those experimentally recorded by Scottish Power in the North Wales region between St. Asaph and Holywell.

The distinguishing characteristics of the cases presented previously are that the transferred current was considerably lower than its rated value. The Fig. 7.9 illustrates another selection of experimental data recorded by Scottish Power when a line conductor had to supply an additional load due to a neighbour line conductor fault.
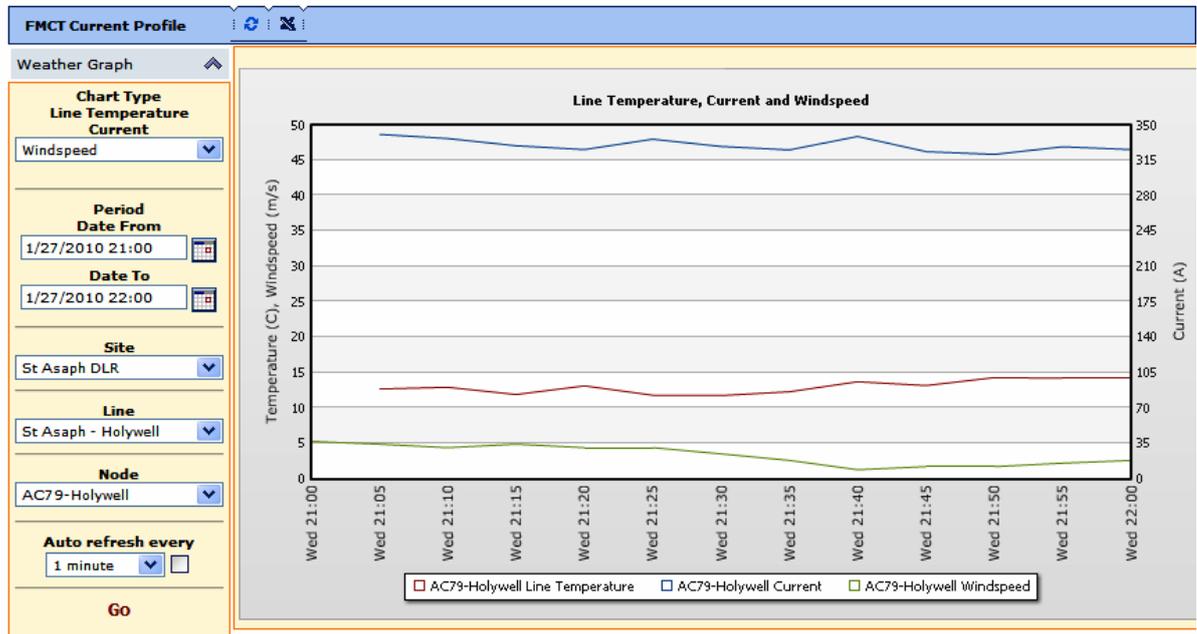
Fig. 7.9 The experimental data recorded by Scottish Power and used for CFD models validation

Eleven sets of data recorded at 5 minute intervals were chosen to perform CFD simulations and calculations using the CIGRE method. The initial data and the results on the temperature of the conductor are summarised in Table 7.4 and in Fig. 7.10. The temperatures of the conductor were calculated assuming a pseudo-steady state case for each CFD simulation. In science and in engineering the Celsius and Kelvin scales are often used simultaneously. Since the experimental data and the CIGRE method measure temperature in ºC, the CFD results were also converted from Kelvin to ºC to make comparison easier.

Table 7.4 Initial data and results on the temperature of the conductor

Case	Time	Ambient temperature, ° C	Wind velocity, m/s	Current, A	Conductor temperature, ºC		
					Experiment	CFD	CIGRE
1	9:10 PM	5.9	4.4	336.49	12.9	9.70	12.15
2	9:15 PM	5.9	4.9	329.23	11.8	9.30	11.60
3	9:20 PM	5.8	4.4	325.37	13.1	9.30	10.54
4	9:25 PM	5.7	4.4	335.49	11.8	9.43	10.75
5	9:30 PM	5.7	3.5	328.53	11.7	9.80	11.48
6	9:35 PM	5.7	2.6	325.15	12.3	10.50	12.84
7	9:40 PM	5.7	1.3	338.31	13.7	10.40	18.87
8	9:45 PM	5.7	1.7	323.37	13.1	11.40	15.48
9	9:50 PM	5.6	1.7	320.69	14.3	11.20	15.20
10	9:55 PM	5.5	2.2	328.28	14.2	10.85	13.78
11	10:00 PM	5.4	2.6	325.27	14.2	10.20	12.54
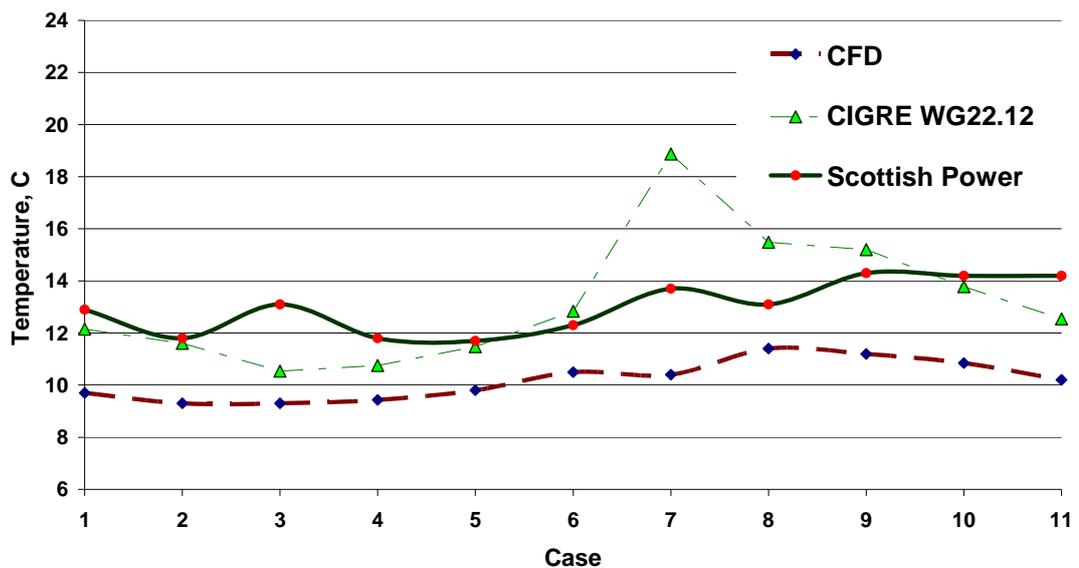
Fig. 7.10 The comparison of the results on Lynx temperature

In Case 7 the initial conditions change, namely the wind velocity decreases from 2.6 to 1.3 and the load increases from 325A to 338 A, which results in a rapid raise in the conductor temperature. Also, there are no straightforward formulae to calculate convective losses at low wind velocity value; the standards suggest calculating them by using three approaches and then submitting the highest value in the heat balance equation. Overall it can be seen that both methods have a good agreement with the experimental data, if it is remembered that the temperature measurement accuracy can vary from ±1.5 ℃ to ± 2.5 ℃.

The CFD curve practically duplicates the shape of the experimental data curve, with the average offset of 2 ℃. The reason that CFD model underestimates the temperature of the conductor can be explained by the fact that the direction of the wind was not taken into account – the CFD model used a cross wind. The discrepancy between the results achieved by the CIGRE method varies from 0.5 ℃ (for wind velocities of 2 and 5 m/s) to 5 ℃ (for a wind velocity of 7 m/s). In the case of a parallel wind the predicted temperature rises by approximately 2-5 degrees depending on the current and wind velocity magnitudes; and therefore reducing the discrepancy between the theoretical and experimental data.

7.2 Transient thermal behaviour of overhead lines - Response to the simultaneous variations in the current and cross-wind conditions

Two cases were numerically simulated with simultaneous variations of the current and the wind velocity over a 2-hour period of time.

Case 1

Fig. 7.11 presents a selection of experimental data monitored by Scottish Power on the variation of the temperature of the Lynx conductor used for numerical modelling in Case 1.
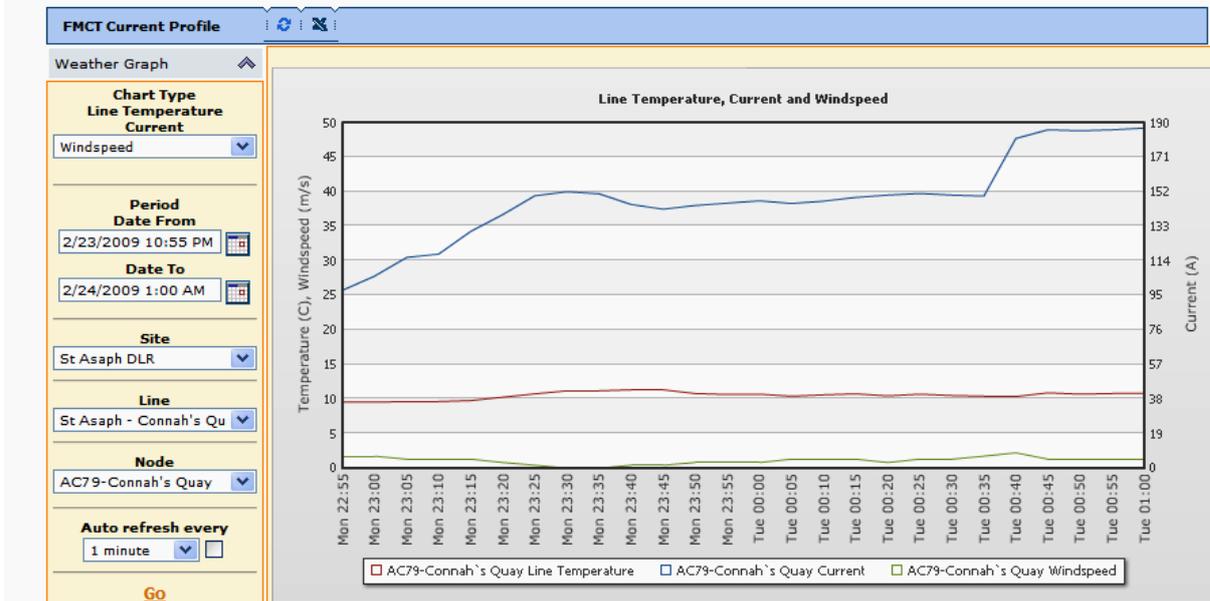
Fig. 7.11. A range of experimental data on the thermal state of the Lynx conductor operating in the variable current, ambient temperature, wind velocity and wind direction conditions for Case 1

A selection of this data is obtained for conditions when there is no heating of the conductor due to insolation (solar radiation is zero in experiments), see Table 7.5.

In Table 7.5 it can also be observed that the direction of the wind velocity changes spontaneously over a wide range and in the simulations it has been assumed that the wind direction was perpendicular to the axis. The experimental curves in Fig. 7.12 are an approximation of real data with a 30-second time step. These curves were used to create input data files for CFD simulations with additional subroutines for CFD modelling in Fluent, see Appendix F.

Table 7. 5 The experimental data on the thermal state of the Lynx conductor operating in variable current, ambient temperature, wind velocity and wind direction for Case 1

	A	B	C	D	E	F	G	AC	AD
	Date	Time	Temperature	Windspeed	Windspeed Avg	Wind Direction	Solar Radiation	T (deg C)	I (A)
2	2/23/2009	10:55 PM	7.2	1.7	1.7	13	0	9.5	97.64
3	2/23/2009	11:00 PM	7.2	0.8	1.7	345	0	9.5	105.52
4	2/23/2009	11:05 PM	7.2	1.3	1.3	340	0	9.6	115.84
5	2/23/2009	11:10 PM	7.2	1.7	1.3	355	0	9.6	117.57
6	2/23/2009	11:15 PM	7.1	1.3	1.3	360	0	9.7	130.10
7	2/23/2009	11:20 PM	7.1	0	0.8	5	0	10.2	139.28
8	2/23/2009	11:25 PM	7.1	0.4	0.4	5	0	10.7	149.63
9	2/23/2009	11:30 PM	7.1	0	0	5	0	11.1	151.91
10	2/23/2009	11:35 PM	7.1	0	0	5	0	11.1	150.75
11	2/23/2009	11:40 PM	7.1	0.4	0.4	348	0	11.2	144.87
12	2/23/2009	11:45 PM	7.1	1.3	0.4	325	0	11.3	142.29
13	2/23/2009	11:50 PM	7.1	1.7	0.8	355	0	10.7	144.39
14	2/23/2009	11:55 PM	7.2	0.8	0.8	355	0	10.6	145.67
15	2/24/2009	12:00 AM	7.2	1.7	0.8	345	0	10.7	146.84
16	2/24/2009	12:05 AM	7.2	1.3	1.3	355	0	10.3	145.40
17	2/24/2009	12:10 AM	7.2	1.3	1.3	315	0	10.6	146.71
18	2/24/2009	12:15 AM	7.1	0.4	1.3	324	0	10.7	148.71
19	2/24/2009	12:20 AM	7.1	0.8	0.8	311	0	10.4	149.92
20	2/24/2009	12:25 AM	7.1	1.3	1.3	322	0	10.7	150.98
21	2/24/2009	12:30 AM	7.1	1.3	1.3	321	0	10.5	150.10
22	2/24/2009	12:35 AM	7	2.6	1.7	319	0	10.4	149.42
23	2/24/2009	12:40 AM	7	2.2	2.2	309	0	10.3	181.10
24	2/24/2009	12:45 AM	7	0.4	1.3	313	0	10.9	185.35
25	2/24/2009	12:50 AM	6.9	0.4	1.3	333	0	10.7	185.94
26	2/24/2009	12:55 AM	6.8	1.3	1.3	317	0	10.7	185.97
27	2/24/2009	1:00 AM	6.8	1.3	1.3	324	0	10.8	186.91
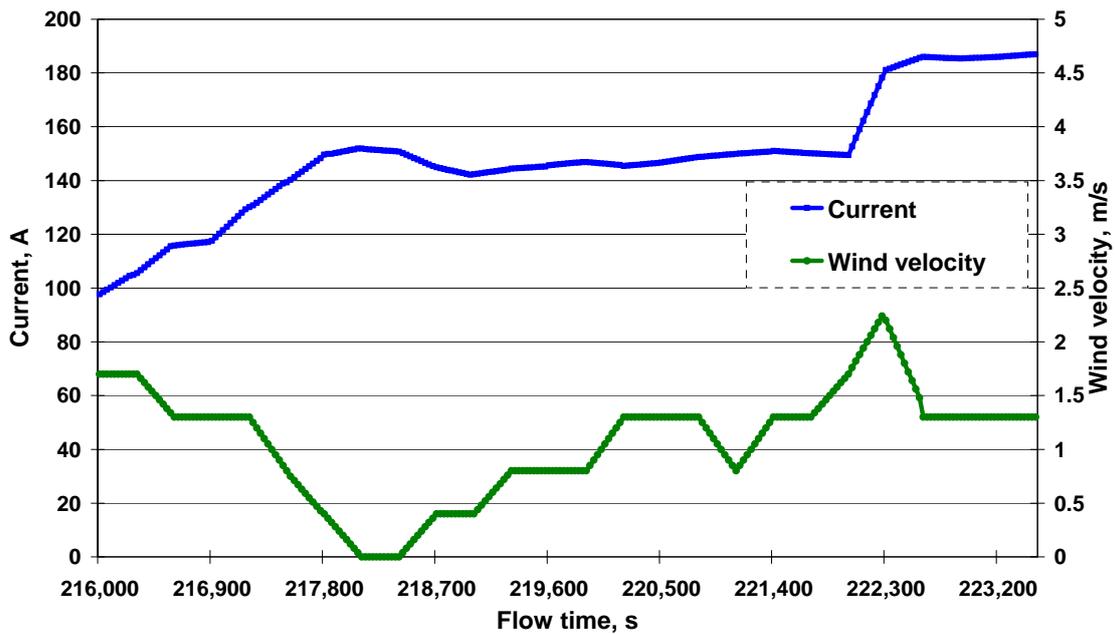
Fig. 7.12 Case 1: Approximation of the experimental variation of the current and the wind velocity

Results obtained from CFD simulations on the change in the thermal state of the conductor are shown in Fig. 7. 13.
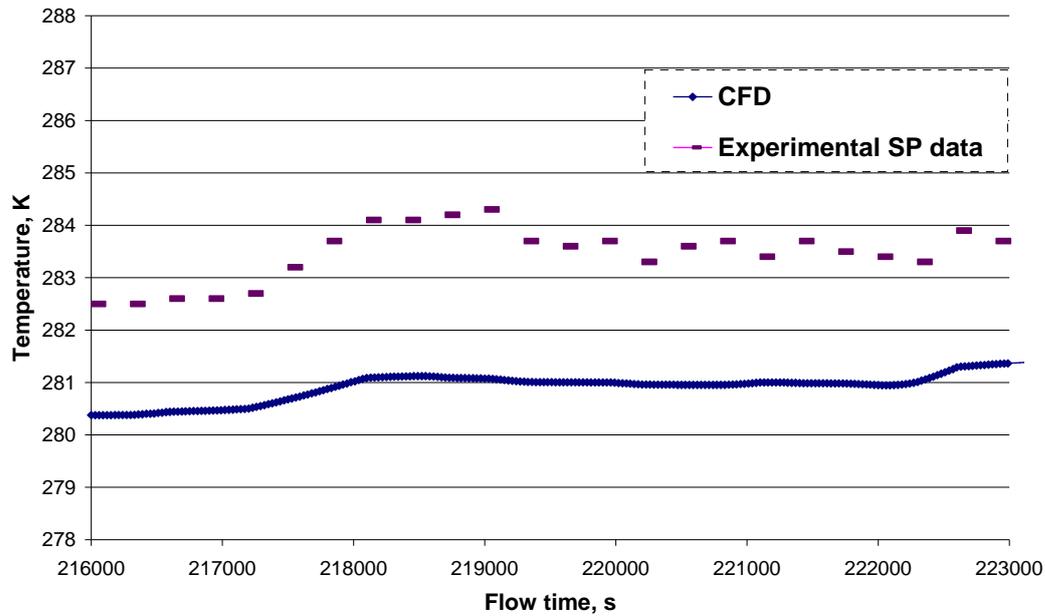
Fig. 7.13 Comparison of the experimental and CFD results on the variation in the conductor temperature for Cases 1

Case 2.

Initial experimental data used for CFD simulations for the case 2 are shown in Fig. 7.14 and Table 7.6.

In order to achieve reasonable accuracy the 5 minute intervals used in collecting experimental data should be divided into smaller intervals in numerical the modelling procedure. The functions used in CFD modelling should change continuously from one point to another. For the CFD modelling a 30 second interval was used to describe variations in the current, velocity of wind and ambient temperature. The missing values in Table 7.6 of current were calculated using plain interpolation.
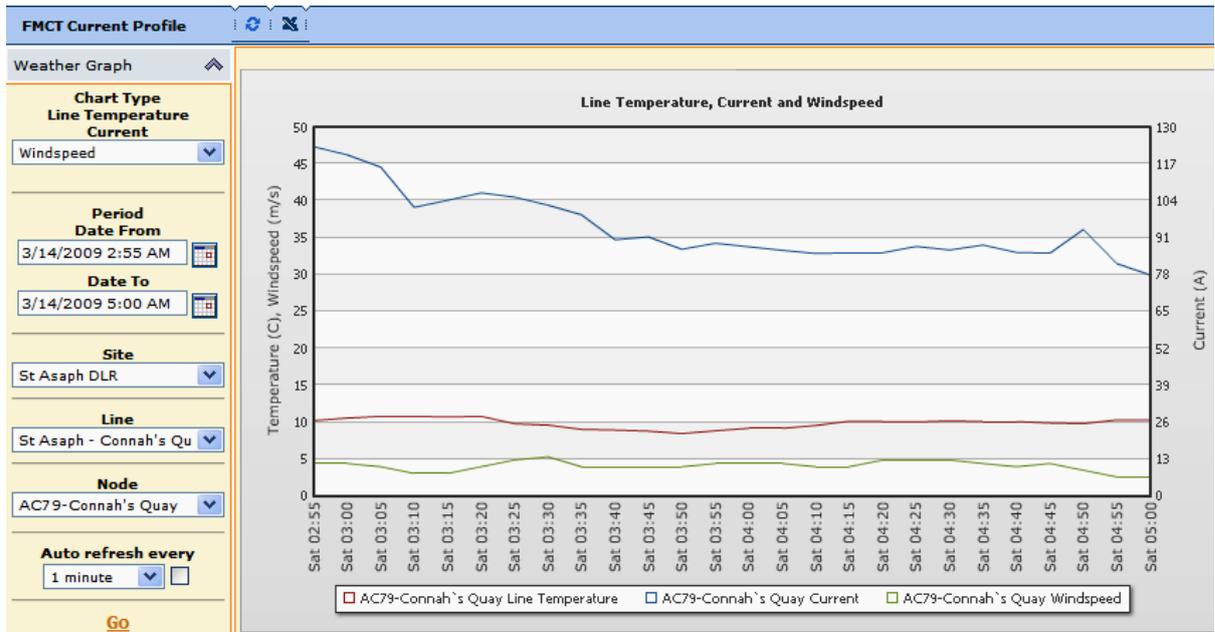
Fig. 7.14. A range of experimental data on the thermal state of the Lynx conductor operating in variable current, ambient temperature, wind velocity and wind direction for Case 2

Table 7. 6. The experimental data on the thermal state of the Lynx conductor operating in variable current, ambient temperature, wind velocity and wind direction for Case 2

	A	B	C	D	E	F	G	AC	AD
1	Date	Time	Temperature	Windspeed	Windspeed Avg	Wind Direction	Solar Radiation	T (deg C)	I (A)
2	3/14/2009	2:55 AM	8.6	4	4.4	219	0	10.2	123.00
3	3/14/2009	3:00 AM	8.7	3.1	4.4	238	0	10.5	120.15
4	3/14/2009	3:05 AM	8.7	4	4	241	0	10.8	115.87
5	3/14/2009	3:10 AM	8.7	4.4	3.1	243	0	10.8	101.71
6	3/14/2009	3:15 AM	8.7	3.5	3.1	263	0	10.6	104.19
7	3/14/2009	3:20 AM	8.7	4.9	4	259	0	10.8	106.83
8	3/14/2009	3:25 AM	8.6	5.8	4.9	272	0	9.7	105.33
9	3/14/2009	3:30 AM	8.2	3.1	5.3	273	0	9.6	102.47
10	3/14/2009	3:35 AM	7.9	4	4	264	0	9.0	99.10
11	3/14/2009	3:40 AM	7.9	3.5	4	260	0	8.9	90.24
12	3/14/2009	3:45 AM	8	4	4	253	0	8.7	91.30
13	3/14/2009	3:50 AM	8	7.1	4	262	0	8.4	86.93
14	3/14/2009	3:55 AM	8.2	4	4.4	260	0	8.8	89.08
15	3/14/2009	4:00 AM	8.3	3.1	4.4	283	0	9.1	87.76
16	3/14/2009	4:05 AM	8.3	1.7	4.4	267	0	9.1	86.54
17	3/14/2009	4:10 AM	8.2	2.6	4	277	0	9.5	85.44
18	3/14/2009	4:15 AM	8.2	4.4	4	257	0	10.1	85.73
19	3/14/2009	4:20 AM	8.2	4.9	4.9	282	0	10.1	85.62
20	3/14/2009	4:25 AM	8.2	5.3	4.9	257	0	10.0	87.87
21	3/14/2009	4:30 AM	8.2	5.8	4.9	257	0	10.1	86.66
22	3/14/2009	4:35 AM	8.1	2.2	4.4	295	0	10.1	88.38
23	3/14/2009	4:40 AM	8.1	4	4	257	0	10.1	85.75
24	3/14/2009	4:45 AM	8.1	2.6	4.4	269	0	9.9	85.55
25	3/14/2009	4:50 AM	8	3.1	3.5	284	0	9.7	93.85
26	3/14/2009	4:55 AM	7.9	1.7	2.6	296	0	10.3	81.80
27	3/14/2009	5:00 AM	8	2.2	2.6	269	0	10.2	77.83

Figures 7.15 and 7.16 show the data files of the current and the wind velocity variations prepared for the CFD modelling using subroutine programs.
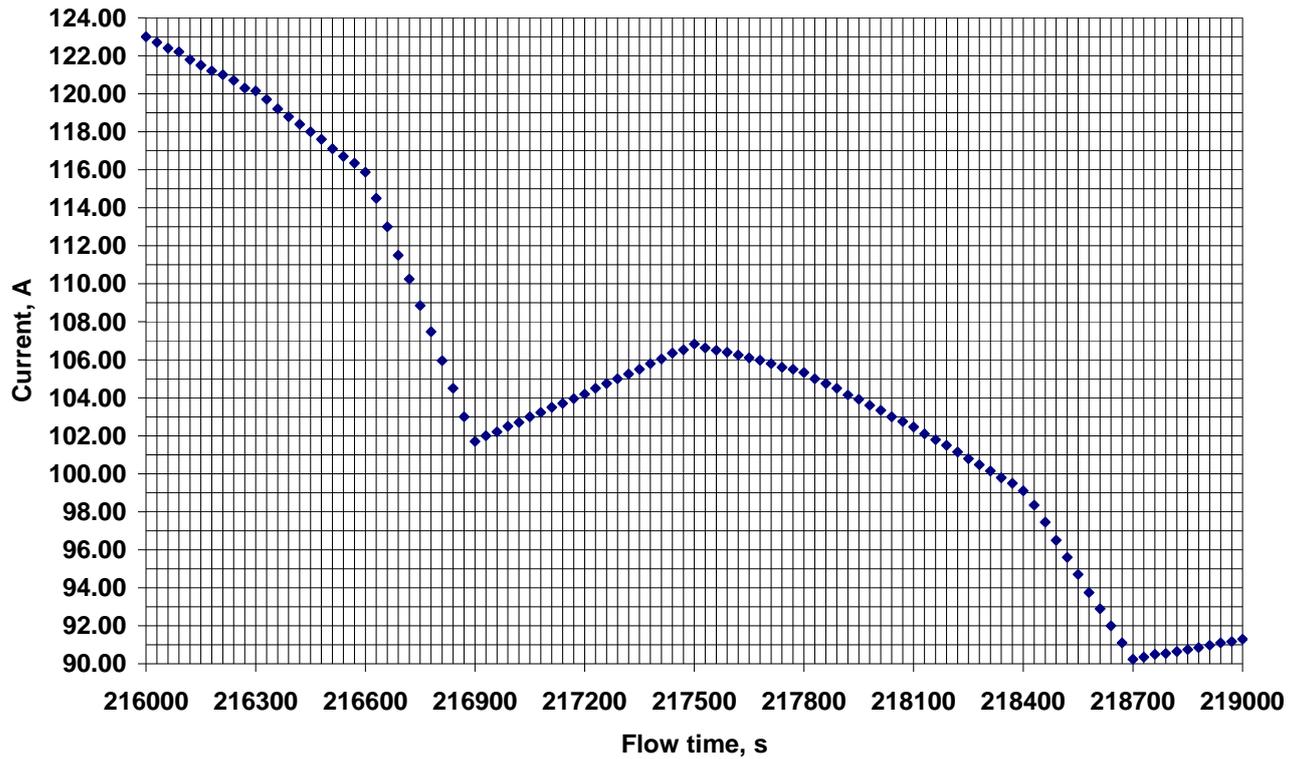
Fig. 7.15 The current variation prepared for CFD modelling
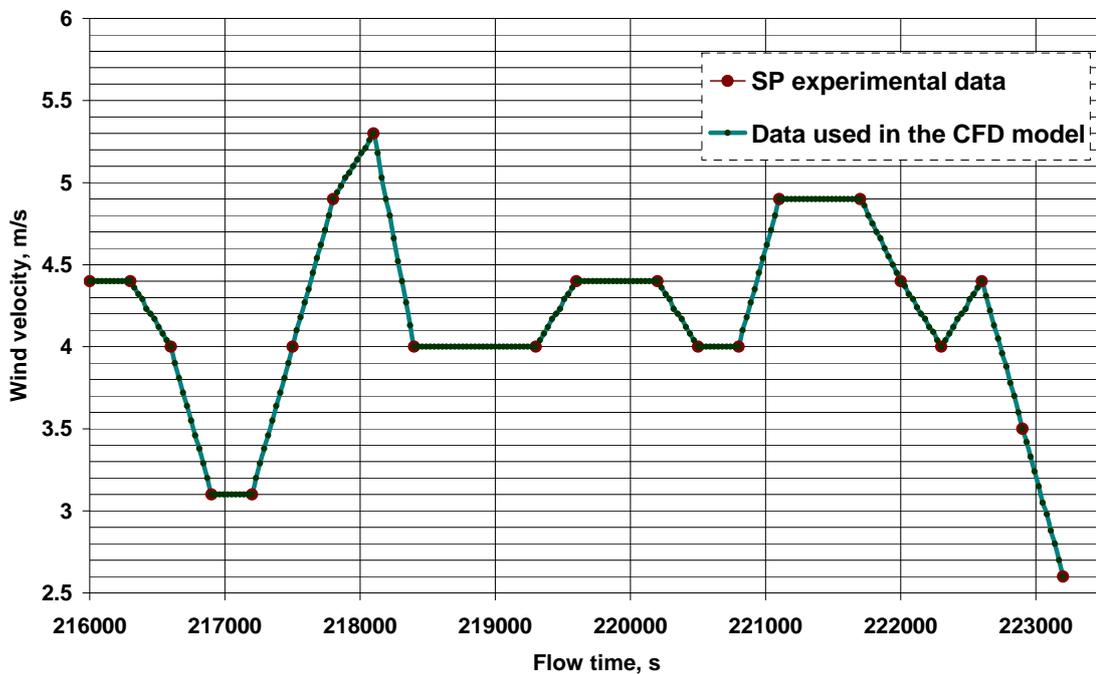
Fig. 7.16 Case 2: The wind velocity variation prepared for CFD modelling

167

Results obtained from CFD simulations on the change in the thermal state of the conductor are shown in Fig. 7.17.
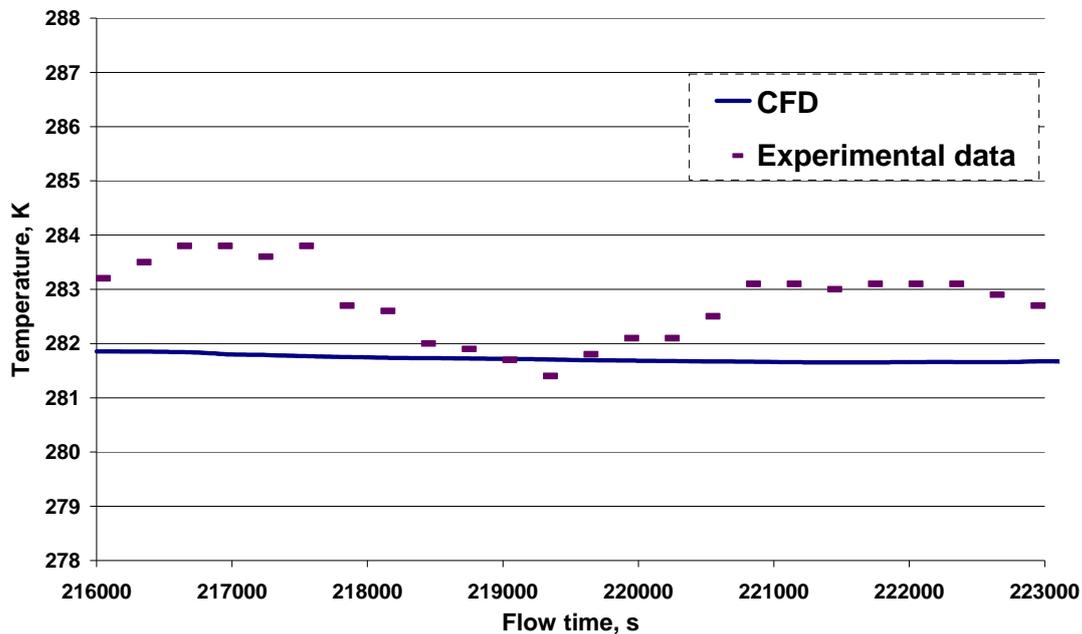
Fig. 7.17 Comparison of the experimental and CFD results on the variation in the conductor temperature for Case 2

It can be seen in Fig. 7.13 and 7.17 that dynamic CFD simulations provide reasonable accuracy in predicting the thermal state of the conductor. The difference between the numerical and experimental data is less than two degrees and for Case 1 the profile of the theoretical curve closely follows that of the experimental data.

The discrepancy between numerical simulation results and experimental data can be explained by the fact that the variation in the ambient temperature and the stochastic character of the change in the wind direction were not taken into account. Additionally, much finer discretisation of experimental data is needed to create an input data for CFD simulations in order to further improve the capability of modelling to more closely predict the unsteady thermal state of the conductor in real exploitation conditions.

7.3 Conclusions

This chapter describes investigations into the possibility of increasing the thermal rating of OHL conductors of a power system. The industrial standards use ratings which are based on the worst operating conditions case, such as 0.5 m/s wind velocity and 20 ºC of ambient temperature for the summer rating.

The experimental data shows that the heat transfer process between the surface of the OHL conductor and surroundings changes continuously and the dynamic changes should not be ignored. Therefore DNO fully supported a number of projects, which could provide additional insights into the heat transfer process in order to investigate the operation limits of the OHL conductors.

The dynamic nature of the temperature of the conductor can be modelled using CFD techniques, taking into consideration a number of real time changes in weather conditions and also in the properties of the conductor. The input data files for wind velocity and current were created with a 30-second time step and incorporated into a subroutine which in turn was integrated with a CFD solver.

Comparison of numerical results with available experimental data demonstrates that the CFD technique provides an acceptable level of accuracy in the prediction of the thermal state of the Lynx overhead conductor for both the steady-state and the transient state, i.e. the temperature difference between the CFD model and the experimental data was within 3.5 degrees.

CHAPTER 8

CFD MODELLING OF THERMAL STEADY STATE OF UNDERGROUND CABLES

The objectives of numerical investigations carried out in this Chapter are to gain a deeper understanding of the steady state thermal behaviour of UGC in order to improve their design. This chapter presents the numerical results regarding the thermal state of single and multiple 33 kV copper conductors with the nominal area of the conductor of 630 mm^2 [66] buried in soil for a single cable and for three cables in flat formation and trefoil formation. Both summer and winter conditions, which differ in ambient temperature and the temperature of the soil, and also by the physical properties of the soil depending on the moisture content [67], are studied.

In all the above cases for comparison purposes a rating of 940 A, which is the sustained current rating for the copper conductor for winter conditions, was chosen as a base case. Additionally, cases with 470 A (which is a half of the sustained rating) and also summer conditions were investigated.

Furthermore, several cases were investigated for flat and trefoil cable arrangements with 100% load and 50% load with ratings recommended in Electric Cables Handbook/BICC Cables (for normal summer conditions) [68] and ENA Engineering Recommendation P17 Part 3 (for winter conditions) [69]

Then the effects of soil moisture content were illustrated using the case with a single directly buried underground cable with 3 and 3.5 A/mm^2 of the current density.

Furthermore, the case of a single cable placed at the bottom of a plastic pipe and buried in soil with a high moisture content was analysed using a free convection model.

Finally, the effect of the wind above the ground on the temperature of the conductors buried in the soil was investigated.

8. 1 Single conductor

8.1.1 Geometry

The physical design of the conductor is shown in Fig. 8.1. The real geometry of the conductor is complex and contains the following components: the copper conductor core made of strands; the conductor screen (polyethylene type material); insulation (cross-linked polyethylene); the insulation screen (polyethylene type material); the copper screen; the binder tape (polyethylene type material) and oversheath (medium density polyethylene). For purpose of creating the computational mesh the real geometry of the conductor was simplified (in order to reduce computational time) and   presented as a combination of four co-axial cylinders, with the outer cylinder

being made of dielectric and the inner cylinder made of copper, see Fig 8.2. The outer diameter of the copper conductor and the oversheath is 28.3 and 60.4 mm, respectively.
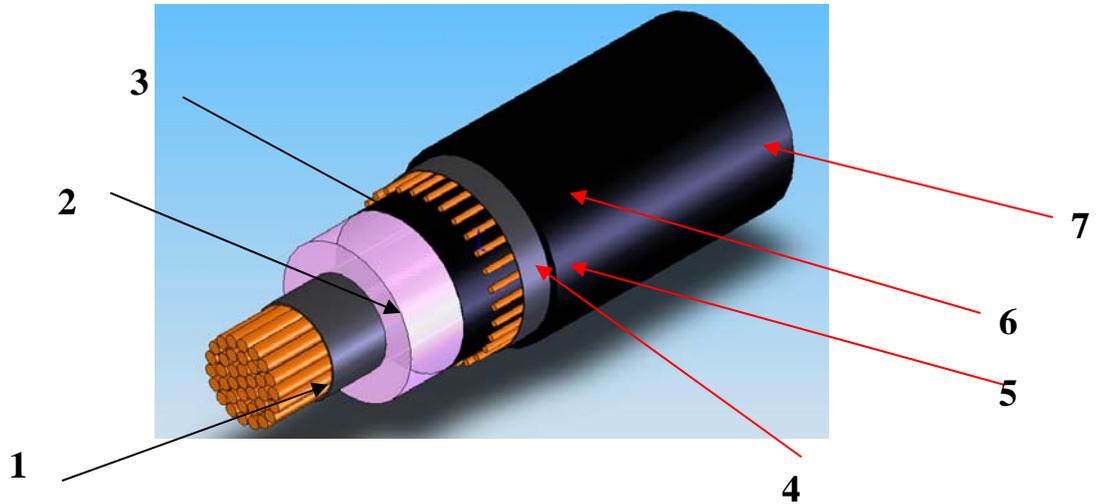
1-copper conductor; 2-conductor screen (polyethylene type material); 3-insulation (cross-linked polyethylene); 4-insulation screen (polyethylene type material); 5-copper screen; 6-binder tape (polyethylene type material); 7-oversheath (medium density polyethylene)

Fig. 8.1 Design of the underground cable
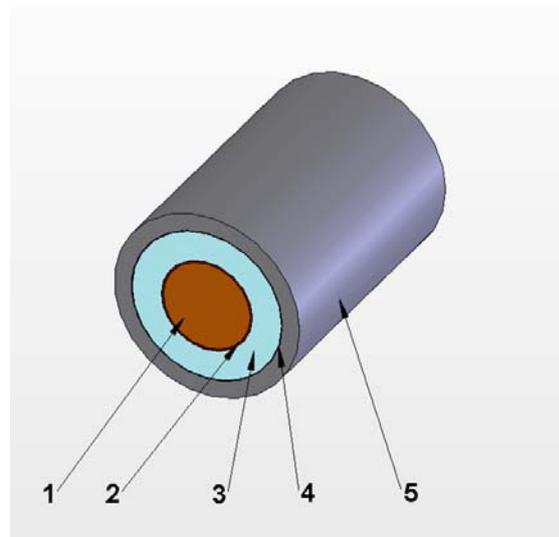
1-copper conductor; 2-conductor screen (polyethylene type material); 3-insulation (cross-linked polyethylene); 4-copper screen; 5-oversheath (medium density polyethylene).

Fig. 8.2 A simplified model used for numerical simulation

172

The dimensions of the simplified model are as follows: the diameter of copper cable with nominal area of conductor of 630 mm^2 is 28.3 mm; the thickness of insulation is 8 mm; the thickness of the copper wire screen is 1 mm and the thickness of oversheath is 2.7 mm, see Appendix G. The simplified geometry allows defining the temperature of the conductor, which will require further work in order to improve the accuracy the results.

8.1.2 The computational domain

Fig. 8.3 presents the computational domain used for the numerical modelling of the thermal state of a single copper cable buried in the soil. In this domain the cable is placed at the centre of the two-dimensional soil sub-domain with 1,600 mm $\times$ 1,600 mm dimensions. These dimensions of the domain are large enough to produce size-independent solutions. As previously, mesh refinement tests were conducted in order to ensure that the solutions are not mesh dependent.
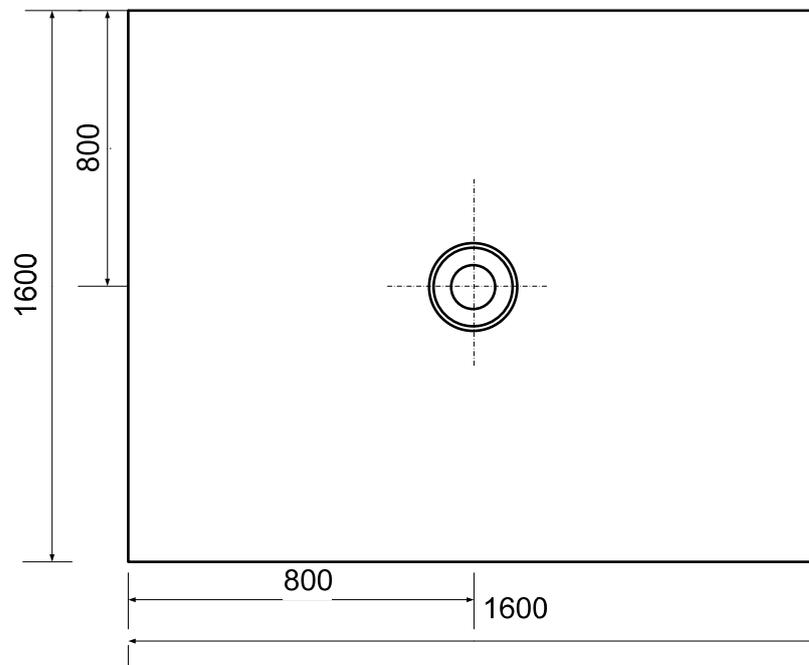
Fig. 8.3 A computational domain for the numerical investigation of the single copper cable buried in soil (the dimensions are in mm)

8.1.3 Initial data for calculations

Soil is considered as a solid medium and not as a porous substance. In winter and summer the soil was assumed to have average and low moisture contents, respectively. An additional case was also analysed when the soil was presented as a combination of three co-axial zones with low, average and high moisture contents, respectively. To each of the above types of soil the corresponding values of the density, the thermal conductivity and the heat capacity were assigned. Thermo-physical properties of the components and of the soil used in calculations are presented in Table 8.1 and 8.2 (see Appendix H), respectively.

Table 8.1 Density, heat capacity and thermal conductivity for components of the cable [67]

Components of the cable	Density, kg/m^3	Heat capacity, J/kg K	Thermal conductivity, W/m K
Copper conductor	8978	381	387.6
Conductor screen (PVC)	1300	1330	0.182
Insulation	950	Piecewise linear: 2300 at 293K; 3750 at 353K	0.333
Copper screen	8900	385	370.4
Oversheath	1600	1500	0.25

Table 8.2 Density, heat capacity and thermal conductivity for different types of soil [67]

Type of soil	Density, kg/m^3	Heat capacity, J/kg K	Thermal conductivity, W/m K
Moist soil (high moisture content)	2100	2000	1.11
Average moisture (average moisture content)	1900	830	0.833
Dry soil (low moisture content)	1400	800	0.408

8.1.4. Heat generation in the cable

The magnitude of heat generation in the conductor was calculated as Joule losses and this value was used in the numerical modelling of a group of underground cables as a heat source:

$$q = \frac{I^2 \times R}{A},\tag{8.1}$$

where R is the AC resistance of the copper conductor (Ω/m); A is the cross-sectional area of the conductor (mm^2) and I is current in the cable (A). According to the BS 6622-1991 [68] the AC resistance of the copper is $R = 0.0405$ Ω/km at 363 K.

Generally, dielectric losses can also be taken into consideration despite the fact that these are small in comparison with the conductor losses. The cables which operate above 50 kV have considerable dielectric losses which cannot be ignored. The dielectric losses are dependent on voltage and the properties of the insulation material being used. The dielectric loss per unit length in each phase is calculated as

$$W_d = \omega \cdot CU_0^2 \cdot \tan\delta,\qquad\qquad(8.2)$$

where ω is the *2πf* (rad/s); *C* is the capacitance per unit length (F/m); U_0 is the voltage to earth (V), δ is the dielectric loss angle [55]. The calculated value of W_d is 1053 W/m^3 and this value was used in the numerical simulations as the second component of the heat source in the cables, but its effect on the temperature of the cable is less than 0.6% (1- 1.5 degrees) of the temperature of the conductor so it was neglected in further numerical investigations.

8.1.5 The base case winter and summer conditions (in accordance to P17) and setting boundary conditions for numerical simulations.

According to Electrical Standards P17 [69] for the winter conditions the soil and ambient temperatures are 283 K and soil has a high moisture content. The thermal rating for the 630 mm^2 cable in the flat formation in winter conditions is 940 A, which corresponds to a heat source, *q*, of 14,200.7 W/m^3. The summer conditions are characterised by average soil moisture content, see Table 8.1, and the soil and ambient temperatures of 288 and 298 K, respectively [68].

Accordingly, in all further simulations of the thermal state of underground cables the temperature at the top and at the bottom of the computational domain was set to be uniform and constant at the 283 K level in winter conditions and at 298 and 288 K levels, respectively, in summer conditions.

Additionally, a zero heat flux boundary condition was set on the left and right sides of the computational domain. This was undertaken since generally a cable or a group of cables in a modern urban area, and very often even in the rural area, is

surrounded by other cables or groups of cables buried in the soil at the same depth level. The distance between locations of single cables or the groups of cables in soil usually vary from one to several metres. Application of the zero flux value at the right and left sides of the computational domain reflects the fact that cables are buried in soil with some periodicity.

Another type of boundary conditions which could have been used in numerical simulations of the thermal state of underground cables is a constant or linearly varying temperature on the left and right sides of the computational domain. However, computational simulations demonstrate that when such the boundary conditions are applied, then the character of the temperature distribution in soil around the cables is to some extent different and temperature levels in the components of the underground cables predicted are lower by 2-5 degrees at high current levels. This is because application of the constant or linearly varying temperature boundary conditions to the right and left boundaries of the computational domain result in the heat thermal capacity of soil outside of the computational domain being greater compared to that in the case of application of the zero flux boundary conditions.

8.1.6 Results of numerical simulations

The results of 2-D unsteady CFD simulations of the thermal state of a single cable directly buried in the soil are presented in Fig. 8.4 and Table 8.3.

Fig. 8.4 presents the distribution of the temperature in the cable and the surrounding soil for winter and summer conditions for the current values of 470 and 940 A,

respectively. As expected the temperature distribution will be symmetrical with reference to a vertical plane passing through the axis of the cable. There is also a symmetry with reference to a horizontal plane passing through the axis of the cable in winter conditions. In summer conditions there exists a low temperature gradient in the soil layers located above the cable since the soil temperature at the top of the domain is 10 degrees lower than that at its bottom. The temperature gradient in the soil is also strongly affected by its moisture content – it is greater in the case when the moisture content is low (this corresponds to the lower value of the coefficient of conductivity). Increasing the current from 470 to 940 A in winter conditions results in a rise in the average temperature of the conductor from about 293 to about 318 K, see Table 8.3.

Table 8.3 The temperature of the single cable under base case winter and summer conditions

Transferred current, A	Conditions	Conductor temperature, K
470 A	Winter	293.43
470 A	Summer	304.95
940 A	Winter	317.77
940 A	Summer	334.74

For summer conditions the rise in the temperature of the conductor is from about 305 to 335 K. It can also be seen from Table 8.3 that the temperature of the conductor at summer conditions is about 17 and 11 K higher for the current of 940 and 470 A, respectively, compared to winter conditions.
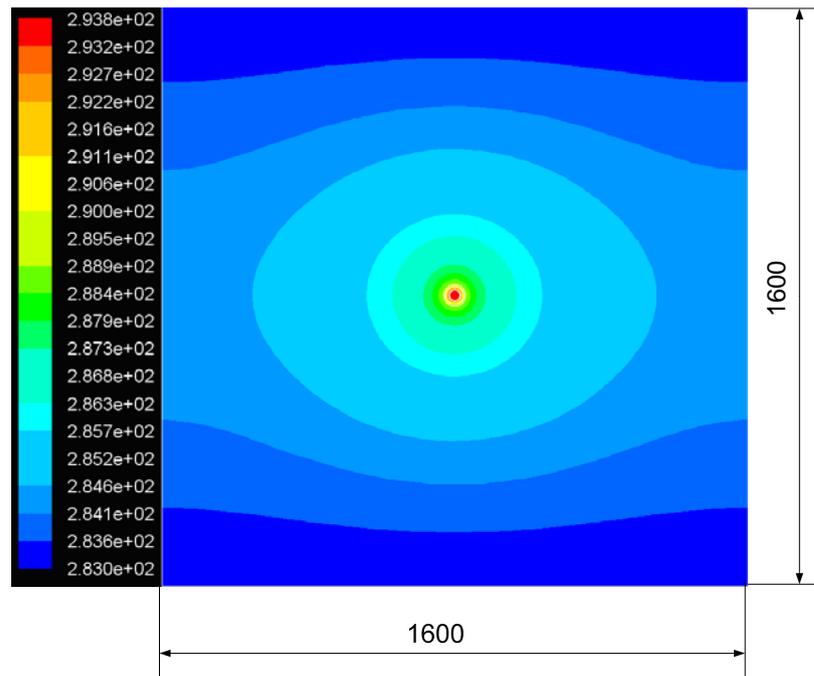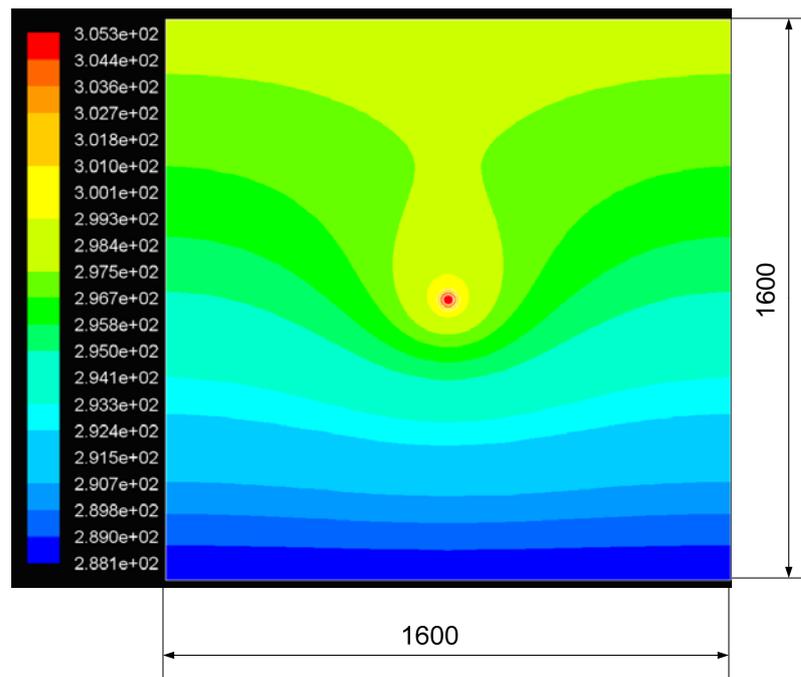
Fig. 8.4 Temperature distribution around the cable for base case a) winter conditions and b) summer conditions. The current is 470 A. All dimensions are given in mm

c)

d)
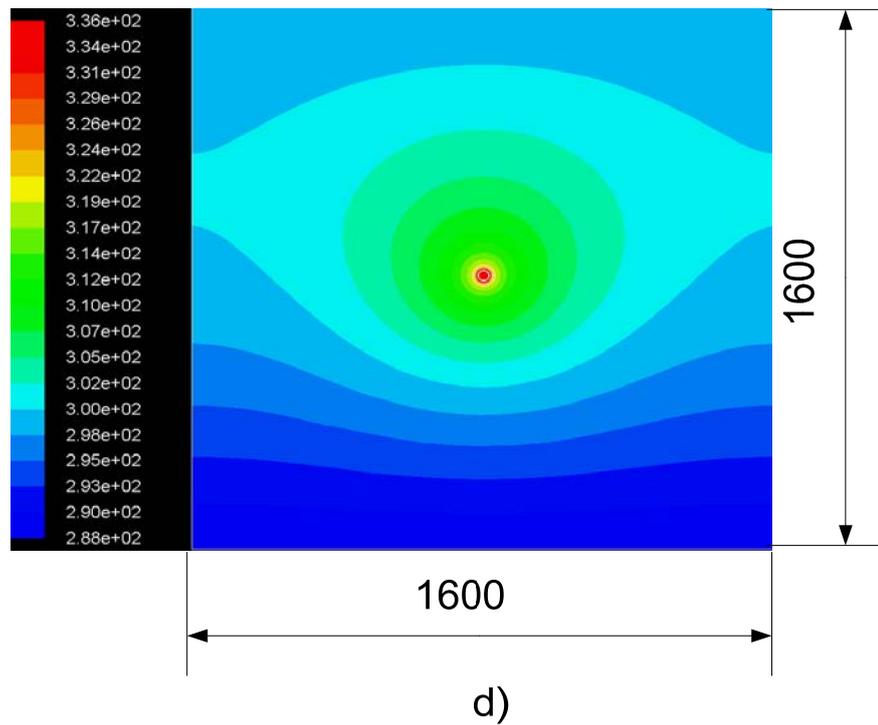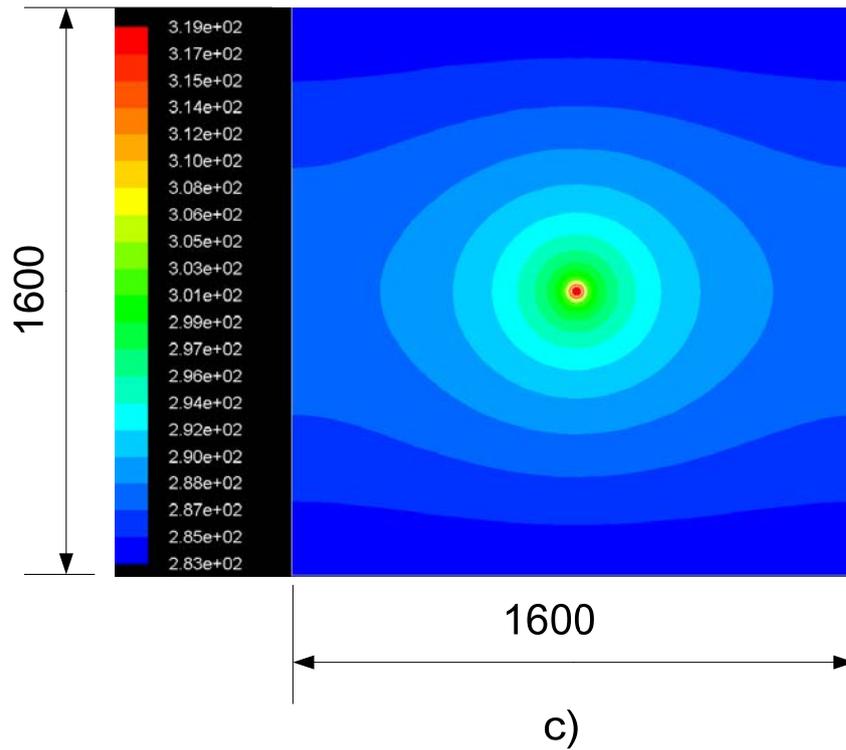
Fig. 8.4 Temperature distribution around cable for base case c) winter and d) summer conditions. The current is 940 A. All dimensions are given in mm

8.2 Three single cables buried in the soil in a flat formation

8.2.1 The simplified geometry of the cable and computational domain

Modelling 3 cables requires considerable greater computing time due to the increased number of the equations and the larger computation domain, therefore for the simulation purpose a simplified model of the cable was implemented in comparison with the cases in which the thermal state of a single cable was analysed This simplified geometry is shown in Fig. 8.5.
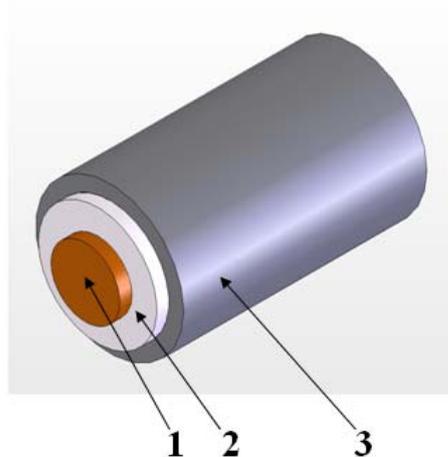
1 –copper conductor; 2 - insulation (cross-linked polyethylene); 3 - oversheath (medium density polyethylene).

Fig. 8.5 A simplified model of a single cable used for investigation of the thermal state of a group of underground cables

In order to obtain information on the temperature distribution around a group of underground cables the case in which three cables are buried in soil and placed at the same level next to each other with some spacing (the flat formation) was analysed. A calculation scheme of the computational domain used in 2–D modelling of the thermal state of three single cables buried in the flat formation is presented in Fig. 8.6. The cables are buried at the depth of 800 mm and the distance between the cables is 120.8 mm. The dimensions of the soil domain surrounding the cables are

2,400 mm   × 2,400 mm.   The dimensions of the domain produce the size-independent solutions and   mesh refinement tests were conducted to ensure that the solutions are not mesh dependent.
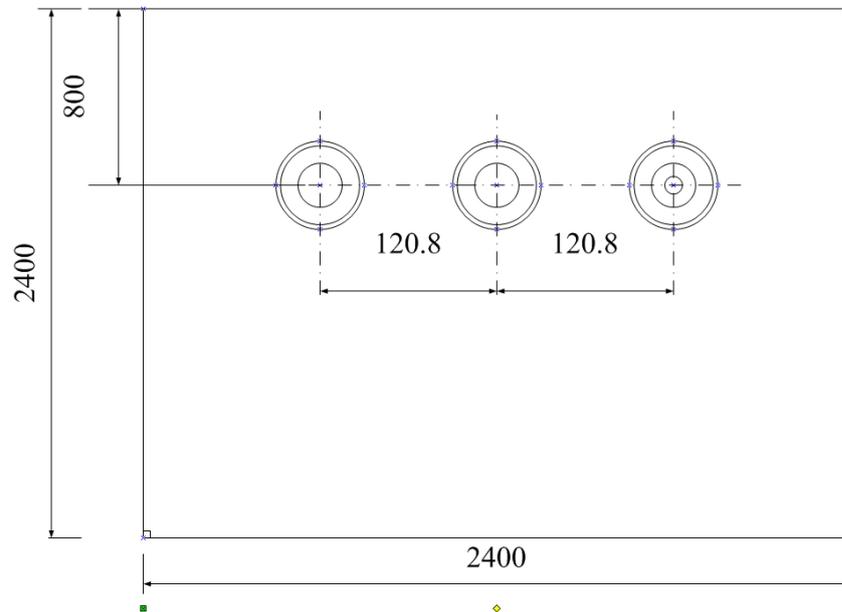
Fig. 8. 6 The computational domain used for investigation of the thermal state of a group of underground cables placed in a row (flat formation)

8.2.2 Discussion of numerical results: three single cables buried in flat formation (operation in winter conditions in accordance with ENA Engineering Recommendation P17 Part 3)

The input data used for CFD simulations are that specified by ENA Engineering Recommendation P17 Part 3 [69] and are as follows:

- High moisture soil, soil resistivity is 0.9 K·m/W;

-- Ground temperature is 283 K;

- Ambient temperature is 283 K;

- Current in each cable – 940 A

The additional case was considered in which all the cables have 50% of the current rating in winter conditions.

Fig. 8.7 presents temperature distribution around the cables for the base case when the transferred current was 940 A and the winter conditions with high moisture content were considered. The temperature distribution is symmetrical with the reference to a vertical plane passing through the axis of the middle cable. The maximum temperature occurs in the middle cable and it is 343.19 K.
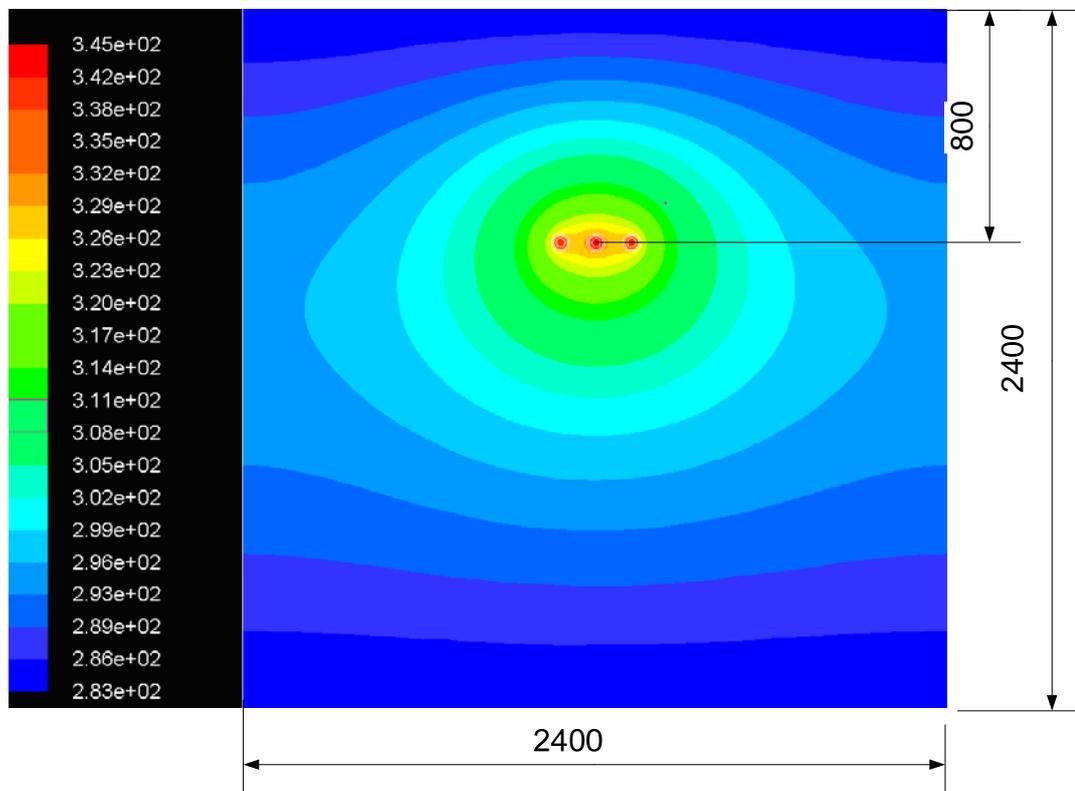
Fig. 8.7 Temperature distribution around the cables for the base case with the transferred current of 940 A under the winter conditions

In the case when the applied current corresponds to 50 % of the recommended rating, which is 470 A, the temperature distribution is similar in character to that in

183

Fig.8.7 with the maximum temperature occurring in the middle cable and it is 299.05 K.

Two additional variant cases were considered with the current ratings of 940 and 470 A and the soil and ambient temperatures of 298 and 288 K, respectively and with average moisture content. These correspond to base case summer conditions (temperatures of the soil and of the ambient and the current rating of 950 A for summer conditions for flat formation are determined by BS 6622 – 1991)

Results of the numerical simulations of the thermal state of three single cables in the flat formation operating in winter conditions in accordance to ENA Engineering Recommendation P17 and variants of summer conditions (base case summer conditions) are presented in Table 8.4.

Increasing the current from 470 to 940 A in winter conditions results in a rise of the average temperature of the conductor from about 299 to about 343 K, see Table 8.4. For base case summer conditions this rise in the temperature of the conductor is from about 314 to 370 K. It can also be seen from Table 8.4 that the temperature of the conductor working at base case summer conditions is about 27 and 15 K higher for the currents of 940 and 470 A, respectively, compared to winter conditions.

In accordance with the BS 6622 – 1991 the maximum temperature of the conductor should not exceed 363 K for the exploitation conditions. It can be seen that for base case summer conditions with the current of 940 A the average temperature of the middle conductor is slightly exceeding the safe limit by about 2 %.

184

Table 8.4 The input data and the resulting temperature of the middle cable in flat formation under winter and base case summer conditions

Base case conditions	Current, A	Soil temperature, K	Ambient temperature, K	Moisture content	Temperature of the middle conductor, K
Winter	470	283	283	High	299.05
Summer	470	288	298	Average	314.28
Winter	940	283	283	High	343.19
Summer	940	288	298	Average	370.48

8.2.3 Discussion of numerical results: three single cables buried in flat formation (operation in summer conditions in accordance with   BS 6622 – 1991)

The following data was used for simulation of operation of cables in the flat formation in accordance with   BS 6622 – 1991:

- Ground temperature 288 K;

- Ambient temperature 298 K;

- Current – 950 A;

- Soil has the average moisture content.

Cases when each cable is carrying 100 and 50% of the maximum current and also the case of summer conditions with the 950 A current combined with the high moisture content are analysed.

The obtained temperature distributions (in K) in the computational domain for cases with 100 and 50% of the maximum current are presented in Figures 8.8 and 8.9, respectively.
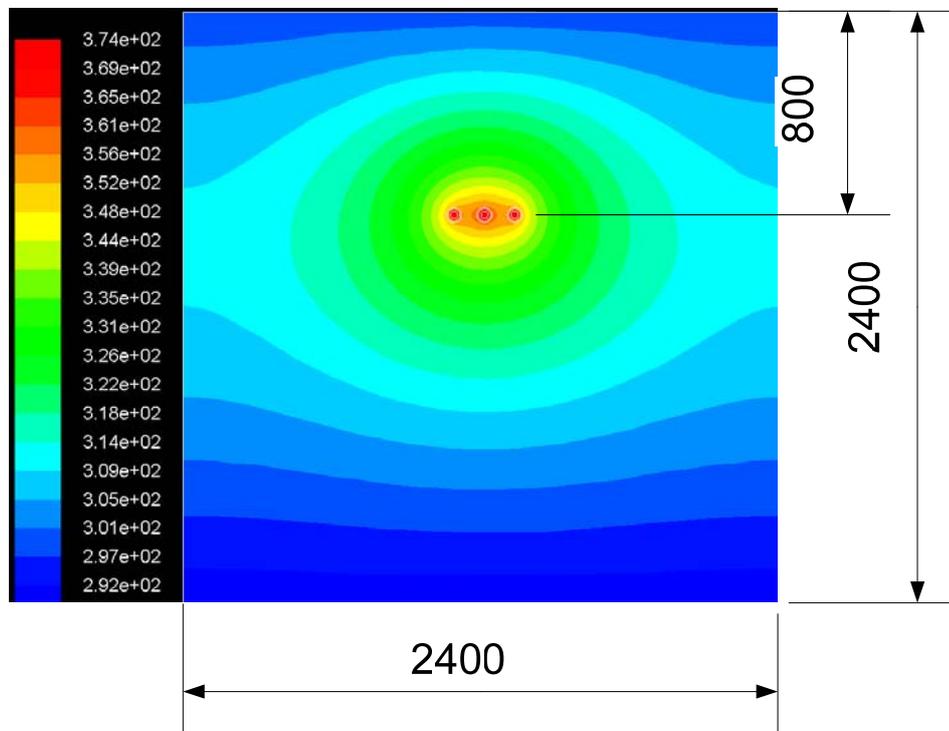
Fig. 8.8 The temperature contours (in K) in the computational domain: all the cables have 100% current (950 A) and the soil has the average moisture content

The temperature distribution in the computational domain is symmetrical with reference to the vertical plane passing through the axis of the middle cable, with the temperatures being highest at 372 K when the current is 950 A. This is 9 degrees higher than the allowed temperature (2.48% greater than permissible safe limit). The temperature distribution around the cables in the flat formation with 50 % of the rating for summer conditions, see Figure 8.9, indicates that the maximum temperature reaches 314.7 K in the middle cable, and this is approximately 48 K lower than the maximum allowed temperature for conductors.
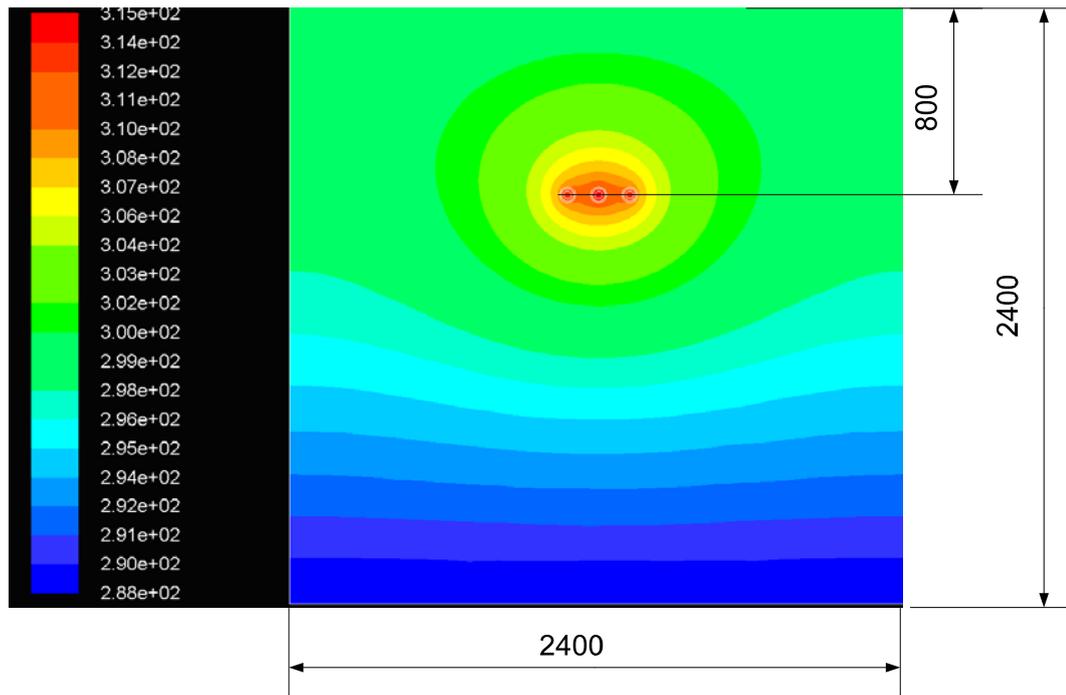
Fig. 8.9 The temperature contours (in K) in the computational domain: the sub-case 1 (all the cables have 50% rating)

As in the case of a single cable directly buried in the soil the maximum value of the cable temperature in the flat formation strongly depends on the soil moisture content. Fig. 8.10 presents the temperature contours (in K) in the computational domain for summer conditions in the flat formation with the current being 950 A in each cable. The group of cables is placed in soil with the high moisture content instead of soil with average moisture content, and as a result of this the maximum temperature of the cable is considerably decreased. The maximum temperature in the middle cable for such a situation reaches 356.13 K, which is approximately 16 K lower than in the similar case with the average moisture content of the soil.
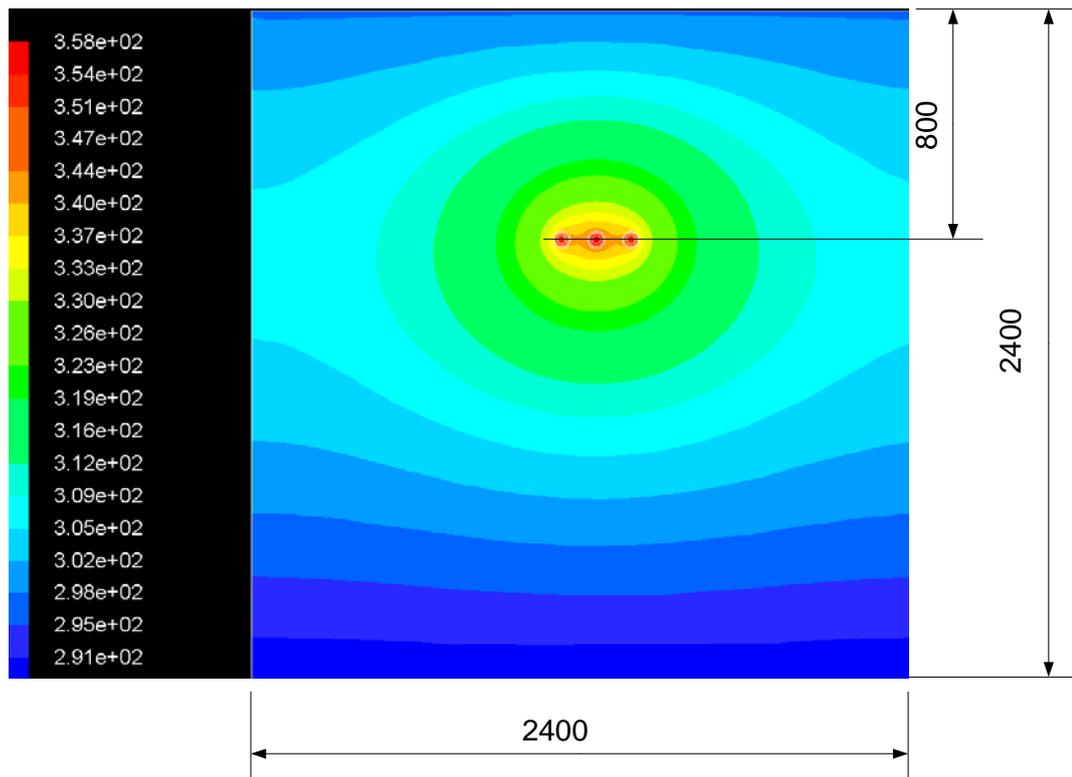
Fig. 8.10 The temperature contours (in K) in the computational domain: the summer conditions, all the cables have 100% current (950 A) and the soil has the high moisture content

More details on the temperature distribution in the walls of the conductors, insulations and oversheaths for the case of flat formation cables with 950 A current in each cable for summer conditions and soil with the average moisture content is provided in Fig. 8.11. It can be seen that the temperature is reduced quite considerably along the thickness of the insulation and oversheath for both currents.

Table 8.5 shows the average temperature of the above three components of the middle cable for cases when the current through each cable is 950 and 475 A. The difference between the maximum temperature of the cable (about 372 K) and the minimum temperature of the oversheaths (about 358.2 K) is approximately 14 K for

the current 950 A and 3.6 K for the current of 475 K. It can be concluded that the temperature difference between the conductor and oversheath strongly depends on the magnitude of transferred current, temperature of the soil and its moisture content.

Table 8.5 The average temperature distributions on the walls of the conductors, insulations and oversheaths

Rating, A	Temperature, K		
	Conductor	Insulation	Oversheath
950	372	362.4	358.2
475	314.7	312.2	311.1

Previously the temperature on the surface of the middle cable was calculated using the IEC 60287 [55] method. The comparison shows that the oversheath temperature determined using CFD modelling is 8 degrees higher.

Finally, Fig. 8.12 presents the average temperature profile in the horizontal plane passing through the axes of the three cables   for the case of summer conditions, 950 A current and the average moisture content of the soil. It can be seen that that the temperature decreases rapidly with the increase of the distance from the cables.

Table 8.6   presents the results on the average temperature of the conductors for the cases when the current is 950 and 475 A.
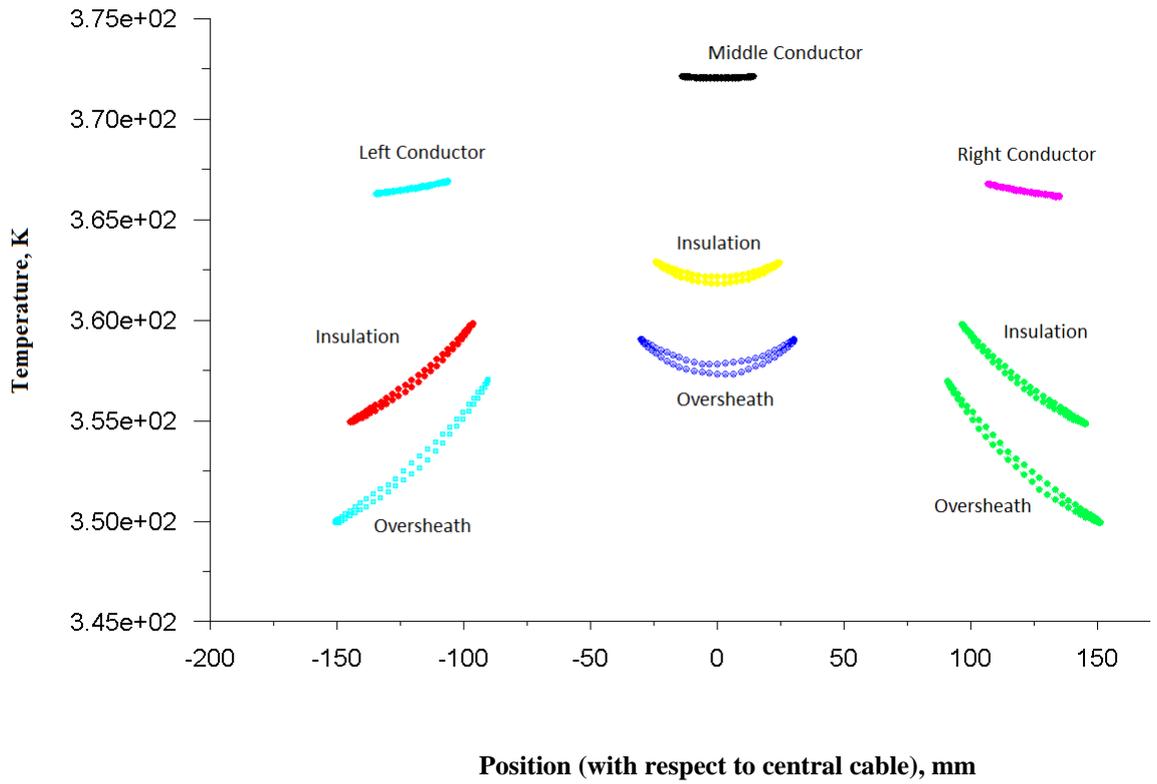
Fig. 8.11 The average temperature distributions on the walls of the conductors, insulations and oversheaths: the sub-case 1 (all the cables have 100% current) and soil has the average moisture content
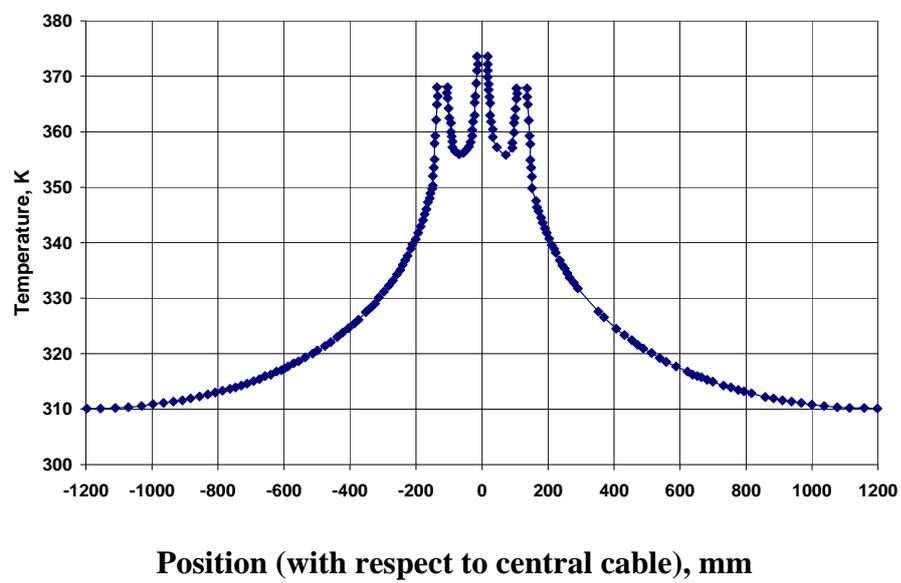
Fig. 8.12 The average temperature profile in the horizontal plane passing through the axes of the three cables for the case of summer conditions, the 950 A current and the average moisture content of the soil

190

Table 8.6 The average temperature of the conductors

Rating, A	Temperature of the conductor, K		
	Left cable	Middle cable	Right cable
950	366.5	372	366.5
475	313	314.7	313

These results indicate that at the current of 950 A   the maximum temperature of the conductor is 372 K, which exceeds the allowed temperature of 363 K by 9 K. This indicates that there is no scope for increasing the ampacity of underground cables for the given arrangement. Temperatures in the right and left cables are almost within the safe operational limit.

8.3 Three single cables buried in soil in a trefoil formation: operation in base case winter and summer conditions

8.3.1 Geometry of the cables and the calculation scheme of the computational domain

A 3-D model of three single copper cables buried in the trefoil formation is presented in   Fig. 8.13.

Fig. 8.13 The geometry of three cables in the trefoil arrangement

Fig. 8.14 presents the computational domain, where the cables are buried at the depth of 800 mm and the distances between the centres of the cables are 60.4 mm. The dimensions of the soil domain surrounding the cables are 2,400 mm × 2,400 mm. The dimensions of the domain and the mesh resolution were selected such that the solutions are independent of both the domain and mesh size.

Base case winter and summer conditions are applied in the numerical modelling at this stage. As it was described in Section 8.1.5 for the winter conditions, the soil and ambient temperatures are 283 K and soil has the high moisture content and the thermal rating is 940 A. The summer conditions are characterised by the average soil moisture and the soil and ambient temperatures of 288 and 298 K, respectively.
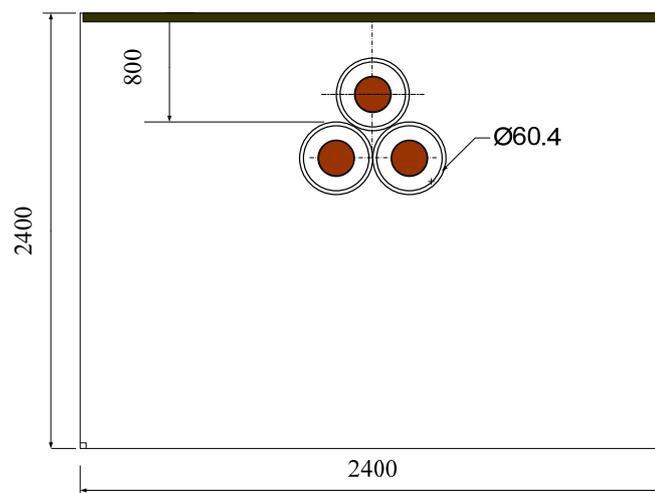
Fig. 8.14 The computational domain with cables buried in the trefoil formation

8.3.2 Discussion of numerical results: three single cables buried in trefoil formation (operation in base case winter and summer conditions)

Fig. 8.15 presents results of the temperature distribution around the cables for the base case winter conditions when the transferred current is 940 A and the soil has

high moisture content. As expected, the temperature distribution is symmetrical with the reference to the vertical plane passing through the axis of the top cable. The maximum temperature of about 352 K occurs in the top conductor and it sharply reduces in the soil with the increase of the distance from cables.

In the case when the applied current corresponds to 50 % of the recommended rating, which is 470 A, the temperature distribution is similar in character to that in Fig. 8.15, with a maximum temperature of 301.5 K occurring in the top cable.
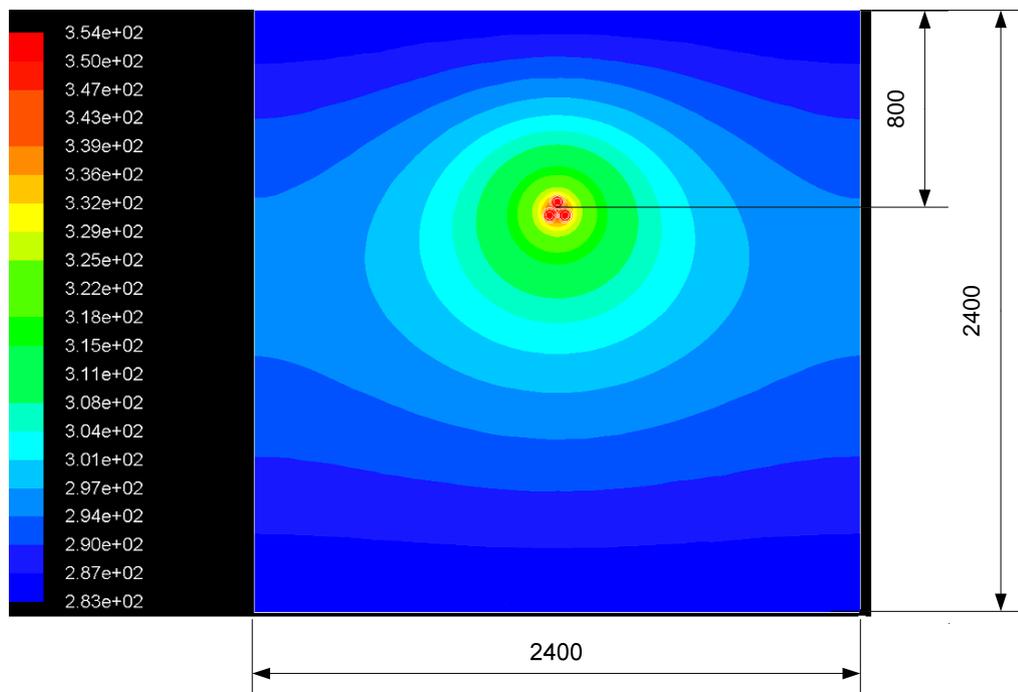
Fig. 8.15 The temperature distribution around the cables for the base case winter conditions with the transferred current of 940 A and the high moisture content of soil

Table 8.7 shows the results of the temperature of the top cable in the trefoil formation for base case summer and winter conditions. Increasing the current from 470 to 940 A in winter conditions results in a rise of the average temperature of the

conductor from about 301 to about 352 K. For the base case summer conditions this rise in the temperature of the conductor is from about 318 to 382 K. It can also be seen from Table 8.7 that the temperatures of the conductor working at the base case summer conditions are about 30 and 16 K higher for the currents of 940 and 470 A, respectively, compared to winter conditions.

Table 8.7 The temperature of the top cable in the trefoil formation

Base case conditions	Current, A	Soil temperature, K	Ambient temperature, K	Moisture content	Temperature of the top conductor, K
Winter	470	283	283	High	301.5
Summer	470	288	298	Average	317.6
Winter	940	283	283	High	352
Summer	940	288	298	Average	381.6

8.3.3 Discussion of numerical results: three single cables buried in trefoil formation (operation in summer conditions in accordance with BS 6622)

Several cases were considered based on the BS 6622 [68] recommendation of the sustained rating of 850 A for summer conditions for the trefoil arrangements.

The heat source inside the conductors with a current of 850 A associated with Joule losses was calculated to be equal to 46,446 W/m^3.

Figure 8.16 presents the temperature distribution around cables in the trefoil formation when the current is 850 A. The maximum temperature of 366 K is reached

in the top cable and this is higher than the allowed maximum temperature of the conductor by approximately 3 K.
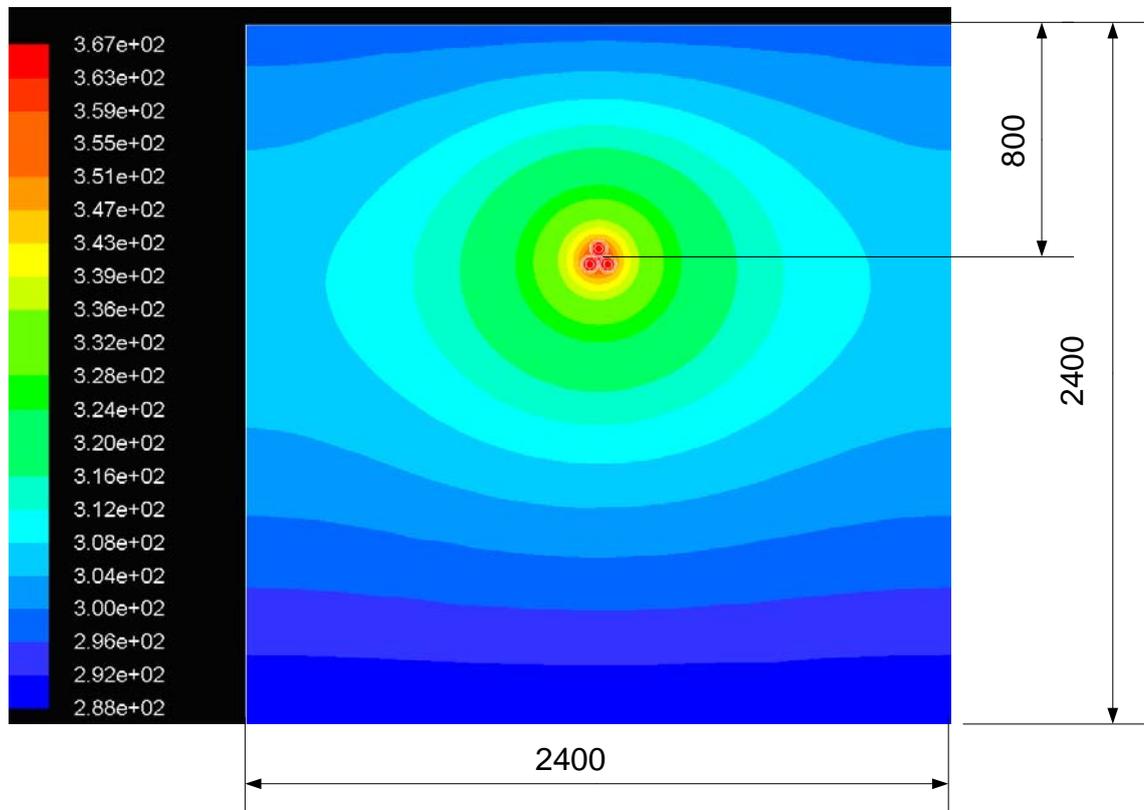
Fig. 8.16 The temperature distribution around the conductors for summer conditions with the transferred current of 850 A and the average moisture content of the soil

Figure 8.17 shows the average temperature profile in the horizontal plane passing through the computational domain at the depth of 0.8 m. It can be seen that that the temperature of the soil reduces rapidly with the increase of the distance from the cables.

Position (with respect to the top cable), mm
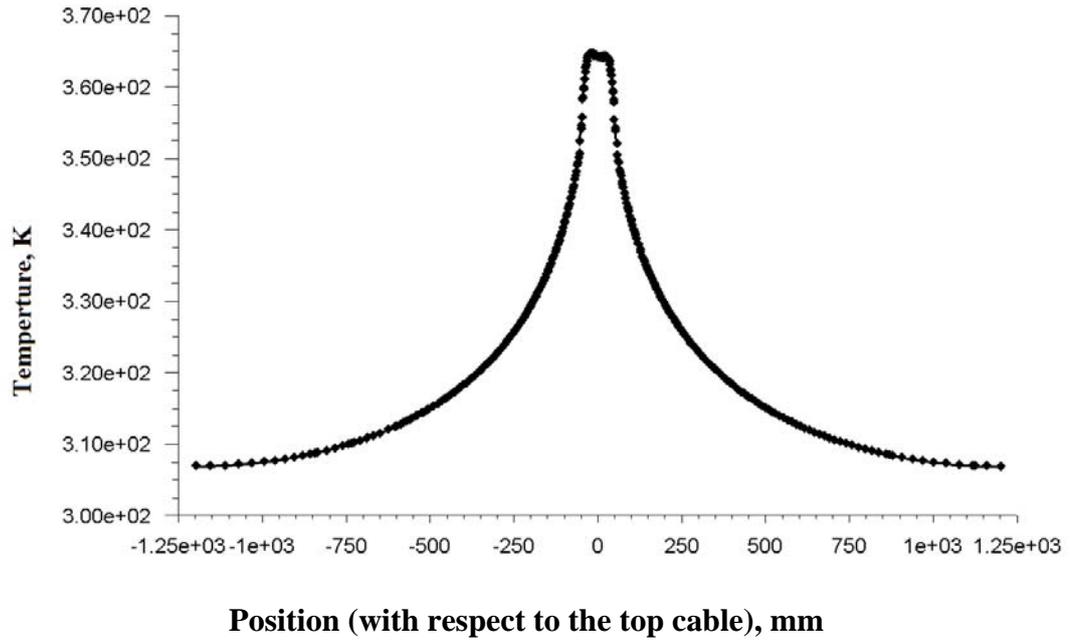
Fig. 8.17 The average temperature profile in the horizontal plane passing through the computational domain at the depth of 0.8 m

More details of the temperature distribution in the walls of the conductors, insulations and oversheaths for the case of the cables in trefoil formation with the 850 A current in each cable for summer conditions and the average moist content soil is provided in Fig. 8.18. It can be seen that the highest temperature of 366 K exists in the top cable with the lowest temperature being about 348 K on the external surface of its oversheath. The temperature is rapidly reduced along the thickness of the insulation and oversheath.

In the case when a current of 425 A in each cable is considered for summer conditions, then the value of the heat source in the copper conductors is 11,611.6 W/m^3. For such case similar results were obtained of the temperature distribution in the computational domain, including the temperature in the conductors, in their insulation and oversheath.

196

Position (with respect to the axis of the top cable), mm
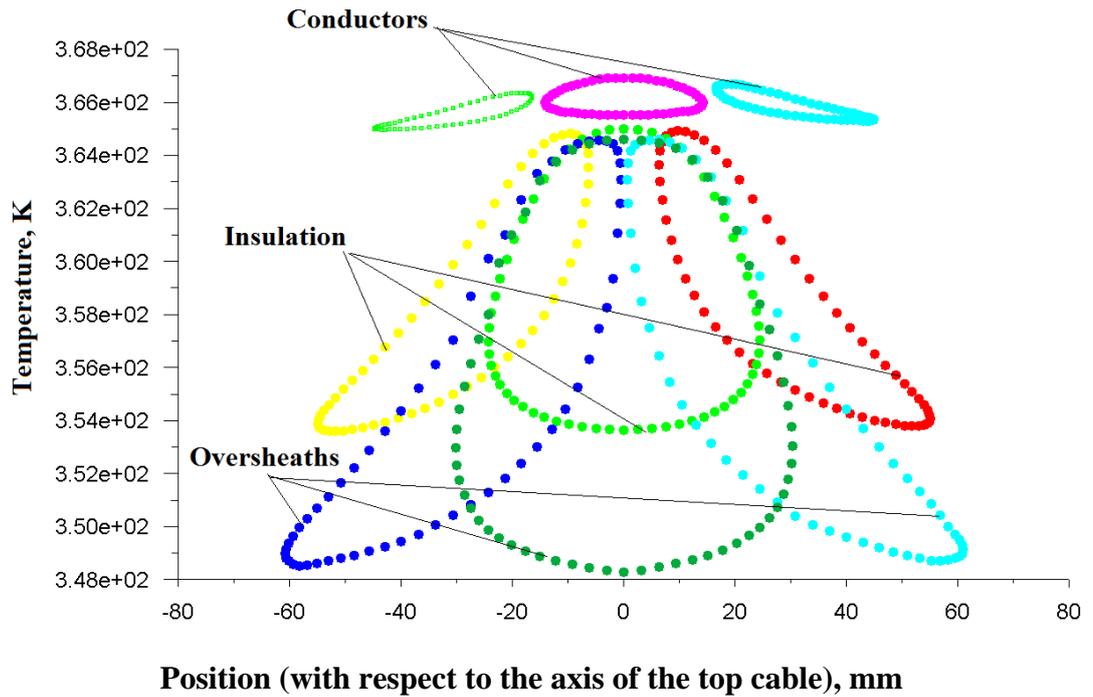
Fig. 8.18 The temperature distributions in all walls of conductors, insulations and oversheaths

The Tables 8.8 and 8.9 present the results of the average temperature of the conductors for the cases when the current is 850 and 425 A.

Table 8.8 The average temperature of the conductors in the trefoil formation for summer conditions

Current, A	Temperature of the conductor, K		
	Left cable	Top cable	Right cable
850A	365. 8	366	365. 8
425A	313.2	313.7	313.2

Table 8.9 The average temperature of the components of the top cable in the trefoil formation for summer conditions

Current, A	Temperature of the components of the top cable, K		
	Conductor	Insulation	Oversheath
850	366	358.2	354.8
425	313.7	311.5	310.6

The results demonstrate that for the three cables in a trefoil formation in the case when there is the full load in all cables the numerical simulations predict the temperature level in the top cable to be about 366 K, which 3 degrees higher than the allowed temperature level (363 K) in accordance with the BS 6622 – 1991 standard. There is approximately an eight degrees temperature difference between the conductor and the insulation and an eleven degrees temperature difference between the conductor and the oversheath of the top cable. These differences in temperatures depend on the value of the transferred current, the ambient and soil temperature and its moisture content.

8.5 Discussion of numerical results: three single cables buried in trefoil formation (operation in winter conditions in accordance with ENA P17)

In accordance with ENA P17 recommendations the steady-state rating of 992 A and high moisture soil content are applied with winter conditions ambient and soil temperatures for the trefoil arrangement.

The heat source in each conductor is 63261.3 W/m^3 based on 992 A of the transferred current. Fig. 8.19 presents the temperature distribution in and around the cables in the trefoil formation for the case in which each cable has 100% load. The maximum temperature occurs in the top cable and is 359.6 K, which is lower than

the allowed maximum temperature of the cable by approximately 3 K. As in the previous cases with the trefoil formation there is symmetry in the temperature distribution with reference to the vertical plane passing through the axis of the top cable. The temperature in the soil reduces rapidly with the increase of the distance from the cables.
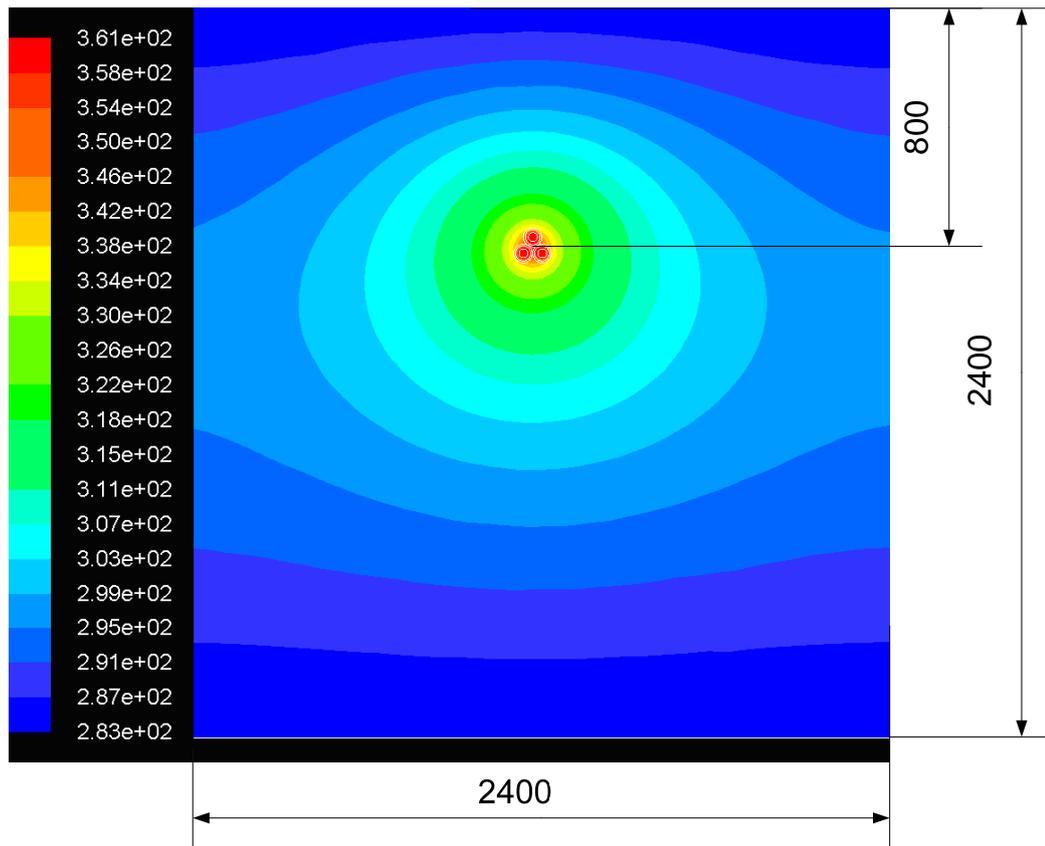
Fig. 8.19 The temperature distribution in the computational domain for the trefoil formation of the cables for the case in which the current is 992 A and there is high moisture content in the soil (winter conditions)

Fig. 8.20 presents details of the temperature distribution in the conductors, insulation and oversheaths. It can be seen that the highest temperature of about 360 K exists in the top cable with the lowest temperature being about 345 K on the external surface of its oversheath. The temperature is rapidly reduced along the thickness of the insulation and oversheath.
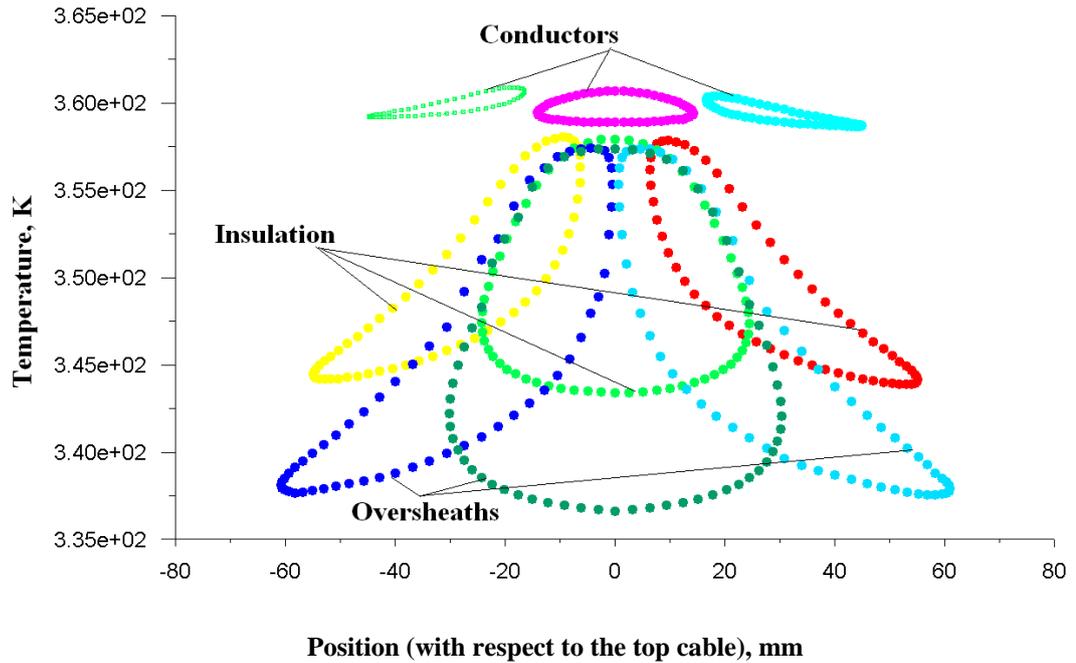
Fig. 8.20 The temperature distribution in the walls of conductors, insulations and oversheaths

When the case of 50% of load was modelled then the value of the heat source in the copper conductors is 15815.31 W/m^3. The temperature distribution in the conductors, insulation, oversheaths and the soil have the same trend in variation as in the case of 100% load, but the maximum temperature of the top conductor only reaches 303.2 K.

The results obtained for the above cases with 100 and 50 % load in the cables are summarised in Tables 8.10 and 8.11. These CFD results indicate that in winter conditions the maximum temperature of about 360 K, which occurs in the top cable, is within the limits for the safe operation of the cables.

Table 8.10 The average temperature of the cables in trefoil formation for winter conditions

Rating, A	Temperature of the conductor, K		
	Left cable	Top cable	Right cable
992	359.3	359.6	359.3
496	302.6	303.2	302.6

Table 8.11 The average temperature of the top cable in trefoil formation for winter conditions

Rating, A	Temperature of the components of the top cable, K		
	Conductor	Insulation	Oversheath
992	359.6	349	344.6
496	303.2	300.3	299.1

8.6 Comparison of the results for the single cable and the cables in the flat and trefoil formation

Summary of the results on the temperature of cables directly buried in the soil and operating for different conditions is presented in Table 8.12. The base case with the same current of 940 A in winter and summer conditions was considered theoretically for all cable configurations for comparison purpose only. It can be seen in Fig. 8.21 that the highest temperature of 381 K would have been achieved at the top cable in the trefoil formation and this is because of the heat generation within a small area where the cables are located. The effect of the mutual heating is considerably less in the case of the single cable or of the plane formation. The temperature difference

between the cables in the flat and trefoil formations depends on the magnitude of the transferred current and it is greater as the current increases; for example in the case of winter conditions the difference is 2.45 K when the transferred current is 470 A and it is 8.81 K for 940 A, where as in the case of summer conditions the maximum conductor temperature difference is 3.32 K and 11.12 K for 470 A and 940 A, respectively.

Table 8.12 Results of CFD modelling on maximum cable temperature

Conditions	Current, A	Temperature of the conductor, K		
		Single cable	Middle cable in the flat formation	Top cable in the trefoil formation
Base case winter	470	293.43	299.05	301.5
Base case summer	470	304.95	314.28	317.6
Base case winter	940	317.77	343.19	352
Base case summer	940	334.74	370.48	381.6
BS6622– 1991: summer	952	-	372	-
BS6622– 1991: Summer	850	-	-	366
ENA-P17: winter	992	-	-	359.6
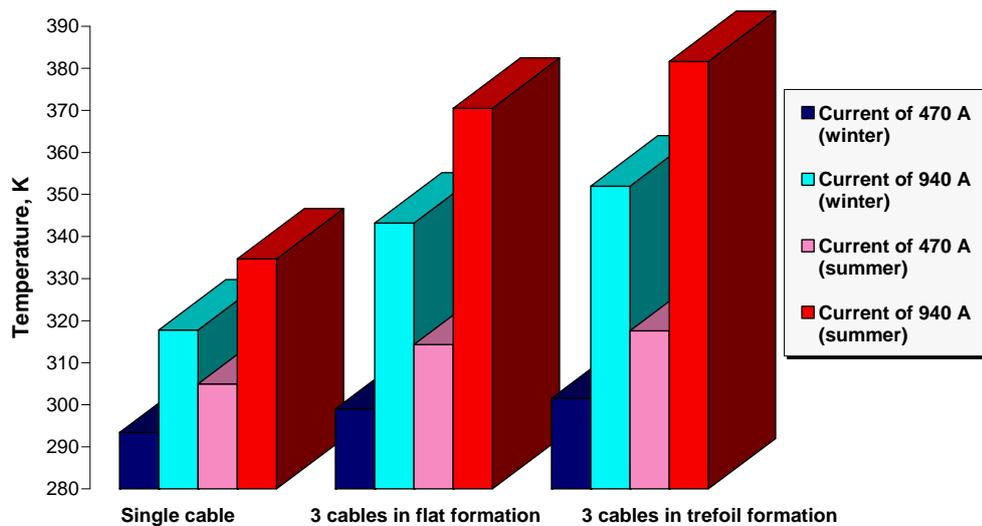
Fig. 8.21 The maximum cable temperature in the conductor in various formations for winter and summer conditions of 470 and 940 A current

In real practice when the current ratings are applied as recommended by BS6622–1991 then CFD results indicate that the temperature of the middle cable in the flat formation reaches 372 K, which is 9 degrees above (2.5 %) the safe limit of 363 K. In the case of the trefoil formation CFD results show that the highest temperature of 366 K which occurs in the top cable is 3 degrees greater than the limit allowed for a safe operation. Such a small excess in the temperature limit will not really affect the safety of the operation of the cables but these results indicate that there is no scope for increasing the ampacity of the cables in flat and trefoil formations.

8.7 The effect of the wind above the surface on the thermal state of the group of underground cables directly buried in soil

Williams et al. [70] proposed a thermodynamic model to estimate the ambient soil temperature at a certain location using meteorological data from several sites around the UK. They investigated the proximity of the meteorological station required to

make an accurate prediction. The lumped parameter model which was developed can be employed to calculate the soil temperature for a given cable depth. In their paper the soil domain was represented as a number of horizontal elements. The main conclusion drawn in this work is as follows: "It has been shown through experimentation with this model that the dominant effect on the estimate of temperature of an underground cable is the air temperature, and that wind speed and solar radiation do not affect the cable temperature greatly."

Swaffield [51] also described several models employed for the calculation of comparative continuous ratings of a directly buried 400 kV cable group. Ratings are obtained using three methods, including the standard "analytical approach (IEC 60287), a 1D finite difference (FD) and a 2D finite element analysis (FEA) approach. An equation for calculation of a resultant heat-flux has been derived to more precisely model the dielectric loss in 2D and 3D FEA models. Comparison of results shows that all the above models are in a good agreement when applying an isothermal ground surface condition. The FEA model developed has been used to investigate "ground surface boundary conditions" and the effect of the wind with the speed of 1 m/s and 10 on the current rating. Results obtained show that at a typical buried depth of 800 mm, the cable rating is slightly lower for the wind speed of 1 m/s and it would be equal to the rating at the 10 m/s wind speed if the buried depth of the cables increases to 900 mm. These results indicate the influence of the wind above the ground on the thermal state of the cables directly buried in the soil.

Overall, there are contradicting statements made by different researchers on the influence of the wind on the temperature of the underground cables.

In this section the effect of the wind on the thermal state of underground cables was investigated using a steady state 2-D CFD model. The airflow was considered in a rectangular domain above the surface of the ground section with the directly buried three underground cables in the flat formation, see Fig. 8.22. As in the previous cases, the dimensions of the domain and the mesh resolution were selected in such the way that the solutions are independent of both the domain and mesh size.
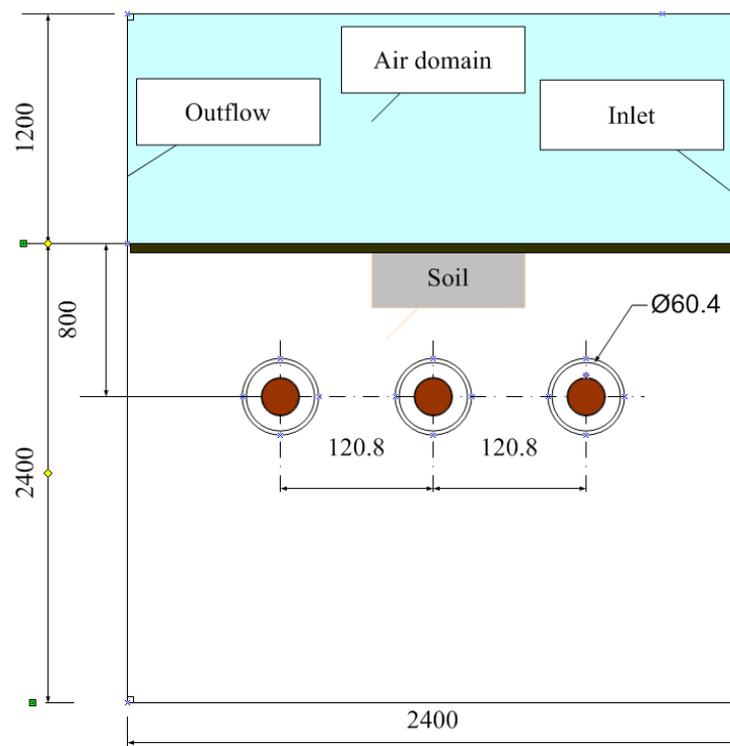
Fig. 8.22 Computational domain used in modelling of the wind effect on the temperature of the cables in the flat formation

When modelling the effect of the wind speed on the thermal state of the underground cables the determination of a range in which the wind velocity varies is of paramount importance. Several projects were dedicated to this task, which resulted in a number of publications in the relevant area. Thus a CFD simulation, coupled with radiation and conduction analysis, was carried out to study the dispersion of air

pollutants during the winter in a built-up area in Kawasaki city, Japan [71]. The authors concluded from analysis of the experimental data that "the average wind velocity in an area of high-density of building is very low". Experimental data on the distribution of the wind velocity above the surface also was published in [72]. In this work monitoring of the peat erosion due to the wind was carried out "at Moss Flats (NY 757 317), the Moor House National Nature Reserve in the North Pennines on a 3 hectares area of relatively flat, sparsely vegetated, peat. The site is at an altitude of 615 m. The climate is 'Upland Maritime', being characterised by cool, cloudy and wet conditions, reflecting the relatively high altitude and proximity to the sea" [72]. An automatic weather station (AWS) was used onsite to measure the wind velocity at four heights (0.3, 0.72, 1.25 and 2.34 m) above the ground, the wind direction, the rainfall, the soil moisture and the soil temperature. The averaged values of the wind velocity (across the above heights) are presented in Table 8.13 [72] and it can be seen that this varies from 2.82 m/s in July to 7.13 m/s in February.

The information in Table 8.13 on the variation of the wind speed above the ground was used in the present numerical simulations to determine the range of the wind velocities to be investigated. The rating at 940 A is used for the numerical calculations in accordance with Industrial Recommendations P17for three single crosslinked polyethylene (XLPE) cables installed horizontally with a spacing between cable centres which is twice the overall cable diameter.

The computational domain deployed consists of two main sub-domains, namely soil and air, see Fig. 8.22. The side walls of the air domain are specified as the velocity inlet and outlet, respectively.

Table 8.13 Summary of monthly weather conditions at Moor House during 2000

Month	Total rainfall (mm)	Average wind speed (m s^{-1})	Minimum temperature (°C)	Maximum temperature (°C)
January	213	5.24	− 0.22	3.62
February	674.6	7.13	− 0.39	3.65
March	152.8	5.34	0.94	5.68
April	205.2	3.09	0.09	6.3
May	103.8	3.27	3.07	11.68
June	125.6	4.06	5.98	13.23
July	73.6	2.82	7.22	14.19
August	99.4	3.23	8.2	15.19
September	224.6	3.64	7.22	13.22
October	290	4.7	3.79	8.63
November	370.6	4.8	1.9	4.89
December	230.2	4.68	0.1	3.4

The ambient temperature and the soil temperature are taken equal to 283 K, according to Industrial Recommendations P17 [63]. Volumetric Joule losses in the cable induced by the electrical current of 940 A are 56,803 W/m^3. Additionally, the dielectric losses of 1,053 W/m^3 were taken into consideration. During simulations the energy conservation equation was solved only for the soil sub-domain containing the cables and the full set of governing equations was solved for the air-domain taking into account the cooling effect of the wind on the surface of ground.
 The numerical simulation was carried out for five cases with the wind speed equal to 0, 1, 4, 7 and 10 m/s and with the ambient temperature equal to 283 K.

The highest temperature occurs in the middle cable and this temperature was chosen as a basis for comparison of the different cases.

Fig. 8.23 shows results of the temperature distribution in soil and air sub-domains for the case when the wind speed is 4 m/s and the diagram demonstrates that the heat

produced in the cables is mainly dissipated in the body of the soil. Although there is only a negligible increase in the temperature of the air flowing over the ground surface the gradient of the temperature in the soil domain above the cables indicate that a noticeable amount of the heat generated in the cables is also dissipated by the air flow.

The numerical results of the temperature in the middle cable and its insulation are summarised in Table 8.14 for the considered range of the wind velocities. It can be seen that the maximum temperature of the conductor (345 K) is approximately 18 degrees lower than the maximum allowed temperature (363 K), and therefore there is scope for the transfer of additional power. In order to reach the maximum temperature of the conductor, namely 363 K, then a current of 1072 A should pass through each conductor. This exceeds the recommended rating by 132 A and results in an additional transfer of power of 7.5 MVA in the 33 kV network. It can also be seen in the table that for the given depth of underground cables, the ambient temperature and the electrical current, there is a noticeable cooling effect due to the airflow above the ground surface.

Thus when the velocity of the wind is between 4 and 7-10 m/s then the highest temperature in the core of the middle cable is reduced by approximately 3-4 degrees. The calculations show that the transfer of power can be increased by about 2.4% (1.27MVA) at the 4 m/s wind velocity and by 3.6% (1.94 MVA) at the 10 m/s wind velocity. It should be kept in mind that the above numerical results were obtained using the simplified calculation scheme which assumes that the magnitude
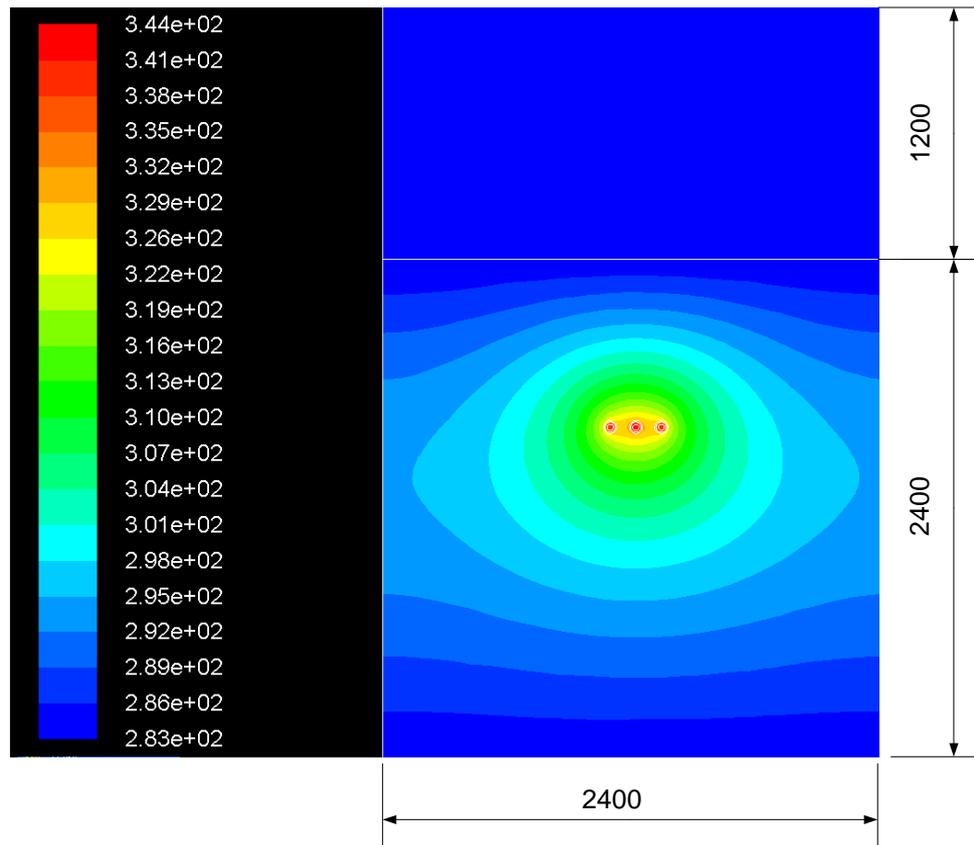
Fig. 8.23 Contours of temperature distribution around a group of underground cables, (K)

Table 8.14 The highest temperature in the middle cable and its insulation

Velocity, m/s	Temperature, K	
	Conductor	Insulation
0	345.2	335.6
1	344.8	335.2
4	342.4	333.2
7	340.9	331.9
10	340.9	331.9

of the wind in the vicinity of the ground surface is the same as in the main air-domain. In fact, the real variation of the air velocity profile in the area close to the ground surface should be considered in detail and this may significantly affect the numerical results of the temperature distribution in the air and soil sub-domains.

8.8   Effect of the moisture content on the temperature of the single cable directly buried in soil

CFD numerical investigations can be efficiently used for the simulation of complex cases with various geometries of a computational domain and boundary conditions. For single underground cables the maximum current density varies from 2.7 to 3.5 A/mm^2 for the copper conductors with PE insulation. For values of the current density equal to 3 and 3.5 A/mm^2, the rate of volumetric heat generation is equal to $q = 155,000$ and   211,463   W/m^3, respectively.   These two rates of heat generation were used in numerical simulations of the thermal state of the single underground cable. In the computational domain the cable is placed in the centre of the two-dimensional soil domain with 1,600 mm $\times$ 1,600 mm dimensions.

The first case considered was that in which the soil sub-domain surrounding the cable was split into three zones (the combined soil sub-domain), see Fig. 8.24.
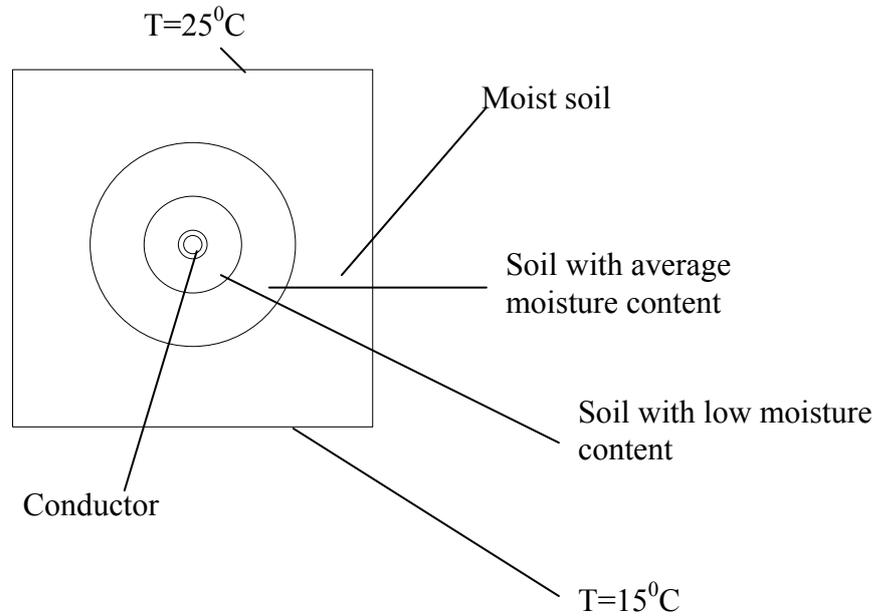
Fig. 8.24 A computational domain for the case with the combined soil domain

This case closely describes the real operational conditions at which the moisture of the soil gradually decreases in the vicinity of the cable due to the continuous heating process. Closest to the cable is the cylindrical zone with the diameter of 150 mm and the lowest moisture content; the next soil sub-domain has the diameter of 300 mm and contains the soil which has the average moisture content. Finally, the third zone covers the region between the second cylindrical zone and the rest of the soil sub-domain. In this last region the moisture content is the highest. It has been assumed in the calculations that the temperature at the top of the sub-domain is equal to that of ambient and it is 25 ^{0}C. At the bottom of the computational domain the temperature was set at 15 ^{0}C.

Additionally, three cases were simulated when the moisture content of the soil in all the sub-domains was assumed to be uniform and being low, medium and high, respectively.

Fig. 8.25a-8.25d show the distribution of the temperature in and around the single underground cable for the current density equal to 3 A/mm^2 and surrounded by the combined soil domain and by soil domains with low, average and high moisture contents, respectively. Fig. 8.25a shows that the maximum temperature in the core of the cable surrounded by the combined soil domain is 354 K (81°C) when the ambient temperature is 25°C. The temperature of the core rises with the increase of the ambient temperature and the temperature of the soil and with the decrease of the moisture content in the soil. Analysis of the obtained results presented in Fig.8.25b-Fig.8.25d demonstrate that the change in the moisture content results in a considerable rise in the cable temperature: from 333 K in the case of the high moisture content to 371 K, i.e. by 40 degrees, in the case of the low moisture content.

The temperature of the cable also increases with the rise of the current density, see Table 8.15, especially when the cable is placed in the soil with low moisture content. It can be seen as the current density increases from 3.0 to 3.5 A/mm^2 the conductor temperature rises from 371 K to 401K.
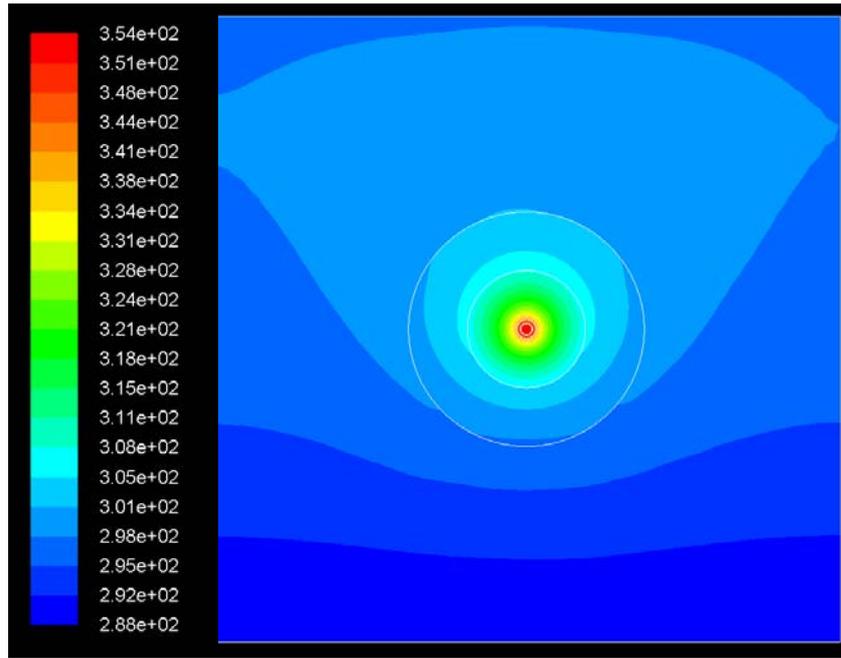
Fig. 8.25a The temperature (K) distribution in and around the underground cable surrounded by the combined soil domain
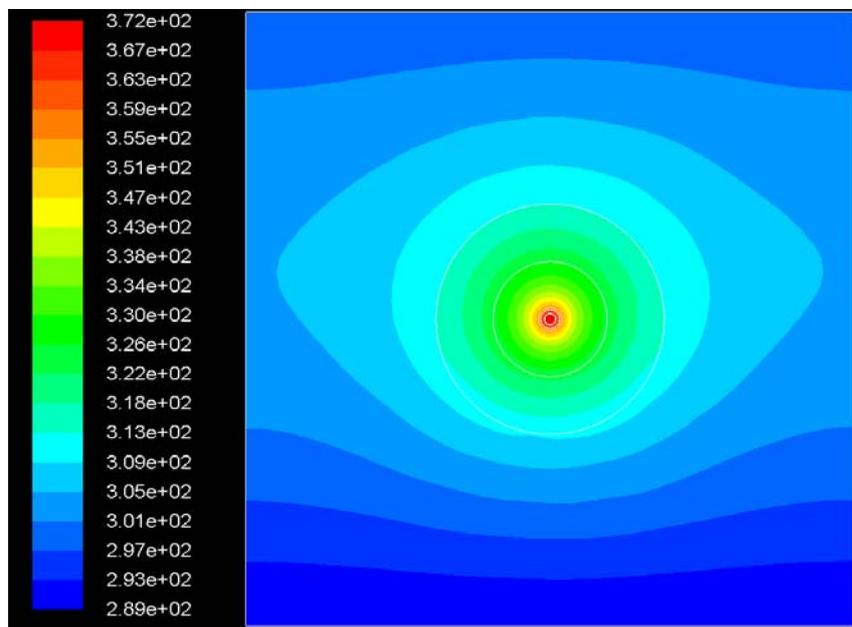
Fig. 8.25b The temperature (K) distribution in and around the underground cable surrounded by the soil domain with the low moisture content
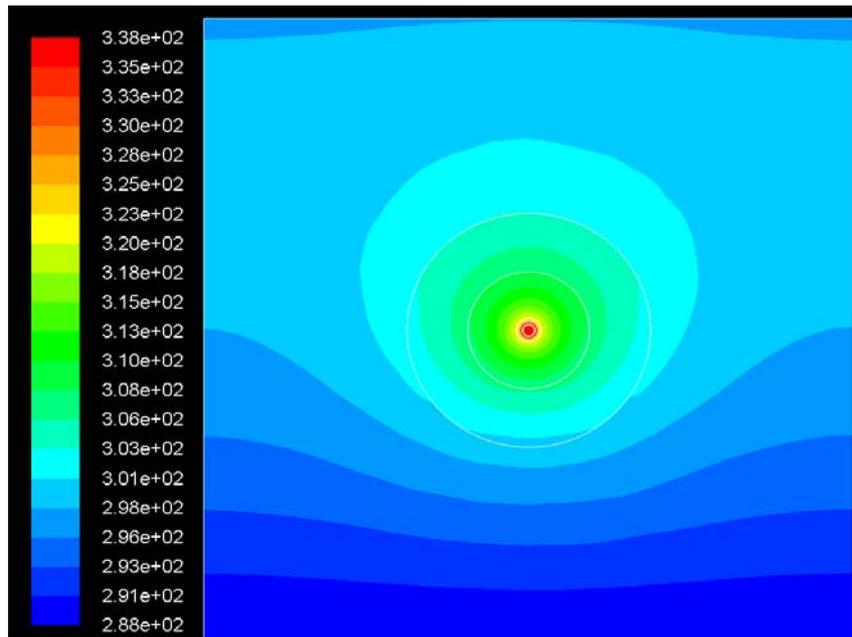
Fig. 8.25c The temperature (K) distribution in and around the underground cable surrounded by the soil domain with the average moisture content
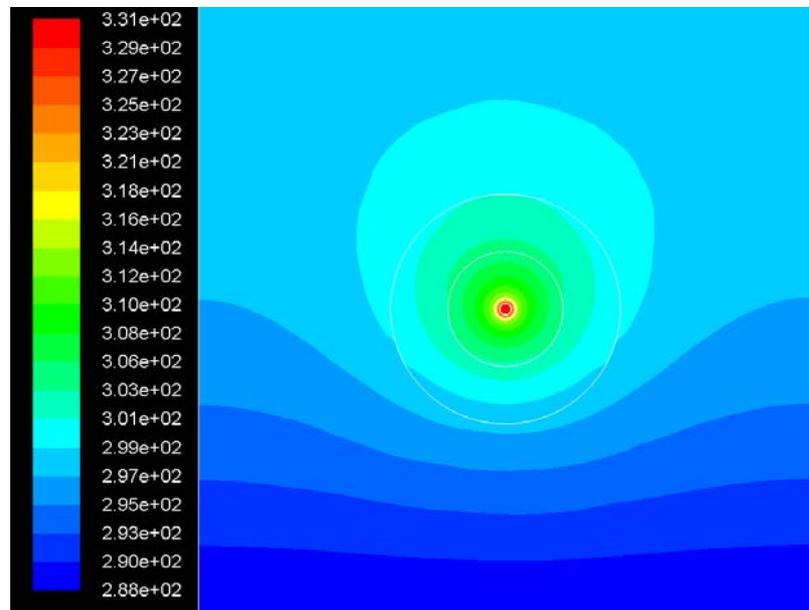
Fig. 8.25d The temperature (K) distribution in and around the underground cable surrounded by the soil domain with the high moisture content

Table 8.15 Temperature of the cable surrounded by different types of soil

Case	Moisture content	Temperature of the conductor, K	
		Current density = 3 A/mm^2	Current density = 3.5 A/mm^2
1	Combined	354	376
2	Low	371	401
3	Average	337.6	355
4	High	331	346

8.9 A single underground cable placed in a plastic pipe buried in soil

Figures 8.26-8.28 present results of the 2D numerical modelling of the thermal state of the cable placed at the bottom of a plastic pipe buried in the soil with the high moisture content. The plastic pipe has a diameter of 200 mm and the thickness of its wall is assumed to be 10 mm. The plastic pipe is place in the centre of the soil domain with 1,600×1,600 mm dimensions. The case considered is for winter conditions (the ambient and soil temperature is 288 K) and the current of 940 and 470 A. Due to its relatively low heat conduction coefficient the plastic pipe represents a significant thermal resistance for the cooling of the cable. The air circulation inside the plastic pipe due to free convection is typical for such a case. The dimensions of the domain and the deployed mesh provide solutions independent of these effects.

Fig. 8.26 shows that air is heated by the outer surface of the cable and flows upwards in the centre of the pipe and forms two symmetrical circulation loops along which air flows first upwards, and then downwards, transferring heat to the soil mainly through the upper part of the plastic pipe. This can also be observed in Fig. 8.27.

The temperature of the cable reaches the level of 392 K level (119 ^{0}C), considerably exceeding the thermal limit for its safe operation.
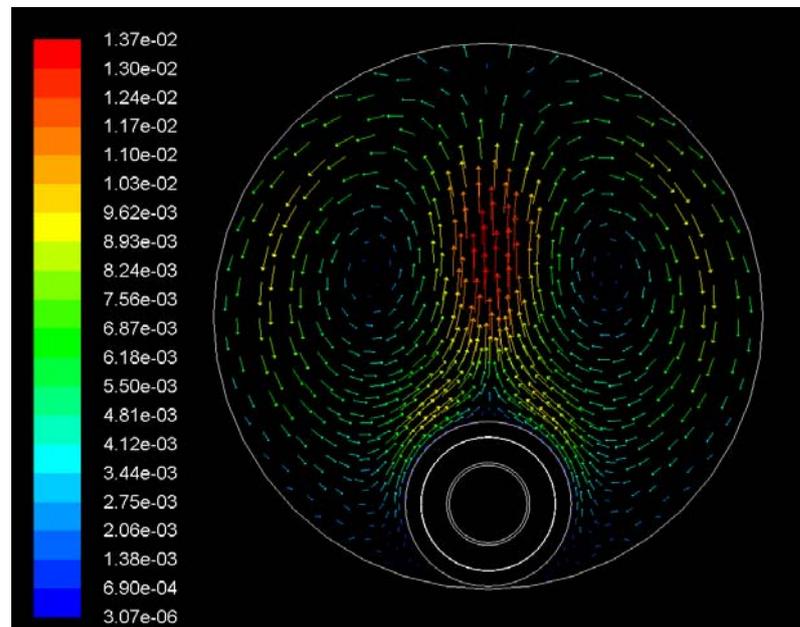
Fig. 8.26 Distribution of velocity vectors (m/s) around the cable placed in a plastic tube with the inner diameter of 200 mm and the wall thickness of 10 mm for the case when the current is 940 A
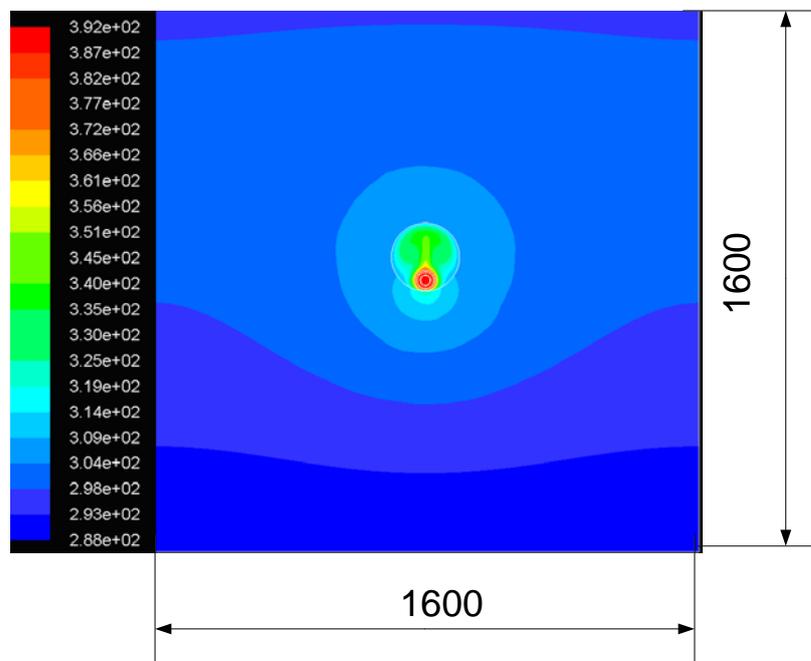
Fig. 8.27 The temperature distribution (K) around a tube with the inner diameter of 200 mm for the case when the current is 940 A

In order to avoid such a rise of temperatures dangerous for the integrity of the insulation of the cable, oil is usually used for cooling purposes. The above results are an illustration of the situation in which a full leakage of the cooling oil takes place.

When the current is 470 A the maximum temperature which is reached in the cable is 320 K, which is below the safety limit, see Fig. 8.28.
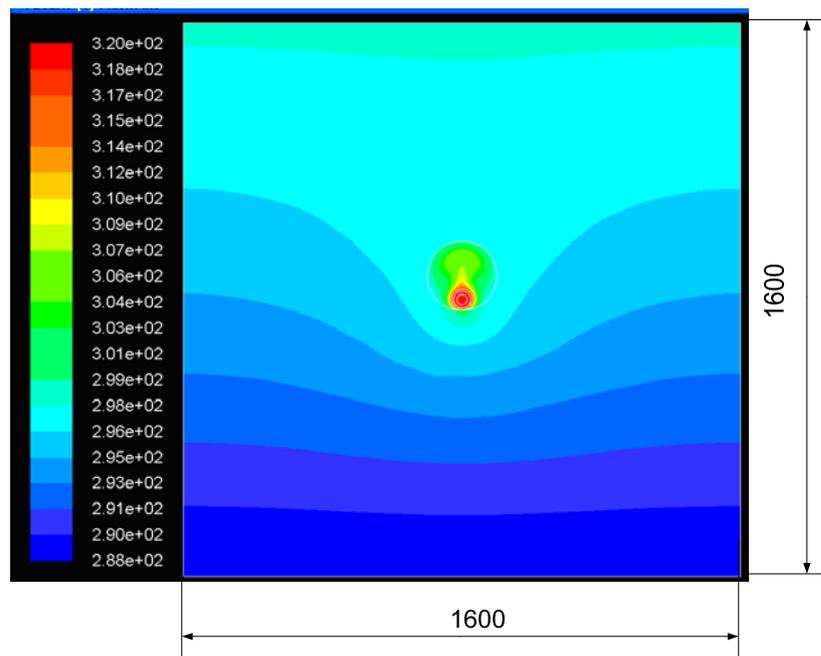
Fig. 8.28 The temperature distribution (K) around a tube with the inner diameter of 200 mm for the case when the current is 470 A

The above results demonstrate that CFD numerical modelling can be efficiently used for the simulation of complex cases with difficult geometries and boundary conditions. The CFD approach can also be used for the simulation of transient thermal states of the underground cables in cases with arbitrary changes of the power load curve.

8.10 Conclusions

The numerical investigations performed in this Chapter on the thermal state of underground cables allow one to make the following conclusions:

- The maximum temperature of a single cable directly buried in the ground is considerably less than that allowed (363 K) for safe operation, namely 335 K in summer conditions and 318 in winter conditions, and therefore there is a considerable scope for increasing its ampacity, especially in winter;

- The thermal state of the underground cables in the flat and trefoil formation operating in summer conditions is very close to the safety limits and there is no scope for increasing the ampacity of these cables.

- The maximum temperature of the conductor is about 343 and 360 K in the flat and trefoil formations, respectively, in winter conditions. Therefore there is a significant scope for the increasing ampacity of the cables in the flat formation.

- When the gradual decrease in the moisture content of the soil in the vicinity of the cable or cables due to continuous heating is taken into account then there is an increase of the temperature of the cables by about 10-15 degrees.

- Computational results show that the temperature of directly buried cables is reduced by the wind above the surface of the ground by 1-5 degrees for wind velocities in the range from 1 to 10 m/s, respectively.

- The temperature of the cable with the full electrical load placed in a plastic pipe buried in the soil will increase to the level (119 ^{o}C). This is dangerous to the integrity of insulation of the cable if it is exposed to air (the situation in which the cooling fluid is leaked from the plastic pipe).

CHAPTER 9

CFD MODELLING OF THE TRANSIENT THERMAL BEHAVIOR OF AN UNDERGROUND CABLE

Lumped parameter type models and methods for the calculation of transient behaviour, commonly used in DNO practice, were described in Chapter 3.

This chapter reports on the development of CFD modelling procedure for determination of transient temperature of underground cables using specific user-defined functions (UDFs) written in C++ language implemented in the commercial CFD code Fluent. These simulate the variation of the amplitude of the current in the conductors buried in different formations for winter and summer operational conditions. During CFD modelling the resistivity of the conductor material was assumed to be constant and its value corresponding to the maximum allowable temperature of 90ºC, namely 0.0405 Ω/km, was used in calculations.

Results were obtained for the variation of the temperature of the middle conductor in the flat formation in the transient process when the current instantaneously changes

from 0 to 470 A and from 0 to 940 A. These two transient processes were investigated for winter conditions and carried out with the deployment of the lumped parameter and CFD models.

9.1 Examples of calculation of the cable transient temperature in the flat formation configuration using Industrial Standards for an instantaneous increase of the current from 0 to 470 A and from 0 to 940 A

The winter conditions correspond to the following physical properties of the surrounding soil with a high moisture content: the soil density is 2100 kgm^{-3}, its specific heat is 2000 Jkg^{-1} ºC^{-1} and the soil thermal resistivity is 0.9 ºCmW^{-1}. The ambient temperature is 10ºC.

A cable with an overall radius of 30.2 mm and buried in the flat formation at the depth of 800 mm is considered. When the current in the cables is switched to 470 and to 940 A then the heat generated in the conductor $W_c = I^2 R$ is 8.95 and 35.8 Wm^{-1}, respectively.

The temperature rise on the surface of the middle cable is determined as

$$\theta = \frac{W_c \cdot g}{2 \cdot \pi} \cdot G(t),$$

where

$$G(t) = \ln \frac{r'}{r} + \frac{1}{2} \int_0^{y_1} \frac{1 - e^{-y_1}}{y_1} dy_1 - \frac{1}{2} \int_0^{y_2} \frac{1 - e^{-y_2}}{y_2} dy_2 .$$

Here

$$y_1 = \frac{r^2}{4\alpha t} \qquad \text{and} \qquad y_2 = \frac{r'^2}{4\alpha t}$$

The thermal diffusivity of the soil is defined as

$$\alpha = \left(\frac{1}{D \cdot C \cdot g}\right) = \frac{1}{2100 \cdot 2000 \cdot 0.9} = 0.246 \cdot 10^{-6} \ \text{m·s}^{-1}.$$

$$\frac{r'}{r} = \frac{2 \cdot 800}{30.2} = 52.98 \ \text{and therefore} \ \ \ln\frac{r'}{r} = 3.97$$

If $t = 3600 \ s$

$$y_1 = \frac{r^2}{4\alpha t} = \frac{0.0302^2}{4 \cdot 0.246 \cdot 10^{-6} \cdot 3600} = 0.2575$$

$$y_2 = \frac{r'^2}{4\alpha t} = 52.98 \cdot 0.2575 = 13.64$$

Applying an approximate formulae

$$\int_0^{y_1} \frac{1-e^{-y_1}}{y_1}dy_1 = y_1 - \frac{y_1^2}{4} = 0.2409$$

and

$$\int_0^{y_2} \frac{1-e^{-y_2}}{y_2}dy_2 = \gamma + \ln y_2 = 0.577216 + 2.613039 = 3.1903$$

Therefore after a one hour period of time has elapsed from switching on the load the

temperature rise on the surface of the conductor is:

for the instantaneous increase of the current from 0 to 470 A -

$$\theta'_{cab} = \frac{8.95 \cdot 0.9}{2\pi}\left[3.97 + \frac{0.2409}{2} - \frac{3.1903}{2}\right] = 3.2 \ ^\circ\text{C};$$

for the instantaneous increase of the current from 0 to 940 A -

$$\theta'_{cab} = \frac{35.8 \cdot 0.9}{2\pi}\left[3.97 + \frac{0.2409}{2} - \frac{3.1903}{2}\right] = 12.8 \ ^\circ\text{C}.$$

The actual temperature of the surface of the conductor is

$$\theta_{cab} = 10 + 3.2 = 13.2 \, ^\circ\text{C}$$

and $\quad \theta_{cab} = 10 + 12.8 = 22.8\,^\circ\mathrm{C}$

for the instantaneous increase of the current from 0 to 470 A and from 0 to 940 A, respectively. The results obtained are summarised in Table 9.1.

Table 9.1 The temperature of the middle cable in the flat formation in winter conditions after a one hour period of time has elapsed from switching on the load

Instantaneous current rise, A	Soil temperature, K	Moisture content	The temperature on the surface of the middle conductor, K
0-470	283	High	286.2
0-940	283	High	295.8

9.2 Comparison of CFD and lumped parameter modelling of the transient response in the thermal state of the cables in flat formation

2-D unsteady CFD simulations of the thermal state of the cables in the flat formation have been carried out in order to compare CFD and lumped parameter model results. The cases considered are the instantaneous increase of the current from 0 to 470 A and from 0 to 940 A. The period of time that has elapsed from the switching on the current in the cables is taken as 1,728,000 s (480 hours or 20 days). The results obtained are presented in Fig. 9.1.
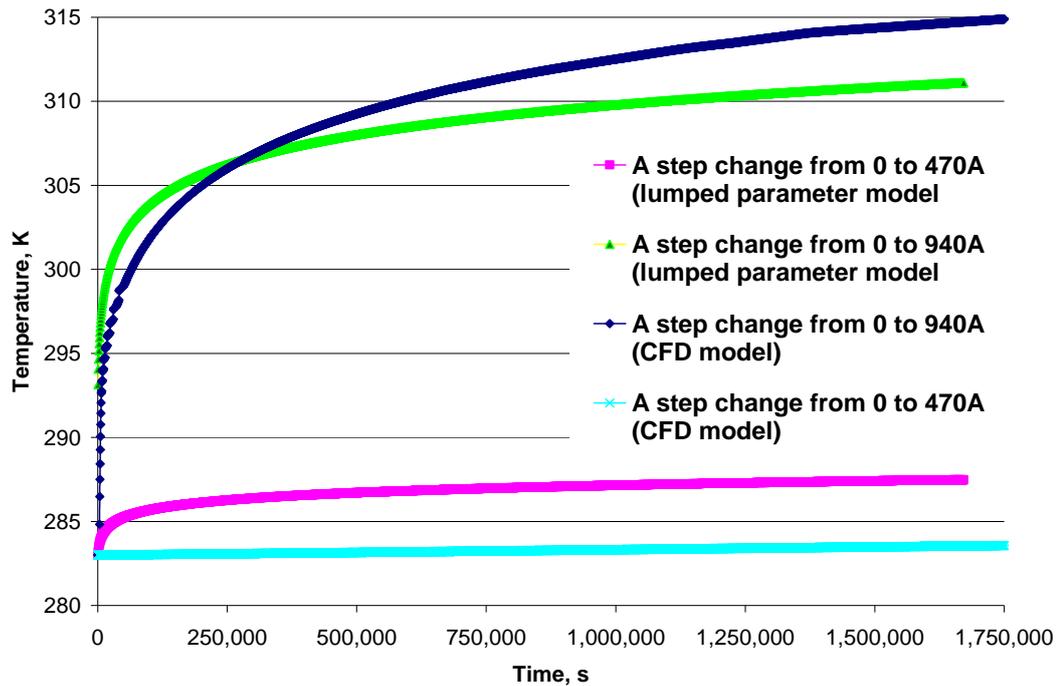
Fig. 9.1 Comparison of the temperature in the middle cable in the flat formation when the current is instantaneously increased, as predicted by lumped parameter and CFD models

It can be seen that in the first 70 hours (approximately 3 days), which corresponds to 252 000 s, the rate of the increases of the temperature in the middle cable after the current was instantaneously switched on was the highest. However, the temperature of the middle cable, calculated using CFD and the lumped parameter model, did not achieve that corresponding to their steady states during the considered period of time. CFD results are close in their trend to those predicted by the lumped parameter model when the current instantaneously changes from 0 to 940 A although the time constant predicted by the lumped parameter model is 7.7 hours and this is approximately 5 times shorter than the value obtained using the CFD model. It should be noted that the temperature calculated using the lumped parameter model is on the surface of the conductor, whilst the CFD model produces the average temperature in the body of the conductor.

223

It can be seen that in the case of the instantaneous 0-940 A rise the difference in predictions of CFD and the lumped parameter models is very small in the first 3 days. However, then the CFD model predicts a higher rate of increase in the temperature of the conductor.

In the case when the current is instantaneously increased from 0 to 470 A the difference between CFD and the lumped parameter model results are more significant, see Figure 9.1. Although the absolute difference in the predicted temperatures is 5-7 K during computational period, the CFD results demonstrate that the temperature rise in the middle cable has a linear tendency. Generally, at the current of 470 A the heat generated in the body of the conductor is relatively small and this heat is dissipated relatively rapidly due to the conductivity of soil.

9.3 CFD modelling of the transient state of UGC for the case when the current instantaneously rises from 470 A to 940 A

The temperature rise in the copper conductor with the highest temperature in the group, namely the middle cable in the flat formation and the top cable in the trefoil formation, was modelled using the CFD model for the case of instantaneous rise in the current from 470 to 940 A in summer and winter conditions, see Table 9.2.

A UDF subroutine in FLUENT was implemented to simulate the transient thermal state of the cable in the case of an instantaneous rise in the current from 470 to 940A. The modelling consists of two parts. The first part lasts 2,880,000 s (800 h) in order to achieve the steady thermal state of the cable when the current is 470 A. At the instance when time $t = 2,880,000$ s the current is instantaneously raised to the

940 A level and simulations continue to monitor the change in the temperature of the conductor. The time step used in the unsteady modelling was equal to 360 s.

Table 9.2 Data for the numerical modelling of the transient state of UGC

	Summer	Winter
Ambient temperature, K	298	283
Soil temperature, K	288	283
Soil moisture content	Average	High

Fig. 9.2 shows the temperature rise in the middle cable operating in summer conditions when the current is instantaneously raised from 470 A to 940 A. Despite the considerable time allocated to the first part of the modelling process (800 h) the steady state temperature of the cable corresponding to the current of 470 A was not reached. It can be seen that at the instance of the modelling time corresponding to 800 h (0 days in Figure 9.2) the temperature of the cable is 301.6 K. The time constant of a transient process is the period of time during which 63 % of the full variation of the transient parameter takes place. The temperature of the conductor which should be achieved when 63% of the full temperature rise in the cable takes place is calculated as

$$T = 301.6 + 0.63 \cdot (354 - 301.6) = 334 \text{ K}$$

The corresponding time constant is 30.1 hours, see Fig. 9.3.
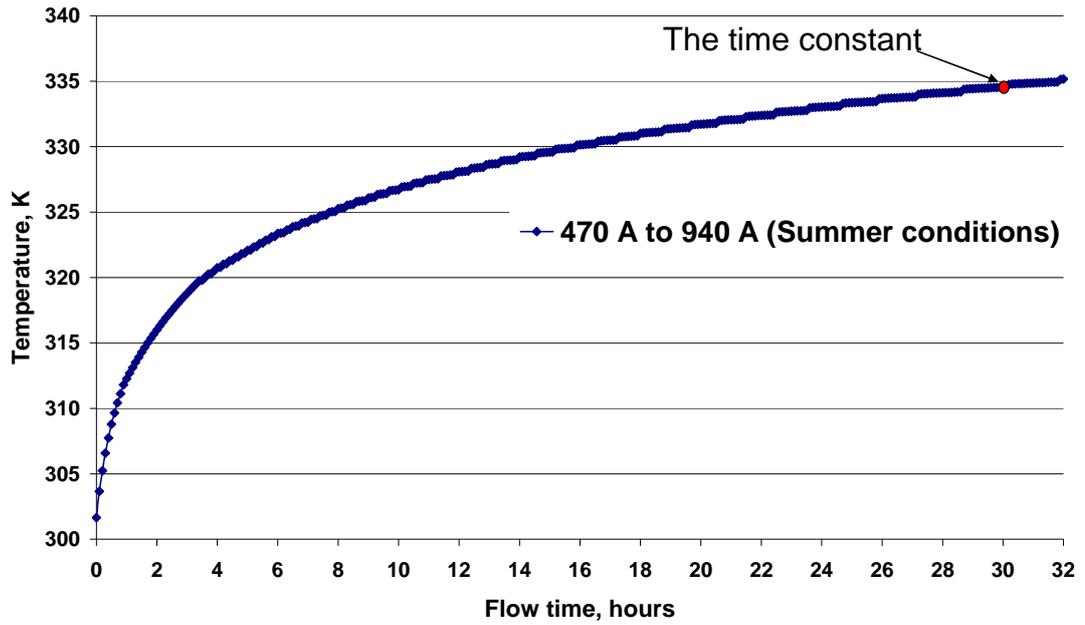
Fig. 9.2 The temperature rise in the cable in the flat formation operating in summer conditions when the current is instantaneously raised from 470 to 940 A
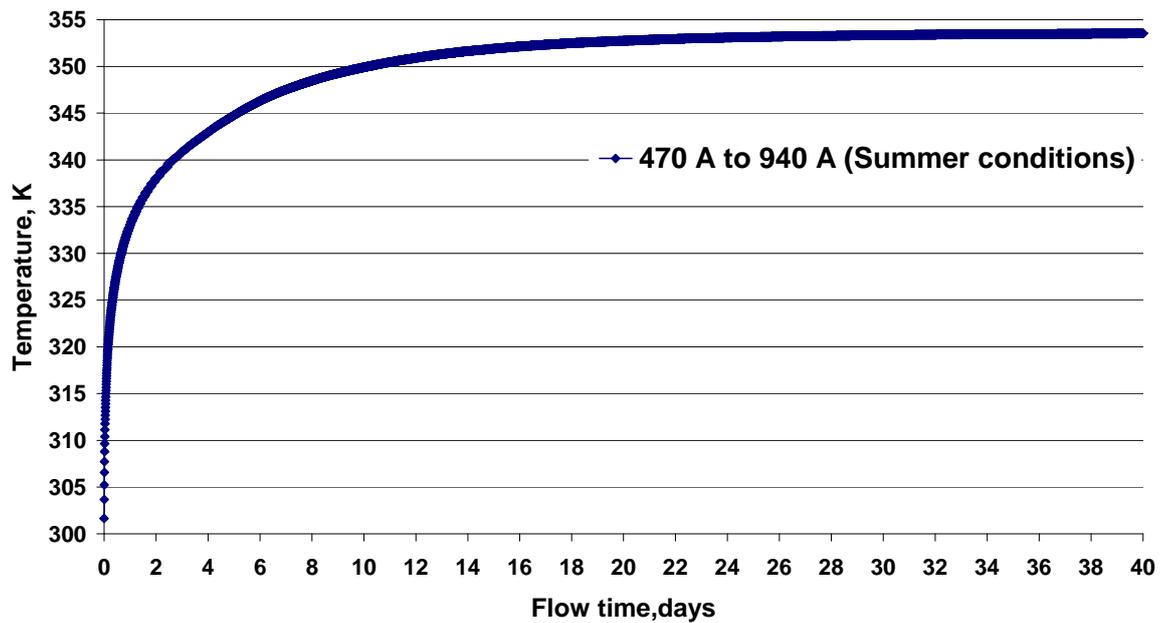
Fig. 9.3 The time constant for the temperature rise in the middle cable in the flat formation operating in summer conditions when the current is instantaneously raised from 470 to 940 A

Fig. 9.4 presents results of CFD modelling on the temperature rise in the middle cable operating in winter conditions when the current is instantaneously raised from 470 A to 940 A. It can be seen that that transient period lasts considerably longer and the calculated time constant for this transient process is 65.5 hours.
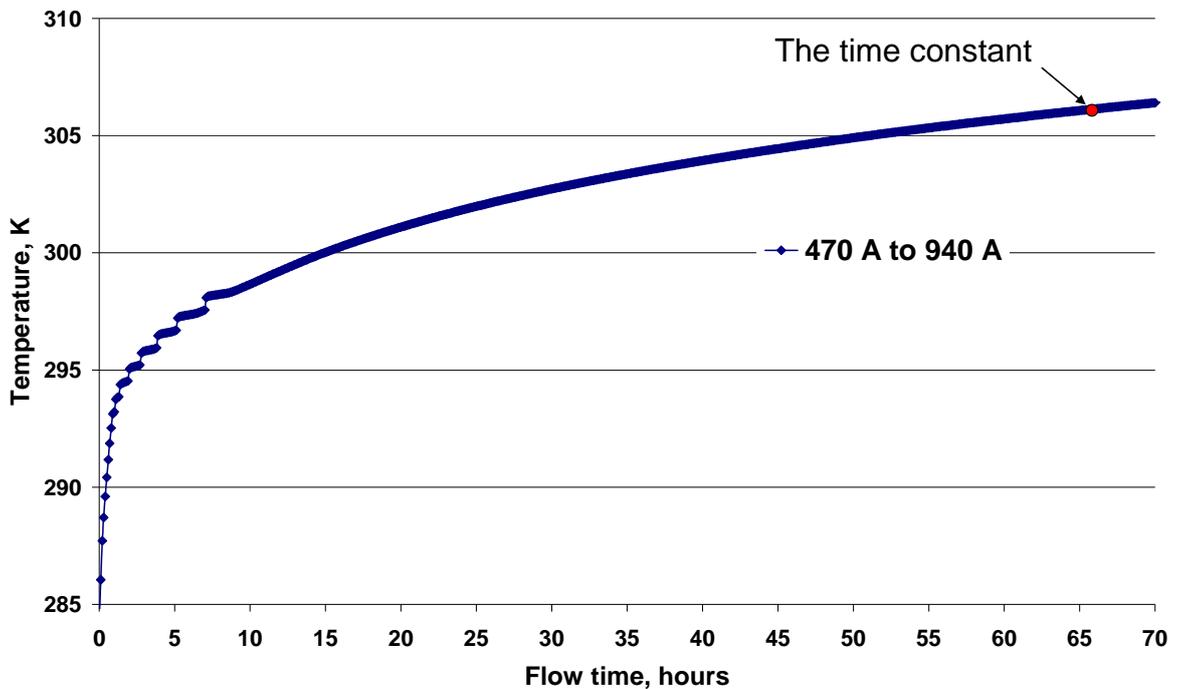
Fig. 9.4 The temperature rise in the cable in the flat formation operating in winter conditions when the current is instantaneously raised from 470 to 940 A

Similar results were obtained for the transient state of the cables in the trefoil formation operating in summer and winter conditions. The trend in the rise in temperature of the top cable is very close to those shown in Figures 9.3 and 9.4. However, the period of the transient processes in the thermal state of the cable in the trefoil formation is shorter compared to that in the flat formation. The corresponding time constant is 25.5 and 55 hours for summer and winter conditions, respectively. Table 9.3 summarises the findings regarding the temperature rise in the middle and top cable in the flat and trefoil in the summer and winter conditions.

Table 9.3 Temperature of the middle cable obtained by the numerical modelling when the transferred current instantaneously made a step change from 470 A to 940 A (load was increased by 100%)

Season	Summer		Winter	
Cable formation				
Steady sate temperature of the middle/top cable, K, at the current of 940 A	334	352	318.9	298.8
Time constant of the transient process when the current instantaneously changes from 470 to 940 A, h	30.1	25.5	65.5	55

9.4 Conclusions

In the case when the current changes from 0 to 940A, the CFD results are very close to the results predicted by the lumped parameter model. It should be stressed that the CFD model predicts the temperature of the cable and the results which were obtained by using the Industrial Standards approach predict the temperature on the surface of oversheath. In the case when the current changes from 0 to 470A, the CFD model predicts lower temperature values than those determined using the lumped parameters model.

Numerical modelling demonstrates that in the case of three directly buried cables when the current instantaneously changes from 470 A to 940 A, reaching the steady state temperature corresponding to the current of 940 A takes a considerable amount of time. This is due to the large thermal inertia of the soil surrounding cables. The corresponding time constant is 25.5 and 55 hours for summer and winter conditions,

respectively, when the cables are buried in the trefoil formation. For the flat

formation these numbers are 30.1 and 60.5 hours.

CHAPTER 10

CONCLUSIONS AND SUGGESTIONS FOR

FURTHER INVESTIGATIONS

10.1 Conclusions

The growth of renewable and distributed power generation results in significant increases in the power flow requirements placed not only on the transmission but also the distribution network. Distribution network operators (DNOs) face a number of challenges, not least those due to load growth, distributed generation growth and the problem of environmental opposition to building new infrastructure. An attribute of current distribution networks are their passive nature, which can be explained by historical reasons. Therefore, it has become very important to try to increase the utilisation of existing power system infrastructure in a safe and cost effective manner and one of the main means to achieve this is increasing power flow transmission through conductors so that they operate closer to their maximum ratings. At these high load conditions monitoring and predicting the thermal state of conductors in electrical distribution networks becomes of paramount importance for the safe operation of the network and the reliable supply of electricity to consumers.

The main objectives of this research have been to provide new insights into the thermal state of OHL and UGC operating under steady state and transient conditions

over a wide range of meteorological/environmental conditions. These conditions strongly affect operational conditions for components of the power distribution systems and determine their ampacity. For example, the cooling effect on components of the power systems at the high wind velocities of 12-16 m/s can be utilised by power system engineers considering the integration of wind power into power systems when wind turbines reach their rated capacity.

Existing calculation methods, which are mainly based on the lumped parameter type mathematical models, quite often may provide conservative ratings. More accurate methods for determining the thermal state of conductors could be employed by electrical network companies in their activities on the evaluation of existing operating methods and the quantification of the scope in ampacity that could be exploited.

Recent progress in the development of advanced numerical simulation methods of heat transfer processes could be an attractive alternative to lumped parameter models and experimental investigations, which are usually costly and time consuming. The sharp rise in computing efficiency, coupled with the reduced costs of CFD calculations, has advanced CFD as a powerful numerical tool for mathematical modelling various phenomena involving heat and mass transfer processes. However, so far this method has not been used extensively for studying the thermal state of OHL and UGC in electrical distribution networks.

Using a novel methodology based on the CFD assessments of the thermal state of the conductors could be a further course of action for DN operators.

In this study CFD modelling was implemented, not only for calculations of the thermal state of OHL and UGC in the steady state, but also in transient operational conditions. Thus, more specifically, 2-D and 3-D numerical modelling of the thermal state of Lynx overhead lines has been performed for a number of cases when they are exposed to cross and parallel wind conditions in the steady state and under transient conditions. During the simulations the conductors were assumed to be a combination of two coaxial cylinders. The internal cylinder was assumed to be made of steel and the external cylinder made of aluminium. In order to maintain the same cross sectional area of the conductor the diameter of the internal cylinder was correspondingly increased.

Simulations were performed for cases when there was no wind (free convection), and for a range of wind velocities by employing models for laminar and turbulent flows. Additionally, the heat losses from the conductor due to re-radiation were taken into account. The resistivity of the Lynx conductor was assumed to be temperature dependent. The obtained CFD results were compared to experimental data and to results obtained using the lumped parameter model. The analysis shows that even in such a simplified model CFD provides a good accuracy in the estimation of the thermal state for wind velocities greater than 1.5-2 m/s.

In order to validate the results a section of the SPEN distribution network has been selected for field trials. Electrical and thermal monitoring equipment has been installed and some data on the temperature of a Lynx conductor as a function of the transferred current and variable conditions, such as the ambient temperature, wind

velocity, its direction and insolation, which were probed every five minutes, were used for CFD modelling.

The results show that the CFD curve practically duplicates the shape of the experimental data curve with an average offset of 2 ºC. The reason that the CFD model underestimates the temperature of the conductor could be explained by the fact that the direction of the wind was not taken into account – the CFD model was run for the cross wind case.

Basic CFD models were also developed for the estimation of the thermal state of a single underground conductor and 3 conductors buried in the flat and trefoil formations for summer and winter conditions. The resistivities of the conductors were assumed to be constant and equal to the resistivity of copper conductors operating at their maximum allowable temperature. Since experimental data for the above cases was not available at this stage then the CFD model was calibrated against the existing lumped parameter model used in this industry. Information obtained from such simulations shows that the temperature levels strongly depend on the moisture content of the surrounding soil and the temperature distribution in the ground. The low content of the moisture in the soil and the high ambient temperature may result in a significant increase in the temperature of the conductors. The effect of the air flow above the ground on the temperature of the conductors was also studied. Additionally, a hypothetical case was considered when the conductor was placed in an underground plastic pipe and cooled down only by the free convection of air. For all cases it was possible to calculate the heat transfer coefficients on the surface of the conductors.

The results obtained in the investigations demonstrate that the CFD approach can be effectively used to numerically estimate the thermal state of the main components of electrical distribution networks operating in complex conditions.

The conducted numerical simulations allow one to draw the following conclusions.

OHL operating in steady-state conditions:

- Comparison of numerical results obtained by CFD modelling and lumped parameter models (which are deployed in industrial standards) for the case when the cross-wind velocity is 0.5 m/s, ambient temperature of 293 K and the current of 433 A shows that the latter overestimates the temperature of the conductor by approximately 18 degrees. This indicates that there is a scope for increasing the ampacity of the Lynx overhead conductor at such low wind velocities;

- The numerical results show that at a wind velocity of 15 m/s the electrical current in a Lynx overhead conductor can be increased from 433A to 1600A without exceeding the design temperature. This results in a 3.7 fold increase in transmittable power. The model also suggests that the theoretical maximum power transmitting capability of the Lynx conductor is increased by a factor 2.3 when the conductor experiences a parallel wind velocity of 15 m/s;

- Numerical results obtained demonstrate that the convective heat transfer from the surface of the conductor can be calculated using the following proposed correlations:

- $Nu=2.2555 \times Re^{0.3065}$ (for cross wind)

- $Nu=1.5035 \times Re^{0.3038}$ (for parallel wind);

- Numerical results show that taking into account the dependency of the heat conduction coefficient and heat capacity in the conductor material has a negligible effect in the estimation of its thermal state. Thus the obtained difference in the temperature of the conductor is less than 2 K at low wind conditions when the temperature of the conductor is approximately 325 K.

- The aging of the conductor leads to a gradual increase in its temperature. For example, the increase in the temperature of the Lynx conductor with a darkened surface, at typical average insolation of 800 W/m^2, is approximately 6 degrees.

UGC operating in steady-state conditions:

- The maximum temperature of a single conductor directly buried in the ground is considerably less than that allowed (363 K) for safe operation, namely 335 K in summer conditions and 318 in winter conditions and therefore there is a considerably scope for increasing its ampacity, especially in winter conditions;

- The thermal state of the underground conductors in the flat and trefoil formation operating in summer conditions is very close to their safety limits and there is no scope for increasing the ampacity of the conductors.

- The maximum temperature of the conductor is about 343 and 360 K in the flat and trefoil formations, respectively, in winter conditions. Therefore there is a significant scope for increasing the ampacity of the conductors in the flat formation.

- When the gradual decrease in the moisture content of soil in the vicinity of the conductor, or conductors, due to continuous heating is taken into account then there is an increase in the temperature of conductors of about 10-15 degrees.

- Computational results show that the temperature of directly buried conductors is reduced by the wind above the surface of the ground by 1-5 degrees for wind velocities in the range from 1 to 10 m/s, respectively. The calculations performed indicate that the transmitted power can be increased by approximately 2.4% (1.27MVA) and 3.6% (1.94 MVA) when the wind velocity is 4 and 10 m/s, respectively.

- When a conductor with its full electrical load is placed in a plastic pipe buried in soil the temperature will increase to the level (119 $^{\circ}$C), which is dangerous to the integrity of insulation of the conductor if it is exposed to air (the situation in which cooling fluid fully leaked from the plastic pipe).

OHL operating in transient conditions:

- CFD modelling results were obtained for transient responses when the current instantaneously increased from 433 A, which is a typical current rating for Lynx conductors, to 866 A. The results show that the temperature of the conductor increased by 56 degrees (from 308 K to 364 K) and the time constant was 29 minutes. Additionally, three intermediate cases, when final current was 25%, 50% and 75% greater than the initial current, were simulated. The time constant was found to be shortest when the current was increased by 100%.

- Four cases were modelled when the current instantaneously decreased by 25%, 50%, 75% and 100% from 866 A level. Again the fastest response, or shortest time constant, was in the case in which the current decreased by 100%. The time constant for this case was 21.5 minutes. The temperature of the conductor reduced by 56 degrees from 308 K to 364 K, when the current decreased from 866 A to 433 A.

- Numerical results demonstrate that with the decrease in the wind velocity from 15 to 10, 5, 2.5 and 0.5 m/s the temperature of the conductor gradually rises by 0.8, 2.6, 4.9 and 10.7K. Furthermore, it was calculated that the time constant in the transition from the steady thermal state of the Lynx conductor, corresponding to the wind velocity of 15 m/s, to a new thermal state corresponding to the wind velocity of 10, 5, 2.5, and 0.5 m/s is approximately 2.3, 5.4, 32 and 85 hours, respectively. It was found that the time constants are considerably increased for the cases when the wind velocity rapidly increases or decreases as compared with the cases when the current instantaneously changes. These are significant periods of time which could be exploited by network operating companies to assist them during unplanned network outages or unexpected demand surges.

- A 3-D model was used to simulate the transient response for parallel wind conditions when the current changed from 433 A to 866 A. Through comparisons between both cases (the transient response for the cross wind conditions and the parallel wind conditions) it was found that in the case of the parallel wind, the temperature in the conductor was 76 K higher and the

time constant was 12 minutes less than in the case for the cross wind. Such difference in temperature shows that the wind direction is a significant factor in determining the rating of an overhead line.

UGC operating in transient conditions:

- In the case when the current changes from 0 to 940A, the CFD results are very close to the results predicted by the lumped parameter model. It should be stressed that the CFD model predicts the temperature on the conductor and the results which were obtained by using the industrial standard approach predict the temperature on the surface of the oversheath. In the case when the current changes from 0 to 470A the CFD model predicts lower temperature values than those determined using the lumped parameters model.

- Numerical modelling demonstrates that in the case of three directly buried cables when the current instantaneously changes from 470 A to 940 A reaching the steady state temperature corresponding to the current of 940 A takes a considerable amount of time due to the large thermal inertia of the soil surrounding the cables. The corresponding time constant is 25.5 and 55 hours for summer and winter conditions, respectively, when the cables are buried in the trefoil formation. For the flat formation these numbers are 30.1 and 60.5 hours.

10.2 Suggestions for further work

Based on the experience gained during conducting this PhD study, the proposed further work could be divided into a series of tasks and these are as follows:

Task 1 – Integrating into CFD models more accurate data of UK seasonal variations in the environmental conditions

More accurate and detailed information on seasonal variations in climatic conditions in the UK is necessary as input data for the numerical modelling of the thermal behavior of components of power distribution networks throughout the year. Information on seasonal variations in the ambient temperature and its humidity, in the magnitude and the direction of the wind, solar radiation, in the temperature of soil and its moisture content, together with soil moisture migration, can be acquired from relevant organizations and open sources.

Task 2 - Advanced CFD modelling of the steady state of overhead lines taking into account the random wind direction and using a more sophisticated geometry of the conductor

The thermal state of a single conductor exposed not only to parallel and cross winds, but also to winds with intermediate angles between 0 and 90°, could be further investigated, taking into account the influence of solar radiation and re-radiation and using a more sophisticated geometry of the conductor. The thermal state of two conductors placed in a row and exposed to cross and parallel winds could be analysed to see the effect of blocking. Heat transfer correlations could be derived from CFD results and compared to available theoretical and experimental data.

Task 3 - Advanced CFD modelling of the response in the thermal state of overhead lines to the dynamic load with more detailed description in the variation of the load

The response in the thermal state of a single conductor or group of conductors exposed to cross and parallel winds to a dynamic load could be analysed in more detail. To perform such investigations the corresponding subroutine describing the variation in the load in more detail as a function of time should be written, compiled and linked to the main body of the Fluent code. The transient governing equations should then be solved using a time-marching procedure in the CFD code with a smaller value of the time-step. Heat transfer correlations could be derived from the CFD results and compared to available theoretical and experimental data.

Task 4 - Advanced CFD modelling of the thermal state of underground conductors using more accurate data on properties of soil

The thermal state of a single directly buried conductor, single conductor in buried troughs, pipes and ducts could be analysed with the use of more accurate data on the thermo-physical properties of the soil. Additionally, a number of directly buried cables in the flat and trefoil formation could be studied in order to derive corresponding heat transfer correlations. The results must be compared to available theoretical and experimental data.

Task 5 - Advanced CFD modelling of the response in the thermal state of underground conductors to a dynamic load with a more detailed description in the variation of the load

The response in the thermal state of underground cables in the above formations and configurations to a dynamic load should be analysed using more detailed information on the variation of the load. Heat transfer correlations from CFD results could be derived which must be compared to available theoretical and experimental data.

REFERENCES

[1] Ilic, M., Black, J.W. and Prica, M. 2007. Distributed electric power systems of the future: Institutional and technological drivers for near-optimal performance. *Electric Power Systems Research*, 77:1160–1177.

[2] Roberts, D.A. 2004. Network Management Systems for Active Distribution Networks – A Feasibility Study, SP Power Systems Ltd, Scottish Power Plc, report number: K/EL/00310/REP (2004).

[3] Belben, P. D. & Ziesler, C. D. 2002. Aeolian uprating: how wind farms can solve their own transmission problems, World Wind Energy Conference and Exhibition, Berlin.

[4] Ainslie, J.1988. Calculating the flow field in the wake of wind turbines. *J. Wind. Eng. & Ind. Aero,* 27:213-224.

[5] Yip, T., Chang, An., Lloyd, G., Aten, M. and Ferri, B. 2002. Dynamic line rating protection for wind farm connections. Magnetic Recording Conference Digest of the Asia-Pacific, 27-29 Aug. 2002, pp 1-5.

[6] McClean, L., Fox, Bryans, L., Colandairaj J. and O'Sullivan, B. 2008. Equipment and methodology for linking overhead line circuit rating to the output of nearby windfarms. The 43rd International Universities Power Engineering Conference, 1-4 September 2008, Padova, Italy.

[7] Strbac, G. 2007. Electric Power Systems Research on Dispersed Generation, *Electric Power Systems Research*, 77:1143-1147.

[8] Aggarwal R.K., Johns A.T., Jayasinghe J.A.S.B. and Su W. 2000. An Overview of the Condition Monitoring of Overhead Lines. *Electric Power Systems Research* **53**:15–22.

[9] Bernauer, C., Bohme, H., Grossmann, S., Hinrichsen, V., Markalous, S., Muhr, M., Strehl T. and Teminova, R. 2007. Temperature Measurement on Overhead Transmission Lines (OHTL), Utilizing Surface Acoustic Wave Sensors. C I R E D, The 19th International Conference on Electricity Distribution, 21-24 May 2007, Vienna.

[10] Douglass, D.A., Motlis Y. and Seppa, T.O. 2000. IEEE's Approach for Increasing Transmission Line Ratings in North America. CIGRE 2000: The 38th Session of the International Conference on Large High-Voltage Electric Systems (CIGRE), Aug. 27–Sept. 1, 2000, Paris.

[11] BS 7884:1997. Specification for copper and copper-cadmium stranded conductors for overhead electric traction and power transmission systems.

[12] EN Standard 50182:2001. Conductors for overhead lines - Round wire concentric lay stranded conductors.

[13] Azevedo, C. R. F. and Cescon, T. 2002. Failure analysis of aluminum cable steel reinforced (ACSR) conductor of the transmission line crossing the Paraná River. *Engineering Failure Analysis*, 9 (6): 645-664.

[14] BS EN 50326:2002. Conductors for overhead lines – Characteristics of greases.

[15] IEEE 738-1993. IEEE Standard for Calculating the Current-Temperature Relationship of Bare Overhead Conductors.

[16] CIGRE.1992. The Thermal Behaviour of Overhead Conductors, CIGRE WG 12, *ELECTRA* 144.

[17] P27 Engineering Recommendation. 1986. Current Rating Guide for High Voltage Overhead Lines Operating in the UK Distribution System.

[18] Schmidt, N.1997. Comparison between IEEE and CIGRE Ampacity Standards*", IEEE Transactions on Power Delivery* 14(4): 1555-1562.

[19] Alawar, A., Bosze, E.J. and Nutt, S.R. 2006. A hybrid numerical method to calculate the sag of composite conductors. *Electric Power Systems Research* 76:389–394.

[20] Fink, D.G. and Beaty, H.W. 1987. Standard Handbook for Electrical Engineers, 12th ed., New York, McGraw-Hill.

[21] Karabay, S. 2009. ACSS/TW aerial high-temperature bare conductors as a remedy for increasing transmission line capacity and determination of processing parameters for manufacturing. *Materials and Design* 30:816–825.

[22] Chen, S.L., Black, W.Z. and Fancher, M.L. 2003. High-Temperature Sag Model for Overhead Conductors, *IEEE Transactions on Power Delivery*, 18(1):183-188.

[23] Smolleck, H.A. and Sims, J.P. 1982. Guidelines for the Selection and Operation of Bare ACSR Conductors with Regard to Current-Carrying Capacity. *Electric Power Systems Research* 5:179–190.

[24] Morgan, V.T. 1982. The Thermal Rating of Overhead-Line Conductors. Part I. The Steady-State Thermal Model. *Electric Power Systems Research* 5(2):119-139.

[25] Black, W.Z., Collins, S.S. and Hall, J.F. 1988. Theoretical model for temperature gradients within bare overhead conductor, *IEEE Transactions on Power Delivery* 3(2):707-715.

[26] Morgan, V.T. 1983. The Thermal Rating of Overhead-Line Conductors. Part II. A Sensitive Analysis of the Parameters in the Steady–State Thermal Model. *Electric Power Systems Research* 6:287-300.

[27] Isozaki, M. and Iwama, N. 2002. Verification of forced convective cooling from conductors in breeze wind by wind tunnel testing. Transmission and Distribution Conference and Exhibition 2002: Asia Pacific, IEEE/PES, 6-10 October, Volume 3, pp. 1890-1894. DOI 10.1109/TD.

[28] Morgan, V.T. 1973. The heat transfer from bare stranded conductors by natural and forced convection in air. *International Journal of Heat and Mass Transfer*, 16(11):2023-2034.

[29] Lin, S.H. 1991. Current load in a high voltage power transmission line. *Electric Power Systems Research* 21(3):181-185.

[30] Lin, S.H. 1992. Heat Transfer in an Overhead Electrical Conductor. *International Journal of Heat and Mass Transfer* 35(4):795-801.

[31] Weedy, B.M. 1988. Dynamic Current Rating of Overhead Lines. *Electric Power Systems Research* 16:11–15.

[32] Ilgevicius, A. and Liess, H.D. 2003. Thermal Analysis of Electrical Wires by Finite Volume Method. *ISSN 1392 – 1215. Electronika ir electrotechnika* 4(46):87-91.

[33] Zdravkovich, M.M. 1990. Conceptual overview of laminar and turbulent flows past smooth and rough circular cylinders. *Journal of Wind Engineering and Industrial Aerodynamics*, 33:53-62.

[34] Wu, M.H., Wen, C.Y., Yen, R.H., Weng, M.C. and Wang, A.B. 2004. Experimental and numerical study of the separation angle for flow around a circular cylinder at low Reynolds number. *Journal of Fluid Mechanics,* 515:233-260

 [35] Pegram, J. B., Orton H. E., & Samm R. 1999. Worldwide Underground Distribution Cable Practices. *IEE Proceedings Paper* 0-7803-5515-6/99:62-67.

[36] Sellers, S.M. and Black, W. Z. 1996. Refinements to the Neher-McGrath Model for Calculating the Ampacity of Underground Cables. *IEEE Transactions on Power Delivery* 11:12-30.

[37] Kemelly, A. E. 1893. Current Capacity of Electrical Cables Submerged, Buried, or Suspended in Air. *Electric World,* 22:183, 201.

[38] Rosch, S.J. 1938. The Current-Carrying Capacity of Rubber-Insulated Conductors. *AIEE Transactions*, 57(3):155-167.

[39] Neher, J. H. and McGrath, M. H.1957. The calculation of the Temperature Rise and Load Capability of Cable Systems. *MEE Transactions*, 76(10):752-772.

[40] Buller, F. H. and Neher J. H. 1950. The Thermal Resistance between Cables and a Surrounding Pipe or Duct Wall. *AZEE Transactions,* 69(1):342-349.

[41] Cox, H. N., Holdup, H. W. And Skipper D. J. Nov.1975. Developments in UK cable-installation techniques to take account of environmental thermal resistivities, *Proc. IEEE*, 122: 1253-59.

[42] IEC 60287: 1994. Electric cables – Calculation of the current rating, Part 3: Sections on operating conditions, IEC- 60287-3-1:1995.

[43] Hartley, J.G. and Black W.Z. 1979. <u>Predicting thermal stability and transient response of soils adjacent to underground power cables.</u> *7th IEEE/PES Transmission and Distribution Conference and Exposition*, April 1-6: 316-320.

[44] Moya, R.E.S., Prata A.T. and Cunha Neto J. A.B. 1999. Experimental analysis of unsteady heat and moisture transfer around a heated cylinder buried into a porous medium. *International Journal of Heat and Mass Transfer* 42:2187-2198.

[45] Anders, G. J. and Brakelmann, H. 2004. Improvement in Cable Rating Calculations by Consideration of Dependence of Losses on Temperature, *IEEE Transactions on Power Delivery,* IEEE 0885-8977: 1-7.

[46] Lu, S., Ren, T., Gong, Y. and Horton, R. 2007. An Improved Model for Predicting Soil Thermal Conductivity from Water Content at Room Temperature. *SSSAJ*, 71(1): 8-14.

[47] Black, W. Z., Brown K. W. and Harshe B.L. 1999. Ampacity of cables in trays surrounded with fire barrier material. *IEEE Transactions on Power Delivery*, 14(1):8-17.

[48] Chaves, C.A., Camargo, J. R., Cardoso, S. and de Macedo, A.,G. 2005. Transient natural convection heat transfer by double diffusion from a heated cylinder buried in a saturated porous medium. *International Journal of Thermal Sciences* 44:720–725.

[49] Al-Saud, M.S., El-Kady, M.A., & Findlay, R.D. 2007. A new approach to underground cable performance assessment. *Electrical Power Systems Research*, DOI:10.1016/j.epsr.2007.06.010.

[50] Millar, R.J. and Lehtonen, M. 2005. Real-time transient temperature computation of power cables including moisture migration modelling. The 15th PSCC, Liege, 22-26 August 2005, 8 pages

[51] Swaffield, D. J., Lewin, P. L. and Sutton, S. J. 2008. Methods for rating directly buried high voltage cable circuits. ISSN 1751-8687. *IET Generation, Transmission & Distribution*, 2(3): 393-401.

[52] Fluent Inc., FLUENT 6.2 Documentation, 2005.

[53] Hatipoglu, F. and Avci, I. 2003. Flow around a partly buried cylinder in a steady current *Ocean Engineering* 30:239–249.

[54] Millar, R.J. and Lehtonen, M. 2006. A Robust Framework for Cable Rating and Temperature Monitoring. *IEEE Transactions on Power Delivery* 21:313-321.

[55] IEC 60287:2006. Electric cables - Calculation of the current rating.

[56] Shaw, C. T. 1992. Using Computational Fluid Dynamics, Prentice Hall.

[57] IEC 853-2:1989. Calculation of the cyclic and emergency current rating of cables.

[58] Van Wormer, F.C. 1955. An Improved Approximate Technique for Calculating Cable Temperature Transients. *Trans. Amer. Inst. Elect. Engrs*, 74 (3):277-280.

[59] Anders, G.J. 1998. Rating of Electric Power Cables - Ampacity Calculations for Transmission, Distribution and Industrial Applications, IEEE Press, New York, McGraw-Hill.

[60] Van Valkenburg, M.E. 1964. Network Analysis. Englewood Cliffs, NJ Prentice-Hall Inc.

[61] Mitchell, A.R. and Griffiths, D.F. 1980. The finite difference method in partial differential equations. Chichester, Sussex, England and New York, Wiley- Inter science.

[62] Zienkiewicz, O. C. and Taylor, R. L. 1989. The Finite Element Method. Vol. 1, 4th Ed., McGraw-Hill.

[63] Aluminium Electrical Conductor Handbook, 1982. 2d ed. Washington, DC: The Aluminum Association.

[64] Black, W.Z. and Byrd, W.R. 1983. Real Time Ampacity Model for Overhead Lines. IEEE *Transactions*, 102 (7):2289-2293.

[65] Incropera, F. P. and De Witt D. 1990. Fundamentals of heat and mass transfer. New York, John Wiley & sons, 503 pages.

[66] BS7870-4.10: 1999 LV and MV polymeric insulated cables for use by distribution and generation utilities. Specification for distribution cables with extruded insulation for rated voltages of 11 kV and 33 kV. Single-core 11 kV and 33 kV cables.

[67] King, S.Y. and Halfter, M.A.1982. Underground power cables. London and New York, Longman, 185 pages.

[68] Moore, G.F. (Editor), Electric Cables Handbook/ BICC Cables, 2004 Third Edition, Blackwell Science.

[69] P17 Part3. Current Rating for distribution cables.: Ratings for 11kV and 33 kV cables having extruded insulation. 2004. Issue 1. Energy Networks Association.

[70] Williams, G. M., Lewin, P. L, and LeBlanc M. 2004. Accurate determination of ambient temperature at burial depth for high voltage cable ratings. IEEE International Symposium on Electrical Insulation, 19–22 September, Indianapolis, Indiana, USA, pp. 458-461.

[71] Huanga, H., Ookaa, R., Chenb, H., Katoa, S., Takahashia, T. and Watanabec, T. 2008 CFD analysis on traffic-induced air pollutant dispersion under non-isothermal condition in a complex urban area in winter. *Journal of Wind Engineering and Industrial Aerodynamics* 96:1774–1788.

[72] Warburton, J.,2003. Wind-splash erosion of bare peat on UK upland moorlands, *Catena 52*:191–207.

[73] Ackerman, T. (Editor). 2005. Wind Power in Power Systems, Royal Institute of Technology, John Wiley & Sons, The Atrium, Southern Gate, Chichester, West Sussex PO19 8SQ, England.

[74] Leithead, W. E., 2007. Wind energy. Phil. Trans. R. Soc. A, 365:957–970.

[75] http://www.talentfactory.dk/en/tour/wres/pwr.htm, last assessed on 17 March 2011.

[76] http://usasolarwind.com/WIND/WLTV15.pdf, last assessed on 17 March 2011.

Appendices

Appendix A

Characteristics of ACSR conductors based on EN 50182:2001 (Conductors for overhead lines - Round wire concentric lay stranded conductors) [12]

Code	Old code	Areas			No. of wires		Wire diameter		Diamter		Mass per unit length	Rated strength	DC resistance
		Al	Steel	Total	Al	Steel	Al	Steel	Core	Cond.			
		mm²	mm²	mm²	Al	Steel	mm	mm	mm	mm	kg/km	kN	Ω/km
11-AL1/2-ST1A	MOLE	10,6	1,77	12,4	6	1	1,50	1,50	1,50	4,50	42,8	4,14	2,702 7
21-AL1/3-ST1A	SQUIRREL	21,0	3,50	24,5	6	1	2,11	2,11	2,11	6,33	84,7	7,87	1,365 9
26-AL1/4-ST1A	GOPHER	26,2	4,37	30,6	6	1	2,36	2,36	2,36	7,08	106,0	9,58	1,091 9
32-AL1/5-ST1A	WEASEL	31,6	5,27	36,9	6	1	2,59	2,59	2,59	7,77	127,6	11,38	0,906 5
37-AL1/6-ST1A	FOX	36,7	6,11	42,8	6	1	2,79	2,79	2,79	8,37	148,1	13,21	0,781 2
42-AL1/7-ST1A	FERRET	42,4	7,07	49,5	6	1	3,00	3,00	3,00	9,00	171,2	15,27	0,675 7
53-AL1/9-ST1A	RABBIT	52,9	8,81	61,7	6	1	3,35	3,35	3,35	10,1	213,5	18,42	0,541 9
63-AL1/11-ST1A	MINK	63,1	10,5	73,6	6	1	3,66	3,66	3,66	11,0	254,9	21,67	0,454 0
63-AL1/37-ST1A	SKUNK	63,2	36,9	100,1	12	7	2,59	2,59	7,77	13,0	463,0	52,79	0,456 8
75-AL1/13-ST1A	BEAVER	75,0	12,5	87,5	6	1	3,99	3,99	3,99	12,0	302,9	25,76	0,382 0
73-AL1/43-ST1A	HORSE	73,4	42,8	116,2	12	7	2,79	2,79	8,37	14,0	537,3	61,26	0,393 6
79-AL1/13-ST1A	RACOON	78,8	13,1	92,0	6	1	4,09	4,09	4,09	12,3	318,3	27,06	0,363 5
84-AL1/14-ST1A	OTTER	83,9	14,0	97,9	6	1	4,22	4,22	4,22	12,7	338,8	28,81	0,341 5
95-AL1/16-ST1A	CAT	95,4	15,9	111,3	6	1	4,50	4,50	4,50	13,5	385,3	32,76	0,300 3
105-AL1/17-ST1A	HARE	105,0	17,5	122,5	6	1	4,72	4,72	4,72	14,2	423,8	36,04	0,273 0
105-AL1/14-ST1A	DOG	105,0	13,6	118,5	6	7	4,72	1,57	4,71	14,2	394,0	32,65	0,273 3
132-AL1/20-ST1A	COYOTE	131,7	20,1	151,8	26	7	2,54	1,91	5,73	15,9	520,7	45,86	0,219 2
132-AL1/7-ST1A	COUGAR	131,5	7,31	138,8	18	1	3,05	3,05	3,05	15,3	418,8	29,74	0,218 8
131-AL1/31-ST1A	TIGER	131,2	30,6	161,9	30	7	2,36	2,36	7,08	16,5	602,2	57,87	0,220 2
158-AL1/37-ST1A	WOLF	158,1	36,9	194,9	30	7	2,59	2,59	7,77	18,1	725,3	68,91	0,182 9
159-AL1/9-ST1A	DINGO	158,7	8,81	167,5	18	1	3,35	3,35	3,35	16,8	505,2	35,87	0,181 4
183-AL1/43-ST1A	LYNX	183,4	42,8	226,2	30	7	2,79	2,79	8,37	19,5	841,6	79,97	0,157 6

Appendix B

Modelling using Fluent

Modelling in Fluent [52] consists of a number of stages, such as building the geometry, generating a computational mesh and checking its quality, specification of boundary conditions, properties of materials, selecting equations of the mathematical model, computation and, finally, visualization and analyzing the results.

Building geometry of a model

Fluent has its own pre-processor, GAMBIT, which allows creating 2-D and 3-D geometry of the computational domain, generation of the computational mesh and dividing the mesh into separate fluid and solid zones for describing the properties of substances used. Zones are of boundary or continuum types. Whereas boundary-type specifications, such as WALL, INFLOW or OUTFLOW define the characteristics of the model at boundaries, continuum-type specifications, such as FLUID or SOLID, specified a number of domains, forming model.

Discretization is the process of transforming a continuous problem into a discrete one. As a part of discretization the domain is split into control volumes (cells). In a 2-D problem the cells are usually either quadrilaterals or triangles, for 3-D problems they can be hexahedral, tetrahedrals and prisms (usually wedges). The   Table AB1 illustrates elements of simple geometry involved in computational modelling.

Table AB1 The mesh elements in 2-D and 3-D modelling

2D Element	Quadrilateral	
	Triangle	
3D Element	Hexahedron	
	Tetrahedron	
	Prism	
	Wedge	

After generation of the computational mesh its quality should be checked and GAMBIT provides tools EquiAngle Skew and EquiSize Skew to evaluate the quality of the mesh using corresponding criteria.

The EquiAngle Skew QEAS criteria is defined as follows:

$$Q_{EAS} = \max\left(\frac{\theta_{max} - \theta_{eq}}{180 - \theta_{eq}}, \frac{\theta_{eq} - \theta_{min}}{\theta_{eq}} \right)$$

(1)

where θ_{max} and θ_{min} are the maximum and minimum angles (in degrees) between the edges of the element, and θ_{eq} is the characteristic angle corresponding to an equilateral cell of similar form:

- for triangular and tetrahedral elements, θ_{eq} equals to 60°,

- for quadrilateral and hexahedral elements, θ_{eq} equals to 90°.

Q_{EAS} ranges from 0 to 1 and an ideally shaped element has Q_{EAS} close to 0 and a very poorly shaped element has Q_{EAS} close to 1.

A3

The EquiSize Skew criteria (Q_{EVS}) is defined as follows:

$$Q_{EVS} = \frac{S_{eq} - S}{S_{eq}} \qquad\qquad (2)$$

where S is the area (2-D) or volume (3-D) of the mesh element, and S_{eq} is the maximum area (2-D) or volume (3-D) of an equilateral cell the circumscribing radius of which is identical to that of the mesh element. By definition

$$0 \le Q_{EVS} \le 1 \qquad\qquad (3)$$

with $Q_{EVS} = 1$ being for a completely degenerate (poorly shaped) element.

After creation of the mesh, and its quality check is carried out, pre-processor highlights cells which should be refined in order to have an acceptable value of Q_{EAS} and Q_{EVS}.

Appendix C

The wind turbine reaches its maximum capacity at a wind velocity between 12-16 m/s [73]. Fig. C1 shows that the wind turbine generated power increases until it reaches the steady state at 12 m/s. In the ranges of the wind velocities less than 4 m/s and greater than 25 m/s the turbines do not operate due to economical or safety reasons.
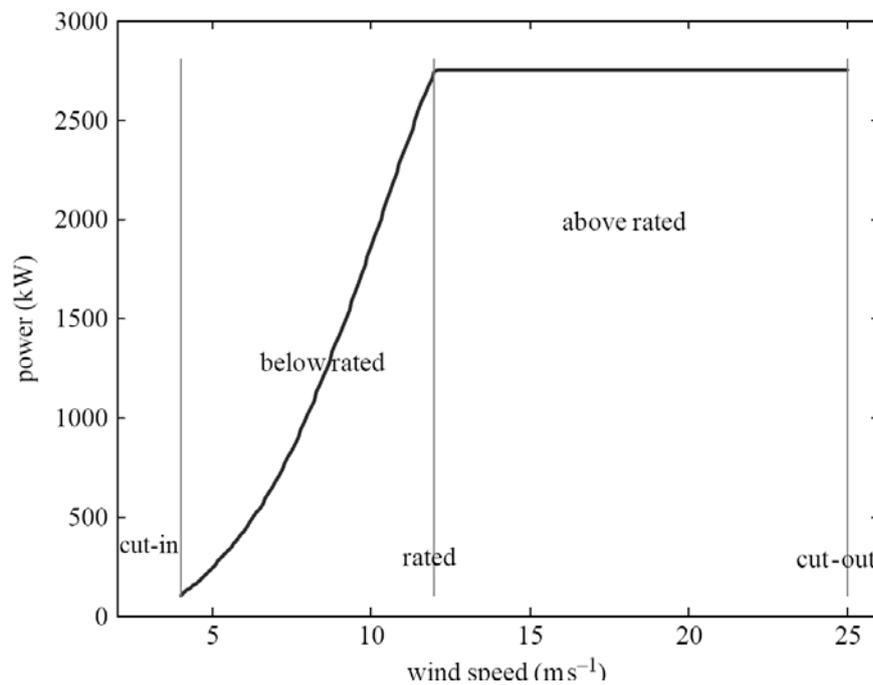
Fig. C1 Typical power curve of a turbine [74]

Fig. C2 shows the power curve presented by The Danish Wind Industry Association (DWIA) which promotes wind energy in Denmark and internationally [75]. The evolution of the Danish energy system has proved wind power to be a reliable, large-scale energy technology. Currently, wind power plants of approximately 3200 MW in Denmark supply more than 20 percent of the annual electricity consumption.
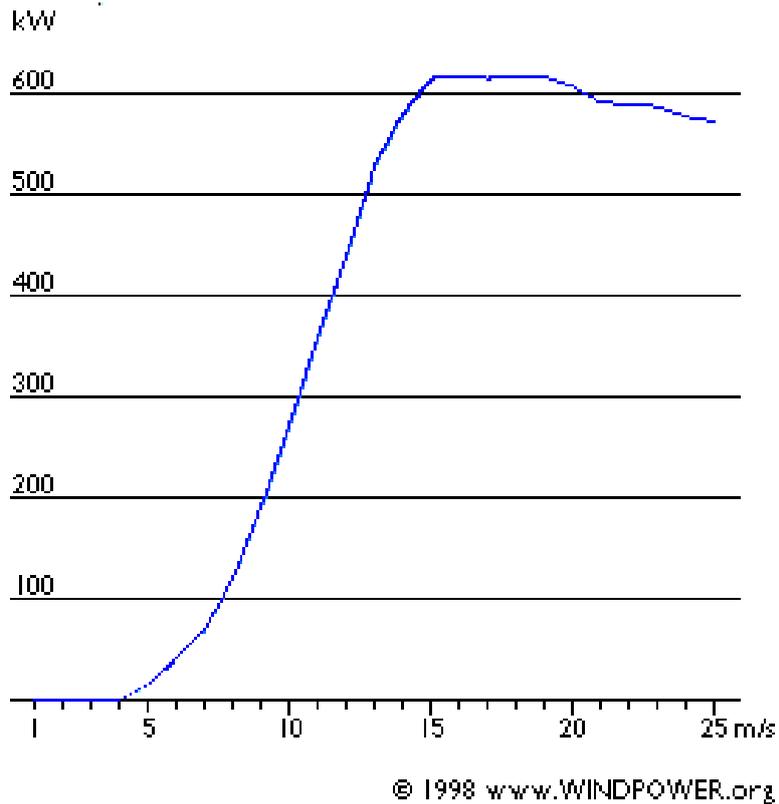
Fig. C2 The Power Curve of the turbine [75]

The Danish manufacturer Vestas is the largest producer of wind turbines. Fig.C3 illustrates the ideal power curve for the Vestas V-15 (65 kW) wind turbine. The turbine is designed to generate electricity in wind speeds as low as 8.9 mph and continues to generate electricity at wind speeds up to 62 mph. Power production is maximized over the wind velocity operating range of the turbine through the use of two induction generators. The small generator is rated at 12.6 kW and operates at wind speeds ranging from approximately 8.9 mph to 15.7 mph. The large generator is rated at 65 kW and operates in wind speeds ranging from approximately 15.7 mph to 62 mph. The controller of the turbine automatically switches between the two generators depending upon wind speeds and rotor revolution rates. When wind speeds exceed 62 mph, the generators are automatically taken off-line from the

power network and the braking mechanisms bring the rotor to a halt. The turbine then waits for the wind to return to production speeds and automatically restarts.
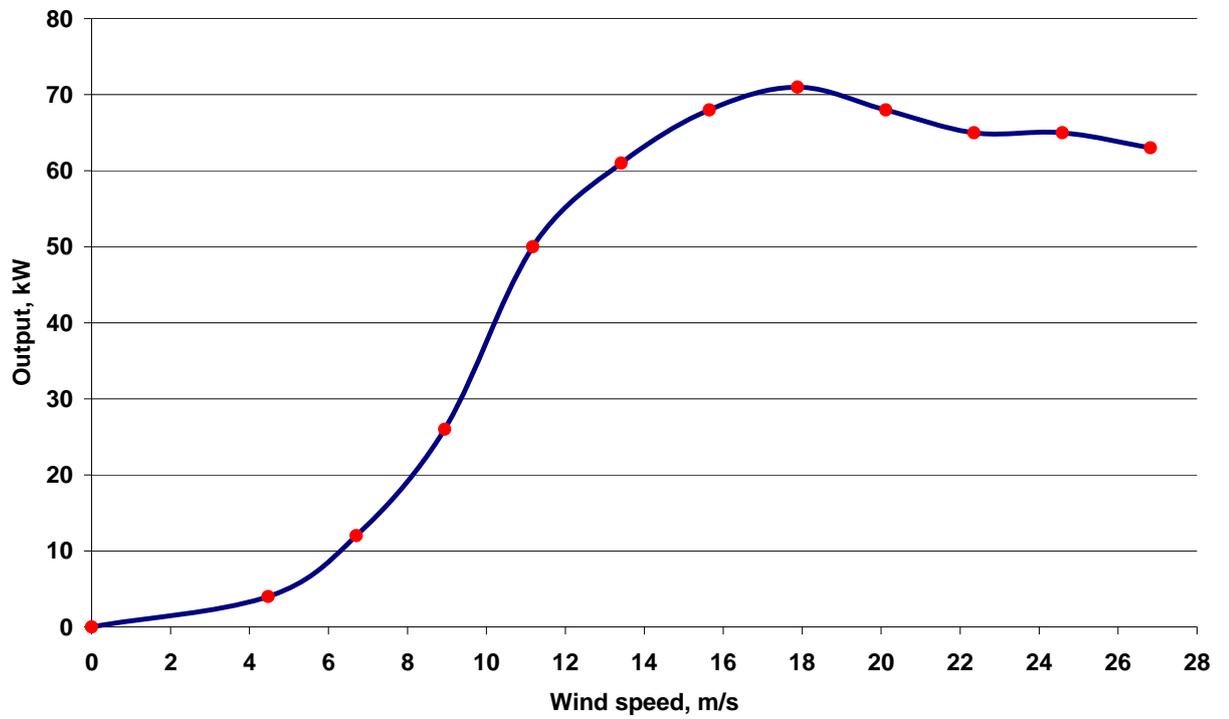
Fig. C3 The ideal power curve for the Vestas V-15 (65kW) wind turbine [76]

Appendix D

Material properties

Table AD1 presents thermal conductivity and heat capacity of material as temperature dependent functions using some tabular data from [65].

Table AD1 Properties of aluminium and steel at varies temperatures [65]

Temperature, K	Aluminium		Steel plain carbon AISI1010	
	k (W/m·K)	c_p (J/kg·K)	k (W/m·K)	c_p (J/kg·K)
200	237	798		
300	237	903	60.5	434
400	240	949	56.7	487
600	231	1033	48	559

Appendix E

UDF subroutine to describe the change in the heat generation source in the case when the current instantaneously increases from 433 A to 866 A using the temperature dependent current values (Chapter 6)

```
#include "udf.h"

DEFINE_SOURCE(heat_source,cell,thread,dS,eqn)
{
 real current;
 real current_time;
 real energySource;
 real currentConst;
 real temp;

 currentConst=433;

 temp = C_T(cell, thread);

 current_time = RP_Get_Real("flow-time");

 if (current_time>=216000)
 {
  current = 866;
 }
 else
 {
  current = currentConst;
 }

 energySource = (current*current/0.0001834)*(0.000157*(1+0.00403*(temp-293)));

 /*Message ("\ntime = %f, Tcon = %f, enSource = %f", current_time, temp,
energySource);*/

 return energySource;
}
```

Appendix F

UDF subroutine describe variations in the wind velocity and the current used in the

modelling Case 1 (Chapter 7)

```
#include "udf.h"
DEFINE_PROFILE(unsteady_velocity, thread, position)
{
face_t f;
real t = CURRENT_TIME;

begin_f_loop(f, thread)
if (t<=216330)
{
F_PROFILE(f, thread, position) = 1.7;
}

if (t>216330 & t<=216390)
{
F_PROFILE(f, thread, position) = 1.6;
}

if (t>216390 & t<=216480)
{
F_PROFILE(f, thread, position) = 1.5;
}

if (t>216480 & t<=216540)
{
F_PROFILE(f, thread, position) = 1.4;
}

.
.

 if (current_time> 223440  & current_time<= 223470)
 {
current=186.87;
}

 if (current_time> 223470)
 {
current=186.91;
}


  energySource =
(current*current/0.0001834)*(0.000157*(1+0.00403*(temp-293)));

  /*Message ("\ntime = %f, Tcon = %f, enSource = %f", current_time,
temp, energySource);*/

  return energySource;
}
```

Appendix G

Table AG1 Dimensions of 33 kV stranded copper conductors

| UTILITY CABLES | MEDIUM VOLTAGE |
| | 19000/33000V |

BS7870-4.10 33kV Stranded Copper Conductor

BS7870 - 4.10

Cross-sectional area	Minimum average thickness of insulation	Nominal diameter over insulation	Nominal area of copper wire screen	Minimum average thickness of oversheath	Nominal overall diameter	Nominal drum length
mm²	mm	mm	mm²	mm	mm	m
70	8.0	28.9	35	2.0	36.9	500
95	8.0	30.6	35	2.1	38.8	500
120	8.0	32.1	35	2.1	41.4	500
150	8.0	33.4	35	2.2	43.0	500
185	8.0	35.2	35	2.2	44.8	500
240	8.0	37.4	35	2.3	47.5	500
300	8.0	39.7	35	2.4	50.0	500
400	8.0	42.4	35	2.5	53.3	250
500	8.0	45.3	35	2.6	56.5	250
630	8.0	48.7	35	2.7	60.4	250

Appendix H

Table AH1 Thermal resistivities, thermal capacities and densities for backfill soil types [67]

Material	Thermal resistivity g (^{o}C m W^{-1})	Thermal capacity (kJ kg^{-1} ^{o}C^{-1})	Density (kg m^{-3})
Soil with higher moisture content, M_c: Clayey sand , M_c=10-12% Sandy clay , M_c=14-28%	0.8-0.9	1.900-2.100	2000-2200
Soil with average moisture content, M_c: Clayey sand , M_c=8-10% Sandy clay , M_c=12-14%	1.2	0.830	1900
Soil with lower moisture content, M_c: Clayey sand , M_c=4-7% Sandy clay , M_c=8-10%	1.8-2.0	0.830	1600-800
Soil with very low moisture content, M_c: Sandy soil, M_c=4-7% Very dry stony soil	2.1-2.8 and higher	0.800	1400

Appendix I

UDF to describe the instantaneous current change from 470 A to 940 A


```c
#include "udf.h"

DEFINE_SOURCE(heat_source,cell,thread,dS,eqn)
{
 real current;
 real current_time;
 real energySource;
 real currentConst;
 real temp;

 currentConst=470;

 temp = C_T(cell, thread);

 current_time = RP_Get_Real("flow-time");

 if (current_time>=2880000)
 {
  current = 940;
 }
 else
 {
  current = currentConst;
 }

 energySource = (current*current/0.00063)*0.0000405;

 /*Message ("\ntime = %f, Tcon = %f, enSource = %f", current_time, temp,
energySource);*/

 return energySource;
}
```

Appendix J

A copy of the conference paper published in electronic proceedings (on CD only) of 43rd International Universities Power Engineering Conference:
Paper Number 51, I. Makhkamova et al. CFD Analysis of the Thermal State of an Overhead line Conductor
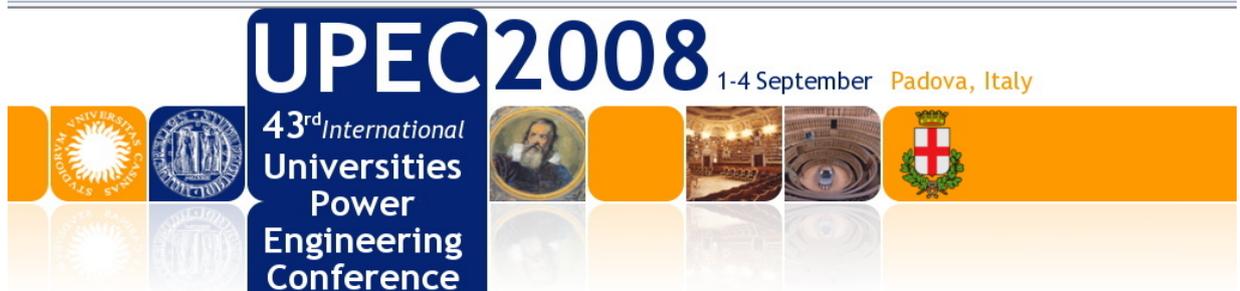
UPEC2008 1-4 September Padova, Italy

43rd International Universities Power Engineering Conference

Conference papers
Full Paper list
List by Topic
List by Author
Technical Sessions
Sponsors

Full Paper list

1 - Investigation into the Use of Hydrogen Technology with a Wind Farm Constrained by the Grid

Blake S., Taylor P.C. (UK)
View Paper | Topic 4 - Renewable Energy Systems

2 - Effects of PWM Chopper Drive on the Torque-Speed Characteristic of DC Motor

Ayasun S., Gelen A. (Turkey)
View Paper | Topic 9 - Electrical Machines and Drives

3 - Power Density Comparison for Various Types of Double-Sided Axial Flux Slotted PM Motors

Abbaszadeh K., Ardebili M., Gholamian S.A. (Iran)
View Paper | Topic 9 - Electrical Machines and Drives

5 - Investigation of Comparison on Porcelain and Epoxy Resin Insulator Conditions from a Coastal Area due to Various Parameters

50 - A Dynamic Modelling Environment for the Evaluation of Wide Area Protection Systems

Abdulhadi I.F., Burt G.M., McDonald J.R., Tumilty R.M. (UK)
View Paper | Topic 2 - Power System Simulation and Analysis

51 - CFD Analysis of the Thermal State of an Overhead Line Conductor

Bumby J.R., Mahkamov K., Makhkamova I., Taylor P.C. (UK)
View Paper | Topic 4 - Renewable Energy Systems

52 - Hybrid Cascaded H-Bridge Multilevel Inverter for Fuel Cell Power Conditioning Systems

Mathur B.L., Seyezhai R. (India)
View Paper | Topic 10 - Power Electronics and Devices

CFD Analysis of the Thermal State of an Overhead line Conductor

I. Makhkamova
irina.makhkamova@durham.ac.uk

P.C. Taylor
p.c.taylor@durham.ac.uk

J.R. Bumby
j.r.bumby@durham.ac.uk

K. Mahkamov
khamid.mahkamov@durham.ac.uk

School of Engineering, Durham University, UK

Abstract- **At present commercial CFD packages such as Fluent, ANSYS CFX, and Star-CD are widely used for investigation of heat and mass transfer processes in various fields of engineering. These codes can also be successfully applied to estimate the thermal state of major components of electrical distribution networks, such as overhead lines, underground cables and transformers. This paper presents some results obtained from numerical modelling of the temperature field in the Lynx overhead conductor in both cross and parallel wind conditions using 2-D and 3-D CFD models. The CFD results obtained demonstrate that for an applied load of 433 A and considering the summer rating (Lynx conductors ER P27 [1]) the maximum temperature in the conductor is considerably lower (16 degrees) than the prescribed design conductor temperature. This indicates that there is headroom for increasing the ampacity of the conductor.**

INTRODUCTION

Distribution network owners and operators face a number of challenges not least those due to load growth, distributed generation growth and the problem of environmental opposition to building new infrastructure. Therefore, it has become very important to try to increase the utilisation of existing power system infrastructure in a safe and cost effective manner. The research described in this paper supports this aim by investigating the heat transfer mechanisms associated with OHLs. This work forms part of a Department for Innovation, Universities and Skills (DIUS) project which seeks to evaluate a prototype Distributed Generation (DG) output controller which will make use of dynamic thermal ratings derived from component power system models and relevant meteorological data.

The thermal ratings of overhead line conductors are calculated using lumped parameter models based on solving the energy balance equation written for the conductors using IEEE and CIGRE methods [2, 3]. The calculations employed by these two methods have slight differences however the general methodologies are very similar. Thus IEEE relies on the use of tabular data to determine various energy balance terms whilst CIGRE uses closed form equations to calculate the same terms. The IEEE method is restricted to the limited environmental situations described in the tables. For most practical line design and operation applications, both methods produce similar results. However, for some less typical applications such as high wind speed and/or parallel wind speed calculations, there are significant variations in the calculated ratings and the engineers need to determine, which of the two methods should be used. There is ongoing work to combine these two standards into one worldwide standard [4].

With the sharp increase in the computational capacity of personal computers, it is now feasible to employ complex CFD techniques for rapid analysis of the thermal state of conductors. The universal fundamental governing equations used in CFD and its geometry and boundary condition flexibility allows the user to assess the influence of a wide range of climatic conditions and loading conditions on both the steady state and transient thermal response of the conductor. Additionally, it is possible to take into account the dependencies of thermo-physical properties of the conductor such as heat capacity, conductivity and resistivity on temperature.

The main objective of this research is to perform numerical analysis of the heat transfer between the Lynx conductor and the ambient air with the use of CFD techniques taking into account the magnitude of the wind velocity and its direction. The commercial CFD package, Fluent [5] was used for solving governing equations of flow around the conductor.

The study was carried out in two stages. In the first stage, a 2-D CFD model was employed for the case when the Lynx overhead conductor was exposed to the cross wind condition to determine the thermal state of the conductor for various wind velocities. In the second stage a universal 3-D CFD model was developed to describe heat and mass transfer processes in the domain, where the conductor was exposed to cross and parallel winds. The calculations of the conductor's thermal state for various cross and parallel wind velocities were carried out for the case in which the transmitted load corresponded to 433 A with a design core temperature of 50°C, which is fixed summer rating for Lynx conductor [1].

2-D CFD MODEL: THE LYNX CONDUCTOR EXPOSED
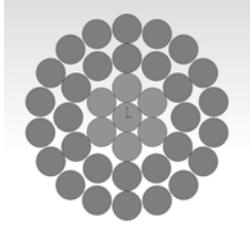
Fig. 1. The real geometry of the LYNX conductor

The maximum diameter of the aluminium cylinder and of the steel core is 19.5 and 8.37 mm, respectively, with the cross sectional area of the aluminium part being 183.4 mm^2. For modelling purpose the conductor was assumed to be a combination of two coaxial cylinders, in order to simplify calculations, as demonstrated in Fig. 2. For this calculation scheme the diameter of the steel core was increased to 12.1 mm to keep the outer diameter and the aluminium cross-section of the conductor equal to the real values.

The temperature distribution within the conductor and its surroundings can be determined by solving the system of governing energy, continuity and momentum equations.

The scheme of the computational domain and the section of the computational mesh are presented in Fig. 3. and Fig. 4. The whole domain incorporates the air domain, the aluminium section and the steel part of the conductor. The equations describing heat and mass transfer in the computational domain are discretised using the finite volume method in which the whole domain is split into the array of much smaller control volumes/elements in the computational mesh. In this case the mesh with 90,539 cells was created. In order to obtain accurate results on the heat transfer, a very fine mesh was created in the vicinity of the surface of the conductor to reflect the specifics of the flow and heat transfer in boundary layer zone around the conductor. The solution of the system of the governing heat and mass transfer equations is subject to the set of boundary conditions.
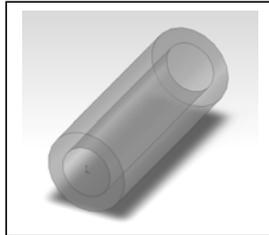
Fig. 2. The model with increased steel core in comparison to the real conductor
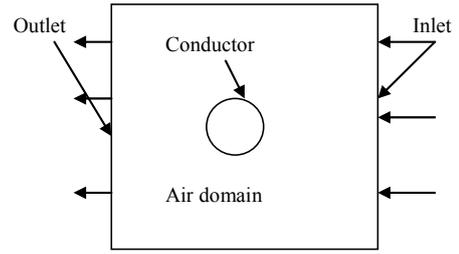
Fig. 3. The scheme of the computational domain

Fig. 4. The section of the computational mesh used in the modelling process

The velocity inlet and the outflow boundary conditions were prescribed on the right and left external boundaries of the computational domain, respectively. The ambient temperature was assumed to be 293 K. The laminar flow model was used in calculations for the wind velocity equal to 0.1 m/s. For greater values of the wind velocity the standard k–ε model with the enhanced wall treatment was employed to model the turbulence within the air domain. The standard k-ε model is a semi-empirical model which includes the turbulence kinetic energy (k) and its dissipation rate (ε) for the calculation the turbulent viscosity [5].

The internal heat generation rate ($S_{heat\ source}$) is included as the energy source term in the energy conservation equation and this represents the amount of heat uniformly generated within the aluminium part of the conductor, but not within the conductor core. It is defined as a ratio of the power generated within the object to its volume. The energy source term can be calculated, using the following equation:

$$S_{heat\ source} = \frac{I^2}{A} \times \frac{R}{L} = \frac{433 \times 0.157}{183.4 \times 10^{-6} \times 10^3} = 160,500\ W/m^3$$

Where:

I is the current through the conductor, A is the cross section area of the aluminium part of the conductor and R/L is the DC resistance of the conductor. The per-unit resistance of the Lynx conductor is 0.157 Ω/Km [6].

A16

The Mathematical Model

The calculation scheme of the conductor in 3-D simulations is identical to that used in 2-D CFD modelling. Due to the computer RAM limitations it was decided that it would not be feasible to employ a computational domain larger than a parallelepiped with dimensions 1m × 1 m ×3 m (L × H × W). The same mathematical models have been used for solving the system of governing equations describing heat and mass transfer processes in the computational domain as in 2-D simulations except that the system of equations was modified to reflect the 3-D geometry.

Fig. 5 presents the geometry of the computational domain used for 3-D CFD modelling (which is the parallelepipedal air domain surrounding the conductor). A 3-D computational mesh, consisting of 627,400 hexahedron elements (10,900 hexahedron elements for steel cylinder; 7,500 hexahedron elements for aluminium part of the conductor and 609,000 mixed elements for air domain) is shown in Fig. 6. When creating the computational mesh special care was taken in order to reflect the presence of boundary layers around the surface of the conductor. The quality of the mesh was assessed by EquiAngle Skew and EquiSize Skew options. More than 90% of the cells had a skewness factor value less than or equal to 0.15, which indicates a high quality mesh.
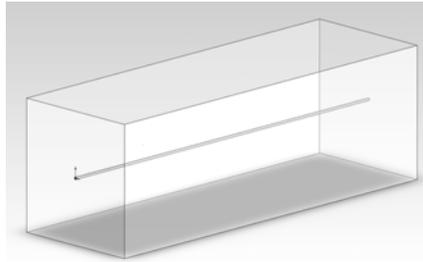
Fig. 5. The scheme of the computational domain
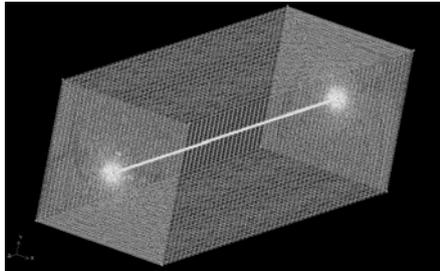
Fig.6. The 3-D computational mesh used in the modelling process

Numerical Results

The numerical simulations were performed for a number of cases in which the wind velocity was varied from 0.1 to 15 m/s. Detailed information on the values of the temperature of the conductor, obtained from 2-D and 3-D CFD modelling is presented in Table I and in Fig. 7.

Calculations performed demonstrate that results obtained using 2-D and 3-D CFD models are almost identical over the wind velocity range varying from 0.1 to 15 m/s. Analysis of our results shows that the temperature difference between 2-D and 3-D modelling is negligible. The temperature of the conductor depends strongly on the wind velocity at low wind conditions (particularly in the range of 0-1 m/s) and the rate of the change in the thermal state of the conductor is reduced when the wind velocity exceeds 10 m/s.

P27 Recommendations indicate that the design core temperature is 323 K (for the cross wind velocity of 0.5 m/s and 433 A loading) and according to the CFD modelling, the temperature of the conductor for the same conditions is 307 K (which is 16 K lower than the limit).

It can also be seen that the temperature of the conductor is approximately 20 K higher for low wind conditions when it is exposed to parallel wind. With the increase of the air velocity this temperature difference gradually reduces and is about 5 K for 15 m/s wind velocity. It is most likely, that results for the different wind angles will be placed within a "cross and parallel wind" results envelope.

If the obtained CFD results are accurate, there is headroom for increasing transmitted power even during fairly modest wind conditions.

TABLE I
TEMPERATURE IN THE CONDUCTOR AS A FUNCTION OF WIND VELOCITY AND THE WIND DIRECTION

Wind velocity, m/s	Temperature, K		
	2-D CFD model, Cross wind	3-D CFD model, Cross wind	3-D CFD model, Parallel wind
0.1	324.85	324.93	346.97
0.5	307.1	306.73	323.44
1	303.35	303.52	317.61
2	300.37	300.41	312.14
3	298.89	298.91	309.18
4	297.98	297.96	307.11
5	297.32	297.27	305.57
10	295.53	295.43	301.45
15	294.74	294.67	299.63

A17
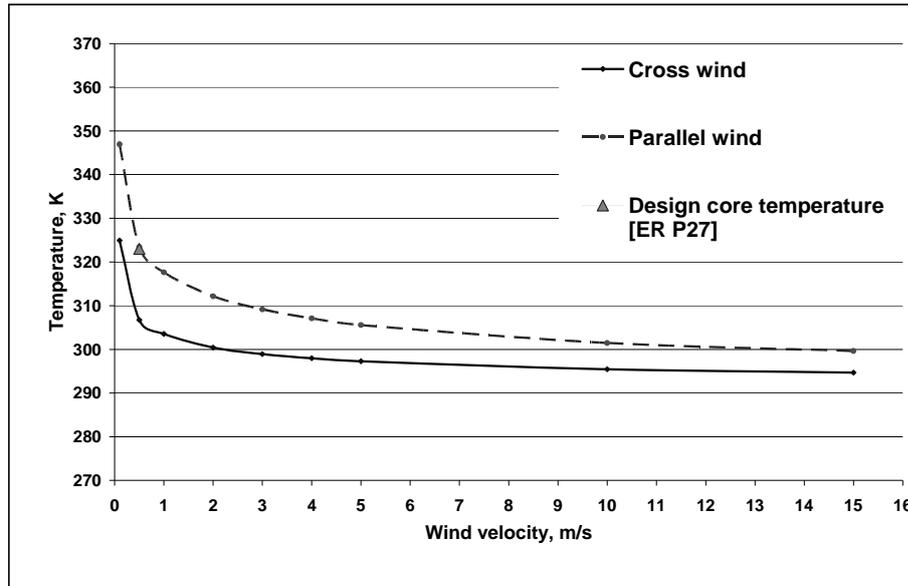
Fig.7. Temperature in the conductor vs. wind velocity for cross and parallel wind conditions

CONCLUSIONS

In this study the heat dissipation process in the Lynx overhead conductor exposed to the cross wind was investigated using 2-D and 3-D CFD modelling techniques. The thermal state of the same conductor for parallel wind conditions was determined using 3-D CFD simulations. Results from these numerical investigations indicate that 2-D and 3-D approaches provide almost identical results for the cross wind conditions.

Compared to P27 Recommendations, CFD modelling shows that there is appreciable headroom for increasing the rating. The preliminary results from this research suggest that with careful management it may be possible to temporarily increase the rating and utilisation of existing overhead lines. This increase could lead to benefits such as the avoidance of costly network reinforcement and improved network access for distributed generation.

FUTURE WORK

It is planned to present results produced from models including the variation of heat transfer coefficients in the form of $Nu = f(\mathrm{Re})$ correlations, where Nu is the dimensionless heat transfer coefficient and Re is dimensionless velocity.

REFERENCES

[1]   Engineering Recommendation P27, 1986. "Current Rating Guide for High Voltage Overhead Lines Operating in the UK Distribution System"

[2]   IEEE "Standard for Calculating the Current Temperature Relationship of Bare Overhead Conductors", IEEE P738-1993

[3]   CIGRE "Thermal Behaviour of Overhead Conductors", ELECTRA No. 144, October 1992.

[4]   N.P. Schmidt, Comparison between I.E.E.E. and CIGRE Ampacity Standards. *IEEE Transactions on Power Delivery,* **14**(4), 1999

[5]   Fluent Inc., Product documentation

[6]   BS EN 50182-2001"Conductors for overhead lines. Round wire concentric lay stranded conductors".

A18

Appendix K

A copy of the journal paper submitted to the   International Journal of Renewable Energy Technology (accepted subject to the completion of the revision)

CFD Modelling of the Thermal State of the Lynx Overhead Conductor in Power Distribution Networks Incorporating Generators Sourced by Renewable Energy

I. Makhkamova*, K. Mahkamov, P.C. Taylor,

School of Engineering and Computing Sciences

Durham University,

South Road, Durham DH1 3LE, UK

Email: irina.makhkamova@durham.ac.uk;
Email: khamid.mahkamov@durham.ac.uk
Email: p.c.taylor@durham.ac.uk

*Corresponding author

Abstract: Results on application of a CFD technique for determination of the thermal sate of a Lynx overhead conductor, used in power distribution networks, are presented in this paper. The thermal state of the conductor is mainly defined by a magnitude of the electrical current, the ambient temperature, the wind velocity and its direction and also by the insolation level. In the process of numerical simulations CFD modelling provides engineers with a capability to fully reflect variations in the above parameters which take place during actual exploitation. Results for both the steady-state and transient operational situations have been obtained and compared to those produced using industrial standards and available experimental data. Analysis of CFD simulation results demonstrate that this numerical technique provides an adequate level accuracy in predicting the thermal state of the overhead conductor in both the steady and transient processes   and therefore can be successfully used in the dynamic analysis and management of power distribution networks, which incorporate renewable energy generators.

Keywords: CFD modelling, Lynx overhead conductor; thermal state; power distribution networks, Renewable energy.

Reference to this paper should be made as follows: Makhkamova, I., Mahkamov, K. and Taylor, P.C. (2010) "CFD Modelling of the Thermal State of the Lynx Overhead Conductor in Power Distribution Networks Incorporating Generators Sourced by   Renewable Energy", Int J. Renewable Energy Technology, Vol. 1, No. 4, pp. xx-zz.

Biographical notes: I. Makhkamova obtained MEng degree from Bauman Moscow Technical University in 1983 in the field of Thermal Engineering and works as a Research Assistant in Energy

Research Group in the School of Engineering and Computing Sciences at Durham University. Her research interests are focused on studying thermal aspects of various energy conversion technologies.

K. Mahkamov obtained his MEng and PhD degrees from Bauman Moscow Technical University in Thermal Engineering area and currently works as a Senior Lecturer in Thermofluids in the School of Engineering and Computing Sciences at Durham University. His main fields of interest are development of Thermo-mechanical energy conversion systems and numerical modelling of heat and mass transfer processes.

P.C Taylor is a Professor in the School of Engineering and Computing Sciences at Durham University and his research involves active Network management techniques, demand side management, Fuzzy control and integration of Renewable energy into electrical networks (both interconnected and stand alone)

1 Introduction

As result of large scale efforts on the reduction of CO_2 emissions, a rapid expansion of power generation using Renewable energy (wind, marine, solar PV etc) and small scale CHP is taking place in numerous European countries including UK. Most of this new generation is embedded into electrical distribution network and this leads to a significant rise in the energy flow within distribution networks. There is a considerable environmental opposition exists to building new infrastructure and, furthermore, upgrading electrical distribution network requires very significant capital investments. Therefore, it has become very important to try to increase the utilisation of existing power system infrastructure in a safe and cost effective manner.

One way to raise the energy delivered by the existing distribution networks is to increase the amount of current carried by overhead conductors. Large benefits can be achieved by a small increase in ampacity. As a result, many utilities are considering operating their overhead conductors at levels when their capacity is close to the critical values.

Modern conductors can successfully operate at the temperatures exceeding 100 ^{o}C. The problem is that higher levels of current result in the increased electrical losses due to resistance and in the elevated conductor temperature. The corresponding thermal expansion of the conductor leads to the grow in the sag and consequently to the decrease in the ground clearance. Additionally, overhead lines are exposed to solar radiation, which noticeably effects the thermal state of the conductor in a summer period. Heat from the conductors is dissipated by circulation of air surrounding the lines (free convection and wind) and also by re-radiation mechanism.

At these high load conditions monitoring and accurate prediction of the thermal state of components in electrical distribution network becomes of a paramount importance for a reliable supply of electricity to consumers. The serious consequence of the excessive temperature level in the overhead line might be its structural damage.

Performing experimental investigations of the thermal state of overhead conductors at different operation and meteorological conditions is a time consuming and costly procedure. Therefore, numerical methods could be attractive alternative for accurate assessment of the conductor's thermal state.

This study is research into the accurate estimation of the thermal state of the conductors in electrical distribution network using a high resolution numerical heat transfer method in order to identify a potential for increasing ampacity of existing overhead lines.

2 Industrial standards used for estimation of the thermal state of overhead conductors

As mentioned above, upgrading and erecting new lines is extremely costly and, therefore, there is pressing necessity to operate distribution lines at higher currents and, consequently, at higher temperatures. There is realisation that some of the existing methods used in the industry for estimation of the thermal state of conductors are restrictive, providing conservative predictions. Rating recommendations may also vary from utility to utility. The thermal ratings of overhead line conductors are normally calculated using IEEE Standard 738-1993 (1993) and CIGRE (1992) methods. These methods are based on solving the energy balance equation written for the conductors. Such mathematical models are also called lumped parameter models. The calculations employed by IEEE and CIGRE methods have some differences however the general methodology used in these both the approaches is very similar and   calculations of line ratings are based on the coincident high ambient temperature, full solar radiation and an effective wind velocity. The value of the latter varies in different standards. For example, UK Engineering Recommendations P27 (1986) uses 0.5 m/s as the wind velocity value for the calculation of ratings. The IEEE/CIGRE survey shows that number of utilities have gradually increased their line ratings by relaxing some of assumptions. Some utilities now assume the effective wind velocity of 0.91 m/s, or even higher, see Douglass et all (2000). The main difference between IEEE and CIGRE methods is that IEEE relies on the use of tabular data to determine various energy balance terms whilst CIGRE uses closed form equations to calculate the same terms. The IEEE method is restricted to the limited environmental situations. For most practical line design and operation applications, both methods produce similar results. However, for some less typical conditions such as a high wind velocity and a parallel wind, there are significant variations in the calculated ratings and the engineers have to make a decision on which of the above two methods should be followed. There is ongoing work to combine these two standards into one worldwide standard, see Schmidt (1997).

IEEE Standard 738-1993 "IEEE Standard for Calculating the Current-Temperature Relationship of Bare Overhead Conductors" (1993) has recently been revised to improve the solar heating calculation and to provide use of SI units throughout.

As highlighted above, the lumped-parameter models are based on the solution of the following basic energy balance equation:

$$q_c + q_r = q_s + I^2 \times R(T_c),$$
(1)

where q_c is the convective heat loss (W/m); q_r is the heat loss due to re-radiation; q_s is heat gain from the sun (W/m); I is conductor current (A) and $R(T_c)$ is 60 Hz AC resistance per meter of the conductor at temperature T_c.

The thermal state of the conductor in the dynamic case is determined by solution of the following equation:

$$q_c + q_r + mc_{pc}\frac{dT_c}{dt} = q_s + I^2 \times R(T_c),$$
(2)

where c_{pc}, m and T_c are the total heat capacity (J/(kgK)); mass (kg) and temperature (K) of the conductor, respectively.

Convective heat losses are due to exposure to the air flow and are determined separately for the case of natural convection and low and high wind conditions taking into account the wind direction relative to the axis of the conductor. These loses are calculated in terms of the conductor's diameter, density, thermal conductivity and dynamic viscosity of air, velocity of the air stream and ambient temperature.

The properties of air are taken at

$$T_{film} = \frac{T_c + T_a}{2},$$
(3)

where T_a is the ambient temperature (K).

Morgan (1982) proposed an extended version of the energy balance equation to determine the correlation between the current of the conductor and its temperature for the steady-state as follows:

$$P_J + P_M + P_s + k_i \cdot P_i = P_c + P_r + (P_W).$$
(4)

Here P_J, P_M, P_s and P_i are the heat gains (per unit length per unit time) due to Joule, ferromagnetic, solar and ionization (corona) heating, respectively, and P_{con}, P_r and P_w are the heat losses due to convection, re-radiation and evaporation, respectively. The coefficient k_i takes into consideration probabilistic nature of ionization. Joule heating was calculated as a function of the current, the ambient temperature and the resistance of the conductor, depending on the conductor's temperature. Accounting for ferromagnetic heating in layered conductors resulted in increased resistance of 5–10 % in the 3rd and 5th

layers at the maximum load. Solar heating depends on the diameter of the conductor and its position to the horizontal, the absorptivity of the surface of the conductor, insolation and the solar altitude.

The heat losses due to evaporation were determined as

$$P_W = \pi \cdot d \cdot L \cdot (x_{ws} - x_{wa}),$$ (5)

where d is the diameter of the conductor; L is the latent heat of evaporation of water, x_{wa} is the mole fraction of water in atmospheric air, x_{ws} is the mole fraction of water in air in the vicinity of the free surface of the water film on the conductor.

In study by Morgan (1982) it was demonstrated that the earlier version of IEEE Standard (1993) produces results similar but not identical to those obtained with the CIGRE method. For a typical rating calculations for a 400 mm^2 ACSR conductor, Schmidt (1997) finds a difference of about 2% in the rating when calculated by the IEEE and CIGRE methods.

According to Howitt and Simpkins (1971) the evaluation and consideration of the thermal limits of a power line due to sag, loss of conductor strength, and fitting limitations usually result in a maximum allowable conductor temperature or thermal rating. For a specified maximum allowable conductor temperature and a given set of weather conditions, "the continuous current-carrying capacity (ampacity) of a power" line can also be determined by applying heat-balance equations to the electrical conductors. The current-carrying capacity of a conductor as a function of the conductor temperature, ambient temperature, wind velocity, elevation, and incident solar radiation have been examined by Howitt and Simpkins (1971) but all calculations were performed using a non-metric system. Calculations performed are based on the same generalised energy balance equation presented in the following form:

$$I = (q_c + q_r - q_s)/R)^{0.5},$$ (6)

where q_c is the convective heat loss (watt per unit of the length of conductor); q_r is the radiated heat loss (watt per unit of the length of conductor); q_s is the heat gain from the sun (watt per unit of the length of conductor); I is conductor current in A, and R is 60 Hz AC resistance per unit of the length of conductor. The above equation states that heat generated in the conductor due its electrical resistivity and gained by the conductor due to insolation are equal to convection and radiation heat losses if the conductor is in a steady thermal state. Components of the above equation are calculated using corresponding semi-empirical correlations.

An ampacity model used by Chen et al. (2002) can predict the temperature of overhead conductors operating at temperatures up to 250 ^{0}C. Main details of the model are presented by Black and Byrd (1983) and Bush et al. (1983). The accuracy of the model was determined by comparing the theoretical predictions with temperatures measured on a full-scale outdoor test span. Two different ACSR conductors were used in the outdoor test span. One conductor was a Curlew conductor (54/7,

≈ 524 mm^2) with an outer diameter of 31.6 mm. Under typical weather conditions, the power supply was able to produce temperatures that were below 150 ^{0}C. The other conductor that was used in the testing program was a Linnet conductor (26/7, $\approx$170.5 mm^2) with an outer diameter of 18.3 mm. Due to greater electrical resistance the Linnet conductor could be heated to temperatures above 200 ^{0}C, when the wind velocity was low. With an increase in the average conductor temperature, the accuracy of calculations decreases.

The current carrying capacity of the overhead line is influenced by forced convection cooling. Isozaki and Iwama (2002) performed experimental investigations of ACSR410 in a wind tunnel for wind velocities in the range from 0.2 m/s to 4 m/s and current equal to 1340 A. Heat dissipation around the conductor was expressed as

$$P_c = \pi\lambda(T_s - T_a)Nu \ . \tag{7}$$

The relationship between *Nu-Re* numbers can be presented as

$$Nu = B \times \mathrm{Re}^n \ . \tag{8}$$

Using experimental results, the authors refined equations used for calculation of the thermal state of the conductor. In the case of forced convection at the wind velocity less than 1 m/s the authors found that

$$Nu = 1.566 \times \mathrm{Re}^{0.343} \text{ for surface roughness} <0.1; \tag{10}$$

$$Nu = 1.325 \times \mathrm{Re}^{0.362} \quad \text{for surface roughness} >0.1. \tag{11}$$

Investigations described by Foss et al. (1983) and Tasic (2000) are examples of analysis of the non-stationary thermal state of the ACSR conductor. Introducing simplifications about re-radiation heat transfer, see Tasic (2000), analytical expressions for evaluation of the temperature inside and on the surface of the conductor were obtained. Comparison of results from the numerically solved set of two differential equations with those, obtained using the simplified model, led to a conclusion that these were practically the same, which justified application of the simplified model.

Overall, analysis of publications indicate that to date a number of lumped parameter models have been developed to determine the thermal state of overhead conductors and which provide high accuracy for a certain range of conditions. However, if the range of exploitation conditions is extended and it is necessary to analyse the dynamic processes then the lumped parameter models provide contradicting results due to differences in assumptions made. An application of more universal theoretical approach with a capability to describe in detail relevant heat and mass transfer processes would be useful for more accurate estimation of the ampacity limits of different conductors. With a sharp increase in the

computational capacity of personal computers, it is now feasible to employ complex Computational Fluid Dynamics (CFD) techniques for rapid analysis of the thermal state of conductors. The universal fundamental governing equations used in CFD and flexibility in describing geometry and boundary conditions allows users to assess the influence of various combinations of climatic and loading conditions on both the steady and transient thermal sates of the conductor. Additionally, it is possible to take into account dependency of thermo-physical properties of the conductor, such as a heat capacity, conductivity and resistivity, on its temperature.

The main objective of this research is to perform numerical analysis of heat transfer between an overhead conductor and ambient air with the use of CFD techniques taking into account the electrical load and the magnitude of the wind velocity and its direction. The Lynx ACSR conductor was the subject of investigations and the commercial CFD package, Fluent, was used for solving governing equations of flow around the conductor. This software deploys the control volume method for discretization of the physical domain and numerical solution of governing equations, describing mass and heat transfer processes, see Hoffmann and Chiang (2000), Vol. 2.

3 Application of CFD for determination of the thermal state of overhead conductors

The ACSR conductor Lynx consists of 30 strands of aluminium wire and 7 strands of steel wire, see Figure 1.
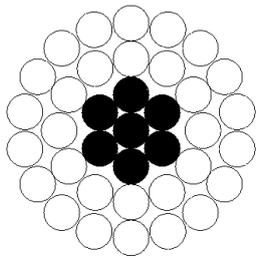
Figure 1 The cross section of the Lynx Conductor
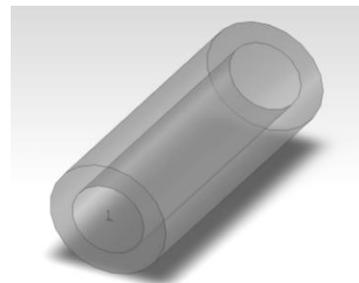
Figure 2 The model with an increased steel core in comparison to the real conductor

The maximum diameter of the aluminium cylinder and of the steel core is 19.5 and 8.37 mm, respectively, with the cross sectional area of the aluminium part being 183.4 mm^2. For modelling purpose the conductor was assumed to be a combination of two coaxial cylinders, in order to simplify calculations, as demonstrated in Figure 2. For this calculation scheme the diameter of the steel core was

increased to 12.1 mm to keep the outer diameter and the aluminium cross-section of the conductor equal to the real values.

The temperature distribution within the conductor and its surroundings can be determined by solving the system of governing energy, continuity and momentum conservation equations.

For conditions in which the conductor is exposed to the cross wind, a two-dimensional (2-D) CFD model can be applied to determine its thermal state. The scheme of the physical domain and the computational mesh, used in these investigations, are presented in Figures 3 and 4. The physical domain incorporates the air sub-domain, the aluminium section and the steel part of the conductor. For the domain, shown in Figure 3, a computational mesh with 90,539 cells was created. In order to obtain accurate results on heat transfer, a very fine mesh was formed in the vicinity of the surface of the conductor to reflect the specifics of the flow and heat transfer in a boundary layer zone located around the conductor. The solution of the system of the governing heat and mass transfer equations is subject to the set of boundary conditions.
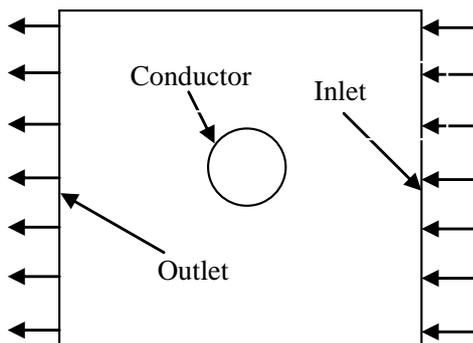
Figure 3 The scheme of the physical
domain
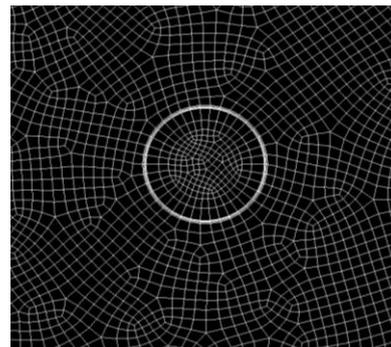
Figure 4 The section of the computational
mesh used in the modelling process

The velocity inlet and outflow boundary conditions were applied on the right and left external boundaries of the computational domain, respectively. The ambient temperature was assumed to be 293 K. The laminar flow model was used in calculations for the wind velocity equal to 0.1 m/s. For a greater value of the wind velocity the standard k–ε model with the enhanced wall treatment technique was employed to model the turbulence within the air domain. The standard k-ε model is a semi-empirical model which includes the turbulence kinetic energy (k) and its dissipation rate (ε) conservation equations for calculation of the turbulent viscosity, see Hoffmann and Chiang (2000), Vol. 3.

The internal heat generation term ($S_{heat\ source}$) is included in the energy conservation equation written for the aluminium part of the conductor and this represents the amount of heat uniformly generated within this part of the conductor, but not within the conductor core. It is defined as a ratio of

the power generated within the object to its volume. The energy source term can be calculated, using the following equation:

$$S_{heat\ source} = \frac{I^2}{A} \times \frac{R}{l} = \frac{433 \times 0.157}{183.4 \times 10^{-6} \times 10^3} = 160,500 \ \text{W/m}^3 \qquad (11)$$

where I is the current through the conductor, A is the cross sectional area of the aluminium part of the conductor and R/l is the resistance of the conductor. The per-unit resistance of the Lynx conductor is 0.157 Ω/Km, see BS EN 50182-2001 (2001).

As the conductor has a higher temperature than its surroundings, the resulting heat losses due to re-radiation from the surface of the conductor have been included in these simulations.

When the conductor is exposed to parallel wind then it is necessary to apply a three-dimensional (3-D) CFD model. The calculation procedure used in 3-D simulations is identical to that used in 2-D CFD modelling. Due to the computer RAM limitations it was decided that it would not be feasible to employ a computational domain larger than a parallelepiped with 1 m $\times$ 1 m $\times$3 m (L $\times$ H $\times$ W) dimensions. The same mathematical models have been used for solving the system of governing equations describing heat and mass transfer processes in the computational domain as in 2-D simulations except that the system of equations was modified to reflect the 3-D geometry.

Figure 5 presents the geometry of the physical domain used for 3-D CFD modelling (which is the parallelepipedal air domain surrounding the conductor). A 3-D computational mesh, consisting of 627,400 hexahedron elements (10,900 hexahedron elements for steel cylinder; 7,500 hexahedron elements for aluminium part of the conductor and 609,000 mixed elements for air domain) is shown in Figure 6. When creating the computational mesh special care was taken in order to reflect the presence of boundary layers around the surface of the conductor.
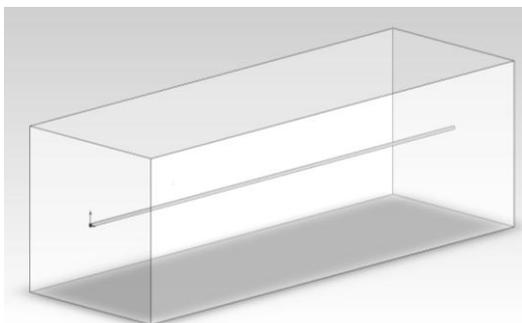
**Figure 5** The scheme of the 3-D physical domain
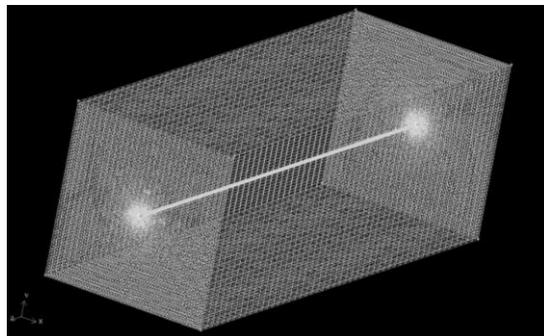
Figure 6 The 3-D computational mesh used in the modelling process

Laminar flow equations

A CFD software package has to produce a prediction of the fluid flow in a given situation with certain boundary conditions. To do this, CFD software solves numerically the equations that govern the flow of fluids. These equations can be derived from the mass and momentum conservations principle.

Figure 7(a) shows a rectangular, two-dimensional patch of fluid ABCD, together with an assumed velocity distribution in terms of the velocity components u and v in the x- and y-directions, respectively. Figure 7(b) shows a horizontal force acting on the fluid patch which caused by a normal stress, σ, and a shear stress, τ.

Mass continuity equation can be written as:

$$\frac{\partial u}{\partial x} + \frac{\partial v}{\partial y} = 0. \tag{12}$$

Momentum equations (or Navier-Stokes equations) are as follows:

in the x-direction,

$$\rho\frac{\partial u}{\partial t} + \rho u\frac{\partial u}{\partial x} + \rho v\frac{\partial u}{\partial y} = -\frac{\partial p}{\partial x} + \frac{\partial}{\partial x}\left(\mu\frac{\partial u}{\partial x}\right) + \frac{\partial}{\partial y}\left(\mu\frac{\partial u}{\partial y}\right); \tag{13}$$

in the y-direction,

$$\rho\frac{\partial v}{\partial t} + \rho u\frac{\partial v}{\partial x} + \rho v\frac{\partial v}{\partial y} = -\frac{\partial p}{\partial x} + \frac{\partial}{\partial x}\left(\mu\frac{\partial v}{\partial x}\right) + \frac{\partial}{\partial y}\left(\mu\frac{\partial v}{\partial y}\right). \tag{14}$$

The flow equations shown above are for 2-D cases.
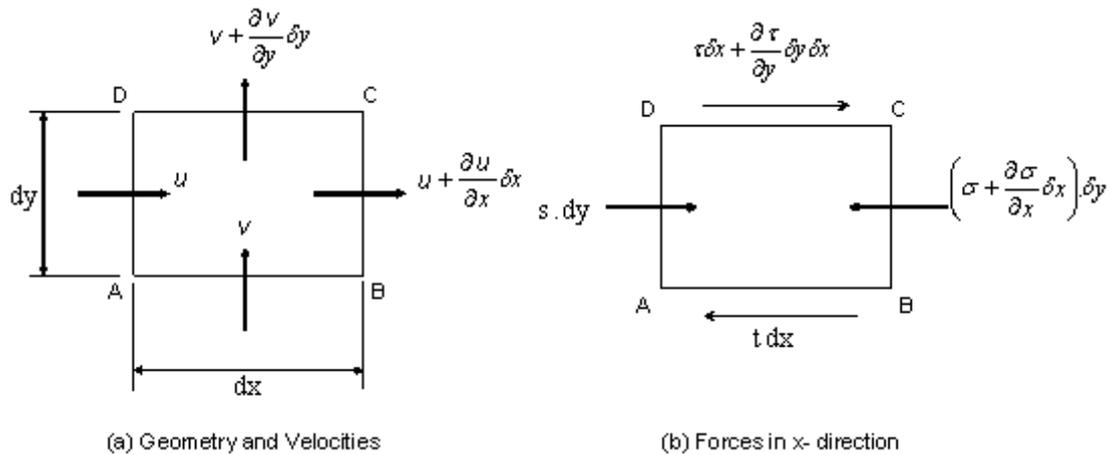
Figure 7 Flow in the control volume

Turbulent flow equations

Turbulent flows are characterized by fluctuating velocity fields:

$$u_i = \bar{u}_i + u_i', \tag{15}$$

where, $\overline{u}_i$ and u_i' are mean and fluctuating velocity components.

These fluctuations mix transported quantities such as the momentum and energy and cause these transported quantities to fluctuate as well:

$$\phi_i = \overline{\phi}_i + \phi_i', \tag{16}$$

where ϕ_i denotes a scalar such as pressure, energy or species concentration.

When substituting (15) into the continuity equation (12) and Navier-Stokes equations (13), we will obtain:

continuity equation,

$$\frac{\partial \overline{u}}{\partial x} + \frac{\partial \overline{v}}{\partial y} = 0 ; \tag{17}$$

Navier-Stokes equations (for x-direction),

$$\rho \frac{\partial \overline{u}}{\partial t} + \rho \overline{u} \frac{\partial \overline{u}}{\partial x} + \rho \overline{v} \frac{\partial \overline{u}}{\partial y} = -\frac{\partial p}{\partial x} + \frac{\partial}{\partial x}\left(\mu \frac{\partial \overline{u}}{\partial x} \right) + \frac{\partial}{\partial y}\left(\mu \frac{\partial \overline{u}}{\partial y} \right) - \rho \frac{\overline{\partial u'^2}}{\partial x} - \rho \frac{\overline{\partial (u'v')}}{\partial y} . \tag{18}$$

One way of simplifying the equations is to treat the additional terms as additional viscous stress produced by the turbulence in the flow. So (18) can be simplified as:

$$\rho \frac{\partial \overline{u}}{\partial t} + \rho \overline{u} \frac{\partial \overline{u}}{\partial x} + \rho \overline{v} \frac{\partial \overline{u}}{\partial y} = -\frac{\partial p}{\partial x} + \frac{\partial}{\partial x}\left((\mu + \mu_t) \frac{\partial \overline{u}}{\partial x} \right) + \frac{\partial}{\partial y}\left((\mu + \mu_t) \frac{\partial \overline{u}}{\partial y} \right) . \tag{19}$$

In the current investigation two- and three-dimensional $k - \varepsilon$ turbulence model for air flow has been used for the numerical analysis. The governing equations, which describe the air/fluid flow and heat transfer processes which occur in the computational domain, are as follows:

The mass conservation equation:

$$\frac{\partial \rho}{\partial t} + \frac{\partial}{\partial x}(\rho u) + \frac{\partial}{\partial y}(\rho v) + \frac{\partial}{\partial z}(\rho \omega) = 0 . \tag{20}$$

The momentum conservation equation:

$$\frac{\partial(\rho u)}{\partial t} + \frac{\partial(\rho u^2 + p)}{\partial x} + \frac{\partial(\rho u v)}{\partial y} + \frac{\partial(\rho u \omega)}{\partial z} =$$
$$\frac{\partial \tau_{xx}}{\partial x} + \frac{\partial \tau_{xy}}{\partial y} + \frac{\partial \tau_{xz}}{\partial z} + \frac{\partial(-\rho \overline{u'^2})}{\partial x} + \frac{\partial(-\rho \overline{u'v'})}{\partial y} + \frac{\partial(-\rho \overline{u'\omega'})}{\partial z} ; \tag{21}$$

$$\frac{\partial(\rho v)}{\partial t} + \frac{\partial(\rho u v)}{\partial x} + \frac{\partial(\rho v^2 + p)}{\partial y} + \frac{\partial(\rho v \omega)}{\partial z} =$$
$$\frac{\partial \tau_{xy}}{\partial x} + \frac{\partial \tau_{yy}}{\partial y} + \frac{\partial \tau_{zy}}{\partial z} + \frac{\partial(-\rho \overline{u'v'})}{\partial x} + \frac{\partial(-\rho \overline{v'^2})}{\partial y} + \frac{\partial(-\rho \overline{v'\omega'})}{\partial z} ; \tag{22}$$

$$\frac{\partial(\rho\omega)}{\partial t} + \frac{\partial(\rho u\omega)}{\partial x} + \frac{\partial(\rho \upsilon\omega)}{\partial y} + \frac{\partial(\rho\omega^2 + p)}{\partial z} =$$

$$\frac{\partial\tau_{xz}}{\partial x} + \frac{\partial\tau_{yz}}{\partial y} + \frac{\partial\tau_{zz}}{\partial z} + \frac{\partial(-\rho\overline{u'\omega'})}{\partial x} + \frac{\partial(-\rho\overline{\upsilon'\omega'})}{\partial y} + \frac{\partial(-\rho\overline{\omega'^2})}{\partial z}.$$

(23)

The energy conservation equation for the air sub-domain is

$$\frac{\partial(\rho e)}{\partial t} + \frac{\partial(u(\rho e + p))}{\partial x} + \frac{\partial(\upsilon(\rho e + p))}{\partial y} + \frac{\partial(\omega(\rho e + p))}{\partial z} =$$

$$\frac{\partial}{\partial x}\left(\left(\lambda + \frac{c_p\mu_t}{\mathrm{Pr}_t}\right)\frac{\partial T}{\partial x}\right) + \frac{\partial}{\partial y}\left(\left(\lambda + \frac{c_p\mu_t}{\mathrm{Pr}_t}\right)\frac{\partial T}{\partial y}\right) + \frac{\partial}{\partial z}\left(\left(\lambda + \frac{c_p\mu_t}{\mathrm{Pr}_t}\right)\frac{\partial T}{\partial z}\right).$$

(24)

The turbulent kinetic energy and its dissipation equations:

$$\frac{\partial}{\partial t}(\rho k) + \frac{\partial}{\partial x}(\rho u k) + \frac{\partial}{\partial y}(\rho\upsilon k) + \frac{\partial}{\partial z}(\rho\omega k) = \frac{\partial}{\partial x}\left[\left(\mu + \frac{\mu_t}{\sigma_k}\right)\frac{\partial k}{\partial x}\right] +$$

$$\frac{\partial}{\partial y}\left[\left(\mu + \frac{\mu_t}{\sigma_k}\right)\frac{\partial k}{\partial y}\right] + \frac{\partial}{\partial z}\left[\left(\mu + \frac{\mu_t}{\sigma_k}\right)\frac{\partial k}{\partial z}\right] + P_k - \rho\varepsilon$$

(25)

$$\frac{\partial}{\partial t}(\rho\varepsilon) + \frac{\partial}{\partial x}(\rho u\varepsilon) + \frac{\partial}{\partial y}(\rho\upsilon\varepsilon) + \frac{\partial}{\partial z}(\rho\omega\varepsilon) = \frac{\partial}{\partial x}\left[\left(\mu + \frac{\mu_t}{\sigma_\varepsilon}\right)\frac{\partial\varepsilon}{\partial x}\right] +$$

$$\frac{\partial}{\partial y}\left[\left(\mu + \frac{\mu_t}{\sigma_\varepsilon}\right)\frac{\partial\varepsilon}{\partial y}\right] + \frac{\partial}{\partial z}\left[\left(\mu + \frac{\mu_t}{\sigma_\varepsilon}\right)\frac{\partial\varepsilon}{\partial z}\right] + c_{\varepsilon 1}P_k\frac{\varepsilon}{k} - c_{\varepsilon 2}\rho\frac{\varepsilon^2}{k}$$

(26)

In the equations (21) - (23)

$$\tau_{xx} = \mu\left[\frac{4}{3}\frac{\partial u}{\partial x} - \frac{2}{3}\frac{\partial\upsilon}{\partial y} - \frac{2}{3}\frac{\partial\omega}{\partial z}\right];$$

(27)

$$\tau_{yy} = \mu\left[\frac{4}{3}\frac{\partial\upsilon}{\partial y} - \frac{2}{3}\frac{\partial u}{\partial x} - \frac{2}{3}\frac{\partial\omega}{\partial z}\right];$$

(28)

$$\tau_{zz} = \mu\left[\frac{4}{3}\frac{\partial\omega}{\partial z} - \frac{2}{3}\frac{\partial u}{\partial x} - \frac{2}{3}\frac{\partial\upsilon}{\partial y}\right];$$

(29)

$$\tau_{xy} = \tau_{yx} = \mu\left[\frac{\partial\upsilon}{\partial x} + \frac{\partial u}{\partial y}\right];$$

(30)

$$\tau_{xz} = \tau_{zx} = \mu\left[\frac{\partial\omega}{\partial x} + \frac{\partial u}{\partial z}\right];$$

(31)

$$\tau_{yz} = \tau_{zy} = \mu \left[\frac{\partial \omega}{\partial y} + \frac{\partial \upsilon}{\partial z} \right]; \tag{32}$$

$$\overline{u'^2} = 2\alpha_2 k \, ; \tag{33}$$

$$\overline{\upsilon'^2} = 2\alpha_3 k \, ; \tag{34}$$

$$\overline{\omega'^2} = 2\alpha_4 k \, ; \tag{35}$$

$$-\rho \overline{u'\upsilon'} = \mu_t \left(\frac{\partial u}{\partial y} + \frac{\partial \upsilon}{\partial x} \right), \tag{36}$$

where $\alpha_2, \alpha_3, \alpha_4$ are structural scale constants and the turbulent viscosity $\mu_t = \rho c_\mu \left(\dfrac{k^2}{\varepsilon} \right)$ with $c_\mu = 0.09$.

In the equations (25) and (26) $\sigma_k = 1$; $\sigma_\varepsilon = 1.3$; $c_{\varepsilon 1} = 1.3$, $c_{\varepsilon 2} = 1.92$.

The parameter P_k is the production of turbulence defined as

$$\begin{aligned}
P_k = \mu_t \bigg(& \left[\frac{4}{3} \frac{\partial u}{\partial x} - \frac{2}{3} \frac{\partial \upsilon}{\partial y} - \frac{2}{3} \frac{\partial \omega}{\partial z} \right] \left(\frac{\partial u}{\partial x} \right) + \left[\frac{4}{3} \frac{\partial \upsilon}{\partial y} - \frac{2}{3} \frac{\partial u}{\partial x} - \frac{2}{3} \frac{\partial \omega}{\partial z} \right] \left(\frac{\partial \upsilon}{\partial y} \right) + \\
& \left[\frac{4}{3} \frac{\partial \omega}{\partial z} - \frac{2}{3} \frac{\partial u}{\partial x} - \frac{2}{3} \frac{\partial \upsilon}{\partial y} \right] \left(\frac{\partial \omega}{\partial z} \right) + \left[\frac{\partial u}{\partial y} + \frac{\partial \upsilon}{\partial x} \right] \left(\frac{\partial u}{\partial y} \right) + \left[\frac{\partial u}{\partial z} + \frac{\partial \omega}{\partial x} \right] \left(\frac{\partial u}{\partial z} \right) + \\
& \left[\frac{\partial \upsilon}{\partial x} + \frac{\partial u}{\partial y} \right] \left(\frac{\partial \upsilon}{\partial x} \right) + \left[\frac{\partial \upsilon}{\partial z} + \frac{\partial \omega}{\partial y} \right] \left(\frac{\partial \upsilon}{\partial z} \right) + \left[\frac{\partial \omega}{\partial x} + \frac{\partial u}{\partial z} \right] \left(\frac{\partial \omega}{\partial x} \right) + \left[\frac{\partial \omega}{\partial y} + \frac{\partial \omega}{\partial x} \right] \left(\frac{\partial \omega}{\partial y} \right) \bigg).
\end{aligned} \tag{37}$$

The equation (24) does not take into account the influence of the viscosity dissipation on temperature of the working fluid   since this effect is negligible compared to the temperature change due to the heat transfer and compression during the cycle.

The above governing equations for the air sub-domain should be coupled to the energy conservation equations for the Lynx conductor. The following are such the equations written for the aluminium and steel parts of the conductor:

$$\frac{\partial T_{al}}{\partial t} = \frac{\lambda_{al}}{c_{pal}\rho_{al}} \left(\frac{\partial^2 T_{al}}{\partial x^2} + \frac{\partial^2 T_{al}}{\partial y^2} + \frac{\partial^2 T_{al}}{\partial z^2} \right) + S_{heat\ source}; \; . \tag{38}$$

$$\frac{\partial T_{st}}{\partial t} = \frac{\lambda_{st}}{c_{pst}\rho_{st}} \left(\frac{\partial^2 T_{st}}{\partial x^2} + \frac{\partial^2 T_{st}}{\partial y^2} + \frac{\partial^2 T_{st}}{\partial z^2} \right). \tag{39}$$

The equations (20)-(26) and (38) are subject to the following boundary conditions: $u = u(s)$ on Γ_u; $\upsilon = \upsilon(s)$ on Γ_υ; $\omega = \omega(s)$ on Γ_ω $T = T(s)$ on Γ_T; $q_x = q_x(s)$ on Γ_x; $q_y = q_y(s)$ on Γ_y; $q_z = q_z(s)$ on Γ_z; $k = k(s)$ on Γ_k; $\varepsilon = \varepsilon(s)$ on Γ_ε.

4 Numerical results of CFD modelling of steady thermal state of the conductor.

CFD modelling of the steady thermal state of the Lynx conductor has been performed for conditions close to those experimentally recorded by Scottish Power. In fact, recorded data is the temperature of the Lynx conductor operating in the transient regime with the variable electrical current and the ambient temperature, wind velocity, its direction and insolation which were measured every five minutes. Analysis of data shows that the variation of the conductor temperature follows random pattern reflecting the stochastic change in the velocity of the wind and in its direction and current. Since experimental data for purely steady conditions was not available then an attempt was made to select time intervals during which the variation of operational and meteorological parameters takes place over a relatively narrow range and to consider these intervals as pseudo-steady regimes of operation. Pseudo-steady regime data for these intervals was produced by time averaging the values of the variable parameters.

Table 1 shows comparison between experimental averaged parameters and CFD results for selected three pseudo-steady conditions when wind is considered to be perpendicular to the conductor's axis.

Table 1 Comparison of experimental data for pseudo-steady conditions and corresponding CFD results.

Case	T_{amb}, K	Average wind speed, m/s	Current, A	Heat source, J/m^3	Experimental data	CFD results, K	Difference, K
1	272 (-1°C)	0	138.11	14,946.66	275.1 K	278.6	3.5
2	276.8 K (3.8 ^{o}C)	0	62.35	3,110.60	278.2 K	276.9	1.3
3	279.6 (6.6 ^{o}C)	5.3	139.09	16,561.21	280.7 K	279.9	0.8

Numerical results in Table 1 were produced using 2-D CFD modelling technique. In the modelling process dependence of electrical resistivity and of the heat conduction coefficient from the

temperature and the effect of solar radiation were neglected. Since the wind velocity is equal to zero in Cases 1 and 2 then a free convection CFD model was employed during the simulation process.

Figures 8 and 9 present some of numerical data obtained from CFD simulations of the thermal state of the Lynx conductor. Figure 8 shows the typical temperature distribution in the Lynx conductor and air-domain for Case 1. In the "no wind" conditions air is heated up from the surface of the conductor and flows upwards with a relatively low velocity which is about few millimetres per second. The maximum temperature in the conductor is 279 K when the current is 138.11 A and the ambient temperature is 272 K.
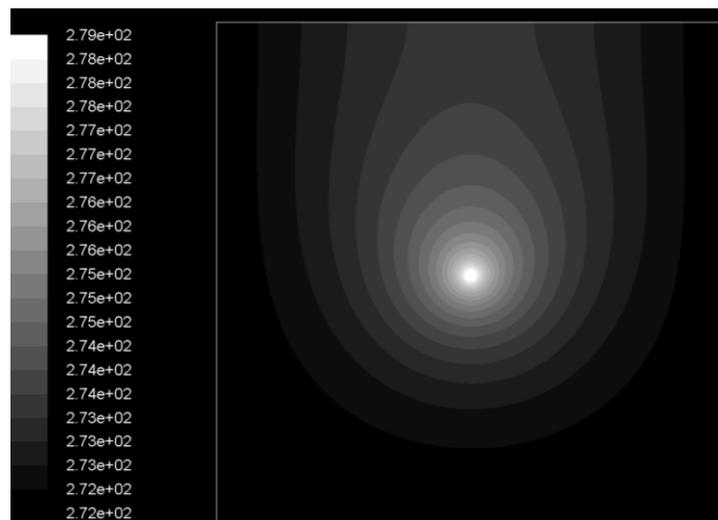

Figure 8 The temperature (K) distribution around the conductor (the free convection case)

The standard k-ε turbulent model is employed in simulations for Case 3 because the wind velocity is 5.3 m/s and this corresponds to Reynolds number of 6,780 indicating that there is a turbulent flow in the air sub-domain. Figure 9 shows the temperature distribution in the Lynx conductor and in the air sub-domain for Case 3 with the maximum temperature of 280 K being in the core of the conductor for the ambient temperature of 279.6 K.
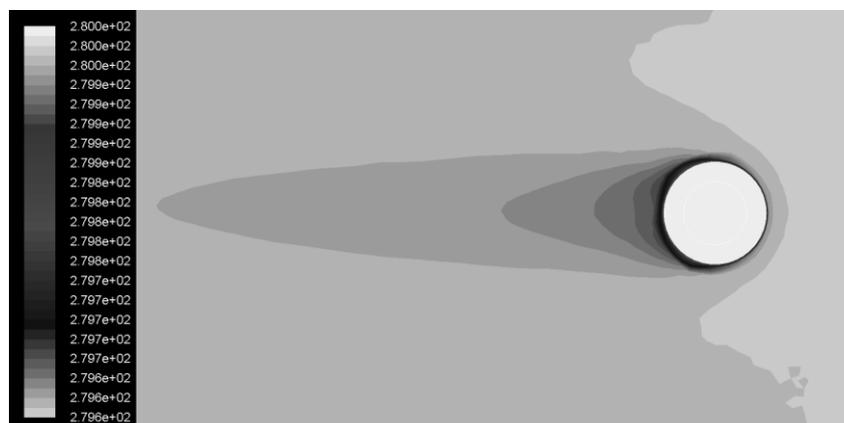

Figure 9 The temperature (K) distribution around the conductor (the turbulent model)

It can be seen that CFD modelling of the thermal state of the conductor generally provides adequate results with the maximum difference of 3.5 K for Case 1. The difference between experimental and numerical data for Case 3 (the turbulent flow) is only 0.8 K. Performed calculations demonstrate that results for simulation of the thermal state of the Lynx conductor operating at the cross wind conditions are identical for 2-D and 3-D simulations for the cases in which the wind velocity was varied from 0.1 to 15 m/s.

Figure 10 additionally presents results obtained on the thermal state of the conductor with electrical current of 433 A, operating at ambient temperature of 293 K (20 ^{o}C), and exposed to the cross and parallel wind. This diagram indicates the low and high temperature boundaries for the thermal state of the conductor for any direction of wind varying in the velocity range from 0 to 5 m/s. Due to more intensive heat transfer from the surface of the conductor to the surrounding air flow the temperature of the conductor is lower in the cross wind conditions. The temperature in the conductor is approximately 20 degrees higher for the low wind conditions when it is exposed to the parallel wind. With the increase of the air velocity this temperature difference gradually reduces and is about 5 K for the 15 m/s wind velocity.
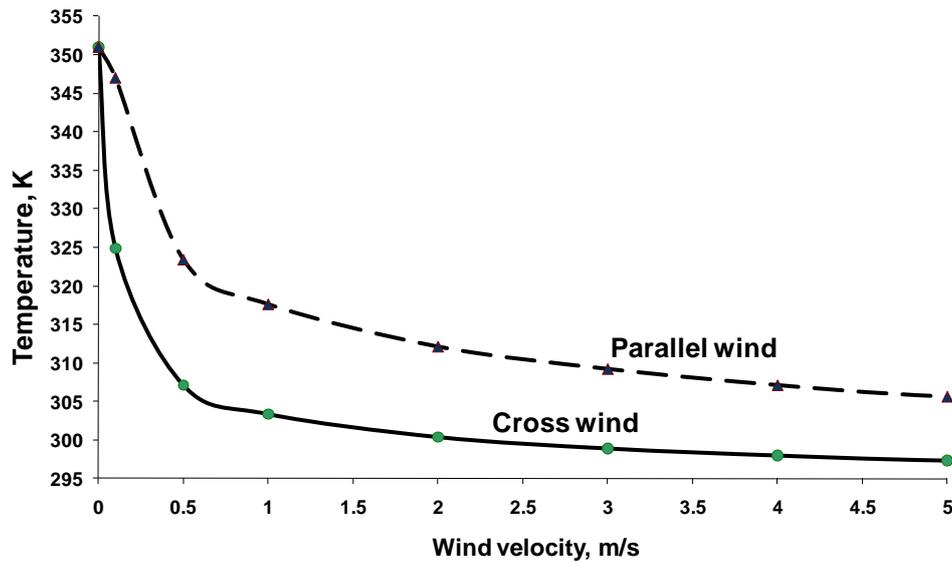
Figure 10 Temperature in the conductor as a function of the wind velocity for the cross and parallel wind conditions

P27 Recommendations indicate that the design core temperature is 323 K for the cross wind velocity of 0.5 m/s and 433 A loading. According to CFD modelling, the temperature of the conductor for the same conditions is 307 K (34 ^{0}C), which is 16 degrees lower than the limit. Compared to P27 Recommendations, CFD modelling indicates that there is an appreciable headroom for increasing the

rating. The preliminary results from this research suggest that with careful management it may be possible to temporarily increase the rating of existing overhead lines. Such an increase could lead to benefits and improved network access for distributed generation.

Finally, Figure 11 presents results on calculations of heat transfer coefficients from the surface of the Lynx conductor. Since the Prandtl number is constant for the Lynx conductor exploitation conditions then heat transfer correlations are presented in the form of $Nu=f\ (Re)$ form:

$$Nu=2.2555\times Re^{0.3065}\ \ \text{(cross wind);} \tag{40}$$

$$Nu=1.5035\times Re^{0.3038}\ \ \text{(parallel wind).} \tag{41}$$

Heat transfer correlations (40)-(41) can be used in lumped-parameter model calculations
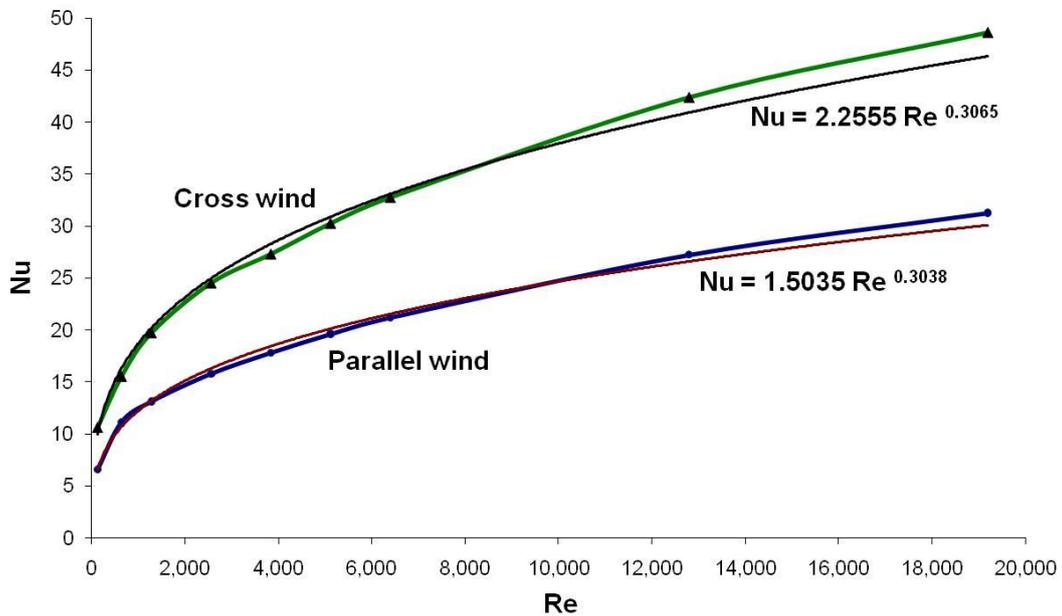

Figure 11 Nusselt number as a function of Reynolds number for the cross- and parallel wind

Effect of taking into account temperature dependence of physical properties of the conductor material and influence of solar radiation

In the numerical modelling of the thermal state of the Lynx conductor the effect of the temperature dependence of physical properties of the conductor material and influence of solar radiation were additionally investigated.

The temperature of the Lynx conductor, operating with the 433 A current and at the 293 K ambient temperature and wind velocities varying in the range from 0 to 3 m/s, was found to be higher by 1-0.5 degrees, respectively, in the case in which the electrical resistivity of aluminium was assumed to be temperature dependent.

Numerical results show that effect of dependency of the heat conduction coefficient from the temperature is very small (fractions of degree) and therefore can be neglected in the analysis.

During the exploitation period there is a considerable duration of time when conductors are exposed to the solar radiation which is an additional source of heat. The temperature of conductors increases depending on the level of insolation and on the state of the surface of the conductor with a corresponding absorption coefficient. The additional source of heat due to solar radiation can be calculated as

$$q_s = \alpha_s \cdot d \cdot I , \qquad (41)$$

where q_s is the solar heat gain in the conductor, W/m; d is the diameter of the conductor, m; α is the solar absorption coefficient, which usually varies from 0.3 to 0.9; I is the intensity of solar radiation, a typical value being between 600 and 800 W/m^2 for a summer period. The conductor which has been in exploitation for a considerable period of time usually has a darkened surface due to oxidation and pollutions and the typical value of the absorption coefficient for such the conductor is about 0.9. The absorption coefficient of a new conductor is about 0.3. Table 2 presents obtained computational results on the thermal state of the Lynx conductor, operating with the 433 A current at the ambient temperature of 293 K, the wind velocity of 2 m/s and 800 W/m^2 insolation.

Table 2 Effect of solar radiation on the thermal state of the LYNX conductor

	CFD model:	CFD model : 800 W/m^2 solar radiation		
		$\alpha = 0.3$	$\alpha = 0.5$	$\alpha = 0.9$
Temperature of the conductor, K	300.78	302.2	303.45	305.9

It can be seen in Table 2 that the temperature of the darkened conductor rises by about 3-5 degrees for the given set of boundary conditions when insolation is taken into account.

5 CFD modelling of the transient thermal state of the Lynx conductor

Power distribution networks operate under variable load and climatic conditions which strongly affect the thermal state of overhead conductors. Controlled increases in current passing through the conductor or drop in the wind velocity are examples of such dynamically changing conditions. In such situations it is essential for network operators to have information on the available time before the conductor reaches the critical temperature or cools down to the safe level. So dynamic modelling results can be used by network operators to develop the short term rating strategy for more efficient exploitation of distributed generation networks.

Figure 12 shows the scenario which was numerically modelled to investigate the effect of the abrupt increase in the electrical current for the situation in which the cross wind velocity is constant and equal to 0.5 m/s and the ambient temperature is 293 K (20 $^{\circ}$C)
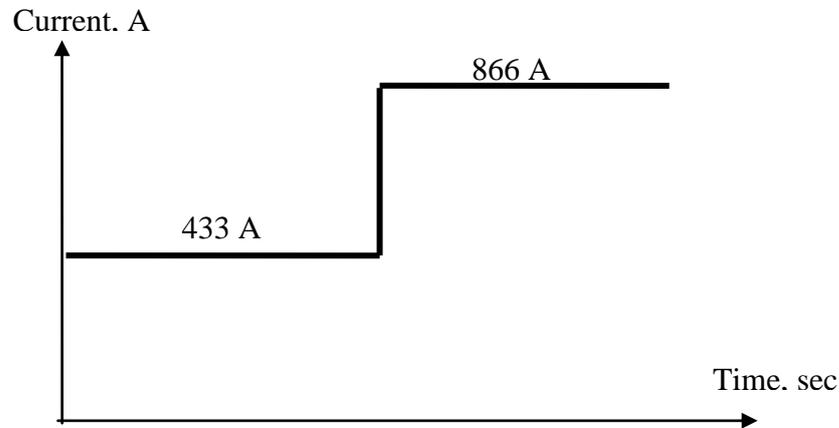

Figure 12 The abrupt increase in the electrical current passing through the LYNX conductor

Figure 13 presents results of numerical simulations. It can be seen that for the current of 433 A the steady-state temperature of the conductor is about 312.5 K and this temperature increases to about 364 K when the electrical current is doubled (the corresponding rise in the temperature is about 52 degrees). Figure 14 presents the variation in the time constant in transient processes in which the temperature of the conductor rises due to the change in current. It can be seen that the time-constant parameter first gradually increases from 42 to about 44 min when the current increases from 433 to 541, from 433 to 649 and from 433 to 750 A, respectively, and then is reduced down to 28 minutes for the current change from 433 to 866 A. Such the variation in the time constant parameter is due to the domination of the Joule heating mechanism in the conductor at the high electrical current.
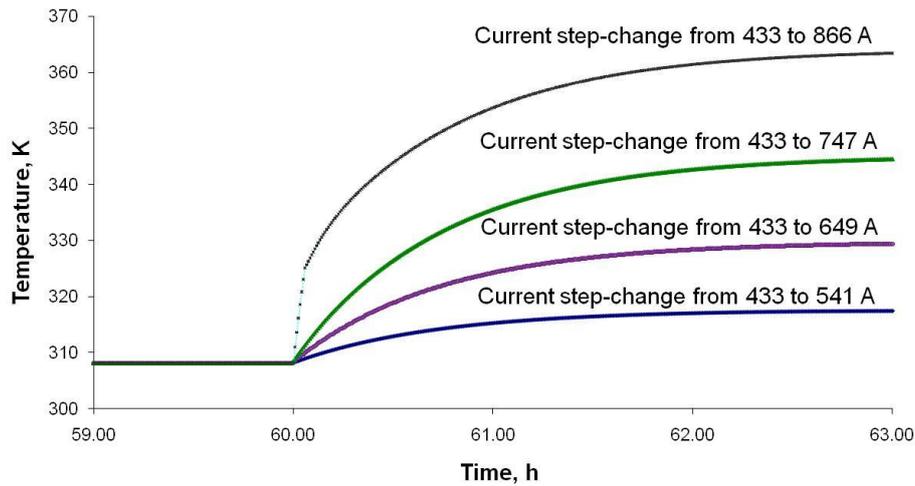
Figure 13 The variation of the temperature of the conductor with increase in the magnitude of the current
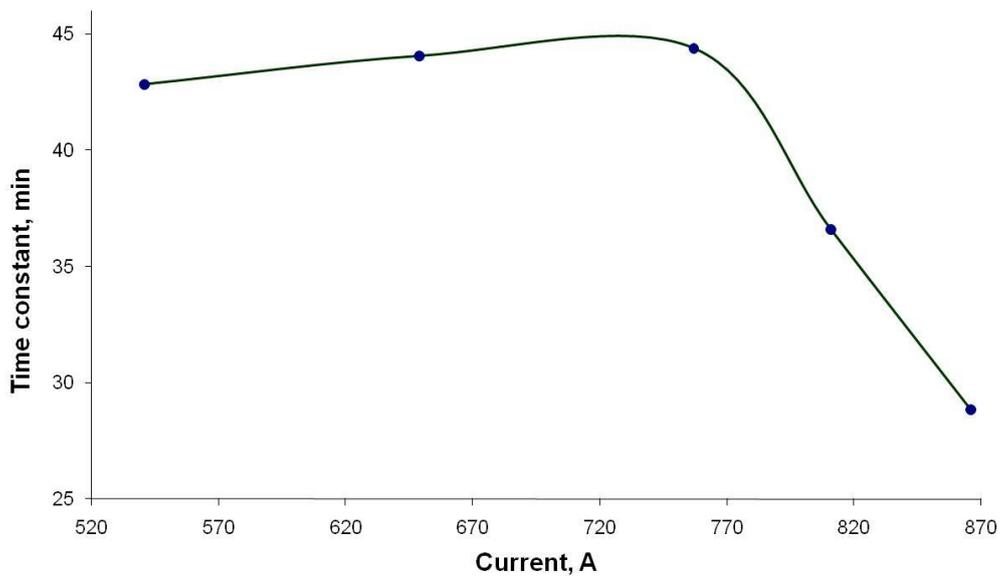

Figure 14 The variation of the time-constant parameter in transient processes caused by the current increase.

In a similar way, the situation when the magnitude of current is abruptly reduced was analysed, see Figure 15. It can be seen that the time constant in the cooling processes is noticeably greater than that in the heating-up cases. Thus, this parameter is about 66 minutes when the current magnitude drops from 866 to 433 A, see Figure 16.
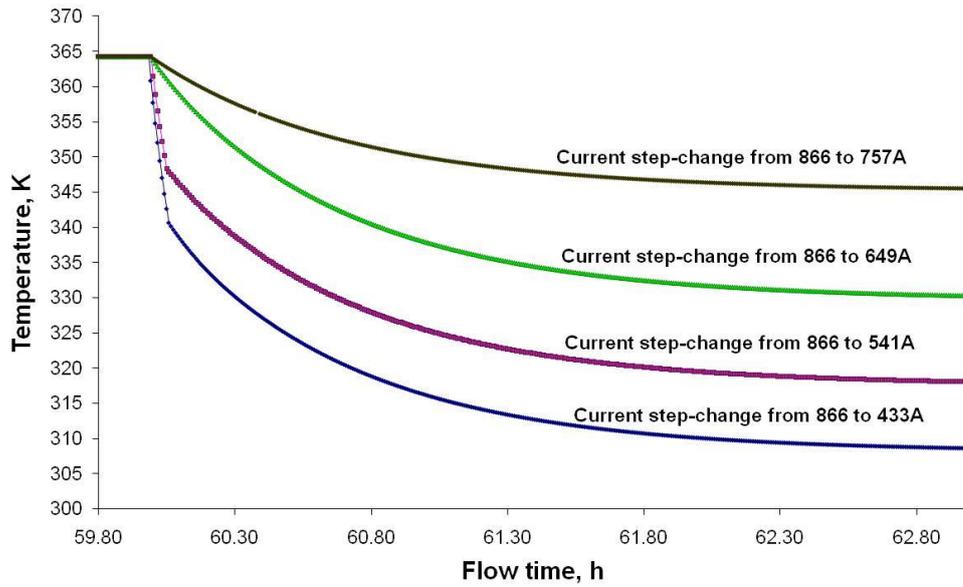
Figure 15 The variation of the temperature of the conductor with the decrease in the magnitude of the current
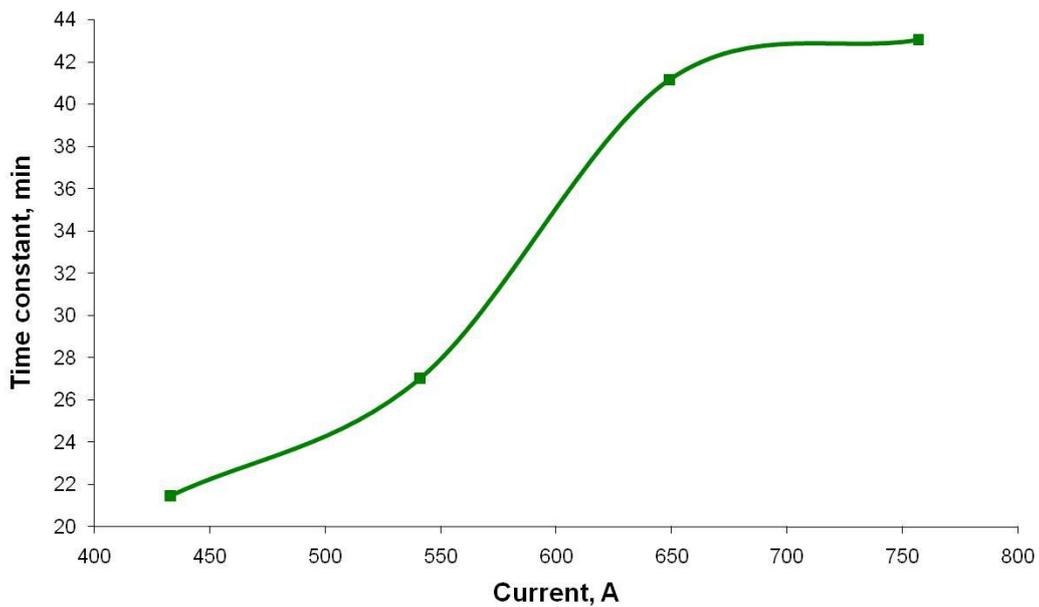
Figure 16 The variation of the time-constant parameter in transient processes caused by an abrupt current decrease

Additionally, unsteady CFD simulations of the thermal state of the Lynx conductor have been carried out for several scenarios in which the amount of the electrical current passing through the conductor remains constant and equal to 433 A at the constant ambient temperature of 293 K but the cross wind velocity sharply decreases from 15 to 10, 5 and 2.5 m/s. Figure 17 presents results obtained and it can be seen that with the decrease in the wind velocity from 15 to 10, 5 and 2.5 m/s the

temperature of the conductor gradually rises up by 0. 8, 2.6 and about 5 K. Furthermore, it was calculated that the time constant in the transition from the steady thermal state of the Lynx conductor, corresponding to the wind velocity of 15 m/s, to a new thermal state corresponding to the wind velocity of 10, 5 and 2.5 m/s is approximately 3.5, 6 and 33 hours, respectively.

The results obtained from transient CFD simulations of the thermal state of the Lynx conductor demonstrate that the rapid decrease in the magnitude of the cross wind velocity results in the increase in the conductor's temperature but over a considerably longer period of time, compared to that in the situation with an abrupt change in the current.
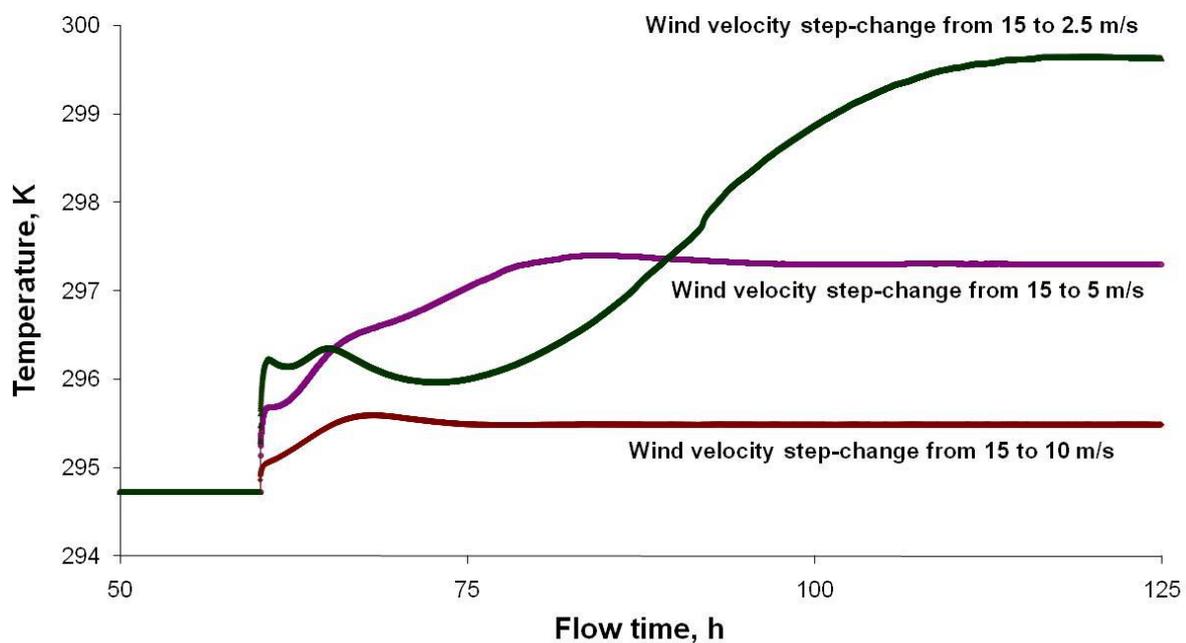
Figure 17 The variation of the temperature of the conductor with decrease in the magnitude of the cross-wind velocity

Finally, the scenario, in which there are simultaneous variations in the current and the cross wind velocity, has been modelled using experimental data in a two hour fragment of records by Scottish Power. Such the specific section of recorded data was selected so that during this interval of time the ambient temperature variation took place in a very narrow range from 6.8 to 7.2 $^{\circ}$C. Information was recorded in conditions when there is no heating of the conductor due to insolation (solar radiation is zero in experiments). Though it was observed in experiments that the direction of the wind changed continuously and randomly, in numerical simulations it has been assumed that the wind direction is always perpendicular to the conductor's axis. In the modelling process the ambient temperature was assumed to be constant and equal to 7.2 $^{\circ}$C. Figure 18 presents variations in the electrical current in the

conductor and in the wind velocity which were used as input data for CFD simulations and Figure 19 presents a comparison of experimental and numerical results on such the transient thermal state of the Lynx conductor.
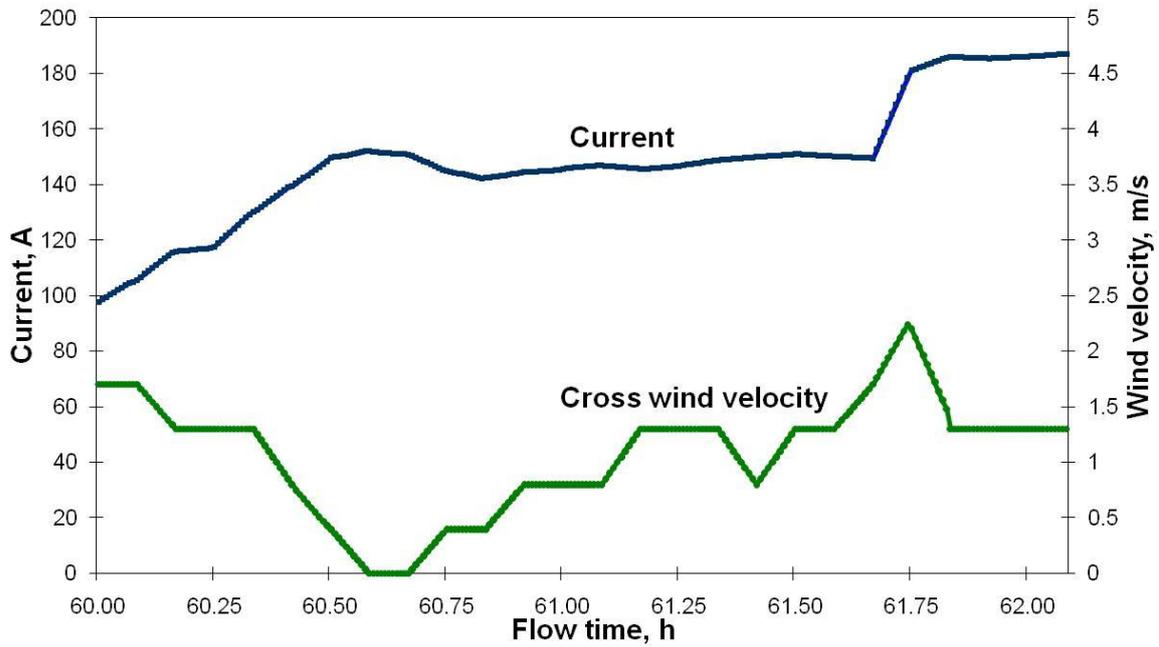

Figure 18 Experimental variations in electrical current and in the wind velocity
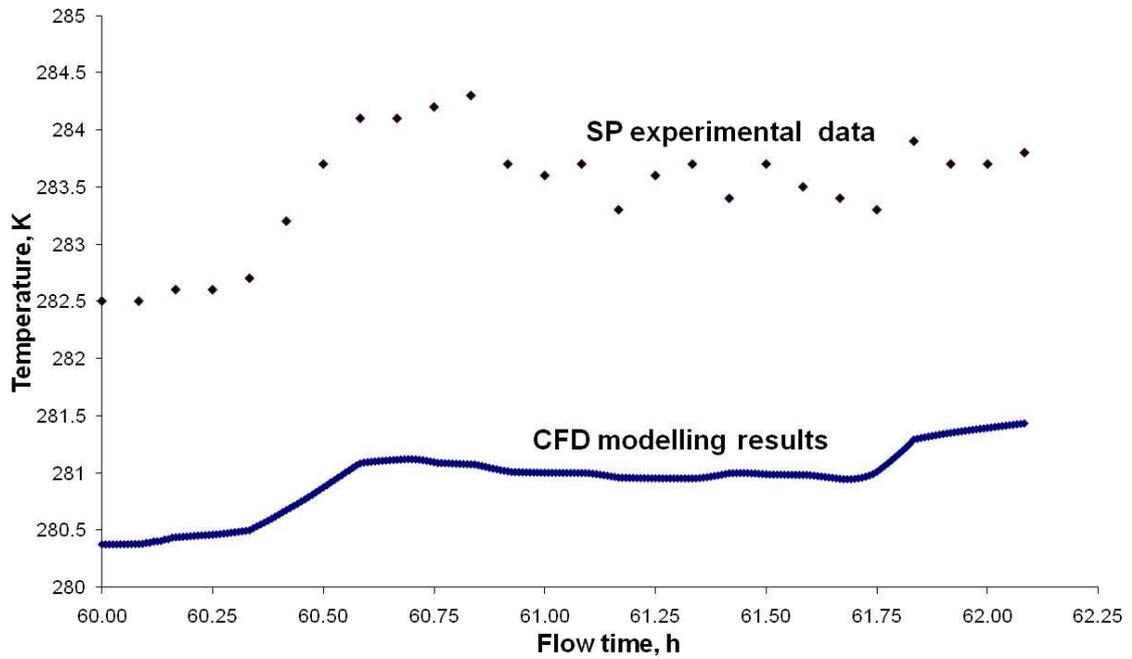

Figure 19 Comparison of the experimental and CFD results on the transient thermal state of the Lynx conductor

The difference between the numerical and experimental temperatures is between 2 and 3 degrees and the theoretical curve follows the general pattern in the variation of the experimental temperature. The discrepancy between the numerical simulation results and experimental data can be explained by the fact that the variation in the ambient temperature and the stochastic character of the change in the wind direction were not taken into account. Additionally, the resistivity of the conductor was assumed to be constant in CFD modelling (which reduces the temperature of the conductor by about 1 degree) and the precise value of emissivity of the conductor surface was not known. Finally, much detailed discretisation of experimental data in time is needed in order to create more accurate input data for CFD simulations.

6 Conclusions

- Comparison of the obtained numerical results with available experimental data demonstrates that the CFD technique provides an adequate level accuracy in prediction of the thermal state of the Lynx overhead conductor for both the steady and transient exploitation conditions.

- Comparison of numerical results obtained by CFD modelling and lumped parameter models (used in industrial standards) for the case, in which the cross wind velocity is 0.5 m/s, the ambient temperature is 293 K and the current is 433 A, indicates that there is a considerable headroom for increasing the ampacity of the Lynx overhead conductor.

- Convective heat transfer from the surface of the conductor can be calculated using the following derived correlations:

  $Nu=2.2555 \times Re^{0.3065}$ (cross wind);

  $Nu=1.5035 \times Re^{0.3038}$ (parallel wind).

- The increase of the temperature of the Lynx conductor with a darkened surface at the insolation level of 800 W/m^2 (corresponding to the mid-summer conditions) is about 5-6 degrees.

- CFD simulations indicate that for the typical operational conditions (the cross wind velocity of 0.5 m/s and the ambient temperature of 293 K) the time constant of the transient process is about 42-44 min when the current abruptly increases from 433 to 750 A. The time constant decreases if the current rises from 433 A to a higher level than 750 A and is about 28 min for a new current level of 866 A.

- Numerical results obtained demonstrate that that for the typical operational conditions (the cross wind velocity of 0.5 m/s and the ambient temperature of 293 K) the time constant of the transient process for the case in which the current abruptly decreases from 866 A to 433 A is about 66 min. The time constant of a cooling-down process is between 30-60 min for cases in which the decrease in the current is smaller.

- Theoretical results obtained in CFD simulations show that the time constant of the heating-up process is about 33 hours if the cross-wind velocity decreases from 15 to 2.5 m/s at the current of 433 A.

Currently further investigations are ongoing on the improvement of accuracy of CFD simulations to predict the thermal state of the Lynx conductor for various operational conditions.

References

IEEE Standard 738-1993 'IEEE Standard for Calculating the Current-Temperature Relationship of Bare Overhead Conductors' (1993), IEEE.

CIGRE 'Thermal Behaviour of Overhead Conductors' (1992), *ELECTRA* **144**.

Engineering Recommendation P27 (1986) 'Current Rating Guide for High Voltage Overhead Lines Operating in the UK Distribution System', Energy Network Association

Douglass D.A., Motlis Y. and Seppa T.O. (2000) 'IEEE's Approach for Increasing Transmission Line Ratings in North America' CIGRE 2000: 38th Session of the International Conference on Large High-Voltage Electric Systems, Paris, Aug. 27–Sept. 1, 2000.

Schmidt, N. (1997) 'Comparison between IEEE and CIGRE Ampacity Standards*', IEEE Transactions on Power Delivery,* Vol 14, pp. 1555-1562.

Morgan, V.T. (1982) 'The Thermal Rating of Overhead-Line Conductors. Part I. The Steady-State Thermal Model', *Electric Power Systems Research,* Vol. 5, pp. 119-139.

Howitt, W. B. and Simpkins, T. E (1971) 'Effect of elevated temperature on the performance of conductor accessories', IEEE Paper C 72 188-6

Chen, S.L., Black, W. Z. and Loard, H.W. (Jr) (2002) 'High-Temperature Ampacity Model for Overhead Conductors', *IEEE Transactions On Power Delivery*, Vol. 17, pp. 1136-1141.

Black, W. Z. and Byrd, W. R. (1983) 'Real time ampacity model for overhead lines', *IEEE Trans. Power App. Syst*., Vol. PAS 102, pp. 2289–2293.

Bush, R. A., Black, W. Z., Champion, T. C. and Byrd, W. R. (1983) 'Experimental verification of a real time program for the determination of temperature and sag of overhead lines'. *IEEE Trans. Power App. Syst.*, Vol. PAS 102, pp. 2284–2288.

Isozaki, M. and Iwama, N. (2002) 'Verification of forced convective cooling from conductors in breeze wind by wind tunnel testing'. Transmission and Distribution Conference and Exhibition 2002: Asia Pacific. IEEE/PES, 6-10 October, 2002. Vol.3, pp. 1890- 1894.

Tasic, D. (2000) 'A procedure for analysis of non-stationary heating states of ACSR conductor'. *Electronics and Energetics*, Vol. 139, pp. 83-94.

Foss, S. D., Lin S. H., Stilwell, H. R. and Fernandes, R. A. (1983) 'Dynamic thermal line ratings. Part II. Conductor temperature sensor and laboratory field test evaluation'. *IEEE Trans. on Power Apparatus and Systems*, Vol. PAS-102, pp. 1865-1873.

Hoffmann, K.A. and Chiang, S.T. (2000) 'Computational Fluid Dynamics', Vol. 2, the 4th Ed., 469 p., Engineering Education System.

Hoffmann, K.A. and Chiang, S.T. (2000) 'Computational Fluid Dynamics', Vol. 3, the 4th Ed., 175 p., Engineering Education System.

BS EN 50182-2001"Conductors for overhead lines. Round wire concentric lay stranded conductors".

Nomenclature

A	Cross sectional area, m^2
B	Constant
I	Electrical current, A
L	Latent heat of evaporation, J/mol
Nu	Nusselt number
P_c (q_c), $P_r(q_r)$, P_w	Heat losses due to convection, radiation and evaporation, respectively, W/m
P_J, P_M, $P_s(q_s)$, P_i	Heat gains due to Joule heating and ferromagnetic, solar and ionisation heating, respectively, W/m
Pr	Prandtl number
R	DC resistance of the conductor, Ω/km
Re	Reynolds number
$R(T_c)$	60 Hz AC resistance, Ω/m
$S_{heat\ source}$	Heat source term, W/m^3
T, T_a,	Temperature of air and ambient temperature, K

T_c, T_{al}, T_{st}	Temperature of the conductor, aluminium and steel part of the conductor, respectively, K
T_f	Film temperature, K
T_s	Temperature on the surface of the conductor, K
$c, c_{pc}, c_{pal}, c_{pst}$	Heat capacity of air, the conductor, aluminium and steel part of the conductor, respectively J/(kgK)
D	Diameter of the conductor, m
E	Energy, J
k_i	Coefficient taking into account probabilistic nature of ionization
L	Length of the conductor, m
M	Mass of the conductor, kg
P	Air pressure, Pa
T	Time, s
x_{ws}, x_{wa}	Mole fraction of water in atmospheric air and in air in the vicinity of free surface of water film on the conductor, respectively
u_i	velocity components in 3-D flows
u, v, ω	Gas velocity components along x, y and z-axis, respectively, m/s

Greek symbols

α_s	Absorptivity of conductor surface
λ, λ_c	Thermal conductivity of air and of the conductor, W/(m·K)
λ	Thermal conductivity of air, W/(m·K)
μ	Molecular viscosity, Pa·s
$\rho,$	Density, kg/m^3
Γ	Boundary

$\alpha_2, \alpha_3, \alpha_4$	Constants
$c_\mu,\ c_{\varepsilon 1},$	
$c_{\varepsilon 2},\ \sigma_k,$	
$\sigma_\varepsilon,\ \gamma_1,$	
γ_2, γ_3	
ϕ	Scalar parameter
$k,\ \varepsilon$	Turbulent kinetic energy and its dissipation, respectively, m^2/s^2
μ	Laminar viscosity, Pa·s
μ_t	Turbulence viscosity, Pa·s
$-\rho\overline{u'^2},\ -\rho\overline{\upsilon'^2},$ $-\rho\overline{\omega'^2}$ $-\rho\overline{u'\upsilon'},$ $-\rho\overline{u'\omega'}$ $-\rho\overline{\upsilon'\omega'}$	Reynolds stresses, Pa
σ	Normal stress, Pa
$\tau_{xx}, \tau_{xy}, \tau_{xz}$ $\tau_{yx}, \tau_{yy}, \tau_{yz},$ $\tau_{zx}, \tau_{zz}, \tau_{zy}$	Shear stress Pa

Superscripts

$\overline{}, '$	Mean and fluctuating components